

# Phenomenology of the vacuum in quantum electrodynamics and beyond

Dissertation

zur Erlangung des akademischen Grades  
doctor rerum naturalium (Dr. rer. nat.)

vorgelegt dem Rat der Physikalisch-Astronomischen Fakultät  
der Friedrich-Schiller-Universität Jena

von Dipl.-Phys. Babette Döbrich  
geboren am 31. Januar 1983 in München

Gutachter:

1. Prof. Dr. Holger Gies, Friedrich-Schiller-Universität Jena, Deutschland
2. Dr. Jörg Jäckel, Durham University, England
3. Prof. Dr. Gerald Dunne, University of Connecticut, USA

Tag der Disputation: 30. September 2011



# Phänomenologie des Vakuums in der Quantenelektrodynamik und Erweiterungen

## *Zusammenfassung*

Die Bestimmung von Kräften, die durch das Anlegen von Randbedingungen an die Quantenfluktuationen entstehen, oder die Beobachtung modifizierter Lichtausbreitung in externen Feldern, sind vielseitige Methoden um die Vakuumstruktur der Quantenelektrodynamik zu untersuchen. Für diese Untersuchungen kann das Vakuum als Medium verstanden und modelliert werden. Eine Erforschung der Eigenschaften dieses Mediums, kann nicht nur unser Verständnis der bekannten Wechselwirkungen testen, sowie erweitern, sondern stellt auch ein nützliches Werkzeug zur Suche nach Teilchen bei niedrigen Energien, die in Erweiterungen des Standardmodells vorhergesagt werden, dar.

In dieser Arbeit untersuchen wir zunächst die Geometrieabhängigkeiten von Fluktuationsmoden im Dirichlet-skalaren Analogon der Casimir-Polder-Kräfte zwischen einem Atom und einer Oberfläche mit beliebiger uniaxialer Struktur. Dazu verwenden wir eine Methode, die vollkommen nichtperturbativ im Höhenprofil ist. Wir parametrisieren die zum planaren Grenzfall veränderte Abstandsabhängigkeit anhand einer anomalen Dimension, die die Abweichung vom Potenzgesetz im planaren Fall quantifiziert. In numerischen Untersuchungen experimentell relevanter Strukturen finden wir ein universelles Regime der anomalen Dimension bei großen Abständen. Wir argumentieren, dass diese Universalität als Mittelung der relevanten Fluktuationen über Strukturen kleiner als der Atom-Platten Abstand interpretiert werden kann.

Sodann gehen wir zur Untersuchung modifizierter Lichtausbreitung als Test der Quantenvakuumstruktur über. Wir zeigen, dass eine Kombination starker, gepulster Magnete mit Gravitationswelleninterferometern nicht nur die Detektion von Starkfeld-QED-Effekten ermöglicht, sondern auch den zugänglichen Parameterraum hypothetischer Teilchen des “hidden sectors” erweitern kann. Wir zeigen auf, dass gepulste Magnete eine geeignete Starkfeldquelle sein können, um Quanten-Nichtlinearitäten zu erzeugen, da ihre Pulsfrequenz genau an den Bereich höchster Sensitivität moderner Gravitationswelleninterferometer angepasst werden kann.

Wir gehen an die Grenze derzeitiger Laborfeldstärken und schlagen eine neuartige Messanordnung vor, die auf der Verwendung von Hochintensitätslasern basiert. Es wird gezeigt, dass diese geeignet ist, um Axion-artige Teilchen und insbesondere das QCD Axion zu messen: Wir argumentieren, dass Testphotonen, die den Fokus einer Überlagerung Gaußscher Strahlen in Grundwellenlänge und frequenzverdoppelter Mode durchqueren, aufgrund ihrer zwischenzeitlichen Propagation als Axion-artiges Teilchen, eine Frequenzverschiebung erfahren können. Dieser Prozess ist für resonante Massen von der Größenordnung verwendeter Laserfrequenzen verstärkt. Wir zeigen, dass rein Laser-basierte Experimente sensitiv auf den eV Massenbereich der Axionen sind, und dadurch konventionelle Messanordnungen bezüglich des zugänglichen Massenbereichs ergänzen können.

Als neue Möglichkeit zur Erforschung des Parameterraums minigeladener Teilchen untersuchen wir zuletzt ein Licht-durch-Wand-Szenario in einem Magnetfeld, in welchem die Durchquerung der Barriere mittels eines virtuellen Teilchen-Antiteilchen Zwischenzustands vonstatten geht. Da die Wahrscheinlichkeit dieses “Tunnelprozesses” sehr von der Masse der Fluktuation abhängt, betrachten wir den ein-Loop Polarisationsensor im Magnetfeld vollkommen nichtperturbativ in einer optimierten Anordnung für Photonpropagation entlang der Magnetfeldlinien. Wir quantifizieren und diskutieren die Übergangswahrscheinlichkeit für eine ausgewählte Propagationsmode und geben damit eine erste Abschätzung für das gegenwärtige Entdeckungspotential für Licht-durch-Wand Experimente mit virtuellen minigeladenen Teilchen im Magnetfeld.

# Phenomenology of the vacuum in quantum electrodynamics and beyond

## *Abstract*

Determining forces that arise by the restriction of the fluctuation modes of the vacuum by the insertion of boundaries or the observation of altered light propagation in external fields is a versatile means to investigate the vacuum structure of quantum electrodynamics. For these quantum vacuum probes, the vacuum can be understood and effectively modeled as a medium. Investigating the properties of this medium cannot only test and broaden our understanding of known interactions but can also be a valuable tool in the search for particles at low energy scales which arise in extensions of the standard model.

In this thesis, we first study the geometry dependence of fluctuation modes in the Dirichlet-scalar analog of Casimir-Polder forces between an atom and a surface with arbitrary uniaxial corrugations. To this end we employ a technique which is fully nonperturbative in the height profile. We parameterize the differences to the distance dependencies in the planar limit in terms of an anomalous dimension quantifying the power-law deviation from the planar case. In numerical studies of experimentally relevant corrugations, we identify a universal regime of the anomalous dimension at larger distances. We argue that this universality arises as the relevant fluctuations average over corrugation structures smaller than the atom-wall distance.

Turning to modified light propagation as a probe of the quantum vacuum, we show that a combination of strong, pulsed magnets and gravitational-wave interferometers can not only facilitate the detection of strong-field QED phenomena, but also significantly enlarges the accessible parameter space of hypothetical hidden-sector particles. We identify pulsed magnets as a suitable strong-field source to induce quantum nonlinearities, since their pulse frequency can be perfectly matched with the domain of highest sensitivity of modern gravitational-wave interferometers.

Pushing current laboratory field-strengths to their limits, we suggest a novel setup based on employing high-intensity lasers. This is shown to be advantageous to the search for axion-like particles as well as the QCD axion: We observe that probe photons traversing the focal spot of a superposition of Gaussian beams of a single high-intensity laser at fundamental and frequency-doubled mode can experience a frequency shift due to their intermittent propagation as axion-like particles. This process is strongly enhanced for resonant masses on the order of the involved laser frequencies. We show that purely laser-based experiments are sensitive to axions in the eV mass range and can thus complement conventional setups with respect to the accessible mass region.

Finally, as a new means to scan the parameter space of minicharged particles, we investigate a light-shining-through-walls scenario in a magnetic field in which the barrier transition is achieved by virtual particle-antiparticle intermediate states. As the probability for this “tunneling” phenomenon to occur is highly dependent on the mass of the fluctuation, we consider the one-loop polarization tensor in the magnetic field fully non-perturbatively in an optimized alignment for photon propagation along the field lines. We quantify and discuss the transition probability for a selected propagation mode and therewith provide a first estimate for the discovery potential of light-shining-through-walls with virtual minicharged particles in a magnetic field.



# Contents

<b>1</b>	<b>Motivation</b>	<b>3</b>
<b>2</b>	<b>Basic concepts and relations</b>	<b>6</b>
2.1	Field theoretic prerequisites and light propagation in external fields . . . . .	7
2.1.1	Generating functional and the Casimir energy . . . . .	7
2.1.2	Effective Action and loop expansion . . . . .	8
2.1.3	The Heisenberg-Euler Lagrangian and birefringence . . . . .	10
2.2	Beyond classic light propagation in external fields . . . . .	12
2.2.1	Minicharged particles and the polarization tensor . . . . .	12
2.2.2	Axion(-like) particles and light that shines through walls . . . . .	17
2.2.3	Shedding light on the vacuum in the laboratory and with astrophysical sources . . . . .	21
<b>3</b>	<b>Geometry as vacuum probe: A nonperturbative treatment</b>	<b>23</b>
3.1	Devising a nonperturbative treatment for scalars . . . . .	24
3.1.1	Constrained-functional-integral approach and the Casimir-Polder limit . . . . .	24
3.1.2	Scalar forces in the plate-sphere configuration . . . . .	26
3.2	Results for uniaxially corrugated surfaces . . . . .	28
3.2.1	Sinusoidally shaped surfaces . . . . .	28
3.2.2	Sawtooth-like corrugation . . . . .	31
3.3	Probing with varied inhomogeneities . . . . .	32
<b>4</b>	<b>Advanced interferometry as a quantum vacuum probe</b>	<b>34</b>
4.1	Elements of the interferometric setup . . . . .	35
4.1.1	Strain & sensitivity at gravitational-wave interferometers . . . . .	35
4.1.2	Pulsed magnetic fields . . . . .	36
4.2	Estimated interferometric discovery potential . . . . .	39
4.2.1	Detection of the QED-induced strain . . . . .	39
4.2.2	Interferometry with MCPs and ALPs . . . . .	39
4.3	Benefits of pulsed fields and a logical upgrade . . . . .	42

<b>5</b>	<b>Searching for axion-like particles with high-intensity lasers</b>	<b>44</b>
5.1	Dynamics of the axion-photon interaction . . . . .	46
5.1.1	Equations of motion . . . . .	46
5.1.2	Parameterization of the fields . . . . .	48
5.1.3	Photon-axion conversion . . . . .	49
5.1.4	Axion-photon conversion . . . . .	54
5.2	The setup’s capabilities and perspectives . . . . .	58
5.2.1	Prospective exclusion limits on axions and ALPs . . . . .	58
5.2.2	Summary and outlook of the purely laser-based ALP search . . . . .	64
<b>6</b>	<b>LSW via virtual minicharged particles in a magnetic field</b>	<b>67</b>
6.1	The probability for LSW and a handling of the polarization tensor . . . . .	68
6.1.1	Setting the stage for LSW via virtual MCPs . . . . .	68
6.1.2	Polarization tensor in a magnetic field at zero incidence . . . . .	71
6.1.3	Transition amplitude in regimes of different field strength . . . . .	75
6.1.4	Transition amplitude for scalar minicharged particles . . . . .	84
6.1.5	Range of validity and general limitations . . . . .	84
6.2	MCP discovery potential for the $\perp$ mode . . . . .	85
6.2.1	Prospective exclusion bounds for minicharged fermions . . . . .	88
6.2.2	Fermionic resonances in the nonperturbative result . . . . .	92
6.2.3	Physics of the low-mass enhancement phenomenon . . . . .	93
6.3	Advantages and perspectives of “virtual LSW” . . . . .	96
<b>7</b>	<b>Résumé and concluding remarks</b>	<b>98</b>
	<b>Bibliography</b>	<b>101</b>
<b>A</b>	<b>Units, conventions and some useful numbers</b>	<b>115</b>
<b>B</b>	<b>The Heisenberg-Euler Lagrangian in constant external fields</b>	<b>117</b>
<b>C</b>	<b>On vacuum polarization in constant external magnetic fields</b>	<b>123</b>
<b>D</b>	<b>Numerical supplement for the geometric vacuum probe</b>	<b>130</b>
<b>E</b>	<b>ALPs in high-intensity lasers at reversed interaction order</b>	<b>134</b>
<b>F</b>	<b>LSW via virtual MCPs: Re-extracting the zero-field limit</b>	<b>138</b>



# Chapter 1

*“Prognosen sind schwierig,  
besonders wenn sie die Zukunft betreffen.”*  
zugeschrieben u.a. Niels Bohr

## Motivation

Since the rise of quantum field theories, the science of physics has undergone a remarkable acceleration of success in the accurate description of particle interactions. However, this brought about the need for a radical departure from classical conceptions of physics.

Taking for example the vacuum, which in its common perception is equivalent to the absence of all matter and energy, we find that it is rather permeated by fluctuations of all quantum fields, restricted only by the symmetries and conservation laws implemented in nature. This comes about naturally in quantum field theories as they combine the conceptions of quantum mechanics and special relativity. The former allows for energy to fluctuate sizably over short instances of time, as manifestation of the uncertainty principle; the latter in turn tells us that energy can be converted into matter. Therefore, the proper conception of the vacuum should be that of a medium whose characteristics can be altered distinctively if subject to external modifications.

It follows that one can think about altering and manipulating these quantum fluctuations in a specific way in order to test and broaden our understanding of particle physics. For instance, classic, i.e., well established means to probe the vacuum of quantum electrodynamics (QED) are to observe forces that come about by restricting vacuum fluctuation modes through the insertion of boundaries or to study the impact of the fluctuations on the propagation of light under the application of external electromagnetic fields.

The former vacuum probe dates back to 1948 and goes nowadays by the name of Casimir physics. It deals with the question of how forces that arise between objects through the modification of the fluctuation modes within the vacuum, depend on the properties of these bodies. This dependence had, considering variables such as the overall temperature, the conductivity of the objects or geometric properties, for a long time only been well understood under the most idealized conditions. For example, spatial configurations different from plane-parallel geometries had widely been dealt with through perturbative approximations with respect to a small geometric parameter accounting for the deviation of the objects from flatness. However, since quantum vacuum fluctuations

occur on all length scales, such approximations often were doomed to failure in describing experimental setups. In the following, a method and technique that overcomes these perturbative approximations will constitute also a part of this work.

The latter vacuum probe which dates back to work of W. Heisenberg and his student H. Euler in 1936, deals with the modification of light propagation in external fields and has among its most famous manifestations the prediction of vacuum birefringence, whose detection is coming into reach as a result of the rapid advancement of optical techniques and technology.

Here, the underlying physics is the spontaneous creation and annihilation of virtual electron-positron pairs whose dynamics are altered under the application of external fields, subsequently modifying the propagation properties of light to which these pairs couple. Proposed experiments aimed at demonstrating these vacuum nonlinearities would test the predictions of *quantum* electrodynamics in the regime of *macroscopic* fields. These are therefore a worthwhile endeavor themselves, thus playing a role in the following.

However, there is a second, maybe even stronger motivation for experiments and theoretical analyses for optical probes of the quantum vacuum. Despite the enormous success of the theories of particle interactions, namely the standard model, some conceptual deficiencies persist (e.g., fine-tuning in the context of CP-violation in quantum chromodynamics (QCD), triviality problem in QED and the Higgs sector, hierarchy, ...) and unified theories reconciling gravity with the other known interactions still await experimental confirmation.

Tackling the remaining shortcomings of the standard model and the attempt of finding a suitable extension often comes along with the proposition of particles that have managed to elude experimental detection so far. Moreover, the belief that yet undiscovered particles most likely exist is underlined by the fact that there is still a lack of reliable knowledge about the nature of dark matter (and dark energy). While proposed new particles are often expected to “hide” at large masses and thus demand for a search at the largest accessible energy scales as, e.g., provided at particle colliders, there exists also a number of good candidates for physics beyond the standard model with much lower masses at, or just below the electron volt scale, where so far only neutrinos have been found to exist. Such particles, in order to have evaded their detection, must be very weakly coupled to the known particle content of the standard model and are thus often subsumed by the term “WISPs”, being short-hand for “weakly-interacting slim particles”. However, assertions of physics beyond the standard model run the risk of remaining but a playground for theoreticians as long as no connection to experimental realities is made.

In consequence, one may be tempted to reverse the concept of investigating the vacuum structure by optical techniques as introduced above: Knowing well how the familiar particle content of the standard model can alter the propagation of light, one can ask *if* and

---

*how* distinct optical signatures can tell us about yet undiscovered particles that may exist at the energy scale that can be screened through optical, i.e., low-energy, techniques. With some luck such experiments, although less involved than collider experiments in terms of manpower and effort, can even teach us about physics at higher energy scales, if, e.g., the WISP is a (pseudo-)Goldstone boson originating from a symmetry breaking at higher energy scales beyond current experimental access.

In large parts of this work, we follow this reasoning from a phenomenological viewpoint. Discriminating conjectured new particles by their very basic properties such as spin and effective coupling structure only, we investigate how we can confirm, exclude or restrict their existence in increasing regions of their parameter space by suggesting experimental settings which can be feasibly realized today or in the next few decades.

In summary, the aim of this work is to carry forward and deepen some earlier concepts as well as to suggest new, original probes of the quantum vacuum in the light of experimental progress in the field.

Accordingly, after introducing the necessary methodological and conceptual prerequisites in chapter 2, we will begin by investigating the influence of non-planar surfaces in the context of Casimir-Polder forces in chapter 3, as motivated by ongoing atomic scattering experiments. In chapter 4, we take on the idea of high-precision interferometry as a tool for the investigation of the vacuum structure and qualitatively extend it in the face of the developments of current and future gravitational-wave interferometers and state of the art pulsed magnets from high-magnetic field laboratories. Furthermore, rapid progress in the field of high-intensity lasers prompts us to explore their capabilities within the search for axions and axion-like particles, as discussed in chapter 5. Finally, in chapter 6, we set out to advance the understanding of a “light-shining-through-walls” scenario which accounts for barrier-transition through virtual particle-antiparticle states in magnetic fields, where up to now only real particles had played a major role.

*The compilation of this thesis is by the author alone, however, a great deal of the presented material has been worked out and published in various articles in kind collaboration with different authors. The study on Casimir-Polder forces of Chapt. 3 was carried out with Maarten DeKieviet and Holger Gies [138, 139]. The proposal for the interferometric setup of Chapt. 4 and the purely laser-based axion search of Chapt. 5 have been elaborated with Holger Gies, see [162, 163] and [183, 184], respectively. Lastly, the results for light-shining-through-walls scenario via virtual minicharged particles, see Chapt. 6, have been obtained in collaboration with Holger Gies, Norman Neitz and Felix Karbstein [204].*

# Chapter 2

“ πάντες ἄνθρωποι τοῦ εἰδέναι  
ὀρέγονται φύσει.”  
Aristoteles, Metaphysik

## Basic concepts and relations

The results and methods of this thesis largely rely on the functional integral formulation of quantum field theory. With hindsight to the concepts and techniques employed in this thesis, we begin by reviewing some of its basic objects and relations in Sect. 2.1. Surely, we cannot reproduce rigorous derivations of all the quantities that are needed here, and reference<sup>1</sup>, e.g., [1–6] which constitute detailed introductions to the field and contain results that will be the basis for our subsequent investigations.

For our purposes, we start from the generating functional in quantum field theories and introduce the concept of the effective action, being the essential starting point of all subsequent phenomenological investigations. Necessarily, we thereby touch on the definition of the vacuum energy, being a vantage point for the treatment of Casimir-type problems. Lastly, we discuss the expansion of the effective action in numbers of loops.

Starting from there, we will review the one-loop correction modifying photon propagation in external (electro-)magnetic fields. This allows us to discuss the related observables and phenomenological implications of light propagation in external fields. Finally, in Sect. 2.2, we introduce and motivate a number of hypothetical, weakly-interacting particles at the (sub-)eV scale, namely WISPs. As will be discussed, these particles can - if realized in nature - modify the phenomenology of light propagation presumably in such a way that they are distinctively separable from the standard model “background”. This general overview in turn enables us to suggest and discuss three distinct experiments that could help to enlarge our knowledge on the allowed properties of such particles in later chapters.

---

<sup>1</sup>Of course, references to general textbooks of quantum field theory are by no means complete and generally suffer from a strong bias by the author. This being said, in this chapter we will take the liberty of referring to selected textbooks for a few general concepts that present the topic in question most coherently from the author’s point of view.

## 2.1 Field theoretic prerequisites and light propagation in external fields

### 2.1.1 Generating functional and the Casimir energy

In the functional integral formulation of Euclidean<sup>2</sup> QFT, a central object is the generating functional  $\mathcal{Z}[J]$ , which is the vacuum-to-vacuum transition amplitude in the presence of an external source  $J(x)$ , reading

$$\langle 0|0\rangle_J = \mathcal{Z}[J] = \int \mathcal{D}\varphi e^{-S[\varphi] + \int_x J\varphi} = e^{W[J]} . \quad (2.1)$$

Here,  $\varphi$  is to be understood as a superfield vector containing all the field degrees of freedom which are meant to be quantized. Accordingly, in  $J\varphi$  a contraction over all associated indices is understood.  $S[\varphi]$  is the corresponding classical or microscopic action for these fields. In addition, we have defined  $W[J]$ , which is the so-called Schwinger functional, see below. The integral in Eq. (2.1) over arbitrary high momentum modes can generate divergencies which necessitate regularization and renormalization procedures.

By multiple functional differentiation of  $\mathcal{Z}[J]$  with respect to  $J$ , one can obtain the  $n$ -point functions or correlators of  $n$  fields:

$$\langle \varphi(x_1) \dots \varphi(x_n) \rangle = \frac{\int \mathcal{D}\varphi \varphi(x_1) \dots \varphi(x_n) e^{-S[\varphi] + \int_x J\varphi}}{\int \mathcal{D}\varphi e^{-S[\varphi]}} = \frac{1}{\mathcal{Z}[0]} \frac{\delta^{(n)} \mathcal{Z}[J]}{\delta J(x_1) \dots \delta J(x_n)} \Big|_{J=0} . \quad (2.2)$$

In accordance with physical intuition, field configurations in the Euclidean formulation of QFT are weighted by an exponential of their action functional, which also accentuates the close analogy to the concepts of statistical mechanics. In Eq. (2.1), the Schwinger functional  $W[J]$  generates all connected  $n$ -point functions [1]. More importantly for our purposes, we note that  $W[J]$  is related to the vacuum or ground-state energy in the presence of an external source, as  $W[J] = \ln \mathcal{Z}[J]$ . On the other hand, the Casimir energy of a system of bodies is determined by the alteration of this ground-state<sup>3</sup> energy caused by the presence of boundaries which impose constraints on the fluctuating fields, cf., e.g., [5].

---

<sup>2</sup>In this chapter, we work in a Euclidean formulation, where the time variable has been rotated as  $t \rightarrow t_E/i$  with Euclidean time  $t_E$  by means of an analytic continuation for convenience. In later chapters, in particular when considering the dynamics for, e.g., photon or axion fields, we have to employ the Minkowski metric as given in Appendix A in order to preserve a causal structure.

<sup>3</sup>What makes the Casimir effect particularly peculiar, is of course the fact that there is no active external source but rather a passive deformation of the ground state due to the insertion of boundaries. In the formalism that will be employed in our studies, we will see, however, that the boundaries are effectively implemented as such source terms. Let us also emphasize that the understanding of the Casimir forces being caused by a ground-state shift is meant to give an intuitive picture, but one should be cautious in taking it too seriously cf., e.g., [7].

This ground-state shift is measurable due to the resulting Casimir forces [8] between the bodies and Casimir-Polder forces [9] between atoms and surfaces. Thus, to be more precise, Casimir forces arise from the Casimir interaction-energy, corresponding to the part of the ground state shift which is dependent on the relative position and orientation of the bodies, whereas Casimir self-energies of the objects do not contribute to the Casimir force. In this work, starting from Eq. (2.1), we introduce a nonperturbative treatment of Casimir-Polder forces of scalar fields in Chapt. 3 and apply the formalism to uniaxially corrugated surfaces of experimental interest.

### 2.1.2 Effective Action and loop expansion

A particularly useful way to store the *same* information as in Eq. (2.1) is through the so-called *effective action*  $\Gamma$ , as it governs the dynamics of the expectation value of the quantum field [1, 2]. For our purposes it will become relevant in the studies of light propagation within a vacuum polarized by external fields. In this context, we are certainly not interested in the microscopic details of vacuum polarization but are rather prompted to employ an effective theory containing only the macroscopic degrees of freedom in order to extract experimentally accessible quantities. Following Eq. (2.2), one defines the classical field  $\Phi$  as the field expectation value in the presence of a source

$$\langle \varphi(x) \rangle_J = \frac{1}{\mathcal{Z}[J]} \frac{\delta \mathcal{Z}[J]}{\delta J(x)} = \frac{\delta W[J]}{\delta J(x)} \equiv \Phi(x), \quad (2.3)$$

whilst the effective action  $\Gamma$  is defined as the Legendre transform of the Schwinger functional  $W[J]$  encountered above:

$$\Gamma[\Phi] = \sup_J \left( \int J\Phi - W[J] \right). \quad (2.4)$$

Here, as one has to find the supremum of  $(J\Phi - W[J])$  with respect to  $J$ ,  $J$  effectively becomes a function of  $\Phi$ . Taking the functional derivative of  $\Gamma[\Phi]$  with respect to  $\Phi$ , one has

$$\frac{\delta \Gamma[\Phi]}{\delta \Phi(x)} = \int_y \frac{\delta J(y)}{\delta \Phi(x)} \Phi(y) + J(x) - \int_y \frac{\delta W[J]}{\delta J(y)} \frac{\delta J(y)}{\delta \Phi(x)} \stackrel{(2.3)}{=} J(x). \quad (2.5)$$

As desired, Eq. (2.5) shows that  $\Gamma[\Phi]$  indeed governs the dynamics of the field expectation value, i.e., if the effective action  $\Gamma[\Phi]$  is known, it is in principle easy to calculate the dynamics of the system with all quantum fluctuations already accounted for.

Lastly, in order to find a conditional equation for  $\Gamma[\Phi]$ , we combine its definition from Eq. (2.4) with the definition of the Schwinger functional  $W[J]$ , cf. Eq. (2.1), resulting in

$$e^{-\Gamma[\Phi]} = \int \mathcal{D}\varphi e^{-S[\Phi+\varphi] + \int \frac{\delta \Gamma[\Phi]}{\delta \Phi} \varphi}, \quad (2.6)$$

where a shift of variables  $\varphi \rightarrow \varphi + \Phi$  has been employed.

However, taking a close look at the structure of Eq. (2.6), it is suggestive that finding an exact expression for  $\Gamma[\Phi]$  is highly unlikely for interacting theories, in particular in a nonperturbative setting. Thus, one has to employ an approximate expression for  $\Gamma[\Phi]$  suited to the physical problems under consideration.

For our<sup>4</sup> purposes, the suited tool is the loop expansion of the effective action. For this one uses that the expansion of Eq. (2.6) in powers of  $\hbar$  (which we temporarily reinstate here) can be mapped onto the graphical expansion in the number of loops [1, 2]. In this expansion, the order of  $\hbar$  counts the number of loops. After a formal substitution  $\varphi \rightarrow \sqrt{\hbar}\varphi$ , the action  $S[\phi]$ , where  $\phi = \Phi + \varphi$ , can be expanded about the classical field

$$\begin{aligned}
 -S[\phi] + \int \frac{\delta\Gamma[\Phi]}{\delta\Phi} \sqrt{\hbar}\varphi &= -(S[\phi])_{\phi=\Phi} \\
 - \int \left( \frac{\delta S[\phi]}{\delta\phi} \right)_{\phi=\Phi} \sqrt{\hbar}\varphi + \int \frac{\delta\Gamma[\Phi]}{\delta\Phi} \sqrt{\hbar}\varphi - \frac{\hbar}{2} \int \varphi \left( \frac{\delta^2 S[\phi]}{\delta\phi\delta\phi} \right)_{\phi=\Phi} \varphi &+ \mathcal{O}(\hbar^{3/2}). \quad (2.7)
 \end{aligned}$$

Above, the first term on the right hand side is the tree level interaction  $\Gamma^{(0)} = S$  where the index assigned to  $\Gamma$  shall denote  $\mathcal{O}(\hbar^0)$ . Thus, the second and third term in Eq. (2.7) are already of order  $\mathcal{O}(\hbar^{3/2})$  in total (as the difference between the classical and the full effective action is of  $\mathcal{O}(\hbar)$  at least) and only the fourth term on the right hand side of Eq. (2.7) contributes to  $\Gamma^{(1)}$ . Therefore, in summary, the one-loop effective action reads

$$e^{-\Gamma^{(1)}[\Phi]} = \int \mathcal{D}\varphi \exp \left[ -\frac{1}{2} \int_x \int_y \varphi(x) \left( \frac{\delta^2 S[\phi]}{\delta\phi(x)\delta\phi(y)} \right)_{\phi=\Phi} \varphi(y) \right], \quad (2.8)$$

which in terms of practical evaluations constitutes an enormous simplification as compared to Eq. (2.6). Of course, one has to keep in mind that Eq. (2.8) is only a first-order perturbative<sup>5</sup> approximation in the number of loops and its applicability has to be always assured through self-consistent results. In  $\Gamma^{(1)}[\Phi]$ , the remaining functional integration over the fields  $\varphi$  is now of Gaußian type and can thus be carried out, such that all physical information is stored within the fluctuation matrix  $S^{(2)} = \delta^2 S / \delta\phi(x)\delta\phi(y)$  (the evaluation of the fluctuation matrix at  $\Phi$  is implicitly understood in the following). However, the result of the Gaußian integration depends on the nature of the field content considered in  $\varphi$ . Thus, we now close these general considerations and explore their applicability in the context of experimentally relevant vacuum probes.

---

<sup>4</sup>Certainly, means exist to find also nonperturbative, approximate solutions to Eq. (2.6), see, e.g., [10, 11]. However, the loop expansion provides a well-established access to the problems considered in this work.

<sup>5</sup>Note that in the following, the terminology “nonperturbative” on the level of the one-loop approximation is to be understood as “nonperturbative in the coupling strength”.

### 2.1.3 The Heisenberg-Euler Lagrangian and birefringence

In the following, we briefly review how the properties of the vacuum are effectively modified within external electromagnetic fields: Accounting for one-loop fermionic corrections in QED, one obtains the Heisenberg-Euler Lagrangian [12–14] which encodes the effect of the charged fermion fluctuations as effective self-interaction of the electromagnetic field.

As we ultimately want to consider light propagation within external electromagnetic fields, the action entering Eq. (2.8) is the action of quantum electrodynamics

$$S = \int \left( \bar{\psi} (i\mathcal{D} - m) \psi - \frac{1}{4} F_{\mu\nu} F^{\mu\nu} \right), \quad (2.9)$$

where, as common,  $\psi$  and  $\bar{\psi} = \psi^\dagger \gamma_0$  denote the Dirac spinor fields and we have abbreviated  $\mathcal{D} = \gamma_\mu (\partial^\mu - ieA^\mu)$ , see also the conventions as summarized in App. A.

Note that the variation  $S^{(2)} = \delta S^2 / (\delta A \delta A)$ , as well as the mixed entries of the fluctuation matrix  $S^{(2)} = \delta S^2 / (\delta \psi \delta A)$  are  $A$ -independent, and therefore of no interest to us. Thus, from Eq. (2.9) it remains to evaluate  $S^{(2)} = \delta S^2 / (\delta \bar{\psi} \delta \psi)$ , where in the variation with respect to  $\bar{\psi}$ , one has to recall that a minus sign enters due to the fermionic nature of  $\psi$  and  $\bar{\psi}$ . Following Eq. (2.8), the one-loop effective action thus reads

$$\Gamma^{(1)}[A] = -i \ln \det (-i\mathcal{D} + m). \quad (2.10)$$

Note that the overall minus sign enters through the fermionic Grassmann integration. Also, we have reinstated the  $i$  belonging to the Lorentzian signature. For constant<sup>6</sup> (or approximately also very slowly varying) external fields, the effective action can be calculated exactly and yields the famous Heisenberg-Euler effective action. In App. B, the evaluation of Eq. (2.10) for a constant magnetic background field is reviewed and the result for the general situation of nonvanishing electric and magnetic fields is motivated. Of particular relevance is the limit of *weak field strengths*. As a rule, in experimentally relevant situations the external fields do not exceed the so-called critical field strength of QED:  $E_{\text{crit}} = B_{\text{crit}} = m^2/e$ , in which case the effective Lagrangian can be given as an algebraic expression. Following Eq. (B.20), the one-loop order Lagrangian in the leading order weak-field limit reads

$$\mathcal{L}_{\text{eff}} = \frac{1}{2} (\vec{E}^2 - \vec{B}^2) + \frac{2\alpha^2}{45m^4} (\vec{E}^2 - \vec{B}^2)^2 + 7 \frac{2\alpha^2}{45m^4} (\vec{E}\vec{B})^2. \quad (2.11)$$

In effect, Eq. (2.11) provides us with the macroscopic effective interaction for the electromagnetic fields, in which the underlying microscopic heavy degrees of freedom, i.e., the electron-positron fluctuations have been integrated out. Obviously, the first term in

<sup>6</sup>In the extensive review on Heisenberg-Euler Lagrangians in [15], in addition some solvable non-constant field configurations are discussed.



Eq. (2.11) constitutes the classic Maxwell Lagrangian, while the second and third term now account for effective self-interactions of the fields. This self-interaction is, however, strongly suppressed by virtue of the combined factor  $\alpha^2/m^4$ , which outmatches typical experimentally attainable field strengths squared, see, e.g., App. A.

A particularly intuitive picture of the phenomenological implications resulting from this self-interaction can be obtained by assigning two tensorial quantities, namely a permittivity  $\vec{\epsilon}$  and a magnetic permeability  $\vec{\mu}$  to the vacuum, which are classically only properties of a medium. Accordingly, one can introduce a dielectric displacement  $\vec{D}$  and an H-field  $\vec{H}$  for the vacuum as

$$\vec{D} = \frac{\partial}{\partial \vec{E}} \mathcal{L}(\vec{E}, \vec{B}), \quad \vec{D} = \vec{\epsilon} \vec{E}, \quad (2.12)$$

$$\vec{H} = -\frac{\partial}{\partial \vec{B}} \mathcal{L}(\vec{E}, \vec{B}), \quad \vec{B} = \vec{\mu} \vec{H}. \quad (2.13)$$

Dividing the electromagnetic fields into contributions of a probe photon field and an external background part, the tensorial quantities  $\vec{\epsilon}$  and  $\vec{\mu}$  can then be used to compute an *index of refraction*  $n$  of the polarized vacuum [16–21], see also [6, 22]. In practical applications, the dispersive properties of the QED vacuum are most favorably<sup>7</sup> tested in an external magnetic field. Thus, in the situation of an external magnetic field alone, pointing, e.g., along the spatial 3-direction, one finds that

$$n_{\perp} = \sqrt{\epsilon_{22} \mu_{33}} \approx 1 + \frac{8}{45} \frac{\alpha^2}{m^4} \vec{B}^2 \sin^2 \theta \quad (2.14)$$

$$n_{\parallel} = \sqrt{\epsilon_{33} \mu_{22}} \approx 1 + \frac{14}{45} \frac{\alpha^2}{m^4} \vec{B}^2 \sin^2 \theta, \quad (2.15)$$

for probe beams polarized orthogonally ( $\perp$ ) or in parallel ( $\parallel$ ) to the plane spanned by the propagation direction of the photons and the external field. Here,  $\theta$  denotes the angle between the magnetic field and the direction of propagation of the probe beam. From Eqs. (2.14) and (2.15) it follows that light effectively travels at a reduced<sup>8</sup> phase velocity  $v = c/n$  in the external field. As the indices of refraction differ for the two polarization components, the polarized vacuum is found to be *birefringent*. In consequence, for a linearly polarized probe beam in the magnetic field, the polarization components acquire a relative phase shift and thus an induced *ellipticity* can be an observable of light-light interaction, see Fig. 2.1.

Over the course of several years, a number of experiments have been designed and carried out to test vacuum birefringence in terms of high-sensitivity polarimetry in strong

<sup>7</sup>For example, note that although modern accelerator cavities can reach (alternating) peak electric field strengths of  $\mathcal{O}(10)\text{MV/m}$  [23], common superconducting dipole magnets provide field strengths of  $\mathcal{O}(10)\text{T}$  which constitutes a larger number in units of the critical field strength of QED, cf. App. A.

<sup>8</sup>As stressed below Eq. (2.8), here we work not only in the limit of weak fields but also in the one-loop approximation implying that  $n$  cannot deviate much from one.

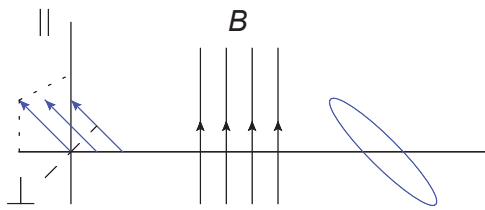


Figure 2.1: Sketch of a polarized light beam (in blue) traversing an external magnetic field (from left to right). Unequal phase velocities for the polarization components induce ellipticity and lead to vacuum birefringence.

dipole magnets, see, e.g., [24–28]. However, the sensitivity limits achieved so far are still above those necessary to observe the QED effect. Nevertheless, as the induced ellipticity grows with greater probe-beam wave-length [6], recent advances in X-ray polarimetry [29] in combination with X-rays generated by photons back-scattered from electron beams, see, e.g., [30–32] or free-electron lasers [33] seem to bring the detection of vacuum birefringence as well as other strong-field physics effects closer to our reach, see, e.g., [34–39].

## 2.2 Beyond classic light propagation in external fields

To segue from “classic” to somewhat “exotic” features of light propagation, let us now turn the argument of the previous section around. As we can infer from polarizing the *known* particle content within the vacuum that light propagation can be specifically altered, can in turn modified light propagation tell us something about an underlying particle content which is *unknown* so far?

Indeed, the phenomenology of light propagation in connection with a number of weakly-interacting slim (or sub-eV) particles (WISPs) that are representative for a wealth of possible “new physics” at low energy scales has been worked out in the literature, cf., e.g., [40–42] for recent overviews. Therein, focusing on the effective coupling of the WISPs to the electromagnetic field is certainly motivated by the fact and also optimal in the sense that QED, owing to its comparably simple structure, is the theory which allows for the most precise theoretical predictions as well as the most well-controlled experimental tests at the same time, see, e.g., [43]. In summary, our main concern will be to investigate how modern experimental advances can be utilized in the detection of QED nonlinearities and the search for new physics at the (sub-)eV scale.

### 2.2.1 Minicharged particles and the polarization tensor

#### Who’s in charge? Coupling the visible to the hidden sector

Minicharged particles (MCPs) arise in a number of extensions of the standard model. Most prominently, they can emerge in theories which contain an extra, hidden U(1) gauge

group [44, 45], such as, e.g., in string theories, cf. [46, 47]. Here, the term “hidden” should reflect the fact that no particles going along with this extra gauge group have been observed so far. However, their existence would be pointless if there were no interactions between standard model particles and the sector of the hidden particles at all. Thus, it is generically assumed that the hidden sector connects to the particle content of the standard model through very heavy messenger particles mediating between both sectors and thus providing for an effective coupling between the respective light particles that are accessible to us in experimental searches.

Following [44], for a model of minicharged fermions, one can, e.g., consider an effective extension of the QED Lagrangian of Eq. (2.9):

$$\mathcal{L} = -\frac{1}{4}F_{\mu\nu}F^{\mu\nu} - \frac{1}{4}B_{\mu\nu}B^{\mu\nu} - \frac{1}{2}\chi F_{\mu\nu}B^{\mu\nu} + e\bar{\psi}A\psi + e_h\bar{h}\beta h, \quad (2.16)$$

where  $B^{\mu\nu}$  now labels the field strength tensor of a hidden photon (also referred to as paraphoton) and  $h$  labels hidden sector Dirac fermion fields with coupling  $e_h$ . In Eq. (2.16) we have omitted mass and kinetic terms for the fermion fields for simplicity. Note that also the hidden photon can have a mass term, allowing for direct photon-hidden photon oscillations, see below. The parameter  $\chi$  is the so-called kinetic mixing<sup>9</sup> parameter, which encodes the effective coupling (kinetic mixing) strength between the hidden sector and the standard model sector through the messenger particles as discussed above. Now, upon diagonalization of Eq. (2.16) with respect to the mixing term through a shift  $B_\mu \rightarrow B_\mu - \chi A_\mu$ , one finds that the hidden fermions  $h$  couple to the photons and acquire an electric charge  $-(\chi e_h) \equiv \epsilon e$ , which is denoted as minicharge, and  $\epsilon$  is a dimensionless number quantifying the fractional charge of the minicharged particle. Note that this is consistent with Dirac’s charge quantization condition, cf. [48]. In the following, such minicharged particles<sup>10</sup> with mass  $m_\epsilon$  will be subject to phenomenological investigations.

### Light propagation in distinct limits: The polarization tensor in external fields

In essence, as once more fermionic fluctuations are considered, one might be tempted to think that the previous review on modified light propagation can be straightforwardly adopted if the fractional charge of the minicharges is accounted for. However, as an MCP could be much lighter<sup>11</sup> than the electron, quantum-induced phase-velocity shifts have to

<sup>9</sup>For a discussion of the phenomenological implications of “magnetic mixing” which involves coupling of the hidden to the visible sector by virtue of their *dual* field strength tensors, see [48, 49].

<sup>10</sup>Starting from a theory in the hidden sector resembling scalar QED, one can also think of charging hypothetical spin-zero bosons in a similar manner cf., e.g., [50]. In the following, we mainly focus on fermionic minicharges, thus the acronym ‘MCP’ will refer to fermions in all subsequent chapters apart from Chapt. 6 where minicharged bosons and fermions are both explicitly investigated.

<sup>11</sup>Since optical experiments are naturally well apt to probe the (sub-)eV region, we will mainly focus on mass scales  $\mathcal{O}(\text{eV})$  and smaller, although larger minicharge masses are also conceivable.

be calculated to all orders in the field strength parameter  $\epsilon e B/m_e^2$  and the approximation of weak field strength  $Be \ll m^2$  as used to arrive at the simple expression for QED in Eq. (2.11) cannot be employed here. Also, minicharge masses could easily be smaller than a further length scale which is implicit in this study, namely the frequency  $\omega$  of the employed probe photons, indicating that also pair production has to be accounted for in the following.

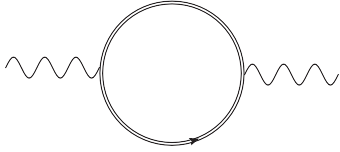


Figure 2.2: Sketch of photon (wiggly lines) propagation in an external field as incorporated in the one-loop polarization tensor. The dressed loop indicates an arbitrary number of couplings of the fermion loop to the external field. The imaginary part of the polarization tensor is associated with absorption (“stimulated” pair production) while the real part relates to dispersive effects of photon propagation.

Accordingly, in order to discuss light propagation beyond the weak-field limit, it is useful to specialize the one-loop effective action, cf. Eq. (2.10), to photon propagation in a constant external magnetic background-field, cf. Fig. 2.2 by introducing the polarization tensor  $\Pi^{\mu\nu}$ , see also App. C. The one-loop effective action then reads

$$\Gamma^{(1)}[A] = -\frac{1}{4} \int_x F_{\mu\nu}(x) F^{\mu\nu}(x) - \frac{1}{2} \int_x \int_{x'} A_\mu(x) \Pi^{\mu\nu}(x, x'|B) A_\nu(x'). \quad (2.17)$$

From Eq. (2.17) one can directly evaluate the equations of motion of the photon within the background field. Employing translational invariance, the polarization tensor satisfies  $\Pi^{\mu\nu}(x, x') = \Pi^{\mu\nu}(x - x')$ . Upon variation of the action, one obtains in momentum space

$$(k^2 g^{\mu\nu} - k^\mu k^\nu + \Pi^{\mu\nu}(k|B)) A_\nu(k) = 0, \quad (2.18)$$

as the equation of motion for the photon field. Above,  $k^2 = k_\mu k^\mu$  and  $|\vec{B}| = B$ . Depending on the spatial direction of the external magnetic field in Eq. (2.18), it is possible to decompose the polarization tensor appropriately, see, e.g., [52]. This allows to study the propagation of the different polarization states of the photons independently. In particular, for  $\vec{k} \not\parallel \vec{B}$ , the polarization tensor can be decomposed with respect to the  $\parallel$  and  $\perp$  polarization modes as defined below Eq. (2.15), such that Eq. (2.18) results in a simple “light cone condition”

$$k^2 + \Pi_{\perp/\parallel} = 0 \quad \leftrightarrow \quad v^2 + \frac{\Pi_{\perp/\parallel}}{|\vec{k}|^2} - 1 = 0. \quad (2.19)$$

Here,  $\Pi_{\perp/\parallel}$  denote scalar functions, cf. App. C for details. Above, we have again employed the phase velocity of the probe beam  $v = \omega/|\vec{k}| = c/n$  such that, as in Eqs. (2.14) and

(2.15) we can extract the indices of refraction  $n_{\perp/\parallel}$ . However, starting from Eq. (2.19) it becomes easier to discuss light propagation beyond the weak field limit and for the situation where the mass of the fluctuating fermion lies below the scale set by  $\omega$ .

Notably, the first finding is that  $n_{\perp/\parallel}$  develops an *imaginary part* for  $2m < \omega$  being associated to the creation of particle-antiparticle pairs from the photons. Note carefully, that in contrast to this “stimulated” pair production, pair production from the pure vacuum, as discussed in the context of the derivation of the Heisenberg-Euler effective Lagrangian in App. B, is only possible in the presence of external electric fields, see, e.g. [15].

In terms of observables, the imaginary refractive index leads to an unequal *attenuation* of the respective polarization components, i.e., a *dichroism*, and thus to a *rotation* of the polarization<sup>12</sup> of the beam, cf. Fig. 2.3. Its detection could<sup>13</sup> thus be a hint of the existence of minicharged particles in experiments with optical lasers, if  $2m_\epsilon < \omega \ll m$ .

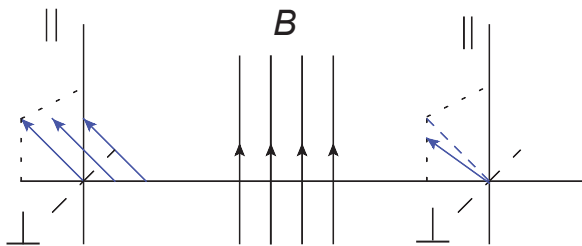


Figure 2.3: Sketch of rotation of a polarized light beam (in blue) traversing a magnetic field (from left to right). Unequal attenuation of the polarization components leads to a vacuum dichroism.

To see this, a treatment of the polarization tensor in the limit of large frequencies is required, being less relevant for the QED situation with optical photons. Nevertheless, this treatment had been worked out even before the idea of minicharged particles had been put forward. In [54], W. Tsai and T. Erber derived approximate indices of refraction for studies of high energy photons ( $\omega \gg m$ ) traversing external magnetic fields. These found their first application [50, 55] in the context of minicharges as a possible explanation for a rotation signal of a probe beam within a magnetic field as reported by the PVLAS collaboration in 2005 [24]. These observations were, however, later found to be instrumental artifacts [25], but promising upgrades of the PVLAS experiment are under way [56].

<sup>12</sup>For a detailed discussion of the connection between attenuation and rotation in this context, the reader is referred, e.g., to [50].

<sup>13</sup>Note that diffractive effects can also lead to an attenuation of the light beam and have of course to be carefully accounted for in such setups, see, e.g., [53].

In summary, the effective indices of refraction induced by the real or virtual production of minicharged particles read<sup>14</sup> for  $\theta = \sphericalangle(\vec{B}, \vec{k}) \neq 0$  [50, 54, 55]

$$n_{\parallel/\perp} \simeq 1 - \frac{\epsilon^2 \alpha}{4\pi} \left( \frac{\epsilon e B}{m_\epsilon^2} \right)^2 \sin^2(\theta) I_{\parallel/\perp}(\tilde{\chi}) , \quad (2.20)$$

where the (generally complex) auxiliary function

$$I_{\parallel/\perp}(\tilde{\chi}) = 2^{1/3} \left( \frac{3}{\tilde{\chi}} \right)^{4/3} \int_0^1 d\nu \frac{\left[ (1 - \frac{\nu^2}{3})_{\parallel}, (\frac{1}{2} + \frac{\nu^2}{6})_{\perp} \right]}{(1 - \nu^2)^{1/3}} \tilde{e}'_0 \left[ - \left( \frac{6}{\tilde{\chi}} \frac{1}{1 - \nu^2} \right)^{2/3} \right] \quad (2.21)$$

carries the information on the distribution of momenta in the minicharge particle loop in the  $\nu$ -integral, see also App. C. Above,  $\tilde{e}'_0(x)$  is short-hand for the derivative of the generalized Airy function  $\tilde{e}_0(x) = \int_0^\infty du \sin(xu - u^3/3)$  and  $\tilde{\chi}$  stands for the dimensionless quantity

$$\tilde{\chi} \equiv \frac{3}{2} \frac{\omega}{m_\epsilon} \frac{\epsilon e B}{m_\epsilon^2} \sin(\theta) , \quad (2.22)$$

which comes about as a combined parameter of the expansion variables in order to execute the proper-time integral in the associated representation of the polarization tensor. Note that the rather elaborate expressions of Eqs. (2.20) and (2.21) must of course contain the comparably simple weak-field limit applicable in QED as presented in Eqs. (2.14) and (2.15). Indeed, this can be seen by substituting  $\epsilon e \rightarrow e$  as well as  $m_\epsilon \rightarrow m$  and upon evaluation of  $I_{\parallel/\perp}(\tilde{\chi})$  the limit  $\tilde{\chi} \ll 1$ . On the other hand, as  $\tilde{e}'_0(x) \stackrel{x \rightarrow -\infty}{\simeq} -x^2$ , it is found that the refractive index in Eq. (2.20) becomes independent on the value of  $m_\epsilon$  in the limit of small minicharge masses. It is for this reason that experimental bounds based on the production of MCPs saturate in the limit of small minicharge masses, see, e.g., the polarimetric data of [25, 58] and also Fig. 4.1 in Chapt. 4.

On the other hand, studying pertinent literature closely, one finds that sometimes even stronger laboratory limits on MCPs are deduced from experiments of the “light-shining-through-walls” type. Yet, before we give meaning to this peculiar expression, it is reasonable to introduce another WISP first, namely axions or, more generally, axion-like-particles.

<sup>14</sup>It should be noted that in the evaluation of the indices of refraction from the QED situation [54] for high energy photons, propagation on the light cone is assumed, i.e.,  $k^2 = 0$  as well as  $eB/m^2 \gg 1$  and  $\omega \sin(\theta) \gg m$ , which transfers to  $\epsilon e B/m_\epsilon^2 \gg 1$  as well as  $\omega \sin(\theta) \gg m_\epsilon$  in the context of minicharges. Here, it seems that the first condition for the minicharges, namely  $\epsilon e B/m_\epsilon^2 \gg 1$ , would obstruct the application of the effective refractive index to a large portion of the minicharge mass-coupling plane. However, it can be shown [57] that the approximation of the polarization tensor as worked out by Tsai and Erber can also be performed in the limit  $m_\epsilon \rightarrow 0$  yielding the same index of refraction, such that Eq. (2.20) holds true for the whole mass coupling range, requiring only  $\omega \sin(\theta) \gg m_\epsilon$ . This statement can also be motivated from the fact that Eq. (2.20) becomes independent of  $m_\epsilon$  in the limit  $m_\epsilon \rightarrow 0$ .

## 2.2.2 Axion(-like) particles and light that shines through walls

### Axions, axion-like particles and their implications for optical measurements

The certainly most prominent particle which could be counted among the WISPs is the axion [59, 60], which is the pseudo-scalar pseudo-Goldstone-boson associated with the spontaneous breaking of the so-called Peccei-Quinn symmetry [61, 62], as put forward as a solution to the strong CP problem in quantum chromodynamics (QCD). The strong CP problem amounts to the question why CP violation in QCD, being effectively encoded in a parameter  $\bar{\theta}$ , is unmeasurably small<sup>15</sup> (or even absent). The effective parameter  $\bar{\theta}$  receives contributions from the  $\theta$ -angle of QCD, being essentially unconstrained a priori, and the quark mass matrix. As these parameters are unrelated from the outset, the question for a natural explanation arises on why  $\bar{\theta}$  takes a value close to zero. In essence, the axion solution to the strong CP-problem makes  $\bar{\theta}$  effectively a dynamical variable which naturally relaxes to zero. However, if the axion meets its purpose, it has to obey a predictive relation between its mass and coupling depending on the scale of symmetry breaking, cf., e.g., [66] for an overview.

According to the phenomenological scope of this work, we consider more generally (pseudo-)scalar axion-*like* particles (ALPs) for which we assume nothing else but an effective coupling to photons, see, e.g., [67]. Particularly, for ALPs no fixed relation between their coupling and mass is presumed. The effective<sup>16</sup> coupling of pseudoscalar and scalar ALPs to the electromagnetic field is therefore encoded as

$$\mathcal{L}_{P/S} = -\frac{1}{4} F_{\mu\nu} F^{\mu\nu} + \frac{1}{2} \partial_\mu \phi \partial^\mu \phi - \frac{1}{2} m_\phi^2 \phi^2 + \begin{cases} \frac{1}{4} g_P \phi F_{\mu\nu} \tilde{F}^{\mu\nu} \\ \frac{1}{4} g_S \phi F_{\mu\nu} F^{\mu\nu} \end{cases}, \quad (2.23)$$

with ALP mass  $m_\phi$  and coupling parameters  $g_{P/S}$ , respectively.

From an experimental point of view, there are again several distinct possibilities to utilize this coupling structure in order to search for axions and ALPs. As already discussed in the context of QED and minicharged particles above, a generic way to search for ALPs are polarimetric measurements, as first suggested in [68], see also [69]. In a constant external magnetic field  $\vec{B}$ , as for pseudoscalar ALPs the term coupling the field vectors

<sup>15</sup>CP violation in QCD would, e.g., manifest itself in properties of hadrons, such as an electric dipole moment of the neutron  $\vec{d}_n$  (nEDM), see, e.g., [63, 64]. An nEDM would point along the spin direction of the neutron. However, time reversal reverses the spin, while the direction of  $\vec{d}_n$  remains unchanged under this operation, resulting in a violation of time reversal ( $\mathcal{T}$ ). By virtue of charge-conjugation, parity and time-reversal invariance ( $\mathcal{CPT}$ ), the combined transformation  $\mathcal{CP}$  would thus be violated in strong interactions by the existence of a nEDM. However, measurements indicate  $|\vec{d}_n| \lesssim 10^{-26} \text{ ecm}$  [65] implying  $\bar{\theta} \lesssim 10^{-10}$ .

<sup>16</sup>For the QCD axion, which in the microscopic theory only couples to quarks and gluons, this coupling structure comes about through higher order processes.

$\{\vec{e}, \vec{b}\}$  of the probe photon with the external field is  $\mathcal{L}_{\text{P,int}} = -g_{\text{P}}\phi \vec{e}\vec{B}$ , it is in essence<sup>17</sup> the  $\parallel$ -mode of the probe beam which can propagate as an ALP. For scalar ALPs, on the other hand, only the  $\perp$ -mode of the probe beam couples, as  $\mathcal{L}_{\text{S,int}} = -\frac{1}{2}g_{\text{S}}\phi(\vec{e}^2 - (\vec{B} + \vec{b})^2)$ . In both cases, however,  $\theta = \sphericalangle(\vec{B}, \vec{k}) = \pi/2$  is the most favorable choice, which we will thus adopt in the following.

As a consequence, given the appropriate polarization mode, the photon-ALP coupling can, as for minicharges, lead to attenuation and ultimately rotation of the polarization of a probe beam within an external magnetic field if  $2m_\phi < \omega$  via the production<sup>18</sup> of ALPs. On the other hand, even for larger ALP masses, one still has virtual production of ALPs, which amounts to a relative phase delay between the polarization components leading to ellipticity as in the QED and minicharge context: The relative phase difference  $\Delta\Phi$  between the polarization components for both scalar and pseudoscalar particles, reads for  $g_{\text{P/S}}B\omega/m_\phi^2 \ll 1$  and  $m_\phi \ll \omega$

$$\Delta\Phi = \frac{\omega LB^2}{2m_\phi^2} g_{\text{P/S}}^2 \left(1 - \frac{\sin(2y)}{2y}\right), \quad y = \frac{Lm_\phi^2}{4\omega}, \quad (2.24)$$

cf. [68, 69] as well as [50]. Here,  $\omega$  again denotes the probe laser frequency and  $L$  is the extent of the external magnetic field along the propagation direction of the photons. In order to extract the corresponding indices of refraction, one employs that photons with polarization components  $\parallel$  and  $\perp$  will accumulate a relative phase shift  $\Delta\Phi$

$$\Delta\Phi = \omega L (n_\parallel - n_\perp). \quad (2.25)$$

As a result of the ALP coupling structure one has that for pseudoscalar ALPs  $n_\parallel^{\text{P}} > 1$ , whereas  $n_\perp^{\text{P}} = 1$ . If, instead of the pseudoscalar coupling, scalars couple, it holds that  $n_\perp^{\text{S}} > 1$ , whereas  $n_\parallel^{\text{S}} = 1$ . Of course, by virtue of Eq. (2.25) not only polarimetric measurements are conceivable but also interferometric setups which measure a shift in the *absolute* phase velocity, cf. also Chapt. 4. Thus, for later convenience, we summarize Eqs. (2.24) and (2.25) in the following form

$$n_\parallel^{\text{P}} - 1 = n_\perp^{\text{S}} - 1 = \frac{B^2}{2m_\phi^2} g_{\text{P/S}}^2 \left(1 - \frac{\sin(2y)}{2y}\right), \quad y = \frac{Lm_\phi^2}{4\omega}. \quad (2.26)$$

<sup>17</sup>Small couplings are feasibly probed by the application of high field strengths. Then again, as shown in the previous section, this simple picture is modified for very high field strengths, as effective self-interactions among electromagnetic fields can play a role, cf. Eq. (2.11).

<sup>18</sup>Notably, the idea of employing an effective interaction structure as in Eq. (2.23) had already been suggested by H. Primakoff [70] in the context of the  $\pi^0$ -meson-to-photon-coupling. As a consequence, also in the context of axions, the notion ‘‘Primakoff process’’ for conversion of photons to ALPs is widely used in the literature.



In conclusion, determining ellipticity and rotation of a polarized light beam induced within an external field are means to probe the parameter space of the ALP mass and coupling, as exploited, e.g., with PVLAS [25], BMV [28] and BFRT [71].

### Light-shining-through-walls scenario for axions and axion-like particles

As a popular alternative to polarimetry, one can utilize the weak coupling between ALPs and ordinary matter in order to shine photons in external fields through light-blocking walls, thus going by the name of “light-shining-through-walls” (LSW) setups. Following P. Sikivie’s idea [72] of establishing a “helioscope”, whose original purpose was to detect solar axions, it was later realized that by direct production of axions from a laser beam [73, 74], one could perform very “clean” measurements by shining axions through a light-blocking wall [75]. Here, “clean” is meant in the sense that the standard model background for common LSW scenarios is safely negligible [42, 76].

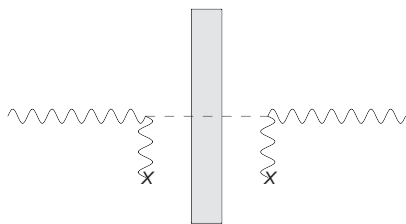


Figure 2.4: LSW scenario with axion-like particles. A photon which enters from the left hand side (wiggly line) can be converted into an ALP (dashed line) in an external field (indicated by the crosses at the end of the photon lines). The ALP can traverse a barrier nearly unhindered due to its weak coupling to matter and can subsequently be reconverted into a photon.

LSW with axion-like particles is possible if the laser probe photons are converted into real ALPs in front of the wall and reconverted into photons behind that wall, cf. Fig. 2.4. In typical laboratory searches the photon-to-ALP conversion processes are induced by strong dipole magnets. Roughly spoken, LSW searches are very sensitive to small ALP couplings as the large number of available photons for the conversion process in front of the wall faces the possibility of even single photon detection behind a light-blocking barrier.

Again, the photon-ALP conversion probability can again most conveniently be obtained for small ALP masses in vacuo<sup>19</sup>, cf. [68, 69, 72–75], reading

$$P_{\gamma \leftrightarrow \phi} = \left( \frac{g_{\text{P/S}} BL}{2} \right)^2 \left( \frac{\sin(y)}{y} \right)^2, \quad y = \frac{Lm_\phi^2}{4\omega}. \quad (2.27)$$

As the functional dependence in Eq. (2.27) is such that the transition probability is largest for small values of  $y$ , it is conceivable that LSW searches, being best known by their acronyms ALPS [77, 79], LIPSS [80, 81], GammeV [82, 83], OSQAR [84] as well as

<sup>19</sup>In an (experimentally preferably gaseous) medium this expression is modified as the photons effectively acquire a mass, see, e.g., [77]. Although a gas insertion generically decreases the conversion amplitude for visible light, it can be used to close the “gaps” in the parameter-space coverage arising from the sinusoidal dependence of the transition probability, cf. Eq. (2.27). Alternatively, an optimized arrangement of magnets can be used to extend the sensitivity of the setup to a larger mass range [78].

a setups at BMV [85] and BFRT [71], have been most successful in constraining the ALP parameter space in the lower mass range.

Even further sensitivity enhancement within forthcoming LSW setups seems attainable by the use of higher photon energies, such as X-rays [86–88] or the installation of a second cavity on the regeneration side, i.e., through so-called “resonant regeneration” [89–92]. Noteworthy, the latter concept has recently been successfully experimentally verified even for regeneration in the sub-quantum regime [93].

In addition, it is important to note that for larger ALP masses on the order of the employed photon frequency, the LSW probability can exhibit a resonant behavior near  $\omega \simeq m$ , as discussed in [94]. A similar feature will be encountered and utilized in Chapt. 5 where ALP search in purely laser-based setups is investigated.

### Light-shining-through-walls scenarios for other WISPs

Intriguingly, LSW setups, although originally aimed at the detection of axions (or ALPs), are not only sensitive to these particles but also to other WISPs, in particular to hidden photons and MCPs, see [42] and references therein for a recent overview.

For example, following Eq. (2.16), in a minicharged model with hidden photons, “light-shining-through-walls” is possible if photons traverse the wall through a real hidden-photon, see Fig. 2.5. Photons can be converted into hidden photons through an intermediate MCP loop within an external magnetic field. Subsequently, similar to the LSW scenario with ALPs, the hidden photons are then assumed to traverse the barrier unhindered and can thereafter be reconverted into photons [95]. Note that direct photon-hidden photon oscillations are also possible if the hidden photon has a mass term: Upon diagonalizing the kinetic mixing term in Eq. (2.16), a term mixing the gauge potentials of the photons and hidden photons themselves is obtained and one acquires a “mass mixing” term. (In a sense the photon-hidden photon oscillations are then very analogous to neutrino oscillations.) However, note carefully that from the LSW scenario depicted in Fig. 2.5 only *combined* bounds on the fractional charge  $\epsilon$  and the hidden-sector coupling  $e_h$  can be derived.

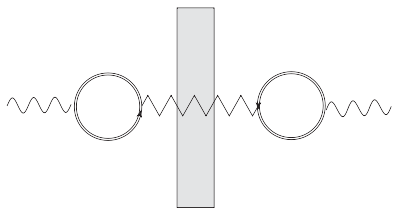


Figure 2.5: LSW scenario with a hidden photon and minicharged particles. A photon (wiggly line) can oscillate into a hidden photon (zig-zag line) through a minicharge loop in an external field. After passing a wall, the hidden photon can be reconverted into a photon through the reverse process. From this LSW scenario, combined bounds on the minicharged coupling  $\epsilon$  for fixed hidden-sector fermion coupling  $e_h$  can be derived, cf. Eq. (2.16).

A second, more direct LSW scenario for minicharged particles is through barrier-transition via virtual particle-antiparticle intermediate states or “tunneling of the 3rd kind”<sup>20</sup> [96] as depicted in Fig. 2.6. Although such a process is in principle also possible with neutrino intermediate states, this standard model background is highly suppressed due to the Fermi scale. It turns out however, that in a zero-field setting, bounds that are derived from this LSW scenario cannot compete with current laboratory limits from polarimetric measurements (which can also provide for direct bounds on the fractional charge of minicharged particles). In Chapt. 6 we extend precisely this LSW scenario to include external magnetic fields and investigate the corresponding sensitivity in a first case study.

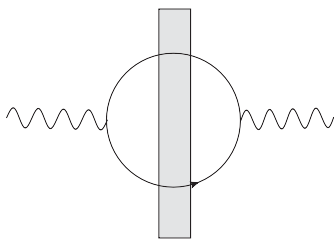


Figure 2.6: LSW scenario with minicharged particles through a virtual intermediate state as first discussed in [96]. A spontaneous oscillation into a minicharged particle-antiparticle pair which traverses a light blocking barrier freely, enables the photon to effectively “shine through a wall”.

### 2.2.3 Shedding light on the vacuum in the laboratory and with astrophysical sources

Lastly, let us remark that the above presentation of optical probes of the particle content in a polarized vacuum is by far not extensive. Particularly, returning to Sikivie’s suggestion of establishing a helioscope, it is noteworthy that also this concept has been realized in a number of experimental setups [97–100]. Here, no laser is employed for axion production; rather, the sun acts as axion source. Based on the non-observation of ALPs as yet, currently the CERN axion solar telescope ‘CAST’ [100–102] provides among the strongest bounds on ALPs in the mass range below  $\mathcal{O}(1\text{eV})$ , which at first sight drastically outmatch the best laser-based laboratory bounds by several orders of magnitude. Essentially, this comes about as the sun can be expected to produce more ALPs than any laser employed in the laboratory.

Furthermore, bounds derived from astrophysical considerations [103] that are, e.g., based on stellar evolution arguments, constrain ALPs and also MCPs mostly well<sup>21</sup> below the parameter regions that are currently accessible in the laboratory.

As a rule, however, the stellar WISP generation processes involve momentum transfers in the keV range, whereas laboratory experiments based on optical probing are naturally

<sup>20</sup>In the sense that the tunneling process via virtual particle-antiparticle pairs complements quantum mechanic tunneling and tunneling of real particles in quantum field theory (i.e., tunneling via a tree-level process, cf. Fig. 2.4), this process has been named “tunneling of the 3rd kind”.

<sup>21</sup>For example, [51] provides bounds on minicharged particles down to  $\epsilon \sim \mathcal{O}(10^{-14})$  for larger minicharge masses, see also [104–106].

sensitive to couplings to ALPs at much lower momentum transfer. However, reasonable models [107–109] have been proposed in which the coupling of the WISPs strongly depends on the momentum transfer and further parameters<sup>22</sup> dictated by the stellar environment, rendering laboratory searches indispensable for a comprehensive search for WISPs. Also, a strong argument for performing dedicated laser-based laboratory searches is the fact that only in such measurements, one can directly influence and modify the *production process* of the WISPs. Thus, it is crucial to note that in the case of hints of new particles, only with dedicated laboratory experiments one will be in the position to clear ambiguities related to their nature and properties which may arise.

To close this section, let us briefly comment on some selected additional concepts and setups employed for WISP search, where details<sup>23</sup> can, e.g., be found in [41]. In particular, let us mention direct axion dark matter searches such as the axion dark matter experiment ‘ADMX’ [113]. These ‘haloscopes’ [72], being conceptually equivalent to an LSW setup, are based on the reasoning that axions could contribute a major amount to the dark matter density through which the earth supposedly<sup>24</sup> passes continuously. However, given the large variety in the matter content within the visible sector, there seems to be no compulsive reason that dark matter should be widely dominated by a distinct particle type.

Lastly, there is a number of conceptually related laboratory setups that could not be considered in this chapter. Among others we would like to point out measurements of axion-induced parity and time-reversal symmetry-violating forces [116], see, e.g., [117], tests of Coulomb’s law [118, 119] and the suggested use of accelerator- [120] or microwave-cavities [90, 121] as production sites for WISPs.

---

<sup>22</sup>It is instructive to read [109] for a comprehensive review of the involved astrophysical parameters and processes and to get a vivid impression of the excitement and the time scales of innovation that followed the positive signal report of the PVLAS collaboration.

<sup>23</sup>Most current developments in this field are also published regularly in a conference proceedings series, see [110–112].

<sup>24</sup>Note that scenarios exist in which dark matter is not needed to explain pertinent astronomical observations, see, e.g., [114]. However, in particular studies of the bullet cluster [115] seem to strongly support the idea that dark matter exists. In addition, the various WISPs are of course not necessarily good dark matter candidates in their entire parameter space, see, e.g., [41].

*“Es sollte stehn: Im Anfang war die Kraft!  
Doch, auch indem ich dieses niederschreibe,  
Schon warnt mich was, daß ich nicht dabei bleibe.  
Mir hilft der Geist! auf einmal seh ich Rat  
Und schreibe getrost: Im Anfang war die Tat!”*

J.W.v. Goethe, Faust I

## Chapter 3

# Geometry as vacuum probe: A nonperturbative treatment

With all basic prerequisites at hand, the first quantum-vacuum probe that we address in this work pertains to non-planar geometries in Casimir-Polder systems. Casimir [8] and Casimir-Polder [9] forces belong to the most straightforward and direct probes of the vacuum structure of QED. These arise when macroscopic bodies or atoms, respectively, modify the spectrum of vacuum fluctuations through the enforcement of boundary conditions on the fluctuations. To briefly pick up on the discussion of the previous chapter, it is intriguing to note that Casimir-force measurements are – by virtue of their remarkable accuracy – also well applicable in the search for physics beyond the standard model, e.g., in terms of modifications to Newtonian gravity at small length scales, see, e.g., [122].

From the viewpoint of theory, much effort has been put into developing calculational techniques that enable to precisely account for influences of geometric variations in Casimir-type experiments, cf., e.g., [123] for an overview of recent experimental and theoretical developments. In particular, standard calculational techniques for simple flat surfaces are insufficient in the context of non-planar settings due to the demonstrated inherent non-additivity of these quantum forces, see, e.g., [124]: Since quantum fluctuations contribute on all length (or momentum) scales, geometry dependencies generally require a profound understanding of the fluctuation spectrum in a given configuration and cannot be dealt with by perturbative expansions with respect to a small geometry parameter.

Thus, a variety of new field-theoretical methods for understanding fluctuation-induced phenomena have been developed in the past few years, superseding very early phenomenological recipes such as, e.g., the proximity-force approximation [125]. Most recently, these developments have been subsumed in a resource letter [126] in particular for Casimir-Polder forces which will be subject to our subsequent investigations.

Motivated by precise Casimir-Polder measurements based on quantum reflection within the atomic-beam spin-echo technique [127, 128], this chapter is devoted to a nonperturbative study of Casimir-Polder forces near a surface with uniaxial corrugation. Our ansatz is

based on the constrained-functional-integral approach [129, 130] which makes it possible to condense the computational effort into a one-dimensional Green's function problem along the direction of nontrivial curvature of the surface. This Green's function problem involves singular kernels and we therefore put emphasis on presenting an appropriate representation that allows for an efficient numerical treatment. For the purpose of a first case study, we consider a fluctuating massless scalar field obeying Dirichlet boundary conditions, whereas, building on the subsequently presented results, a partial generalization to the electromagnetic case has also been successfully worked out, cf. [131].

In this chapter, we proceed as follows: In Sect. 3.1 we review the framework of the analytical treatment of this problem only briefly as this is devised in [132] in detail. Subsequently, in Sect. 3.2, we extensively discuss an appropriate numerical access to this problem which is applicable for arbitrary uniaxial corrugations and provide detailed results for experimentally relevant sinusoidal and saw-tooth-like shapes.

## 3.1 Devising a nonperturbative treatment for scalars

### 3.1.1 Constrained-functional-integral approach and the Casimir-Polder limit

We aim at calculating the Casimir interaction-energy of a system of bodies, separated by a distance measure  $H$  which serves as a potential energy for the Casimir force, cf. Sect. 2.1. With the generating functional as defined in Eq. (2.1), this is achieved by evaluating

$$E(H) = -\frac{1}{T_E} \ln \frac{\mathcal{Z}_D}{\mathcal{Z}_\infty}, \quad (3.1)$$

where  $T_E$  denotes the length in Euclidean time direction and the label ‘‘D.’’ refers to the ground state energy with Dirichlet boundary conditions implemented by virtue of the insertion of bodies into the vacuum. On the other hand, ‘‘ $\infty$ ’’ indicates that the boundary conditions have been effectively removed through formally separating all bodies to infinite distance. In this way, Casimir self-energies are eliminated.

In our treatment, we follow the constrained-functional-integral approach. We restrict ourselves to an idealized two-body problem, in which the influence of the bodies on the fluctuating fields can be implemented by the insertion of a  $\delta$  functional into  $\mathcal{Z}$ . Thus, the Euclidean generating functional, cf. Eq. (2.1), becomes for a massless scalar field  $\phi$

$$\mathcal{Z}_D = \int \mathcal{D}\phi \prod_{\alpha=1}^2 \prod_{x_\alpha} \delta(\phi(x_\alpha)) \exp\left(-\frac{1}{2} \int d^4x (\partial\phi(x))^2\right). \quad (3.2)$$

For the case of Dirichlet boundary conditions, the corresponding  $\delta$  functional is represented by a product of  $\delta$  functions  $\delta(\phi(x_\alpha))$  for all 4-vectors  $x_\alpha$  pointing onto a surface  $S_\alpha$ , where here  $\alpha$  labels the two disjoint surfaces.

In order to evaluate the integral over the fields  $\phi$ , a Fourier representation is used for the  $\delta$  functional with the help of auxiliary fields<sup>1</sup> that have support only on the surfaces  $S_\alpha$ . First performing the Gaussian integral over  $\phi$  leaves us – apart from a factor which drops out upon evaluation of the Casimir energy and thus is irrelevant – with another Gaussian integral for the auxiliary fields which can accordingly also be carried out.

With the resulting constrained functional integral we thus find by virtue of Eq. (3.1), upon expansion of the logarithm, the Casimir interaction energy between two surfaces  $S_1$  and  $S_2$ , separated by a distance measure  $H$

$$E(H) = -\frac{1}{T_E} \frac{1}{2} \sum_{n=1}^{\infty} \frac{1}{n} \text{Tr} (\mathcal{M}_{11}^{-1} \mathcal{M}_{12} \mathcal{M}_{22}^{-1} \mathcal{M}_{21})^n . \quad (3.3)$$

Here,  $\mathcal{M}_{\alpha\beta}$  is the propagator of the scalar fluctuations, i.e., the functional inverse of  $\partial^2$

$$\mathcal{M}_{\alpha\beta}(\zeta, \vec{x} - \vec{x}') = \frac{1}{4\pi|\vec{x} - \vec{x}'|} \exp(-|\vec{x} - \vec{x}'||\zeta|) . \quad (3.4)$$

In Eq. (3.4), the propagator has been partially transformed to frequency space as the problem is translationally invariant in time direction. Thus,  $\zeta$  denotes the imaginary frequency, while  $\vec{x} = (x_1, x_2, x_3)$  and  $\vec{x}'$  are three-vectors to be evaluated on the surfaces  $S_\alpha$  and  $S_\beta$ , respectively. As the surfaces respond to the field by “charge” fluctuations, the inverse propagator  $\mathcal{M}_{\alpha\alpha}^{-1}$  can be interpreted as propagator of charge fluctuations within the surface, cf. also footnote 1. The trace in Eq. (3.3) has to be taken over the coordinates of the surfaces, demanding the inclusion of appropriate metric factors for the integration measures. To control the singularity structure that arises within Eq. (3.4) upon the evaluation of the trace, it is expedient to treat the propagators within a proper-time formulation. Lastly, note carefully that the functional inverse of  $\mathcal{M}_{\alpha\beta}$  is generally not known analytically for surfaces of nontrivial shape.

In the following, we evaluate the Casimir energy between a surface  $S_1$  which is uniaxially corrugated along the  $x_1$  direction and a sphere  $S_2$  with radius  $r$ . The latter constitutes the scalar substitute for the “atom” in the case of QED, cf. Fig. 3.1. As also visible in the figure, the absolute and mean distances between surface and sphere are henceforth labeled by  $H$  and  $\bar{H}$ , respectively, whilst  $A$  denotes a typical amplitude of the corrugation and  $\lambda$  a typical corrugation wavelength with corresponding frequency  $\omega = 2\pi/\lambda$ . The shape of the corrugation along  $x_1$  is stored in a height function  $h(x_1)$ . As we consider only periodic

---

<sup>1</sup>Drawing the analogy to the electromagnetic case, the auxiliary fields can be thought of as charged sources which enforce the boundary conditions by means of their coupling to the fluctuating field, see also [133].

height profiles in the following, also a phase  $\phi$  is introduced in the height function. In all subsequent evaluations, we are interested in the Casimir-Polder limit ( $r \ll H$ ), where the analytical result for a flat surface  $S_1$  is known to be  $\mathcal{O}(\frac{r}{H^2})$  to leading order, see, e.g., [134].

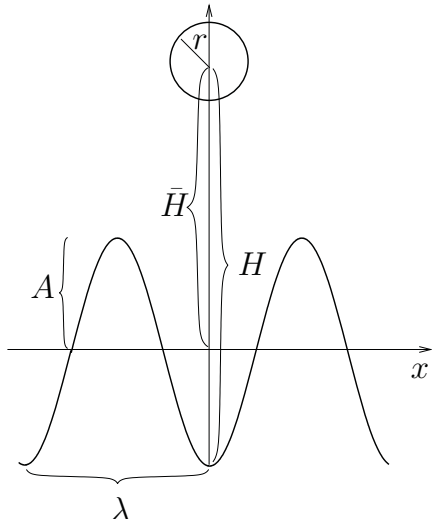


Figure 3.1: Casimir-Polder setup with a uniaxially corrugated surface. Here, a sphere of radius  $r$  at a mean distance  $\bar{H}$  above a surface sinusoidally corrugated along  $x$  with amplitude  $A$  and wavelength  $\lambda$  is depicted. In our conventions, we fix the sphere at the lateral coordinate  $x = 0$ . Thus, to allow for different positions of the sphere above the surface, we effectively shift the structure function  $h(x)$  by varying the phase  $\phi$ . The distance parameter  $H$  measures the sphere-surface distance along the global normal, such that  $H = 0$  corresponds to sphere-surface contact for all values of  $\phi$ .

### 3.1.2 Scalar forces in the plate-sphere configuration

Let us now evaluate the (inverse) propagators in the plate-sphere configuration. The inverse propagator on the sphere,  $\mathcal{M}_{22}^{-1}$ , is straightforwardly computed from  $\mathcal{M}_{22}^{-1}\mathcal{M}_{22} = \mathbb{1}$ , where  $\mathcal{M}_{22}$  is given through Eq. (3.4): By expansion of the equation in terms of spherical harmonics  $Y_{lm}$ ,  $\mathcal{M}_{22}^{-1}$  can be calculated to arbitrary order in  $l$ . For the computation of the *leading* order Casimir energy in the scalar setup, however, it is sufficient to consider the monopole contribution  $l = 0 = m$ , which reads  $\mathcal{M}_{22}^{-1}(\zeta) = |\zeta| \exp(r|\zeta|) / [4\pi r^2 \sinh(r|\zeta|)]$ .

In order to extract the leading order Casimir interaction energy, we next go over to dimensionless variables by a rescaling with the distance parameter  $H$ :  $\vec{x} \rightarrow \tilde{x}H$ ,  $\zeta \rightarrow \tilde{\zeta}/H$ . Recalling that the Casimir interaction energy is  $\mathcal{O}(\frac{r}{H^2})$  to leading order, the rescaling procedure unveils that it suffices to consider the  $n = 1$  term of the sum in Eq. (3.3). Furthermore, it is crucial to note that in this limit the propagators  $\mathcal{M}_{12}$  and  $\mathcal{M}_{21}$  become independent of the coordinates on the sphere  $S_2$ . As the monopole contribution of  $\mathcal{M}_{22}^{-1}$  is also independent of these coordinates, the two integrations over the surface of the sphere  $S_2$  contribute only a factor of  $16\pi^2$  in Eq. (3.3) and only the integration over  $\tilde{\zeta}$  and the coordinates of  $S_1$  are nontrivial. As we intend to investigate uniaxially corrugated surfaces  $S_1$ , we exploit the translational invariance of the surface  $S_1$  along the 2-component by a partial Fourier transformation of Eq. (3.3) to momentum space with respect to this direction. In this manner, integrations along the direction of corrugation  $\tilde{x}_1$  and along the momentum space variables  $\tilde{\zeta}$  and  $\tilde{p}_2$  remain to be evaluated in the trace.



In the final step, it is feasible to combine the variables  $\tilde{\zeta}$  and  $\tilde{p}_2$  by the substitution to polar coordinates. Thus, employing  $\tilde{q} = \sqrt{\tilde{\zeta}^2 + \tilde{p}_2^2}$ , Eq. (3.3) reduces to:

$$E = -\frac{1}{2} \frac{r}{H^2} \underbrace{2 \int_0^\infty d\tilde{q} \int_{-\infty}^\infty d\tilde{x} \sqrt{g(\tilde{x})} \tilde{q} \Delta \tilde{\mathcal{M}}_{12}(\tilde{q}; \tilde{x}) \tilde{\mathcal{M}}_{21}(\tilde{q}; \tilde{x})}_{:= \alpha} + \mathcal{O}\left(\frac{r^2}{H^3}\right), \quad (3.5)$$

where we have defined  $\Delta \tilde{\mathcal{M}}_{12} = \tilde{\mathcal{M}}_{11}^{-1} \tilde{\mathcal{M}}_{12}$  (which includes explicitly the metric factor characterizing the surface  $S_1$ ) and dropped the coordinate subscript “1” along the direction of corrugation to simplify notation:  $\tilde{x}_1 \rightarrow \tilde{x}$ . Furthermore, we have defined a dimensionless factor  $\alpha$  that depends on the geometry parameters of the configuration (measured in units of  $H$ ). The metric factor of the corrugation is related to its height profile  $h(\tilde{x})$  by

$$\sqrt{g(\tilde{x})} = \sqrt{1 + \left(\partial_{\tilde{x}} \tilde{h}(\tilde{x})\right)^2}, \quad \tilde{h}(\tilde{x}) = \frac{1}{H} h(\tilde{x}H). \quad (3.6)$$

As the derivative of the height function appears in Eq. (3.6), we consider only surfaces described by continuous height functions. The dimensionless propagators  $\tilde{\mathcal{M}}_{12} \equiv \tilde{\mathcal{M}}_{21}$  and  $\tilde{\mathcal{M}}_{11}$  that enter Eq. (3.5) are found to be given in terms of Bessel functions:

$$\tilde{\mathcal{M}}_{11}(\tilde{q}; \tilde{x}'; \tilde{x}) = \frac{1}{2\pi} K_0 \left( \tilde{q} \sqrt{(\tilde{x}' - \tilde{x})^2 + \left(\tilde{h}(\tilde{x}') - \tilde{h}(\tilde{x})\right)^2} \right), \quad (3.7)$$

$$\tilde{\mathcal{M}}_{12}(\tilde{q}; \tilde{x}') = \frac{1}{2\pi} K_0 \left( \tilde{q} \sqrt{(\tilde{x}')^2 + \left(\tilde{h}(\tilde{x}') - 1\right)^2} \right). \quad (3.8)$$

In the planar limit, computing the energy in Eq. (3.5) is now very simple. For a flat surface  $S_1$ , the height function becomes a constant and the remaining integrations in Eq. (3.5) can be carried out analytically. Thus, in the planar case, the energy between the sphere and the plane yields in the Casimir-Polder limit  $r \ll H$

$$E(H) = -\frac{1}{8\pi} \frac{r}{H^2} + \mathcal{O}\left(\frac{r^2}{H^3}\right), \quad (3.9)$$

which agrees with a number of recent previous calculations [134–137] and will serve as analytical cross-check for the performance of our numerical evaluations in Sect. 3.2. Turning to arbitrary uniaxial corrugations, the combined propagator  $\Delta \mathcal{M}_{12}$ , being the crucial ingredient in obtaining the Casimir-energy in Eq. (3.5), is evaluated by solving

$$\int_{\tilde{x}} \sqrt{g(\tilde{x})} \tilde{\mathcal{M}}_{11}(\tilde{q}; \tilde{x}'; \tilde{x}) \Delta \tilde{\mathcal{M}}_{12}(\tilde{q}; \tilde{x}) = \tilde{\mathcal{M}}_{12}(\tilde{q}; \tilde{x}') \quad (3.10)$$

numerically<sup>2</sup>. However, the treatment of the above equation is nontrivial due to the singular structure of  $\tilde{\mathcal{M}}_{11}$  at the origin, see Eq. (3.7).

The Casimir-Polder limit is obtained in the situation where the sphere radius  $r$  is much smaller than any other scale,  $r \ll H, A, \lambda, \dots$ . The factor  $\alpha$  thus is a function of  $\alpha = \alpha(A/H, \lambda/H, \dots)$ , but it is independent of  $r$ . Notably, from a technical perspective, the result of Eq. (3.5) is very simple. It should be stressed that already the first trace term in the initial Casimir-energy formula in Eq. (3.3) includes nine integrations for the trace: one over the imaginary frequency and four times two integrations over the lateral surface coordinates. Due to the trivial dependency of the integrand on the lateral coordinates of the sphere in the Casimir-Polder limit, the number of integrations is then reduced by four; moreover, the  $n$  sum is just replaced by its first term in this limit. The emerging translational invariance vertical to the direction of corrugation reduces the number of integrations by another two. Thus – instead of nine – we are left with three integrations: two of them are directly visible in Eq. (3.5), the third one is needed for the construction of  $\Delta\mathcal{M}_{12}$  as a solution of Eq. (3.10). These simplifications make the Casimir-Polder limit accessible to numerical integration for arbitrary height profiles.

The resulting two integrals in Eq. (3.5) are both convergent, non-oscillatory and generically exhibiting a simple one-peak structure. The treatment of the singularity structure in the Green's functions equation (3.10), however, requires some care and is outlined in App. D.

## 3.2 Results for uniaxially corrugated surfaces

### 3.2.1 Sinusoidally shaped surfaces

As a first nontrivial example, let us calculate the scalar Casimir-Polder potential for a sinusoidal corrugation, see Fig. 3.1. The potential for this structure is given by Eq. (3.5), where we use  $h(x) = A \sin(\omega x + \phi)$  as height function appearing in the propagators Eqs. (3.7) and (3.8) as well as in the surface metric factor of Eq. (3.6). The parameters  $A$  and  $\omega$  enable us to vary the corrugation amplitude and periodicity of the structure, respectively. The phase  $\phi$  is used to modulate the relative position of the structure beneath the sphere, since the latter is always kept fixed at  $x = 0$ . As  $H$  characterizes the distance of the atom to the surface along the global surface normal,  $H$  can be viewed as a function of  $\phi$  in our conventions,  $H = H(\phi)$  with  $H(-\pi/2) = \bar{H} + A$  at the sine minimum and  $H(\pi/2) = \bar{H} - A$  at the sine maximum, i.e.,  $H = 0$  always corresponds to sphere-wall contact, where the limit  $r \ll H$  is implicitly understood.

<sup>2</sup>Note that the only quantity for computing the Casimir energy which is not known analytically here is  $\mathcal{M}_{11}^{-1}$ . In principle, one could thus be tempted to evaluate  $\mathcal{M}_{11}^{-1}\mathcal{M}_{11} = \mathbb{1}$  numerically. However, Eq. (3.10) provides us with  $\Delta\tilde{\mathcal{M}}_{12}$ , being directly applicable in Eq. (3.5).

As the crucial building block for the Casimir-Polder potential, we solve the Green's function equation Eq. (3.10) numerically on a one-dimensional lattice in  $x$ -direction. This requires to invert the propagator  $\tilde{\mathcal{M}}_{11}$  on the corrugated surface. Even though the singularity of this propagator at coincident points is integrable in the continuum, the discretized version needs to deal with this singularity explicitly. This is done by introducing a regularization parametrized by a short-distance cutoff  $\epsilon$ , which can be removed after the continuum limit has been taken. Details of how this procedure is implemented numerically are given in App. D.

In the following, we display our results for the Casimir-Polder energy always normalized with respect to the planar-surface case (for consistency, the normalization factor is also determined numerically), since in this manner, the geometry-induced effects are better visible. Furthermore, we expect that these results for the scalar case give a qualitative estimate also for the electromagnetic case for which the normalizing prefactor has a different distance dependence.

In Fig. 3.2, we display  $E_{\text{sine}}/E_{\text{planar}}$  as a function of the vertical position<sup>3</sup> of the sphere above a minimum of the corrugation ( $\phi = -\pi/2$ ) for different corrugation frequencies  $\omega A = 1, 2, 3$ . In the limits  $H/A \rightarrow \infty$  and  $H/A \rightarrow 0$ , we find that  $E_{\text{sine}}/E_{\text{planar}} \rightarrow 1$ . This is expected, since in the first limit the corrugation of the plate cannot be resolved as it is too small compared to the distance. In the second limit, the corrugation is irrelevantly large compared to the distance, i.e., the sphere does not notice it locally. In the region where  $H \sim A$ , the potential for the corrugated surface clearly deviates from the corresponding planar case. One can see that this effect becomes more pronounced for larger corrugation frequencies, i.e., shorter surface periodicity.

We identify various regimes which can be classified in terms of an anomalous dimension  $\eta$  which measures the deviation of the Casimir-Polder potential from the planar case,

$$E_{\text{corrugation}} \sim \frac{1}{H^{2+\eta}}, \quad (3.11)$$

with  $\eta = 0$  for the planar case, cf. Eq. (3.9). At small distances,  $H/A \ll 1$ , we find a linear increase of the normalized potential  $E_{\text{sine}}/E_{\text{planar}}$  with  $H/A$ , implying an anomalous dimension of  $\eta = -1$ . A linear fit to the short-distance data in the well of the structure (not shown in Fig. 3.2) yields  $E_{\text{sine}}/E_{\text{planar}} \simeq 1 + \beta(H/A)$ . The linear coefficient  $\beta$  depends on the frequency,  $\beta = \beta(\omega/A) \simeq 0.5, 2.3, 5.2$  for  $\omega A = 1, 2, 3$ ; within the numerical accuracy, this dependence is compatible with a power law  $\beta \sim (\omega A)^2$ .

---

<sup>3</sup>In [138], cf. also [139], the dependence of  $E_{\text{sine}}/E_{\text{planar}}$  on the horizontal position of the sphere with respect to the corrugation has been also studied. Here, however, we limit ourselves to a study of the energy dependence along the vertical axes, as this constitutes the limit in which perturbative approximations are most expected to become unreliable.

At larger distances  $H/A \sim \mathcal{O}(1)$ , the normalized energy develops a peak. Various regimes can be identified near the peak and also in the drop-off region. The increase towards the peak as well as the decrease right beyond the peak can be characterized by power laws parametrized by an  $\omega$ -dependent anomalous dimension. Towards the peak, we find  $\eta \simeq -0.33, -0.57, -0.67$  for  $\omega A = 1, 2, 3$ , and the fit beyond the peak yields  $\eta \simeq 0.4, 1.0, 1.6$  for  $\omega A = 1, 2, 3$ . For even larger distances near  $H/A \simeq 10$ , we observe that all normalized energies approach a universal curve being characterized by an anomalous dimension  $\eta = 0.2$ ; in particular, the anomalous dimension shows no sizeable  $\omega$  dependence anymore.

Notably, this large-distance universality behavior has recently also been observed in an independent, full electromagnetic calculation for a dielectric grating using a scattering formulation [140]. In this formulation, the difficulties lie in the computation of the exact scattering matrices of the nontrivially shaped bodies, see, e.g., [141, 142]. To gain an intuitive understanding of this feature one can, e.g., employ the framework of the worldline picture of the quantum vacuum [143]. In this picture, quantum fluctuations are mapped onto random paths characterizing their space-time trajectories. To contribute to the Casimir interaction energy, these trajectories have to intersect with both surfaces, implying that the fluctuation has an average extent of the order of the surface separation  $H$ , and by isotropy of the vacuum fluctuations, also a lateral extent of this order. By this, the fluctuation integral averages over structures of the corrugation which are smaller than  $H$ . Higher corrugation frequencies with  $\omega H \gg 1$  thereby become irrelevant for the Casimir-Polder potential, as is demonstrated by the universal drop-off for larger  $H/A$ .

For even larger distances  $H/A \gg 10$ , the power law cannot continue for arbitrarily large  $H/A$ , since the Casimir-Polder potential eventually has to approach the planar limit. In this large-distance regime, we have only a few reliable numerical data points<sup>4</sup>, as the discretization artifacts increase, once the lattice spacing approaches the corrugation wavelength. The available data is compatible with a logarithmic approach towards  $E_{\text{sine}}/E_{\text{planar}} \rightarrow 1$  for  $H/A \rightarrow \infty$ .

Finally, we compute the Casimir-Polder potential above a maximum of the sine structure at  $\phi = +\pi/2$ . As expected, the Casimir-Polder energy is always smaller than in the planar case as the surfaces bends away from the atom and approaches the planar result in the two limits  $H/A \rightarrow 0$  and  $H/A \rightarrow \infty$ , see Fig. 3.3. Starting from an initial decrease of the normalized energy for small distances  $H/A$ , a power-law decrease develops towards the dip with  $\eta \simeq 0.09, 0.11, 0.11$  for  $\omega A = 1, 2, 3$ . Beyond the dip near  $H/A \sim 1$ , a power-law increase follows with an anomalous dimension  $\eta = -0.13, -0.16, -0.19$  for  $\omega A = 1, 2, 3$ , respectively. Here, we observe a linear  $\omega$ -dependence of  $\eta$  in this regime. Also, a second power-law regime is found for larger distances  $H/A \gtrsim 10$  with an anomalous dimension

<sup>4</sup>Details of the numerical implementation are given in App. D. Note that all numerics have been performed on a standard desktop computer with standard linear algebra packages.

$\eta = -0.07$  for the  $\omega A = 1$  data. Due to an increase of the discretization artifacts, no reliable data for larger  $\omega$  is available, such that the expected universality in this distance regime still needs to be shown<sup>5</sup>.

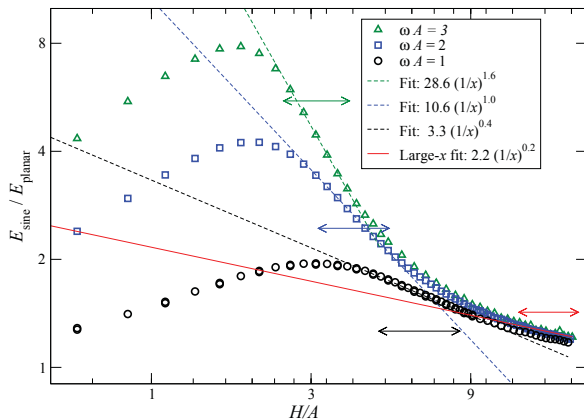


Figure 3.2: Normalized Casimir-Polder energy  $E_{\text{sine}}/E_{\text{planar}}$  above a corrugation minimum  $\phi = -\pi/2$  versus the normalized distance  $H/A$  for three different corrugation frequencies. Small distances are governed by a linear increase with anomalous dimension  $\eta = -1$ , cf. Eq. (3.11). The drop-off beyond the peak is characterized by an  $\omega$ -dependent anomalous dimension  $\eta \simeq 0.4, 1.0, 1.6$  for  $\omega A = 1, 2, 3$ . At larger distances  $H/A \sim 10$ , all normalized energies approach a universal curve with  $\eta \simeq 0.2$ . The corresponding fit regions are indicated by horizontal arrows.

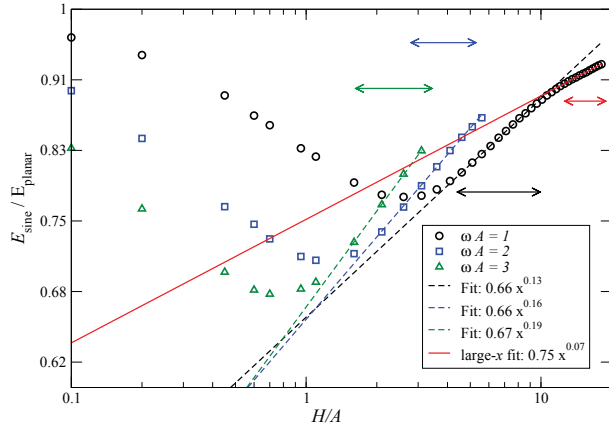


Figure 3.3: Normalized Casimir-Polder energy  $E_{\text{sine}}/E_{\text{planar}}$  above a corrugation maximum  $\phi = \pi/2$  versus the normalized distance  $H/A$  for three different corrugation frequencies  $\omega A = 1, 2, 3$ , respectively. All units are set by the corrugation amplitude  $A$ . The increase beyond the dip is characterized by an  $\omega$ -dependent anomalous dimension  $\eta \simeq -0.13, -0.16, -0.19$  for  $\omega A = 1, 2, 3$ . At larger distances  $H/A \gtrsim 10$ , a power law with  $\eta \simeq -0.07$  is observed for the  $\omega A = 1$  curve. The corresponding fit regions are indicated by horizontal arrows.

### 3.2.2 Sawtooth-like corrugation

To see if the universality behavior is also invariant under the form of the corrugation, let us study, as a second example, the Casimir-Polder potential for a sawtooth structure, where the wavelength  $\lambda$  is 2.8 in terms of the amplitude  $A$ . I.e., the dominant frequency of its Fourier decomposition is  $\omega A \simeq 0.45$ . These parameters reflect the specifications of a sawtooth structure used in an experimental setup [144]. In our numerical studies, we use a smoothed, continuous sawtooth-like structure function with wavelength  $\lambda$ , starting at  $h(0) = 0$ , rising linearly to its maximum amplitude  $A$  at  $h(0.8\lambda)$  and dropping linearly to zero again at  $h(\lambda) = h(0)$ .

In Fig. 3.4, we plot  $E_{\text{sawtooth}}/E_{\text{planar}}$  above the corrugation minimum. Qualitatively, the result is similar to that obtained for the sine structure and reveals the various analogous

<sup>5</sup>It seems, however, worthwhile to check this behavior directly in full QED.

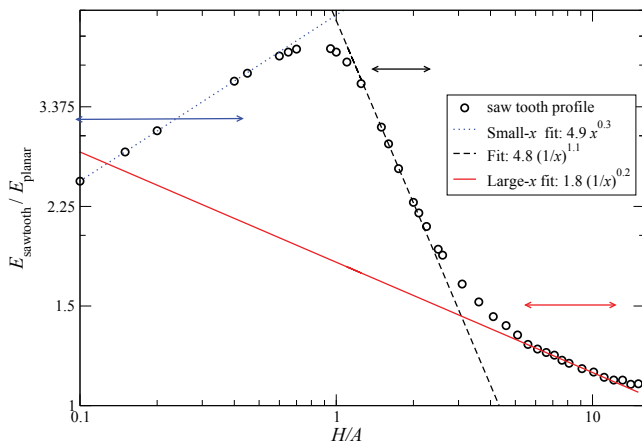


Figure 3.4: Normalized Casimir-Polder energy  $E_{\text{sawtooth}}/E_{\text{planar}}$  above a corrugation minimum of the saw-tooth profile versus  $H/A$  for  $\omega A \simeq 0.45$ . The increase towards the peak is governed by a power-law with anomalous dimension  $\eta = -0.3$ . The drop-off beyond the peak is characterized by  $\eta \simeq 1.1$ . At larger distances  $H/A \sim 10$ , the normalized energy approaches a curve similar to the ones for the sine structure with  $\eta \simeq 0.2$ . The corresponding fit regions are indicated by horizontal arrows.

regimes. Quantitatively, the peak and consequently some of the anomalous dimensions are more pronounced. The increase towards the peak follows a power-law with anomalous dimension  $\eta \simeq -0.3$ . For the decrease right beyond the peak at  $H/A \gtrsim 1$ , we find  $\eta \simeq 1.1$ . At larger distances  $H/A \sim 10$ , we again observe a second power law with anomalous dimension  $\eta \simeq 0.2$  which agrees quantitatively with the anomalous dimension in the sinusoidal case. According to our previous considerations, this agreement can immediately be understood from the fact that the fluctuation integrals again average over the corrugation structures small compared to the distance parameter  $H$ .

### 3.3 Probing with varied inhomogeneities

#### Brief summary and perspectives of the geometric vacuum probes

In this chapter, based on the constrained-functional-integral approach, we devised a novel access to arbitrary uniaxial corrugations in Casimir-Polder systems, whose main feature consists in its nonperturbative treatment of the height profile of the corrugation. In a numerical study for two periodic corrugation profiles we parameterized the geometry dependence of the Casimir-Polder energy by introducing an anomalous dimension  $\eta$ , which quantified the difference in the distance dependency with respect to the planar setup. The main finding of this chapter was the identification of a larger-distance regime where all data above a corrugation minimum could be characterized by a universal anomalous dimension. Although this anomalous dimension still depended on the position above the corrugation, no dependence neither on the shape of the periodic profile nor on the frequency was found as long as the product of corrugation frequency and surface separation was sufficiently large.

This phenomenon was attributed to the fact that the corrugations, constituting small-scale structures within the setup, become irrelevant at larger distances as they are averaged out by virtue of the isotropic vacuum fluctuations.

The universality behavior as well as the nontrivial power-law dependence would not have been accessible through a perturbative calculation which constitutes a Taylor expansion in *integer* powers of the amplitude of the corrugation. Intriguingly, the feature of universality found in the large-distance regime has only recently been confirmed [140] in a complementary calculation for the electromagnetic case using a scattering-theory approach, see, e.g., [142] for a recent overview of the different formulations of this approach.

However, to finally compare the results from this chapter to Casimir-Polder measurements from experiments employing quantum reflection, see, e.g., [127, 128, 145], not only a full extension to the electromagnetic situation is needed, but also the dynamics of the scattering problem needs to be worked out. In particular, atoms near the corrugated surface can move into all directions and not only along the global surface normal. Thus, the full Casimir-Polder potential needs to be mapped out, and the time-dependent quantum-reflection problem in this potential has to be solved.

In summary, the approach presented here constitutes a basis for this research.

### Probing with inhomogeneities: From objects to fields

In this chapter, we have argued that a better understanding of global effects through inhomogeneities in geometric probes of the quantum vacuum is needed to enable an accurate theoretical description of rapidly improving Casimir-Polder force measurements. Also in the other vacuum probe considered in this thesis, inhomogeneities are in large parts an open issue: In particular, the influence of temporal and spatial inhomogeneities in external fields on the propagation of light (cf. Sect. 2.2) is widely under investigation and also subject to the aforementioned worldline techniques. In particular, numerical and analytical techniques going beyond the constant external field approximation will be central to the understanding of upcoming optical probes of the vacuum employing, e.g., high-intensity lasers [34–39].

In the following two chapters – although still safely staying in the constant-field approximation – we will consider phenomenological implications of light propagation in two setups where inhomogeneities in the external field are also found to play a crucial role. To begin with, we employ pulsed magnets at gravitational-wave interferometers whose sensitivity curve is found to have a good match with the external magnetic pulse length, displaying them as a potential site for optical probes of the quantum vacuum. Thereafter we will outline a purely-laser-based axion-like particle search whose potential success will greatly rely on a perfect laser frequency match.

# Chapter 4

*“Do not fear mistakes. There are none.”*

Miles Davis

## Advanced interferometry as a quantum vacuum probe

Following the discussion of Sect. 2.2, vacuum nonlinearities – be their origin due to standard physics or an hitherto undiscovered particle content – are effectively probed by letting a probe light beam propagate in preferably strong external electromagnetic fields. In this context, particularly the implications of polarimetric measurements were reviewed, whose most important observables were argued to be ellipticity and rotation. In addition, an alternative to polarimetry is given by *absolute* phase velocity measurements which are most easily carried out in an interferometric setup.

Realizing that – for a distinct frequency range – most precise interferometers are already in place around the globe, the employment of gravitational-wave interferometers in the detection of QED nonlinearities was first suggested in [146], subsequently also in [147, 148]. However, a challenge that arises in such setups is due to the fact that the actual experimental scope of gravitational-wave interferometers is of course to infer the effects of the gravitational rather than the electromagnetic field. For this reason, experimentalists aim at achieving the highest sensitivity for optical-path variations which relate to the frequency of gravitational radiation for preferably very common astronomical events, which at first sight is rather disadvantageous for a naive quantum vacuum experiment with common static dipole magnets.

Thus, the first main aim of this chapter is to identify *pulsed* magnets as a suitable strong-field source in this context, since their pulse frequency can be matched perfectly with the domain of highest sensitivity of gravitational-wave interferometers. In addition, pulsed magnet systems are developed and used in a stable manner in a number of laboratories worldwide at field strengths approaching 100 Tesla. Therefore, we derive the strain of the optical path induced by repeated magnet pulses, as this is the central observable at gravitational-wave interferometers. We also compute the signal-to-noise ratio for selected interferometers as a criterion for measurability. A second main task of this chapter is to demonstrate that not only strong-field QED phenomena can be investigated in such



setups but also further regions of the parameter space for minicharged and axion-like particles will become accessible.

## 4.1 Elements of the interferometric setup

### 4.1.1 Strain & sensitivity at gravitational-wave interferometers

Ground-based gravitational-wave interferometers consist of two perpendicular interferometer arms of equal length  $L$ , where mirrors are placed at the end of each arm and form an evacuated cavity for two in-phase laser beams. An incoming perturbation such as a gravitational wave leads to a relative change  $\Delta L$  of the length of the interferometer arms, manifesting itself as a phase difference of the two laser beams. The so-called “strain”  $h(t) = \Delta L/L$  then corresponds to the amplitude of the incoming perturbation. Remarkably, present day interferometers are, in certain frequency ranges, sensitive to a strain of  $h \sim 10^{-22}$ ; future upgrades aim at further improvements of one or two orders of magnitude.

In our context, it is not the arm length itself which is varied but the corresponding optical path length  $L$  which can be modified by a strong magnetic field, cf. Chapt. 2. If an external field is applied in a region of length  $x < L$  in one of the interferometer arms, an optical-path difference  $\Delta L = x(1 - v)$  is induced. First considering a QED-induced strain, we concentrate on the parallel mode for which the velocity shift is maximal.

By means of Eq. (2.15), the resulting strain is

$$h(t) = \frac{\Delta L}{L}(t) = \frac{x}{L} (1 - v_{\parallel}(t)) = \frac{x}{L} \frac{14}{45} \frac{\alpha^2}{m^4} B(t)^2 \approx \frac{x}{L} (9.3 \times 10^{-24}) \left( \frac{B(t)}{[1\text{T}]} \right)^2. \quad (4.1)$$

It is visible that for a sizable strain, the magnet-length-to-detector-arm ratio  $x/L$  should be as large as possible. However,  $x$  is constrained by the technical realizability of the magnetic field coil, see below, and the detector sensitivity requires long arm lengths to maximize the strain. Thus, a suitable compromise between detector arm length and sensitivity has to be found.

The detector sensitivity to the relative shift of the length of the interferometer arms  $\Delta L/L$  is limited by various sources of noise. At low frequencies  $f \lesssim 40\text{Hz}$ , the main limitation for ground-based detectors arises from seismic activities. For instance, for a temporal modulation of the external magnetic field at  $f \sim 10\text{Hz}$  (as could be achieved, e.g., by a rotating dipole magnet) the sensitivity measure  $S_h(f)$  (as described below) is suppressed by more than three orders of magnitude compared to the peak sensitivity and depletes rapidly for even smaller frequencies. Alternatively, pulsed magnets have a temporal modulation in the frequency range of highest sensitivity, as we will argue below.

At intermediate and higher frequencies, thermal and shot noise, respectively, limit the detector sensitivity, see, e.g., [149–151].

Information about the optimal frequency range is encoded in the total spectral density function  $S_h(f)$  of the noise, see, e.g., [151]. For our estimates, we concentrate on advanced LIGO [152] and GEO600 [153]. The projected sensitivity of both detectors depends on the details of the event acting as a source for the interferometric signal. In the case of LIGO, we use the strain sensitivity for neutron-star binaries [154] for our calculations, which is satisfactory over a wide range of intermediate frequencies (for a typical expected sensitivity curve of the advanced LIGO, see [155]). For GEO600, we use the typical sensitivity data available at [153], which can be well approximated by a fit function of the form

$$S_h(f) = S_0((f_0/f)^{p_1} + 2(f/f_0)^{p_2} + 2)/5, \quad (4.2)$$

where  $f_0 = 560\text{Hz}$ ,  $S_0 = 7 \times 10^{-44}\text{Hz}^{-1}$ ,  $p_1 = 3.8$  and  $p_2 = 3$  near the sensitivity maximum. For the advanced LIGO data, no simple fit function is available and a numerical interpolating function is employed instead. Note that as the signal induced by QED or other hypothetical particles can be well predicted, it seems feasible that the interferometer sensitivity can even be optimized accordingly.

As a measure for the observability of a shift of the optical path  $\Delta L/L$ , we determine the signal-to-noise ratio (SNR) of the induced strain. In the present case, the SNR equals the expectation value of the detector output divided by the standard deviation of the output variable due to noise. An SNR bigger than 1 indicates an enhanced probability that the observed output is not just due to statistical fluctuations of the detector output but rather due to a shift  $\Delta L/L$  which is not caused by detector noise. Using a matched filter (or “Wiener filter”) for the signal, the SNR  $d$  for a gravitational wave interferometer is given by (see, e.g., [151, 156, 157] and references therein)

$$d^2 = 2 \int_0^\infty \frac{|\tilde{h}(f)|^2}{S_h(f)} df, \quad \tilde{h}(f) = \int_{-\infty}^\infty h(t) e^{-2\pi i f t} dt, \quad (4.3)$$

where  $\tilde{h}(f)$  denotes the Fourier transform of the induced strain.

### 4.1.2 Pulsed magnetic fields

For the presented setup, we consider pulsed fields that can be obtained, e.g., at the Dresden High Magnetic Field Laboratory (Hochfeld-Magnetlabor Dresden, HLD) [158–160]. The HLD aims at providing 100T fields generated by a solenoid in a non-destructive setup, i.e., the infrastructure is maintained and the experiment can in principle be repeated arbitrarily often.

Let us first discuss a magnet coil geometry which is suited for inducing quantum nonlinearities in the interferometer and subsequently detail on the associated magnetic-pulse form.

As the magnetic pressure is given by  $p_{\text{mag}} = B^2/2\mu_0$ , already at fields strengths of about  $B = 50\text{T}$ , the pressure on the coils is four orders of magnitude above the atmospheric pressure, demanding a careful coil design. As a consequence, the coils are usually heavily mantled and it is difficult to render the interferometer laser beam orthogonal to the external magnetic field, as required for a maximum velocity shift, cf. Eqs. (2.14) and (2.15). Thus, in order to maximize the shift of the optical path, a pair of Helmholtz coils has to be used instead of the solenoid configuration. In this manner the laser beam of the interferometer can be aligned in parallel to the field coils and thus mainly orthogonal to the magnetic field lines without interfering with the coil mantle.

For such “split coils”, field strengths of  $\mathcal{O}(10\text{T})$  are technically feasible, at a coil diameter of about  $x = 0.2\text{m}$  and a coil separation of  $\mathcal{O}(1\text{cm})$  [161]. As the beam waist of the interferometer lasers is of the order of cm, the cross section of the interferometer beam can fit in between the magnet coils, even though the issue of stray photons may require further discussion. In addition, for standard Helmholtz setups, the field is roughly constant at a sizable extent only along the direction of the magnetic field lines, whereas the detection of vacuum nonlinearities requires a sizable field length perpendicular to the field lines; the length of the latter is of the order of the coil separation. For the proposed setup, the coil design thus needs to be optimized to provide for high (but not necessarily constant) magnetic field strengths, spatially extending orthogonally to the direction of the field lines.

A typical pulse undergoes a damped oscillation with pulse frequency  $\nu_B$  and damping rate  $\gamma$ . For  $N$  subsequent pulses at times  $t_0 \dots t_{N-1}$ , a satisfactory description is given by

$$B(t) = B_0 \sum_{i=0}^{N-1} \theta(t - t_i) \sin(2\pi\nu_B(t - t_i)) \exp(-\gamma(t - t_i)). \quad (4.4)$$

Here, we have ignored that successive pulses have no temporal overlap in a single-magnet setup. However, as the pulse repetition rate  $\nu_P \equiv 1/(t_{i+1} - t_i)$  of the considered magnets is much smaller than the damping rate (see below), Eq. (4.4) is a well justified approximation. The pulse frequency  $\nu_B$  in Eq. (4.4) depends on the total capacity of the capacitor banks and can lie in the range  $\mathcal{O}(\text{ms} \dots \text{s})$ . The damping rate  $\gamma$  is mainly determined by the heat capacity of the coil, which – as a rule – requires to re-cool after each pulse. In addition, the achievable pulse repetition rate  $\nu_P$  in a non-destructive mode depends strongly on the desired peak field strength. In the following we consider an ambitious, but nevertheless feasible Helmholtz setup [161] which achieves a maximum field strength of  $B_{\text{max}} = 60\text{T}$ , followed by a reverse field of  $B_{\text{min}} = -6\text{T}$  and thus a damping to about

10% of the peak field strength<sup>1</sup>. This choice fixes the amplitude of the model pulse in Eq. (4.4) to  $B_0 \approx 148\text{T}$  and implies the constraint

$$\gamma = 2\nu_B \ln \left| \frac{B_{\max}}{B_{\min}} \right|. \quad (4.5)$$

We use the remaining free parameter  $\nu_B$  for optimizing the SNR, cf. Eq. (4.3), within the technical limitations. For this, we need the modulus of the Fourier transform of the strain. For the model pulse of Eq. (4.4) one obtains<sup>2</sup>

$$|\tilde{h}(f)|^2 = \frac{x^2}{L^2} (9.3 \times 10^{-24})^2 \left( \frac{B_0}{[1\text{T}]} \right)^4 \sin^2 \left( \pi \frac{f}{\nu_P} N \right) \csc^2 \left( \pi \frac{f}{\nu_P} \right) \times \frac{(\pi\nu_B)^4}{(\gamma^2 + \pi^2 f^2)(\gamma^4 + \pi^4 (f^2 - 4\nu_B^2)^2 + 2\gamma^2 \pi^2 (f^2 + 4\nu_B^2))}. \quad (4.6)$$

For a single pulse  $N = 1$ , the trigonometric functions in Eq. (4.6) cancel and the dependence on the repetition rate  $\nu_P$  drops out, as expected. For a large number of pulses  $N$ , the trigonometric functions approximate<sup>3</sup> a  $\delta$  comb,

$$\sin^2 \left( \pi \frac{f}{\nu_P} N \right) \csc^2 \left( \pi \frac{f}{\nu_P} \right) \approx N \sum_{n \in \mathbb{N}} \delta \left( \frac{f}{\nu_P} - n \right). \quad (4.7)$$

At large  $N$ , only frequencies which are multiples of the pulse repetition rate  $\nu_P$  thus contribute to the SNR in Eq. (4.3). As  $\nu_P$  is much smaller than the frequencies dominating the SNR, the contributing frequencies form a quasi-continuum such that the sum in Eq. (4.7) can well be approximated by an integral<sup>4</sup>. As a result, the square of the SNR for  $N$  pulses can to a good accuracy be expressed in terms of the single-pulse result:

$$d^2|_N \approx N d^2|_1. \quad (4.8)$$

The reproducibility of the signal by non-destructive pulsed magnets thus is a lever arm for an enhancement of the SNR by a factor of  $\sqrt{N}$ .

<sup>1</sup>It can be assumed that also pulses with damping to about 70% will be obtainable in the near future. The above pulse parameters are in this sense conservative, since a smaller damping factor  $\gamma$  leads to a higher strain (cf. Eq. (4.6)).

<sup>2</sup>We use the opportunity to point out a typographical error in Eq. (8) and below Eq. (9) in [162]. In these places, the pulse repetition rate should be correctly referenced as  $\nu_P$ .

<sup>3</sup>For large  $N$ , the poles of the cosecant dominate and one has:  $\sin^2(Nx) \csc^2(x) \simeq \sum_n \sin^2(N(x - n\pi)) / (x - n\pi)^2 \stackrel{N \rightarrow \infty}{\simeq} N\pi \sum_n \delta(x - n\pi)$ . Note that as the frequencies in Eq. (4.7) are positive, here  $n$  has to be understood as positive integer also.

<sup>4</sup>Note that the squared SNR  $d^2 \sim N \int df \sum_n g(f) \delta(\frac{f}{\nu_P} - n) \stackrel{f = \tilde{f}\nu_P}{=} N\nu_P \int d\tilde{f} g(\tilde{f}\nu_P) \sum_n \delta(\tilde{f} - n) = N\nu_P \sum_n g(n\nu_P) \stackrel{\nu_P \rightarrow 0}{\simeq} N \int df g(f)$ , where  $g(f)$  summarizes the  $f$ -dependence outside the  $\delta$  distribution.

## 4.2 Estimated interferometric discovery potential

### 4.2.1 Detection of the QED-induced strain

We now have all the ingredients in order to calculate the SNR due to the QED-induced strain. The first interferometer investigated is the advanced LIGO with  $L = 4000\text{m}$ . Its sensitivity is optimal for frequencies ranging from approximately 50Hz to 500Hz with a sensitivity measure on the order of  $S_h(f) \approx 10^{-47}\text{Hz}^{-1}$ . Maximizing  $d^2$  by varying the pulse parameter  $\nu_B$  yields  $\nu_B \approx 47\text{Hz}$ , implying  $\gamma \approx 217\text{Hz}$  by means of Eq. (4.5). Inserting these values into Eq. (4.3), we obtain the SNR for a single pulse,

$$d_{|1}^{\text{LIGO}} \approx 1.9 \times 10^{-2}. \quad (4.9)$$

As a result, by virtue of Eq. (4.8), about  $N \approx 2763$  pulses are required in order to achieve a total SNR of  $\mathcal{O}(1)$ . Depending on the details of the setup, an SNR of  $\mathcal{O}(10)$  would be preferable. For the following feasibility study, however, we only demand for an SNR of  $\mathcal{O}(1)$ . This is also justified because the expected signal can be predicted to a high accuracy which will most likely allow for an adapted noise filtering.

As mentioned above, the re-cooling time for the magnet system which determines the pulse-repetition rate depends mainly on the pulse energy. A realistic estimate lies in the order of several minutes. To observe the QED vacuum nonlinearities, this would imply a continuous operation of the facility for a few days, which appears reasonable.

GEO 600 is considerably less sensitive than advanced LIGO but, for our purposes, profits from the shorter arm length of  $L = 600\text{m}$ . Maximizing  $d^2$  with respect to  $\nu_B$  yields  $\nu_B \approx 273\text{Hz}$  with  $\gamma \approx 1259\text{Hz}$  and thus a pulse length below 1ms. As a result,  $N \approx 2.3 \times 10^6$  pulses are necessary to observe the QED induced strain at GEO, corresponding to an unrealistic measurement time of a few years. In consequence, GEO in combination with presently available pulsed magnets is not well suited for the observation of the QED induced strain. Nevertheless, it still has a discovery potential for light particles beyond the standard model, see below.

### 4.2.2 Interferometry with MCPs and ALPs

As argued in Chapt. 2, the investigation of QED vacuum nonlinearities implicitly searches also the parameter space of a number of hypothetical WISPs. Here, we discuss potential velocity shifts induced by minicharged spin-1/2 fermions and axion-like particles, cf. Sect. 2.2.

### Velocity shifts due to minicharged particles

Firstly note that MCP masses corresponding to a Compton wavelength larger than the extent of the magnetic field cannot be fully resolved within the setup. Thus, the Helmholtz coil separation of  $\mathcal{O}(1\text{cm})$  constrains the search for MCP masses to approximately  $m_\epsilon \gtrsim 2 \times 10^{-5}\text{eV}$ . Again, we concentrate on the effect for the polarization component parallel to the external field which maximizes the velocity shift as in the QED case.

We can extract the velocity shifts induced by minicharges from Eqs. (2.20-2.22). As the auxiliary function  $I_{\parallel}$  entering the velocity shift depends on the magnetic field  $B(t)$  in a nontrivial manner, the Fourier transform of the strain, as required for the computation of the SNR (cf. Eq. (4.3)) cannot be given in closed form and a careful numerical implementation is needed. A useful check for the numerical accuracy is given by the two asymptotic limits of the velocity shift:  $1 - v \sim \epsilon^4 B^2 / m_\epsilon^4$  for large masses (in consistency with the QED strain in Eq. (4.1)) and  $1 - v \sim -\epsilon^{8/3} B^{2/3} / \omega^{4/3}$  for small masses. For an interferometer laser with  $\omega = 1.2\text{eV}$  and the pulse shape as used for the QED effect, we obtain exclusion limits in the fractional charge-mass plane  $\{\epsilon, m_\epsilon\}$  by demanding an SNR of  $\simeq 1$ .

As visible from Fig. 4.1, already a single-pulse ( $N = 1$ ) measurement at the advanced LIGO can approach among<sup>5</sup> the best laboratory bounds on minicharged particles [58] derived from PVLAS data [24] with potential minor improvements in the larger-mass range. Assuming a measurement time of ten days at GEO with a magnet re-cooling time of 5 minutes, implying  $N \simeq 2880$  pulses would arrive at a similar bound. The small-mass asymptotics of the GEO bounds for  $N = 1$  and  $N = 2880$  are also shown in Fig. 4.1. Advanced LIGO with  $N = 2763$  (as needed for to observe the QED effect) can reach a sensitivity of  $\epsilon \simeq 10^{-7}$  for  $m_\epsilon \lesssim 0.01\text{eV}$ . Noteworthy, this would compete with current cosmological bounds obtained from CMB data [104] (see also the dash-dotted line in Fig. 6.4 which will be discussed in more detail in Sect. 6).

We conclude that an investigation of the QED effect can also broadly improve current laboratory bounds on MCPs.

### Interferometry via axion-like-particles

We now turn to the discussion of ALPs. Here, an effective reduction of the phase velocity arises from the fact that the corresponding photon partly propagates as a massive ALP component. Following Eq. (2.26), the corresponding velocity shifts read

$$1 - v_{\parallel}^{\text{P}} = 1 - v_{\perp}^{\text{S}} \simeq \frac{B^2}{2m_\phi^2} g_{\text{P/S}}^2 \left( 1 - \frac{\sin(2y)}{2y} \right), \quad y = \frac{xm_\phi^2}{4\omega}, \quad (4.10)$$

<sup>5</sup>LSW setups as, e.g., at ALPS [77] can provide even stronger bounds on minicharged particles. However, as these rely on a hidden-photon intermediate state, cf. Sect. 2.2.1, we rather compare our estimates to polarization data obtained from PVLAS.

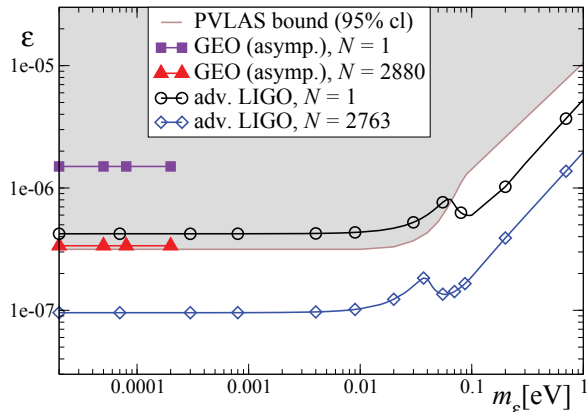


Figure 4.1: Discovery potential of minicharged fermions in the coupling-mass plane. Already a single-pulse measurement at advanced LIGO (or  $N \simeq 2880$  at GEO) can approach or slightly improve the laboratory bounds from PVLAS. The use of  $N = 2763$  pulses as needed for the QED effect can lead to sizable improvements over the whole mass range.

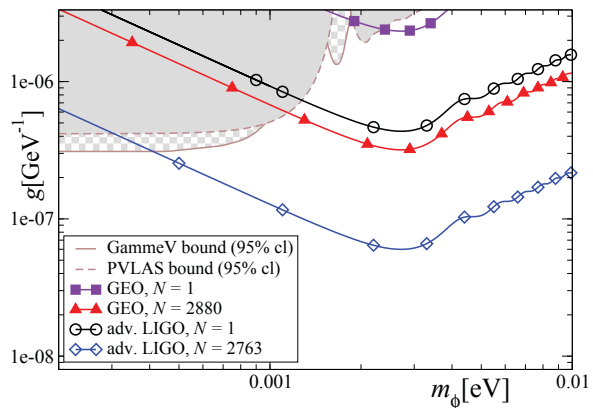


Figure 4.2: This figure shows the discovery potential in the coupling-mass plane for ALPs at LIGO and GEO, respectively. The laboratory bounds by GammeV (LSW) and PVLAS (rotation) can be improved significantly in the meV mass range and above by advanced LIGO as well as already by GEO.

for pseudoscalar and scalar ALPs, respectively. As discussed in detail, e.g., in [50], cf. also Sect. 2.2, the polarimetry of strong-field particle searches can distinguish between the various particle scenarios: As visible from Eq. (4.10), by choosing the polarization of the probe beam appropriately, the parameter space of scalar and pseudoscalar ALPs, respectively, can be covered. However, in the following, we concentrate on the velocity shift irrespective of the polarization dependence and thus set  $g_{P/S} \equiv g$ .

Let us first consider the ALP parameter range for the coupling  $g$  and mass  $m_\phi$  that can be probed by a single magnet pulse. Using the pulse shape as employed for the studies of QED-induced velocity shifts, we obtain the accessible region in the mass-coupling plane, see Fig. 4.2. For a comparison<sup>6</sup>, laboratory limits from PVLAS and GammeV are provided in the figure. As visible, already a single-pulse measurement at advanced LIGO can largely improve existing bounds for masses above 1meV. Intriguingly, even a single pulse measurement at GEO can cover a small fraction of hitherto unexplored parameter space. At advanced LIGO, for  $m_\phi \gtrsim 4 \times 10^{-4}$ eV, assuming a number of pulses as required to observe the QED effect give access to a parameter space which is largely uncovered by current laboratory limits, however, cf. also footnote 6.

<sup>6</sup>Note that at the time of publication of this study in [162, 163], data from PVLAS polarization measurements and the GammeV LSW setup provided for the strongest laboratory bounds on ALPs. In the meantime, the ALPS collaboration has published new limits from LSW [77] reaching down to  $g \geq 10^{-7}$ GeV<sup>-1</sup> in the  $m_\phi \leq 10^{-3}$ eV mass range, cf. also Fig. 5.2.

Lastly, note that the shape of the exclusion lines for the proposed experiment differs from the GammeV and PVLAS bounds in Fig. 4.2 as the latter arise from LSW and rotation, respectively, cf., e.g., [50] as well as Sect. 2.2.

### 4.3 Benefits of pulsed fields and a logical upgrade

#### A physics case for joining pulsed magnets with high-sensitivity interferometry

The sensitivity goal of ground-based gravitational-wave interferometers appears well suited to be used in the exploration of the strong-field domain of QED. In order to generate a strongly magnetized quantum vacuum in such an interferometric experiment, we have suggested pulsed magnets as an advantageous strong-field source for two reasons: they provide extremely strong laboratory magnetic fields, and their pulse frequency can be matched perfectly with the region of highest sensitivity of the gravitational-wave interferometers.

For quantitative estimates, the above studies were concentrated on the advanced LIGO detector, as its sensitivity goal matches with currently available field strengths already in a rather conservative estimate. Pushing the various components to their limits may facilitate a detection also at the gravitational-wave interferometers which are currently operational such as GEO 600. Also the fact that the quantum-induced signal can be predicted theoretically to a good accuracy may give rise to an improved noise filtering.

Generally, the QED velocity shift as well as the MCP signal in the large-mass domain and the dispersive ALP effect scale with  $xB^2$ , with magnetic field amplitude  $B$  and spatial field extent  $x$ , cf. Chapt. 2. As shown, for the use of gravitational-wave interferometers, also a suitable time variation of the magnetic field is needed<sup>7</sup>. Whereas pulsed fields profit from extremely high fields and a suitable time variation, their deficit is a smaller extent in comparison to dipole magnets. Since pulsed fields win roughly an order of magnitude in the field strength and lose an order of magnitude in the field extent, the quantity  $xB^2$  can generically still be an order of magnitude larger for pulsed fields than for dipoles. A similar consideration has inspired the development and use of pulsed magnets in the BMV experiment [28] which finally aims at a parameter goal of  $xB^2 \simeq 600\text{T}^2\text{m}$  (recent experimental results of BMV have been achieved with  $xB^2 \simeq 40\text{T}^2\text{m}$ ) [28]. The pulsed Helmholtz coil configuration considered in this work as inspired by ongoing experiments at the Dresden High Magnetic Field Laboratory would yield  $xB^2 \simeq 720\text{T}^2\text{m}$ .

---

<sup>7</sup>Though note that a rotating dipole magnet might also be able to overcome these difficulties [148].



### Further requirements and next steps

Ahead of an experimental realization of the suggested setup, surely many engineering issues need to be worked out. For example, the diameter of the vacuum beam pipe employed in the interferometer is commonly much larger than the beam waist of the interferometer laser. Thus, an advantageous installation of the magnet coils within the beam pipe has to be found that assures a maintenance of the vacuum pressure levels in the beam pipe and allows for a preservation of the sophisticated laser alignment. Also, it has to be assured that mechanical vibrations which might arise in the magnet pulse production do not have a sizable impact on the sensitivity measure of the gravitational-wave interferometer in the specified frequency range. Lastly, let us note that also the implications of an operation of an interferometric setup directly at the HLD seems to deserve a more detailed investigation, in particular as a radiation facility (F)ELBE is also in operation at Rossendorf, cf. [164].

In summary, the prospect of exploring a new parameter regime of QED with implications for the search for new particles could make the establishment of a strong-field quantum-vacuum program at gravitational-wave interferometers a worthwhile task for the future.

### Increasing the external field strength by pulse shortening

Finally, let us remark that although the key feature of our proposed experiment is the matching between the frequency of the pulsed magnet and the optimal sensitivity range of the interferometer, a crucial ingredient is also the fact that the achievable external field strength and thereby the sensitivity of the setup can be increased through the use of short magnet pulses instead of the commonly used static or slowly rotating dipole magnets. Further pursuing this thought, one finds that using a second, strong laser as external field seems desirable as modern high-intensity lasers provide the highest field strengths within a laboratory, though necessarily at low temporal and spatial extent.

In this chapter, however, the use of a further (high-intensity) laser as external field is disfavored as the temporal pulse extent of a femtosecond high-intensity laser would dominate the denominator of Eq. (4.6) and thereby decrease the SNR as there no match to the optimal sensitivity range of the gravitational-wave interferometer could be established.

By contrast, in the following chapter we discuss the requirements and advantages for a *purely laser-based* setup and find that the fact that the external field then varies on the same scales as the probe beam, can actually be utilized to deduce an appropriate observable for signatures of axion-like particles.

*“The great tragedy of Science-  
the slaying of a beautiful hypothesis by an ugly fact.”*

Thomas H. Huxley

## Chapter 5

# Searching for axion-like particles with high-intensity lasers

In the previous chapter, we have investigated a dedicated interferometric setup which would – among other things – be sensitive to a new region of the axion-like particle parameter space. In addition, as discussed in Sect. 2.2.2, also polarimetric measurements and light-shining-through-walls are viable methods for ALP searches. In this chapter, we want to introduce an additional scenario for ALP search which aims at utilizing the advantages and the development potential of modern high-intensity lasers.

In polarimetry, interferometry as well as LSW, the decisive parameter for the best obtainable bounds on the ALP mass and coupling is the product of the field strength of the external magnetic field  $B$  and its spatial extent  $L$  which is a measure for the optical path length. Typically, the dipole magnets which are employed in these setups provide field strengths of  $B \sim \mathcal{O}(1 - 10)\text{T}$  extending over a length of  $L \sim \mathcal{O}(1 - 10)\text{m}$ . By use of cavities for the probe beam, the interaction region can be extended by a few orders of magnitude, depending on the details of the setup. On the other hand, the highest field strengths which are obtainable nowadays in a laboratory are present within the focal spots of high-intensity laser systems.

Current Multi-Terawatt lasers achieve peak field strengths of  $B \sim \mathcal{O}(10^5 - 10^6)\text{T}$ , however, naturally at the cost of spatial extent of these fields, which ranges from  $L \sim \mathcal{O}(1 - 10)\mu\text{m}$ . Nevertheless, the parameter  $BL$  in the laser focus lies within the same ballpark as for the dipole searches, calling for proposals of ALP search within high-intensity laser-based setups: It should be noted that the achievable laser intensity has gone up by more than six orders of magnitude since the introduction of “chirped pulse amplification” [165]. Also it is expected that the parameter  $BL$  within planned facilities such as the Extreme Light Infrastructure (ELI) [166] will considerably exceed the equivalent parameter at dipoles within the near future.

On closer inspection, however, the above mentioned optical techniques, namely polarimetry and LSW setups for ALP detection seem to be obstructed by the nature of the electromagnetic field configuration within high-intensity lasers. Firstly, high intensities and thus high field-strengths can only be attained by pulsed lasers with typical pulse lengths of  $\tau \sim \mathcal{O}(10 - 100)$ fs and repetition rates of  $f_{\text{rep}} \lesssim 1$ Hz. In addition, high intensities require strongly focused pulses with focal spots of  $\mathcal{O}(1 - 10)\mu\text{m}$ . Thus, the cavity enhancements which are used for polarimetric measurements at dipoles are not as easily available for purely laser-based setups relying on high intensity. Secondly, also the insertion of a light-blocking barrier in a purely laser-based setup is disfavored: In order to avoid damaging of the wall by the high-intensity lasers, the two focal spots for the conversion and reconversion processes, cf. Fig. 2.4, would in practice be required to be separated by  $\mathcal{O}(\text{cm})$ . As the spatial extent of the focal spots of lasers is by orders of magnitude smaller, the generic angular spread of the beam of ALPs released from the first focal spot would significantly reduce the number of ALPs that could possibly hit the second spot for reconversion. Even if the angular spread could be minimized, a purely laser-based LSW experiment would demand for a temporally very well-synchronized setup: The propagation time of the ALPs from the first to the second focal spot depends on the mass of the ALPs which is unknown a priori. Thus, the temporal delay of the pulses would repeatedly have to be adjusted anew to scan through viable fractions of the ALP mass range.

In this chapter, we suggest another mechanism for ALP search with high-intensity lasers which does neither rely on polarimetry nor on light-blocking walls. The electromagnetic field provided by high-intensity lasers varies at a scale which can be of the same order of magnitude as the wave length of a probe photon. As will be shown, probe photons can thus experience a frequency shift when crossing the focal region of the external field by virtue of their modified wave equation due to the photon-axion coupling term, cf. Eq. (2.23). In essence, the vacuum effectively acts as a medium and frequency-mixing processes, which are well-known from Nonlinear optics, can occur. Consequently, the detection of such frequency-mixed photons could point towards the existence of ALPs. In the following, we compute this effect quantitatively and discuss the required setup and specifications of lasers which are necessary for its detection. We proceed as follows: In Sect. 5.1, we first give the equations of motion for the ALPs and probe photons, which we reduce to one spatial dimension for simplicity, and discuss the necessary parameterization of the high-intensity laser beams. Subsequently, we compute the photon-axion conversion and back-conversion amplitudes in a specific laser configuration and discuss the physical reasons why this setup can lead to a frequency shift for the probe photons. Finally, in Sect. 5.2, we summarize our findings and give ALP exclusion bounds achievable for the operational high-intensity laser facility at the Institute of Optics and Quantum Electronics in Jena as well as the planned Exawatt facility ELI [166].

## 5.1 Dynamics of the axion-photon interaction

### 5.1.1 Equations of motion

We specialize to pseudoscalar ALPs in the following in order to account also for the QCD axion in particular<sup>1</sup>. Note however that the scalar case can be evaluated in an analogous calculation.

Following Eq. (2.23), one has

$$\mathcal{L} = -\frac{1}{4} F_{\mu\nu} F^{\mu\nu} + \frac{1}{2} \partial_\mu \phi \partial^\mu \phi - \frac{1}{2} m^2 \phi^2 + \frac{1}{4} g \phi F_{\mu\nu} \tilde{F}^{\mu\nu} , \quad (5.1)$$

where  $m$  in the remainder of this chapter is the ALP mass and  $g$  the pseudoscalar coupling such that we have dropped corresponding labels for clarity.

As we are interested in the effects of the nonlinear interaction of laser photons, let us give the equations of motion for the photon and the axion field that follow from Eq. (5.1):

$$\partial_\mu \partial^\mu \phi + m^2 \phi - \frac{1}{4} g F_{\mu\nu} \tilde{F}^{\mu\nu} = 0 , \quad (5.2)$$

$$\partial_\mu F^{\mu\nu} - g (\partial_\mu \phi) \tilde{F}^{\mu\nu} = 0 . \quad (5.3)$$

Below, we study these equations in a rather general setup, assuming the interaction of three independent electromagnetic fields, which we all presume to be provided by high-intensity lasers. As it will turn out later, experimentally there is actually just the need for at most two sources.

We split up the field strength tensors into contributions of a probe beam  $a_{\text{in}}^\mu$  and two external fields  $A_j^\mu$  and  $A_k^\mu$ , where  $j$  and  $k$  label the two external lasers. In addition, we neglect self-interactions of these fields. By coupling to  $A_j^\mu$ , the probe photons can be converted into ALPs, see Eq. (5.2). Successively, in Eq. (5.3), these axions can be reconverted into photons  $a_{\text{out}}^\mu$  by the coupling to a field  $A_k^\mu$ . For simplicity, we specialize to a one-dimensional<sup>2</sup> setup. In addition, since we do not intend to focus on polarimetry

<sup>1</sup>As the following calculation holds both for axions and ALPs, we use their names interchangeably with a reference to both implicitly understood. In the discussion of the exclusion limits, cf. Sect. 5.2.1, it is of course important to distinguish between them.

<sup>2</sup>As a side remark, note that Eqs. (5.2) and (5.3) can, for a probe field  $\{\vec{e}, \vec{b}\}$  and an external field  $\{\vec{E}, \vec{B}\}$  also be written as

$$\begin{aligned} (\partial_t^2 - \vec{\nabla}^2 + m^2) \phi &= -g (\vec{e} \vec{B} + \vec{b} \vec{E}) , \\ (\partial_t^2 - \vec{\nabla}^2) \vec{e} &= g \left[ \partial_t^2 (\phi \vec{B}) - \vec{\nabla} (\vec{\nabla} (\phi \vec{B})) + (\vec{\nabla} \times \partial_t) (\phi \vec{E}) \right] , \end{aligned}$$

where self-interactions of the probe field and the external field are neglected. Here, the second equation can be understood as nonlinear wave equation for the electric field where the nonlinearity is due to a magnetization  $\vec{M} = \phi \vec{B}$  and a polarization  $\vec{P} = \phi \vec{E}$ , where  $\phi$  is determined by the first equation above. This features nicely the magnetoelectric properties of ‘‘axion electrodynamics’’ [167–169] with discontextual applications to solid state physics, cf., e.g., [170, 171].

later on, we assume the incoming probe photons to be polarized along the  $y$ -axis and to propagate along the positive  $z$ -axis without loss of generality.

Under these presumptions, employing Coulomb gauge and following the metric conventions for the field strength tensor (cf. Eq. (A.1)), Eqs. (5.2) and (5.3) can now be written as

$$(\partial_t^2 - \partial_z^2 + m^2) \phi(z, t) = -g [e_{\text{in}}^y(z, t) B_j^y(z, t) + b_{\text{in}}^x(z, t) E_j^x(z, t)] , \quad (5.4)$$

$$(\partial_t^2 - \partial_z^2) a_{\text{out}}^y(z, t) = -g [B_k^y(z, t) \partial_t \phi(z, t) + E_k^x(z, t) \partial_z \phi(z, t)] . \quad (5.5)$$

For the external fields, we consider different cases of propagation along the  $\pm z$ -axis or orthogonal to the  $z$ -axis. In the first case of parallel propagation, the external lasers interact through both their electric and magnetic field components. In the second case of orthogonal propagation, the external fields can couple only through either their electric or magnetic field component.

In particular we see from Eq. (5.4) that the axion amplitude vanishes trivially in a setup where the fields  $e_{\text{in}}^y$  and  $E_j^x$  propagate both along the  $+z$ -axis, since then  $e_{\text{in}}^y = -b_{\text{in}}^x$  and  $E_j^x = B_j^y$ . By contrast, for counter-propagation of the two beams, the fields on the right-hand side of Eq. (5.4) add up, since then we have  $E_j^x = -B_j^y$ .

If the propagation axis of the external field lies orthogonal to the  $z$ -axis, either the magnetic or the electric field component can mediate the conversion process. However, the axion amplitude in Eq. (5.4) is invariant under this choice for a linearly polarized external beam. On the other hand, the back-conversion from the axions into photons is not independent of whether the axion couples to the electric or magnetic field component, due to the asymmetric coupling structure in Eq. (5.5). This is due to the pseudoscalar nature of  $\phi$ . If we had taken  $\phi$  to be a scalar field, then the coupling structure in Eq. (5.5) would be given by interchanging  $B_k^y$  and  $E_k^x$ .

In the following, we solve, along the general lines of [94], Eqs. (5.4) and (5.5) using the retarded Green's functions for the massive and massless differential operators in the equations of motion

$$G_m^{\text{R}}(z, t) = \frac{1}{2} J_0 \left( m \sqrt{t^2 - |z|^2} \right) \theta(t - |z|) , \quad (5.6)$$

$$G_0^{\text{R}}(z, t) = \frac{1}{2} \theta(t - |z|) , \quad (5.7)$$

where  $J_0(x)$  constitutes a Bessel function of the first kind.

The solutions to Eqs. (5.4) and (5.5) naturally depend on the details of the kinematic setup. In the following, we choose with hindsight a specific setting for which the conversion process of photons into axions and vice versa leads ultimately to a frequency shift of the

probe beam. If this frequency shift exceeds the natural line width of the probe beam, it can constitute a measurable signal, possibly indicating the existence of ALPs.

### 5.1.2 Parameterization of the fields

In order to solve Eqs. (5.4) and (5.5) we need a parameterization for the electric and magnetic fields of the three laser beams. A good model for the spatial inhomogeneities of a focused beam is given by Gaussian beams [172], see also [173, 174], which are solutions to the paraxial wave equation.

In consistency<sup>3</sup> with our dynamically one-dimensional model, we restrict ourselves to the lowest-order contribution in the aspect ratio  $\theta_0 \simeq \frac{w_0}{z_r}$ , where  $w_0$  is the waist size and  $z_r$  the Rayleigh length of the beam. The waist size of a Gaussian beam is a measure for the transversal extent of the beam at the focus, whereas the Rayleigh length parameterizes the broadening of the focus along the propagation direction, cf. Fig. 5.1. They are related through the wavelength of the beam as  $z_r = \frac{\pi w_0^2}{\lambda}$ . To maximize the interaction of the lasers, their focal spots should have a sizable overlap. Here, we assume the waist size to be minimized at the origin  $x = y = z = 0$  for the probe beam as well as for the two external fields.

Note that for Gaussian beams, the existence of the peak external field strength is, of course, also limited by a temporal pulse length  $\tau$ . This scale must be larger than the time it takes the probe photons to traverse the external fields:  $\tau_{\text{ext}} \gtrsim z_r^{\text{ext}}$  and  $\tau_{\text{ext}} \gtrsim w_0^{\text{ext}}$ . In the present study, we formally work in the limit of infinite pulse length for both external field and probe beam:  $\tau_{\text{ext}}, \tau_{\text{in}} \rightarrow \infty$ . Our final result will thus be phrased in terms of a transition probability (rather than a transition rate) for the photons of the probe field. In practice, as real facilities are limited in energy, intensity and power, an optimization of the effect under such constraints can typically be expected for all pulse parameters of probe and external field being roughly of the same order.

Under these presumptions, the electric and magnetic field for the incoming probe beam propagating along the positive  $z$ -axis reads

$$e_{\text{in}}^y(z, t) = -b_{\text{in}}^x(z, t) = \frac{E_{\text{in}}}{\sqrt{1 + (z/z_r^{\text{in}})^2}} \sin \left( \omega_{\text{in}} t - k_{\text{in}} z + \arctan \left( \frac{z}{z_r^{\text{in}}} \right) \right), \quad (5.8)$$

where  $E_{\text{in}}$  is the amplitude of the field,  $\omega_{\text{in}}$  the frequency,  $k_{\text{in}}$  the  $z$ -component of the wave vector and  $z_r^{\text{in}}$  the Rayleigh length of the probe beam, as discussed above. From Eq. (5.8) it can be seen that the Rayleigh length not only characterizes the longitudinal extent of the field, but also appears in the so-called Gouy phase shift that a focused light beam undergoes, when passing through its focus [175, 176]. In addition, it holds in Eq. (5.8)

<sup>3</sup>At higher orders in the aspect ratio, the beam acquires polarization components which are neglected in the one-dimensional calculation and loses transversality.

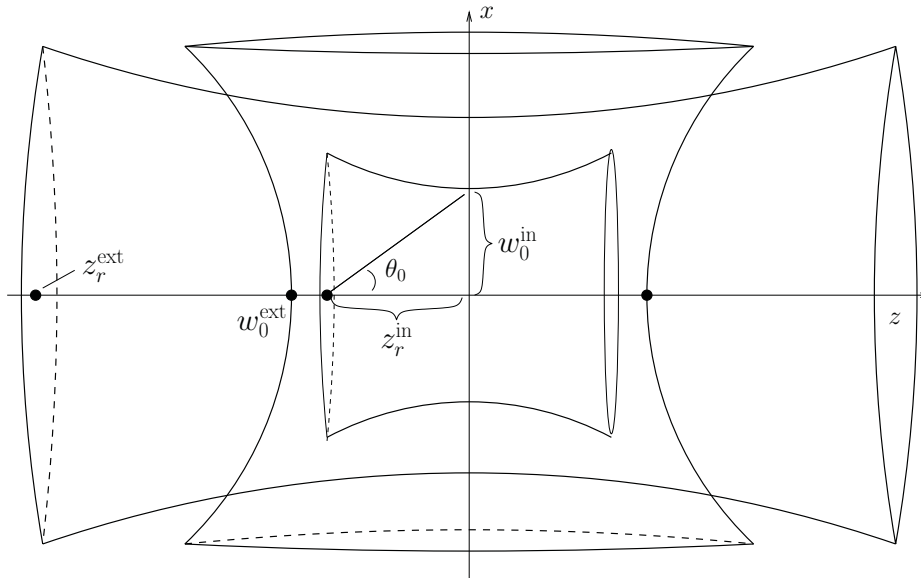


Figure 5.1: Spatial overlap of three focused laser beams at the coordinate center  $x = y = z = 0$ . In this picture, the innermost beam gives the Gaussian probe beam embedded in two external beams which propagate orthogonally and transversally to it, respectively. The waist size  $w_0^{\text{ext}}$  as well as the Rayleigh lengths  $z_r^{\text{in}}$  and  $z_r^{\text{ext}}$  constitute scales for the extent of the beam foci along the propagation direction of the probe beam and thus parameterize the drop-off of the electric and magnetic field components of the lasers. The aspect ratio is typically  $\theta_0 \ll 1$ .

that  $\omega_{\text{in}} = k_{\text{in}}$  in vacuum; nevertheless, we stick to this notational distinction, since it will simplify the discussion of energy and momentum conservation later on. Lastly, the probe beam model in Eq. (5.8) as well as the external beams can in general include also a constant phase factor. However, since only the relative phase between the three beams is important, we omit such a phase factor in the above definition.

### 5.1.3 Photon-axion conversion

We can now calculate the photon-axion conversion amplitude by solving Eq. (5.4). With hindsight, we choose the external field to propagate orthogonal ( $\perp$ ) to the  $z$ -axis and discuss the implications of other possible settings later.

Without loss of generality, we choose the external field to couple through its electric field component, and plug in its Gaussian beam form

$$E_j^x(z, t) = E_{\perp} \sin(\omega_{\perp} t + \psi_{\perp}) e^{-(z/w_0^{\perp})^2}, \quad (5.9)$$

$$B_j^y(z, t) = 0, \quad (5.10)$$

where  $E_{\perp}$  is the amplitude,  $\omega_{\perp}$  the frequency,  $w_0^{\perp}$  the waist size and  $\psi_{\perp}$  the phase of the external beam. Thus, combining the ALP equation of motion, Eq. (5.4) with the Green's

function of Eq. (5.6) and the parameterization of the fields, Eqs. (5.8) and (5.9), we obtain for the axion field:

$$\begin{aligned} \phi(z', t') &= \frac{1}{2} g E_{\text{in}} E_{\perp} \int_{-\infty}^{\infty} dz'' \frac{1}{\sqrt{1 + (z''/z_r^{\text{in}})^2}} e^{-(z''/w_0^{\perp})^2} \int_{-\infty}^{\infty} dt'' \theta((t' - t'') - |z' - z''|) \\ &\times J_0\left(m\sqrt{(t' - t'')^2 - |z' - z''|^2}\right) \sin\left(\omega_{\text{in}} t'' - k_{\text{in}} z'' + \arctan\left(\frac{z''}{z_r^{\text{in}}}\right)\right) \sin(\omega_{\perp} t'' + \psi_{\perp}) . \end{aligned} \quad (5.11)$$

Here we have used primed arguments for the ALP field  $\phi$  in order to indicate that these are variables over which we still have to integrate in the back-conversion process later on.

As typical laboratory scales are many orders of magnitude larger than the spatial extents of the beams, it is justified to perform the  $z''$  integration from  $-\infty$  to  $\infty$ . Following the constraints for the respective pulse lengths  $\tau_{\text{ext}}$  and  $\tau_{\text{in}}$ , which were discussed in the previous section, we let also the integration over  $t''$  extend from  $-\infty$  to  $\infty$  for computational simplicity.

We rewrite the sines as sum of exponentials and substitute  $t'' \rightarrow t' - T$  in Eq. (5.11), yielding

$$\begin{aligned} \phi(z', t') &= -\frac{1}{8} g E_{\text{in}} E_{\perp} \int_{-\infty}^{\infty} dz'' \frac{1}{\sqrt{1 + (z''/z_r^{\text{in}})^2}} e^{-(z''/w_0^{\perp})^2} \\ &\left[ e^{-ik_{\text{in}} z''} e^{i(\omega_{\text{in}} + \omega_{\perp}) t'} e^{i(\arctan(z''/z_r^{\text{in}}) + \psi_{\perp})} \int_{|z' - z''|}^{\infty} dT J_0\left(m\sqrt{T^2 - |z' - z''|^2}\right) e^{-i(\omega_{\text{in}} + \omega_{\perp}) T} - \right. \\ &e^{-ik_{\text{in}} z''} e^{i(\omega_{\text{in}} - \omega_{\perp}) t'} e^{i(\arctan(z''/z_r^{\text{in}}) - \psi_{\perp})} \int_{|z' - z''|}^{\infty} dT J_0\left(m\sqrt{T^2 - |z' - z''|^2}\right) e^{-i(\omega_{\text{in}} - \omega_{\perp}) T} \\ &\left. + \text{c.c.} \right] . \end{aligned} \quad (5.12)$$

The two integrals over  $T$  which appear in the above equation evaluate [177] to

$$\begin{aligned} &\int_{|z' - z''|}^{\infty} dT J_0\left(m\sqrt{T^2 - |z' - z''|^2}\right) e^{-i(\omega_{\text{in}} \pm \omega_{\perp}) T} = \\ &-\frac{i\theta(|\omega_{\text{in}} \pm \omega_{\perp}| - m) \text{sgn}(\omega_{\text{in}} \pm \omega_{\perp})}{k_{\text{ax}}^{\pm}} e^{-i\text{sgn}(\omega_{\text{in}} \pm \omega_{\perp}) |z' - z''| k_{\text{ax}}^{\pm}} + \frac{\theta(m - |\omega_{\text{in}} \pm \omega_{\perp}|)}{k_{\text{os}}^{\pm}} e^{-|z' - z''| k_{\text{os}}^{\pm}} , \end{aligned} \quad (5.13)$$

where we have abbreviated  $k_{\text{ax}}^{\pm} = \sqrt{(\omega_{\text{in}} \pm \omega_{\perp})^2 - m^2}$  and  $k_{\text{os}}^{\pm} = \sqrt{m^2 - (\omega_{\text{in}} \pm \omega_{\perp})^2}$ .

Considering the combined  $t'$  and  $z'$  dependence of the axion field  $\phi$  in Eqs. (5.12) and (5.13), we can already interpret this intermediate result. The first contribution of the integral in Eq. (5.13) encodes the situation where the axion is on shell and the frequency of the outgoing axion is equal to the sum or the difference of the frequencies of the interacting



laser beams. The outgoing axion then propagates with  $\omega_{\text{ax}}^{\pm} \equiv \omega_{\text{in}} \pm \omega_{\perp}$  and wave vector  $k_{\text{ax}}^{\pm}$ . As already suggested by physical intuition, this can only happen if  $|\omega_{\text{in}} \pm \omega_{\perp}|$  is larger than the mass of the axion  $m$ , as encoded by the theta function in front. In addition, the axion wave carries transmitted and reflected parts, depending on the sign of  $(z' - z'')$ .

The second contribution of the integral in Eq. (5.13) corresponds to the situation where the mass of the axion is larger than the sum or the difference of  $\omega_{\text{in}}$  and  $\omega_{\perp}$ , respectively. In these situations, the axion production is off shell, and the axion wave decays exponentially fast with a decay constant of  $k_{\text{os}}^{\pm}$ . Here, this is not the physical situation in which we are interested.

Specializing to  $|\omega_{\text{in}} \pm \omega_{\perp}| > m$  in the following, we find with Eqs. (5.13) and (5.12):

$$\begin{aligned} \phi(z', t') = & \frac{1}{8} g E_{\text{in}} E_{\perp} \left[ \frac{i}{k_{\text{ax}}^{+}} e^{i(\omega_{\text{in}} + \omega_{\perp})t'} e^{-i \text{sgn}(z' - z'') k_{\text{ax}}^{+} z'} e^{i\psi_{\perp}} \right. \\ & \times \int_{-\infty}^{\infty} \frac{dz''}{\sqrt{1 + (z''/z_r^{\text{in}})^2}} e^{-(z''/w_0^{\perp})^2} e^{i(-k_{\text{in}} + \text{sgn}(z' - z'') k_{\text{ax}}^{+})z''} e^{i \arctan(z''/z_r^{\text{in}})} \\ & - \frac{i \text{sgn}(\omega_{\text{in}} - \omega_{\perp})}{k_{\text{ax}}^{-}} e^{i(\omega_{\text{in}} - \omega_{\perp})t'} e^{-i \text{sgn}(z' - z'') \text{sgn}(\omega_{\text{in}} - \omega_{\perp}) k_{\text{ax}}^{-} z'} e^{-i\psi_{\perp}} \\ & \left. \times \int_{-\infty}^{\infty} \frac{dz''}{\sqrt{1 + (z''/z_r^{\text{in}})^2}} e^{-(z''/w_0^{\perp})^2} e^{i(-k_{\text{in}} + \text{sgn}(z' - z'') \text{sgn}(\omega_{\text{in}} - \omega_{\perp}) k_{\text{ax}}^{-})z''} e^{i \arctan(z''/z_r^{\text{in}})} + \text{c.c.} \right]. \end{aligned} \quad (5.14)$$

In Eq. (5.14) we have introduced a  $\text{sgn}(z' - z'')$  factor in the exponent in the prefactor of the  $z''$ -integral in order to remind us of the transmitted and reflected components of the amplitude. This reminder is also used below, when appropriate.

In order to evaluate the remaining integrals over  $z''$ , it is useful to employ the identity

$$\frac{e^{i \arctan(z/z_r)}}{\sqrt{1 + (z/z_r)^2}} = \frac{1}{1 - i(z/z_r)} = \int_0^{\infty} dS e^{-(1 - i(z/z_r))S}. \quad (5.15)$$

In this way, the integration over  $z''$  in Eq. (5.14) is Gaussian and can easily be performed. The remaining integration over  $S$  is then most conveniently written in terms of the Error function  $\text{erf}(x) = (2/\sqrt{\pi}) \int_0^x dS \exp(-S^2)$ .

Equation (5.14) evaluates to

$$\begin{aligned}
 \phi(z', t') = & -\pi z_r^{\text{in}} \frac{1}{4} g E_{\text{in}} E_{\perp} \left[ \frac{1}{k_{\text{ax}}^+} \sin((\omega_{\text{in}} + \omega_{\perp}) t' - \text{sgn}(z' - z'') k_{\text{ax}}^+ z' + \psi_{\perp}) \right. \\
 & \times \left( 1 - \text{erf} \left( \frac{z_r^{\text{in}}}{w_0^{\perp}} + \frac{\Delta k_{\perp}^+ w_0^{\perp}}{2} \right) \right) \exp \left( \Delta k_{\perp}^+ z_r^{\text{in}} + \left( \frac{z_r^{\text{in}}}{w_0^{\perp}} \right)^2 \right) \\
 & - \frac{\text{sgn}(\omega_{\text{in}} - \omega_{\perp})}{k_{\text{ax}}^-} \sin((\omega_{\text{in}} - \omega_{\perp}) t' - \text{sgn}(z' - z'') \text{sgn}(\omega_{\text{in}} - \omega_{\perp}) k_{\text{ax}}^- z' - \psi_{\perp}) \\
 & \left. \times \left( 1 - \text{erf} \left( \frac{z_r^{\text{in}}}{w_0^{\perp}} + \frac{\Delta k_{\perp}^- w_0^{\perp}}{2} \right) \exp \left( \Delta k_{\perp}^- z_r^{\text{in}} + \left( \frac{z_r^{\text{in}}}{w_0^{\perp}} \right)^2 \right) \right) \right], \quad (5.16)
 \end{aligned}$$

where we have defined

$$\Delta k_{\perp}^+ = -k_{\text{in}} + \text{sgn}(z' - z'') k_{\text{ax}}^+, \quad (5.17)$$

$$\Delta k_{\perp}^- = -k_{\text{in}} + \text{sgn}(z' - z'') \text{sgn}(\omega_{\text{in}} - \omega_{\perp}) k_{\text{ax}}^-. \quad (5.18)$$

In summary, Eq. (5.16) tells us that the induced axion wave is composed of two partial waves with frequencies  $\omega_{\text{ax}}^{\pm} = (\omega_{\text{in}} \pm \omega_{\perp})$ , which both have transmitted and reflected parts corresponding to  $\text{sgn}(z' - z'') = \pm 1$ , respectively.

We find that each of these partial waves in the case of transmission and reflection is tied to a corresponding amplitude, which is a combination of an exponential and an error function. The basic effect of this factor is that for given beam parameters the partial waves have maximal amplitude for  $\Delta k_{\perp}^{\pm} \simeq 0$  if  $z_r^{\text{in}} \gtrsim w_0^{\perp}$  and for  $\Delta k_{\perp}^{\pm} \lesssim 0$  if  $z_r^{\text{in}} \lesssim w_0^{\perp}$  and decay quickly otherwise. The quantitative impact of this damping term, of course, depends on the absolute values of  $z_r^{\text{in}}$  and  $w_0^{\perp}$ . As we will see later on, for experimentally feasible  $z_r^{\text{in}}$  and  $w_0^{\perp}$ , it is reasonable to assert the condition  $\Delta k_{\perp}^{\pm} \simeq 0$ . In particular, we will also find an additional damping term for the back-conversion process below.

As one can conclude from Eqs. (5.17) and (5.18), the origin of this damping is conservation of three-momentum of the photon and the ALP: Only if the momentum in the conversion process is conserved to a good approximation, the amplitude of the partial wave will persist undamped. Let us emphasize that the momentum of the external beam does not enter  $\Delta k_{\perp}^{\pm}$  at this point, since the external beam propagates transversal to the  $z$ -axis and thus there is no net transfer of momentum in the  $z$ -direction. This will become important later on.

Note also that this damping factor in practice determines the sensitivity to the mass of the axion which is contained in  $k_{\text{ax}}^{\pm}$ . I.e., given two laser frequencies, efficient conversion into axions can only happen, if the mass of the axion is next to resonance, such that the

sum of momenta vanishes approximately<sup>4</sup>:  $\Delta k_{\perp}^{\pm} \simeq 0$ . It also follows that there is exactly one resonant ALP mass for given frequencies  $\omega_{\text{in}}$  and  $\omega_{\perp}$ .

Before we proceed with the calculation of the back-conversion of the ALPs into photons, let us determine the resonant ALP masses  $m$  in the conversion process. In vacuum ( $k = \omega$ ), we have the requirements

$$\Delta k_{\perp}^{+} = -\omega_{\text{in}} + \text{sgn}(z' - z'') \sqrt{(\omega_{\text{in}} + \omega_{\perp})^2 - m^2} \stackrel{!}{\simeq} 0, \quad (5.19)$$

$$\Delta k_{\perp}^{-} = -\omega_{\text{in}} + \text{sgn}(z' - z'') \text{sgn}(\omega_{\text{in}} - \omega_{\perp}) \sqrt{(\omega_{\text{in}} - \omega_{\perp})^2 - m^2} \stackrel{!}{\simeq} 0. \quad (5.20)$$

Eq. (5.19) is solved in the case of transmission, i.e.,  $\text{sgn}(z' - z'') = +1$ , by choosing  $m = \sqrt{\omega_{\perp}^2 + 2\omega_{\text{in}}\omega_{\perp}}$ . For Eq. (5.20), there is in principle the resonant solution  $m = \sqrt{\omega_{\perp}^2 - 2\omega_{\text{in}}\omega_{\perp}}$  which implies  $\omega_{\perp} > 2\omega_{\text{in}}$  for positive axion masses implying reflection, i.e.,  $\text{sgn}(z' - z'') = -1$ , but requiring also a negative value for  $\omega_{\text{ax}}^{-} = \omega_{\text{in}} - \omega_{\perp}$ . Thus, the latter is an unphysical solution.

Let us summarize our findings from Eq. (5.16): induced by the interaction of the probe field  $\omega_{\text{in}}$  with the external beam  $\omega_{\perp}$ , one obtains transmitted and reflected axion waves with frequencies  $\omega_{\text{ax}}^{\pm} = \omega_{\text{in}} \pm \omega_{\perp}$ . For our purposes, we focus on the transmitted partial wave with frequency  $\omega_{\text{ax}}^{+} = \omega_{\text{in}} + \omega_{\perp}$  since it acquires an undamped amplitude for ALP masses  $m$  which are close to a resonant mass<sup>5</sup>

$$m_{\perp} = \sqrt{\omega_{\perp}^2 + 2\omega_{\text{in}}\omega_{\perp}}. \quad (5.21)$$

Thus, for the following calculation of the reconversion process, we employ for clarity only the transmitted (T) axion wave with frequency  $\omega_{\text{ax}}^{+}$ :

$$\begin{aligned} \phi^{(\text{T})}(z', t') \approx & -\pi z_r^{\text{in}} \frac{1}{4} g E_{\text{in}} E_{\perp} \left[ \frac{1}{k_{\text{ax}}^{+}} \sin((\omega_{\text{in}} + \omega_{\perp})t' - k_{\text{ax}}^{+}z' + \psi_{\perp}) \right. \\ & \left. \times \left( 1 - \text{erf} \left( \frac{z_r^{\text{in}}}{w_0^{\perp}} + \frac{\Delta k_{\perp}^{+} w_0^{\perp}}{2} \right) \right) \exp \left( \Delta k_{\perp}^{+} z_r^{\text{in}} + \left( \frac{z_r^{\text{in}}}{w_0^{\perp}} \right)^2 \right) \right]. \quad (5.22) \end{aligned}$$

Let us finally remark that the damping factor of the amplitude encountered above is in fact *not* an artifact of the Gaussian beam form. This can easily be checked by omitting all factors containing  $w_0^{\perp}$  and  $z_r^{\text{in}}$  in Eq. (5.14), which amounts to calculating the interaction

<sup>4</sup>The above conversion properties are reminiscent of the processes of sum-frequency and difference-frequency generation, known from Nonlinear Optics, see, e.g., [178]. For these processes, a suitable medium with nonlinear dielectric permittivity is used to produce light beams whose frequency is equal to the sum or difference of the frequencies of the input beams. There, an efficient conversion can only happen, if so called phase-matching conditions are fulfilled. These phase-matching conditions are analogous to the above condition of three-momentum conservation.

<sup>5</sup>Here, we assign a label “ $\perp$ ” to the resonant mass in order to point out that it is the resonant mass which arises in the process with a primary interaction with the external *orthogonal* field. Details on the resonant mass belonging to the process at reversed interaction order  $\perp \leftrightarrow \parallel$  will be discussed below.

between two plain waves. Then, integrating over  $z''$  over a length  $L$  of the interaction region, one finds that the amplitudes of the axion partial waves are proportional to a factor of  $\sin(\Delta k_{\perp}^{\pm} L/2)/(\Delta k_{\perp}^{\pm})$ , respectively. Hence, also for a plain wave approximation, the amplitudes are peaked around  $\Delta k_{\perp}^{\pm} \simeq 0$ .

From this ansatz, the conversion amplitude for the ALP in a temporally and spatially constant external field follows for  $\omega_{\perp}, k_{\perp} \rightarrow 0$ . The square of this amplitude in the limit<sup>6</sup>  $m \ll \omega_{\text{in}}$  will be used later on for a qualitative comparison to dipole LSW experiments, cf. also Eq. (2.27).

### 5.1.4 Axion-photon conversion

We now turn to the back-conversion of the ALPs into photons, by virtue of Eq. (5.5). With the Green's function of Eq. (5.7) and using  $e_{\text{out}} = -\partial_t a_{\text{out}}$  (recall that we have employed Coulomb gauge), we have to evaluate

$$e_{\text{out}}(z, t) = \frac{1}{2} g \int_{-\infty}^{\infty} dz' \int_{-\infty}^{\infty} dt' \delta((t - t') - |z - z'|) \times \left[ [B_k^y(z', t') \partial_{t'} \phi(z', t')] + E_k^x(z', t') \partial_{z'} \phi(z', t') \right]. \quad (5.23)$$

As in the previous section we choose the external field for the back-conversion with hindsight: Assuming propagation of the electromagnetic wave along the negative  $z$ -axis, i.e. counter-propagating to the transmitted axion wave, we set

$$E_k^x(z, t) = \frac{E_{\parallel}}{\sqrt{1 + (z/z_r^{\parallel})^2}} \sin \left( \omega_{\parallel} t + k_{\parallel} z - \arctan \left( \frac{z}{z_r^{\parallel}} \right) + \psi_{\parallel} \right), \quad (5.24)$$

$$B_k^y(z, t) = -E_{\parallel}^x(z, t) = -\frac{E_{\parallel}}{\sqrt{1 + (z/z_r^{\parallel})^2}} \sin \left( \omega_{\parallel} t + k_{\parallel} z - \arctan \left( \frac{z}{z_r^{\parallel}} \right) + \psi_{\parallel} \right), \quad (5.25)$$

with beam parameter definitions as introduced previously, cf. Sect. 5.1.2.

In the following it is convenient to use the axion and photon wave again in complex notation. Plugging the approximate transmitted axion wave from Eq. (5.22) and the field

---

<sup>6</sup>Note that in this situation for large axion masses  $m \simeq \omega_{\text{in}}$ , the computation of the conversion probabilities requires great care, as discussed in detail in [94]. However, generically, the most stringent exclusion bounds on ALPs for constant external fields are obtained for masses  $m \ll \omega_{\text{in}}$ . In the end, we will compare the discovery potential for the purely-laser based setup to these bounds.

characteristics of the external beam (Eqs. (5.24) and (5.25)) into Eq. (5.23), evaluating the derivatives acting on  $\phi(z, t)$  and upon integration over  $t'$ , we find

$$\begin{aligned}
e_{\text{out}}(z, t) &= \frac{1}{32} g^2 \pi z_r^{\text{in}} E_{\text{in}} E_{\perp} E_{\parallel} \\
&\times \left( 1 - \text{erf} \left( \frac{z_r^{\text{in}}}{w_0^{\perp}} + \frac{\Delta k_{\perp}^+ w_0^{\perp}}{2} \right) \right) \exp \left( \Delta k_{\perp}^+ z_r^{\text{in}} + \left( \frac{z_r^{\text{in}}}{w_0^{\perp}} \right)^2 \right) \left( \frac{\omega_{\text{in}} + \omega_{\perp}}{k_{\text{ax}}^+} + 1 \right) \\
&\times \left[ \frac{1}{i} e^{i(\omega_{\text{in}} + \omega_{\perp} + \omega_{\parallel})(t - \text{sgn}(z - z')z)} e^{i(\psi_{\perp} + \psi_{\parallel})} \int_{-\infty}^{\infty} dz' \frac{1}{\sqrt{1 + (z'/z_r^{\parallel})^2}} e^{i\Delta k_{\parallel}^+ z'} e^{-i \arctan\left(\frac{z'}{z_r^{\parallel}}\right)} \right. \\
&\left. - \frac{1}{i} e^{i(\omega_{\text{in}} + \omega_{\perp} - \omega_{\parallel})(t - \text{sgn}(z - z')z)} e^{i(\psi_{\perp} - \psi_{\parallel})} \int_{-\infty}^{\infty} dz' \frac{1}{\sqrt{1 + (z'/z_r^{\parallel})^2}} e^{i\Delta k_{\parallel}^- z'} e^{i \arctan\left(\frac{z'}{z_r^{\parallel}}\right)} + \text{c.c.} \right].
\end{aligned} \tag{5.26}$$

Here we have defined

$$\Delta k_{\parallel}^+ = -k_{\text{ax}}^+ + k_{\parallel} + \text{sgn}(z - z')(\omega_{\text{in}} + \omega_{\perp} + \omega_{\parallel}), \tag{5.27}$$

$$\Delta k_{\parallel}^- = -k_{\text{ax}}^+ - k_{\parallel} + \text{sgn}(z - z')(\omega_{\text{in}} + \omega_{\perp} - \omega_{\parallel}). \tag{5.28}$$

Eq. (5.26) resembles the situation of the ALP production, as the outgoing electromagnetic wave  $e_{\text{out}}$  essentially consists of two partial waves with frequencies  $\omega_{\text{out}}^{\pm} = \omega_{\text{in}} + \omega_{\perp} \pm \omega_{\parallel}$ . Again, each partial wave has a transmitted, i.e.,  $\text{sgn}(z - z') = 1$ , and a reflected, i.e.,  $\text{sgn}(z - z') = -1$ , contribution. In order to determine the corresponding amplitudes of the partial waves, it is necessary to perform the remaining integration over  $z'$ . To this end, we make use of the first identity in Eq. (5.15) and perform the spatial integration over a closed contour in the complex  $z'$ -plane. In this manner, we find for the integrals in Eq. (5.26):

$$\int_{-\infty}^{\infty} dz' \frac{e^{i\Delta k_{\parallel}^{\pm} z' \mp i \arctan\left(\frac{z'}{z_r^{\parallel}}\right)}}{\sqrt{1 + \left(z'/z_r^{\parallel}\right)^2}} = \int_{-\infty}^{\infty} dz' \frac{e^{i\Delta k_{\parallel}^{\pm} z'}}{1 \pm i \left(z'/z_r^{\parallel}\right)} = \pi z_r^{\parallel} \left( 1 \pm \text{sgn}(\Delta k_{\parallel}^{\pm}) \right) e^{-z_r^{\parallel} |\Delta k_{\parallel}^{\pm}|}. \tag{5.29}$$

Analogous to the previous section, the partial wave amplitudes in Eq. (5.29) entering  $e_{\text{out}}$  are strongly peaked at vanishing  $\Delta k_{\parallel}^{\pm}$ . As in the photon-ALP conversion, this peak structure can be understood in terms of three-momentum conservation, cf. Eqs. (5.27) and (5.28), where the last term incorporates the momentum of the outgoing photon.

In addition, sharp cutoffs arise for  $\Delta k_{\parallel}^+ < 0$  and  $\Delta k_{\parallel}^- > 0$  in Eq. (5.29) through the signum function, respectively. Physically, this is due to the Gouy phase anomaly [175]; this behavior is also well known in the context of nonlinear interactions with focused Gaussian beams in media, see, e.g., [178]. However, one can check by numerical integration

that the sharp cutoff of the signum function is in fact washed out for integrations over finite interaction regions. Thus, for finite, physical interaction regions, the amplitudes are maximized for  $\Delta k_{\parallel}^{\pm} \simeq 0$ .

Before we continue with the evaluation of  $e_{\text{out}}$ , let us check the *compatibility* of the three-momentum conservations for the conversion and reconversion processes. Only if the conservation of three-momentum is obeyed in both conversions at the same time, the overall amplitude is undamped. Supplementary to conservation of three-momentum, we make the important additional requirement that  $\omega_{\text{out}} \neq \omega_{\text{in}}$ , as experimental signature for the conversion processes to have taken place at all.

To this end, we consider Eqs. (5.27) and (5.28) again in vacuum, i.e.,  $\omega = k$  in the one-dimensional setting with fixed propagation direction. In order to compare with the conservation of momentum in the photon-axion conversion process encoded in  $\Delta k_{\perp}^{\pm}$  (see Eq. (5.19)), we multiply  $\Delta k_{\parallel}^{\pm}$  by  $-1$ . This is justified, since the exponential damping depends only on the modulus of  $\Delta k_{\parallel}^{\pm}$ . Eqs. (5.27) and (5.28) then read:

$$-\Delta k_{\parallel}^{+} = \sqrt{(\omega_{\text{in}} + \omega_{\perp})^2 - m^2} - \text{sgn}(z - z')(\omega_{\text{in}} + \omega_{\perp} + \omega_{\parallel}) - \omega_{\parallel} \stackrel{!}{\simeq} 0, \quad (5.30)$$

$$-\Delta k_{\parallel}^{-} = \sqrt{(\omega_{\text{in}} + \omega_{\perp})^2 - m^2} - \text{sgn}(z - z')(\omega_{\text{in}} + \omega_{\perp} - \omega_{\parallel}) + \omega_{\parallel} \stackrel{!}{\simeq} 0. \quad (5.31)$$

By comparing the above conditions for  $\Delta k_{\parallel}^{\pm}$  with that for  $\Delta k_{\perp}^{\pm}$  in Eq. (5.19), we notice that we need the transmitted part of the outgoing wave, corresponding to  $\text{sgn}(z - z') = +1$  also for the back-conversion process. Otherwise the required relative sign between  $\omega_{\text{in}}$  and the axion wave vector in order to satisfy Eq. (5.19) cannot be reproduced. In order to fulfill the condition for  $\Delta k_{\parallel}^{+}$  in Eq. (5.30) and the condition for  $\Delta k_{\perp}^{+}$  at the same time, a negative frequency contribution of either  $\omega_{\perp}$  or  $\omega_{\parallel}$  would then be needed which is clearly unphysical. For this reason we drop this option in the following.

By contrast, it can be seen that it is possible to obey momentum conservation for the conversion and back-conversion processes simultaneously via Eq. (5.31): By setting  $\omega_{\perp} = 2\omega_{\parallel}$ , we see that  $\Delta k_{\parallel}^{-} = \Delta k_{\perp}^{+} = 0$  if the axion mass satisfies Eq. (5.21). In addition, the outgoing electromagnetic wave in this situation has a frequency  $\omega_{\text{out}} = \omega_{\text{in}} + \frac{1}{2}\omega_{\perp} = \omega_{\text{in}} + \omega_{\parallel}$  which is different from the frequency of the incoming wave. We conclude that also our second requirement for  $e_{\text{out}}$  is met.

At this point, it also becomes clear why it is crucial for the frequency shift of the outgoing wave to arise that the momentum of the first external laser beam does not enter the requirement for  $\Delta k_{\perp}^{+}$  in Eq. (5.17): Depending on the relative signs of the momenta in the two conversion processes, conservation of momentum could only be simultaneously achieved in both processes for  $\omega_{\perp} = \omega_{\parallel}$ . However, this would immediately imply  $\omega_{\text{in}} = \omega_{\text{out}}$  being problematic for experimental observation and require again an LSW setup which is difficult to conceive for high-intensity fields.

In total, it is the above “mismatch” of momentum conservation (as encoded in  $\Delta k_{\perp/\parallel}$ ) and energy conservation (as encoded in the difference  $\omega_{\text{out}} - \omega_{\text{in}}$ ), which is essential for a net transfer of energy to the outgoing photon, favoring experimental detectability.

To summarize, it is the transmitted contribution of the second partial wave in Eq. (5.26) for which both respective momentum conservation conditions can be fulfilled simultaneously and a frequency shift with respect to the incoming wave arises. Combining Eq. (5.26) and Eq. (5.29) and substituting  $\omega_{\perp} = 2\omega_{\parallel}$ , we focus for the remainder on

$$e_{\text{out}}^{(\text{T})}(z, t) \approx -\frac{1}{16} g^2 \pi^2 z_r^{\text{in}} z_r^{\parallel} E_{\text{in}} E_{\perp} E_{\parallel} \left( 1 - \text{erf} \left( \frac{z_r^{\text{in}}}{w_0^{\perp}} + \frac{\Delta k w_0^{\perp}}{2} \right) \right) \exp \left( \Delta k z_r^{\text{in}} + \left( \frac{z_r^{\text{in}}}{w_0^{\perp}} \right)^2 \right) \\ \times (1 - \text{sgn}(\Delta k)) e^{-z_r^{\parallel} |\Delta k|} \left( \frac{\omega_{\text{in}} + 2\omega_{\parallel}}{k_{\text{ax}}^+} + 1 \right) \sin \left( (\omega_{\text{in}} + \omega_{\parallel})(t - z) + \psi_{\perp} - \psi_{\parallel} \right), \quad (5.32)$$

where we have set  $\Delta k_{\perp}^+ = \Delta k_{\parallel}^- \equiv \Delta k$ .

In practice it is of course not directly experimentally assessable which of the two external beams mediates conversion and which one back-conversion. So far, we have assumed conversion to be induced by the field with  $\perp$  orientation, and back-conversion due to the counter-propagating  $\parallel$  field. The result for the outgoing wave, however, will depend on the order of interaction.

As demonstrated in App. E for reasons of clarity (the calculational steps can be performed in complete analogy to the discussion above), the conversion process with the opposite interaction order  $\perp \leftrightarrow \parallel$  results in an outgoing wave with frequency  $\omega_{\text{out}} = \omega_{\text{in}} - \omega_{\parallel}$ , if one chooses  $\omega_{\perp} = 2\omega_{\parallel}$ . The resonant mass satisfying momentum conservation in both conversion processes is then given by<sup>7</sup>  $m_{\parallel} = 2\sqrt{\omega_{\text{in}}\omega_{\parallel}}$ , being different from the resonant mass at interchanged interaction order. In consequence, it is possible to probe the axion coupling space around two resonant masses within one setup.

### Implications for a high-intensity laser-based axion search

Our calculations suggest the following experimental setup: Probe photons, which traverse one counter-propagating and one perpendicularly propagating laser field with frequencies  $\omega_{\parallel}$  and  $\omega_{\perp}$ , respectively, can experience a frequency shift due to ALP-photon mixing. This happens if the frequency of the external perpendicular laser has twice the frequency of the external counter-propagating laser:  $2\omega_{\parallel} = \omega_{\perp}$ . The requirement for this process is the existence of ALPs with masses close to one of the two resonant masses, which are a function of the involved laser frequencies.

These resonant masses are of the same order of magnitude as the involved frequency scales of the lasers, which in optical setups corresponds to  $\sim \mathcal{O}(\text{eV})$ . As this mass regime

<sup>7</sup>The label “ $\parallel$ ” at the resonant mass denotes that primary interaction of the probe beam is due to the  $\parallel$  external field, in contrast to Eq. (5.21), where the primary interaction is due to the  $\perp$  external field.

is so far largely unexplored in laboratory ALP-searches, the proposed experimental setup can be *complementary* to the search involving dipole magnets, see below.

It is worth emphasizing that the required frequency ratio for the two external lasers in fact constitutes an enormous experimental advantage, since it implies that indeed only *one* high-intensity laser is needed as external field source, since frequency doubling or “second harmonic generation” [179] is a standard technique even for high-intensity lasers. In addition, the corresponding beam parameters of the frequency doubled beam, such as the focal area can in principle be tuned independently by the use of appropriate lens systems.

## 5.2 The setup’s capabilities and perspectives

### 5.2.1 Prospective exclusion limits on axions and ALPs

Let us first explore the parameter range in the ALP mass and coupling plane which can be probed within the presented setup. The number of photons in the beams is proportional to the square of the field amplitudes, being a function of time. However, as the pulse lengths in consideration imply a large number of wave trains, a good approximation of the number of frequency shifted outgoing photons  $N_{\text{out}}$  as a function of the number of incoming photons  $N_{\text{in}}$  can be read off from a comparison of Eq. (5.32) (or (E.16)) with the incoming field  $e_{\text{in}}$  in Eq. (5.8).

$$N_{\text{out}}(\omega_{\text{in}} \pm \omega_{\parallel}) \simeq N_{\text{in}}(\omega_{\text{in}}) N_{\text{shot}} \alpha_{\pm}^2. \quad (5.33)$$

The parameter  $N_{\text{shot}}$  counts the number of laser shots used for a measurement. It is determined by the total measurement time of data accumulation times the repetition rate of the lasers. The quantity  $\alpha_{\pm}^2$  is a measure for the probability of the photon-axion-photon conversion. Here,  $\alpha_{+}$  denotes the conversion amplitude for outgoing photons of frequency  $\omega_{\text{out}} = \omega_{\text{in}} + \omega_{\parallel}$  whereas  $\alpha_{-}$  is the conversion amplitude for photons with frequency  $\omega_{\text{out}} = \omega_{\text{in}} - \omega_{\parallel}$ . They read:

$$\begin{aligned} \alpha_{+} &= -\frac{1}{16} g^2 \pi^2 z_r^{\text{in}} z_r^{\parallel} E_{\perp} E_{\parallel} \left( 1 - \operatorname{erf} \left( \frac{z_r^{\text{in}}}{w_0^{\perp}} + \frac{\Delta k w_0^{\perp}}{2} \right) \right) \left( \frac{\omega_{\text{in}} + 2\omega_{\parallel}}{\sqrt{(\omega_{\text{in}} + 2\omega_{\parallel})^2 - m^2}} + 1 \right) \\ &\quad \times \exp \left( \Delta k z_r^{\text{in}} + \left( \frac{z_r^{\text{in}}}{w_0^{\perp}} \right)^2 \right) (1 - \operatorname{sgn}(\Delta k)) e^{-z_r^{\parallel} |\Delta k|}, \end{aligned} \quad (5.34)$$

$$\begin{aligned} \alpha_{-} &= \frac{1}{8} g^2 \pi^{3/2} \frac{z_r^{\text{in}} z_r^{\parallel}}{z_r^{\text{in}} + z_r^{\parallel}} w_0^{\perp} E_{\parallel} E_{\perp} \frac{\omega_{\text{in}} + \omega_{\parallel}}{\sqrt{(\omega_{\text{in}} + \omega_{\parallel})^2 - m^2}} \\ &\quad \times \left[ (1 - \operatorname{sgn}(\delta k)) e^{\delta k z_r^{\text{in}}} + (1 + \operatorname{sgn}(\delta k)) e^{-\delta k z_r^{\parallel}} \right] e^{-\frac{1}{4} (w_0^{\perp} \delta k)^2}, \end{aligned} \quad (5.35)$$



where we have inserted the respective axion wave vectors  $k_{\text{ax}}$  for clarity. The parameters  $\Delta k$  and  $\delta k$  reduce to

$$\Delta k = -\omega_{\text{in}} + \sqrt{(\omega_{\text{in}} + 2\omega_{\parallel})^2 - m^2}, \quad (5.36)$$

$$\delta k = -\omega_{\text{in}} + \omega_{\parallel} + \sqrt{(\omega_{\text{in}} + \omega_{\parallel})^2 - m^2}. \quad (5.37)$$

As already discussed above, in order to experimentally assess the induced frequency shift, it is sufficient to have just one high-intensity laser as external field source in this configuration. One part of the external beam has to be frequency doubled, such that  $\omega_{\perp} = 2\omega_{\parallel}$ , while a delay line must ensure the simultaneous overlap of the focal spots of the fundamental and the frequency doubled beam mode as well as the focal spot of the probe beam.

In addition, we demand that the three frequency modes satisfy  $\omega_{\text{in}} + \omega_{\parallel} \approx \omega_{\perp}$ , in order to make the frequency shifted photons at  $\omega_{\text{out}}$  distinguishable from the frequency components already used in the process. We will detail on this requirement below.

Further, it appears advisable in practice to realize the setup with a slight deviation from the exact orthogonal geometry in order to facilitate the detection of the frequency shifted photons off the main optical axis in order to reduce the noise amplitude. For a quantitative discussion of a non-orthogonal setup, the above calculation has to be extended to three spatial dimensions, as further commented in Sect. 5.2.2. Qualitatively, we expect that, for deviations from the orthogonal geometry, the resonance conditions  $\Delta k \simeq 0$  and  $\delta k \simeq 0$  receive an angular dependence based on the three-momentum transfer in all spatial directions. In consequence, the necessary condition  $\omega_{\perp} = 2\omega_{\parallel}$  is expected to be modified as well. However, as this relation is experimentally easily accessible by frequency doubling, a beam geometry close to the orthogonal setup appears to remain viable.

### A case study: axion-like particle search with JETI and POLARIS

Let us now determine the discovery potential in the ALP mass-coupling plane for an operational high-intensity facility. First, we discuss a possible setup at Jena. In the near future, the Multi-Terawatt class laser JETI and the Petawatt class laser POLARIS [180] can be focused simultaneously and synchronized into a single target chamber. Thus we can employ the lower-intensity laser JETI for providing the probe photons, while POLARIS is used to create the two external fields for the conversion processes.

Let us first consider the focal parameters of the two lasers. To achieve maximum field strengths for POLARIS and a good bunching of the probe photons of JETI, we need very small focal spots on the order of the diffraction limit. To be more precise, if we define the effective diameter of the focal spot to contain 86% (which is denoted as  $1/e^2$ -criterion, since  $1/e^2 \approx 0.14$ ) of the focused beam energy, see below, one has the estimate [181]

$w_0 \simeq f^\# \lambda$ , with the so-called  $f$ -number  $f^\#$  of the focusing lens, which characterizes the ratio of the focal length and the focusing aperture diameter. Ambitious, but feasible values for the  $f$ -number can be as low as  $f^\# = 1$ . Recall that the corresponding Rayleigh length is obtained from the waist size through  $z_r = \frac{\pi w_0^2}{\lambda}$ .

The laser system POLARIS is designed to provide a peak power of around  $P = 1\text{PW}$  (attained through 150J at pulse lengths  $\tau_{\text{ext}} \simeq 150\text{fs}$ ), optimized for a central wavelength of  $\lambda_{\text{ext}} = 1035\text{nm}$ , corresponding to  $\omega_{\parallel} = 1.20\text{eV}$  and thus  $\omega_{\perp} = 2.40\text{eV}$ . In consequence, we find  $w_0^{\perp} \simeq 5 \frac{\lambda_{\text{ext}}}{2} \approx 13.1\text{eV}^{-1}$ , for the frequency doubled beam where we have chosen an  $f$ -number  $f^\# = 5$  in order to fit the probe photons into the external field, see below.

Further, we estimate the Rayleigh length for the counter-propagating fundamental beam as  $z_r^{\parallel} \simeq \pi (f^\#)^2 \lambda_{\text{ext}} \simeq 16.4\text{eV}^{-1}$  for an  $f$ -number of  $f^\# = 1$ .

The obtained intensities within the focal spot yield  $I_{\parallel} = 0.86 \frac{1}{2} \frac{P}{A_{\parallel}} = 2.05 \times 10^{16}\text{eV}^4$  and  $I_{\perp} = 0.86 \frac{1}{2} \frac{P}{A_{\perp}} = 3.28 \times 10^{15}\text{eV}^4$ , where the reduction of intensity for the  $\perp$  beam through losses in the frequency doubling process will be accounted for below. Here,  $A_{(\perp/\parallel)} = \left(w_0^{(\perp/\parallel)}\right)^2 \pi$  is the area of the focal spot and the factor of 1/2 enters due to the splitting of POLARIS into two separate beams  $\omega_{\parallel}$  and  $\omega_{\perp}$ . It is clear, however, that these are upper theoretical estimates for the achievable intensities which will be certainly modified by the circumstances of the experimental setup.

From these intensities, the peak electric field strength for the fundamental mode is  $E_{\parallel} = \sqrt{I_{\parallel}} \simeq 1.43 \times 10^8\text{eV}^2$ . Further, it is appropriate to assume a relatively moderate conversion efficiency of 40% for the frequency doubled beam at these field strengths, yielding  $E_{\perp} = \sqrt{0.4I_{\perp}} \approx 3.62 \times 10^7\text{eV}^2$ .

For high intensities, the external pulses as well as the probe beam must not only be spatially but also temporally well focused. Naturally, the pulses then have a spectral width  $\Delta\omega$ , which, for Gaussian pulses is related to the pulse length as  $\Delta\omega \simeq 0.44 \frac{2\pi}{\tau}$ .

In order to detect the frequency shifted photons at  $\omega_{\text{out}} = \omega_{\text{in}} \pm \omega_{\parallel}$  with low noise, these photons should lie well outside the spectral widths  $\Delta\omega_{\text{in}}$ ,  $\Delta\omega_{\parallel}$  and  $\Delta\omega_{\perp}$ , centered around  $\omega_{\text{in}}$  and  $\omega_{\parallel}$  and  $\omega_{\perp}$ , respectively.

As the external pulses are comparatively long, we obtain a small spectral width of  $\Delta\omega_{\text{ext}} \simeq 0.01\text{eV}$ . With the above pulse length, we see that  $\tau_{\text{ext}} \gtrsim z_r^{\text{ext}}$  as well as  $\tau_{\text{ext}} \gtrsim w_0^{\text{ext}}$  are well obeyed if we assume similar focal properties for the fundamental beam mode and the frequency doubled beam.

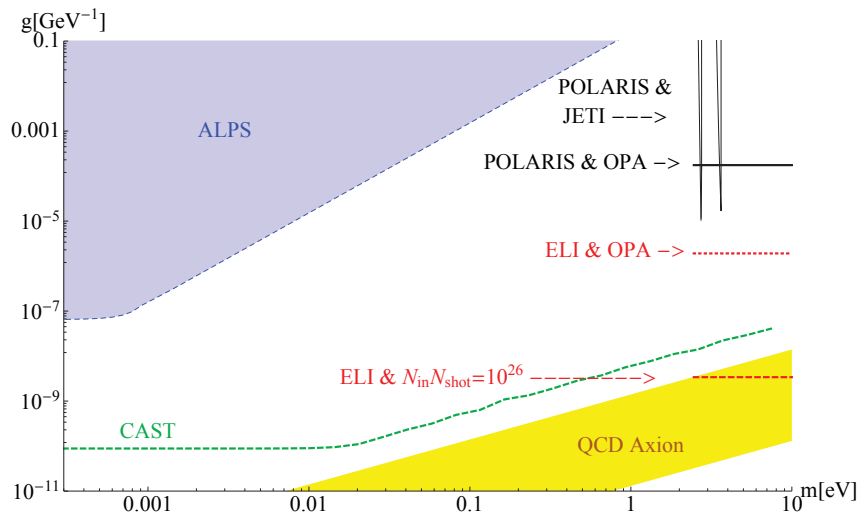
JETI provides an energy of around  $\mathcal{E} = 3\text{J}$  per shot at a central wavelength of around  $\lambda_{\text{in}} = 800\text{nm}$  ( $\omega_{\text{in}} = 1.55\text{eV}$ ) with pulse lengths as small as  $\tau_{\text{in}} \simeq 30\text{fs}$ . Assuming  $f^\# = 1$ , the smallest Rayleigh length for the probe beam is therefore  $z_r^{\text{in}} \approx 12.7\text{eV}^{-1}$ . From the pulse energy, the number of incoming photons per shot is given by  $N_{\text{in}} = \mathcal{E}/\omega_{\text{in}} \approx 1.21 \times 10^{19}$ . In addition, the requirements  $\omega_{\text{out}} \notin \Delta\omega_{\text{in}}, \Delta\omega_{\perp}, \Delta\omega_{\parallel}$  are well obeyed, since the spectral width is only  $\Delta\omega_{\text{in}} \simeq 0.06\text{eV}$ . As  $\tau_{\text{in}} \ll \tau_{\text{ext}}$ , all  $N_{\text{in}}$  JETI photons are

available for the conversion process as long as  $z_r^{\text{in}} \lesssim z_r^{\parallel}, w_0^{\perp}$ , which is implemented above by the choice of the focusing geometry, see also Fig. 5.1.

A decisive experimental parameter is the pulse repetition rate which determines the number of laser shots  $N_{\text{shot}}$  for a given measurement time. As the computation of the necessary statistics for the photon detection requires detailed knowledge of the laser specifications and the setup, we perform our estimates for  $N_{\text{shot}} = N_{\text{out}} = 1$ . In particular, nonlinear processes within the experimental setup tend to modify the idealized Gaussian frequency spectra of the laser beams. If larger statistics for the outgoing photons are required, this can always be accommodated by a larger number of shots. In the present example, POLARIS, due to its higher energy, has the smaller repetition rate of both lasers, which is expected to approach  $f_{\text{rep}} \simeq 0.1\text{Hz}$ . In practice,  $\mathcal{O}(100)$  shots per day can be achieved, being a huge accomplishment for a Petawatt-class laser. In the future, improved cooling schemes for the amplifying medium may even lead to a further enhancement of the repetition rate.

For these parameters, the discovery potential follows from Eqs. (5.33-5.35). In Fig. 5.2, we obtain two black wedge-like curves around the resonant masses  $m_{\parallel} = 2.73\text{eV}$  and  $m_{\perp} = 3.63\text{eV}$ , which are determined by the photon energies of POLARIS and JETI. The peaks of the wedges and thus the minimal accessible coupling strength lie at  $g \approx 7.7 \times 10^{-6}\text{GeV}^{-1}$  and  $g \approx 1.7 \times 10^{-5}\text{GeV}^{-1}$ , respectively.

Figure 5.2: Axion-like-particle exclusion bounds for purely laser-based setups in comparison to searches with dipole magnets, see main text for parameters and attainable coupling values. The blue-shaded area in the upper left corner gives the currently best laboratory bounds on axion-like-particles from the ALPS collaboration [77], while the best limits on solar axions are provided by the CAST experiment [102], denoted by a green-dashed line.



The black wedges denote the exclusion limits for a setup involving the JETI and POLARIS laser systems at Jena for one shot at single photon detection. The black line indicates the obtainable exclusion bounds at this setup by frequency-tuning through optical parametric amplification. The red dotted line corresponds to an estimate for the best obtainable bounds with ELI with a present-day OPA system. The red dot-dashed line suggests the necessary requirements at ELI for testing the parameter regime of typical QCD axion models, which are plotted as a yellow band.

### Complementing dipole searches through optical parametric amplification

As outlined in Sect. 2.2.2, the currently best laboratory limits on ALPs are derived from the LSW setup of the ALPS collaboration, as indicated as blue-shaded area in Fig. 5.2, while the best limits on solar axions are provided by the CAST experiment, denoted by a green-dashed line. However, as discussed in Sect. 2.2.3, the latter cannot be directly compared with constraints derived from low-energy experiments.

In dipole experiments, the external magnetic field  $B$  is essentially constant, and the photon-ALP conversion and reconversion probability are well approximated by

$$P_{\gamma \rightarrow \phi, \phi \rightarrow \gamma} = \left( \frac{gBL}{2} \right)^2 \frac{\sin^2(y)}{y^2}, \quad (5.38)$$

cf. Eq. (2.27). Above,  $y = m^2 L / (4\omega_{\phi/\gamma})$ , where  $L$  denotes the length of the dipole magnet and  $\omega_{\phi/\gamma}$  is the axion and photon energy, respectively. From Eq. (5.38) it is obvious that the best exclusion bounds are obtained for small arguments  $y \ll 1$ , i.e. for small axion masses at fixed energies  $\omega_{\phi/\gamma}$  and dipole length  $L$ , cf. Fig. 5.2. If the axion masses become too large, the conversion probability suffers from a  $y^{-2}$  suppression.

As the CAST-experiment utilizes  $\omega_{\phi} \sim \text{keV}$  solar axions, the best bounds are obtained for masses below  $m \lesssim 1\text{eV}$ . By contrast, in laboratory experiments generically  $\omega_{\gamma} \sim \text{eV}$ , and thus the drop-off sets in at even lower masses  $m \sim 10^{-3}\text{eV}$ . In both situations, the accessible mass regions can be slightly extended to higher masses by the use of buffer gas. However, the generic form of the conversion probability for constant external fields, see Eq. (5.38), disfavors dipole searches for the exploration of higher ALP mass ranges.

For both ALPS and CAST, the exploration of the  $m \simeq 1\text{eV}$  region is difficult and thus the purely laser-based search can complement the existing ALP searches in the large mass region as detailed above. An additional feature of the purely laser-based search is the strong sensitivity to the axion mass which originates from the requirement of momentum conservation. On the one hand this can be advantageous, since it allows for a direct estimate of the axion mass if a signal is detected. On the other hand, it would of course be desirable to explore a larger range of the axion-mass-coupling plane within a single setup.

For this purpose, it would be favorable if the involved laser frequencies were tunable within a certain frequency range. In fact this can be realized by the use of optical parametric amplifiers (OPAs), which are employed to tune the frequency of an optical pump laser over a wide frequency range while retaining the temporal structure of the pulse to a good approximation. However, for today's OPAs, the pump energy is limited to approximately 1mJ. Since this requirement strongly limits the available intensity, we choose to tune the frequency of the probe beam rather than the external beam which enters twice in the setup in its fundamental and frequency doubled mode. For optical probe lasers,

we have thus a limitation of the number of incoming photons to around  $N_{\text{in}} \simeq 10^{15}$ . Yet, as  $N_{\text{out}} \sim g^4$ , cf. Eqs. (5.33-5.35), for the above considered setup the sensitivity to the coupling is reduced by just around one order of magnitude.

A feasible tuning range for today's OPAs covers a large spectrum from the infrared to the ultraviolet, see, e.g., [182], which can in principle be even further extended to larger frequencies by higher harmonic generation. Thus, asserting a conservative tuning range of  $\lambda \lesssim 2 \times 10^{-5}\text{m}$  ( $\omega \gtrsim 0.06\text{eV}$ ), one could in principle explore axion mass ranges above  $m_{\perp} \gtrsim 2.46\text{eV}$  for  $\omega_{\text{out}} = \omega_{\text{in}} + \omega_{\parallel}$  as indicated by the black solid vertical line in Fig. 5.2 for POLARIS intensities and frequency<sup>8</sup>. We find that, employing OPAs, the exclusion bounds on ALPs could be extended to  $g \gtrsim 1.8 \times 10^{-4}\text{GeV}^{-1}$ .

However, it is important that the outgoing probe photons are shifted to frequencies outside the spectral widths of the employed lasers as discussed above. Therefore, the efficiency of the OPAs and the higher harmonic generation processes have to be taken into account in detail. Here, we give only an order of magnitude estimate of these effects.

### Forthcoming perspectives of axion search: Employing 'extreme light'

In order to estimate the discovery potential at future facilities, let us extend our considerations to the planned Exawatt facility ELI [166]. At this facility, a potentially feasible intensity aim is  $I = 10^{26} \frac{\text{W}}{\text{cm}^2}$ . According to the previous estimates for the available intensity, we thus obtain the ELI field strengths  $E_{\parallel} \simeq 8.29 \times 10^9 \text{eV}^2$  and  $E_{\perp} \simeq 5.25 \times 10^9 \text{eV}^2$ . These field strengths exceed those of the POLARIS/JETI setup by roughly two orders of magnitude. The achievable focal parameters can be expected to be of the same order of magnitude as in our previous estimate.

In Fig. 5.2, the red dotted vertical line indicates the region which could be probed at ELI with an additional OPA with tuning range and  $N_{\text{in}}N_{\text{shot}} \simeq 10^{15}$  as above. Here we find that the coupling region above  $g \gtrsim 1.9 \times 10^{-6}\text{GeV}^{-1}$  could be explored. Intriguingly, already a moderate demand on the number of interacting laser photons can almost complement the bounds of ALPS in the higher ALP mass region.

Ultimately, the red dot-dashed vertical line suggests the necessary requirements at ELI for tests of typical QCD axion models, which are plotted as a yellow band, see [102] and references therein. In order to make contact with the range of QCD axion models, in the attainable mass region,  $N_{\text{in}}N_{\text{shot}} \approx 10^{26}$  is needed at ELI to explore an ALP mass range up to  $g \gtrsim 3.4 \times 10^{-9}\text{GeV}^{-1}$ . This is a rather strong requirement for current technology, but with the advance of OPA technology and in high-intensity laser technology this could be a worthwhile long-term aim for the future.

---

<sup>8</sup>Here, we neglect the  $m_{\parallel}$  solution, since for this mass the outgoing frequency is  $\omega_{\text{out}} = \omega_{\text{in}} - \omega_{\parallel}$  and thus the frequency of the incoming probe photon cannot be reduced below  $\omega_{\parallel}$ .

## 5.2.2 Summary and outlook of the purely laser-based ALP search

### The employment of high-intensity lasers as a next stage of axion searches

In this chapter, we have investigated the feasibility of a search for axion-like-particles in a purely laser-based setup. In particular, we have concentrated on modern high-intensity laser systems, since the available field strengths in these lasers can serve as a lever arm for probing the weak coupling  $g$  of axions and axion-like-particles (ALPs) to electromagnetism.

In a first case study, we investigated in a one-dimensional setting the conversion of a probe beam with frequency  $\omega_{\text{in}}$  into an ALP beam in an external laser and its reconversion into a photon beam by a second external laser for Gaussian beam profiles in the formal limit of infinite pulse lengths. The important difference to conventional photon-axion mixing in homogeneous fields such as provided, e.g., by dipole magnets, arises from a split of the incoming probe-beam into several partial waves whose frequencies are given by all non-negative sums and differences of the three laser frequency scales. The amplitude of these partial waves is proportional to two damping terms induced by the conservation of three-momentum at the conversion points.

The constraints imposed by momentum conservation, together with the practical requirement that the outgoing photon should be frequency shifted with respect to  $\omega_{\text{in}}$  for reasons of detectability, constitute the basic experimental prerequisites. We have argued that these prerequisites can be satisfied in a specific setup involving one external beam of frequency  $\omega_{\parallel}$  to counter-propagate with respect to the probe beam and another external beam of frequency  $\omega_{\perp}$  to propagate orthogonally to the probe beam. For the situation where  $\omega_{\perp} = 2\omega_{\parallel}$ , momentum is conserved at both conversion points at the same time while the frequency of the outgoing beam is different from the frequency of the incoming beam:  $\omega_{\text{out}} = \omega_{\text{in}} + \omega_{\parallel}$  or  $\omega_{\text{out}} = \omega_{\text{in}} - \omega_{\parallel}$  depending on the order of the interaction of the beams. As emphasized [183, 184], this mechanism exhibits a close resemblance to sum-frequency generation and difference-frequency generation known from Nonlinear optics, as also pointed out in a different study, cf. [185].

The amplitudes of these frequency-mixing processes are peaked around certain resonant masses which are determined by momentum conservation: For the frequency up-converted probe photons with  $\omega_{\text{out}} = \omega_{\text{in}} + \omega_{\parallel}$ , the resonant mass is  $m_{\perp} = 2\sqrt{\omega_{\parallel}^2 + \omega_{\text{in}}\omega_{\parallel}}$ , whereas  $m_{\parallel} = 2\sqrt{\omega_{\text{in}}\omega_{\parallel}}$  for the down-conversion process with  $\omega_{\text{out}} = \omega_{\text{in}} - \omega_{\parallel}$ , cf. Eq. (5.21) and Eq. (E.9) with  $\omega_{\perp} = 2\omega_{\parallel}$ , respectively.

To overcome the restriction to two single resonant masses, frequency tuning by means of optical parametric amplification could be employed and extend the region of accessible ALP masses to a large part of the  $\mathcal{O}(\text{eV})$  mass range.

### Remaining limitations and essential further steps

Before an actual experimental realization of the axion search with high-intensity lasers can be envisaged, several continuative studies are in order (cf. also similar suggestions in [186, 187]). Firstly, the background of frequency-shifted photons not caused by ALP intermediate-states needs to be carefully taken into account. As already discussed in previous sections, nonlinear QED processes can in theory provide a standard model background for frequency shifted photons via photon-photon interactions in vacuum, cf. also App. B.

On the other hand, far before these processes could play a role, frequency variations in successive pulses due to frequency-dependent amplification properties of the lasing medium will most likely pose the greatest experimental challenge. For the POLARIS/JETI setup, these frequency variations are on the order of 1-2% [188]. In this case, the requirement on the number of frequency shifted outgoing photons must be chosen such that parasitic frequency shifts become subordinate. Also, the decoupling of a reference beam from the main pulse facilitates the exclusion of measurement artifacts.

Of course, our setup demands also for a sophisticated laser alignment resembling a pump-probe-type experiment. However, this is a lesser experimental challenge, in particular, if the probe laser and the external laser are synchronized by the employment of a single seed laser as could be realized for the combined POLARIS/JETI setup. Let us also briefly mention that the warranty of an adequately low vacuum pressure in the interaction region is simplified in the high-intensity laser setup: A prepulse with adjusted temporal delay can be eventually used to ionize the remaining gas in the target chamber. The ions could then be removed prior to the arrival of the main pulse by applying a small electric field.

On the theoretical side, the limitation of our calculation to the one-dimensional situation is likely an issue for experimental setups in which the waist size of the probe beam is of a similar order of magnitude as the orthogonal variation of the high-intensity pulse. In addition to our main observable, the frequency shift, the deviation from the ideal one-dimensional case will then lead to diffractive effects, as have been discussed, e.g., in [38, 189, 190]. The leading-order sensitivity estimates discussed in this chapter still hold in this case if the on-axis photodetector is, e.g., replaced by an ensemble of detectors suitably positioned in the diffraction zone. Also, in the suggested setup precise information about diffraction is not required as long as a signal in the form of a frequency shift is detected.

Possibly, diffraction and frequency shift information may be combined to reach even higher sensitivity. In particular, if the frequency-shifted photons are scattered off the axis of the main pulse, their detection is considerably simplified: To measure the frequency spectrum of the high-energy pulse, the pulse has likely to be attenuated first by a di-

electric mirror and can then be spectrally decomposed, e.g., by a grating. However, the need for attenuation is of course unfavorable as too many frequency-shifted photons are potentially lost. Yet, attenuation might be necessary as for too large photon numbers the photodetectors are possibly damaged. Therefore, as diffractive effects could be predicted in a higher-dimensional calculation, such investigations remain a worthwhile challenge as the frequency-shifted photons might in fact be distinctively separated from the main pulse.

Let us summarize that, if further studies in this direction underline the practicability of the suggested setup, purely laser-based experiments hold the prospect of providing the strongest laboratory bounds on axion-like particles in the  $\mathcal{O}(\text{eV})$  mass range. As laboratory searches with dipole magnets generically probe only lower mass ranges, purely laser-based experiments could complement them in an essential manner.

### **Towards an appropriate scenario for the study of minicharged particles**

To close our studies of the purely laser-based search for distinct “new physics” at the  $\mathcal{O}(\text{eV})$  scale, it is notable that this chapter focused on the study of axion-like particles alone. Presumably, a search for minicharged particles as introduced as a second generic WISP in Sect. 2.2 would not be feasible within the scenario discussed in this chapter: In contrast to a production of real ALPs in the focus of high-intensity lasers, it seems likely that real minicharge particle-antiparticle pairs become separated quickly in the overlapping laser foci, depending, of course, highly on the magnitude of their mass and fractional charge. By virtue of the separating forces due the oscillating electromagnetic field on the oppositely charged particle-antiparticle-pairs, a recombination of these particles would seem to be obstructed. Thus again, only a vacuum dichroism (as well as ellipticity) would supposedly constitute a practical observable indicating the presence of minicharges for high-intensity lasers with definite polarization, cf. Sect. 2.2.

The next chapter will thus be dedicated to the study of a suitable scenario aimed in particular at the search for minicharged particles. As will be outlined, an LSW scenario with *virtual* minicharge particle-antiparticle-pairs in an external magnetic field could have the potential to greatly enhance the accessible minicharge parameter space below the  $\mathcal{O}(\text{meV})$  mass region.



# Chapter 6

“Ob ihr wirklich richtig steht,

seht ihr wenn das Licht angeht.”

aus “1, 2 oder 3”

## LSW via virtual minicharged particles in a magnetic field

As discussed in Sect. 2.2, light-shining-through-walls scenarios constitute an important cornerstone among the various laboratory searches for WISPs, particularly in the low-mass regime. Commonly, LSW scenarios employ that *real* axion-like particles and hidden photons can traverse a light-blocking barrier due to their negligible interaction with the wall. As argued, also indirect bounds on minicharged particles can be derived from LSW scenarios with hidden photons if the photon-hidden photon conversion is mediated by minicharged particles (cf. Fig. 2.5).

On the other hand, a *direct* LSW scenario for minicharged particles is provided by the transition of a barrier through *virtual* particle-antiparticle intermediate states, as first considered for the zero-field situation in [96] (depicted in Fig. 2.6). It is easily conceivable that the probability for this tunneling phenomenon to occur should depend on the wall thickness, in contrast to LSW scenarios based on a tree-level process: In crude terms, the “size” of the loop, which is determined by the Compton wavelength of the minicharged particles, has to outmatch the thickness of the barrier. Thus, if the Compton wavelength is large enough, the transition probability can even grow in the small mass regime: Roughly spoken, the available phase space for the process grows for larger wavelengths. Nevertheless, even in the limit of very thin walls, an LSW scenario via virtual minicharged particles in the absence of external fields was shown to be non-competitive with established laboratory experiments [96]: Although for small minicharge masses, i.e., large Compton wavelengths, the transition probability exhibits a log-like increase as function of the mass, tunneling of the 3rd kind cannot improve existing bounds in relevant regions of the parameter space of the minicharged particles in a zero-field setting.

In this chapter we thus set out to investigate this LSW scenario in an external magnetic field, cf. Fig. 6.1. In LSW scenarios with real particles, the transition probability

is independent of the exact location of the photon-WISP conversion and reconversion processes as long as they occur on the left- and right-hand side of the light-blocking barrier, respectively. By contrast, the transition probability for barrier-transition via virtual particles depends on the location of the particle fluctuation.

In summary, for the scenario based on the *virtual* process, it becomes crucial to account for the *full* momentum dependence of the photons in the setup. Thus, although different in context, but similar to the reasoning of Chapt. 3, a perturbative treatment of this problem is rendered inapplicable.

Therefore, building on a nonperturbative treatment of the polarization tensor, we present a first case study of this LSW scenario in a magnetic field for a selected photon polarization mode. Our findings suggest that by the application of an external magnetic field, the log-like increase of the transition probability can eventually be transformed into a power-law increase. Essentially, this is attributed to a dimensional reduction phenomenon which occurs upon Landau-level quantization.

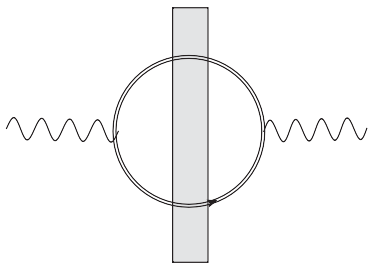


Figure 6.1: LSW scenario via virtual bosonic or fermionic particle-antiparticle intermediate states, also referred to as “tunneling of the 3rd kind”, cf. [96]. In the following, this process is investigated in a constant external magnetic field in a first case study. The dressed minicharge propagator, i.e., that involving an arbitrary number of external field insertions, is depicted by the solid double line.

In this chapter, we proceed as follows: In Sect. 6.1, the general formalism describing the LSW scenario depicted in Fig. 6.1 is outlined and the photon-to-photon transition probability is derived. Thereafter, we focus on finding an adequate analytical treatment of the photon polarization tensor, which enters the photon-to-photon transition probability as the central quantity. Appropriate limiting cases which ultimately allow for an exact numerical evaluation of the transition probability are worked out. Specializing to a specific, experimentally feasible setup in Sect. 6.2, we give a first estimate for obtainable exclusion bounds for a selected photon propagation mode.

## 6.1 The probability for LSW and a handling of the polarization tensor

### 6.1.1 Setting the stage for LSW via virtual MCPs

In this section, we briefly review the basic setting as introduced in [96] and extend it to account for an external magnetic field  $\vec{B} \neq 0$  pointing in the direction of the wave-vector

$\vec{k}$  of the incident photons. For reasons of clarity and easy comparability, let us also adapt the metric convention  $g_{\mu\nu} = \text{diag}(-1, +1, +1, +1)$  as employed in [96] in this chapter such that the momentum four-vector squared reads  $k^2 = \vec{k}^2 - \omega^2$ .

As we study photon propagation in a homogeneous external magnetic field, we start from the equation of motion of the photons in momentum space, cf. Eq. (2.18), which we state here once more for convenience

$$(k^2 g^{\mu\nu} - k^\mu k^\nu + \Pi^{\mu\nu}(k|B)) A_\nu(k) = 0 . \quad (6.1)$$

Although a solution to Eq. (6.1) has been worked out in many limiting cases, see [52] for an overview, solving the equation of motion for this LSW scenario in general becomes a challenging task: Essentially, complications arise since our investigations can from the outset not be expected to be comprehensive within a perturbative small field approximation alone, as for minicharged particles the critical field strength can be already exceeded by rather modest laboratory magnetic field strengths, cf. also the discussion in Sect. 2.2.1. At the same time, the full momentum dependence has to be preserved in the polarization tensor for this LSW scenario. Thereby, well-established approximations, e.g., [54], are rendered inapplicable.

Given these constraints, to choose a proper, physically relevant setting in which Eq. (6.1) can be evaluated, guidance can be found in earlier studies of the polarization tensor in the strong-field limit [52, 191–195]. In particular, it was shown that for field strengths above the critical field strength, photon propagation orthogonal to the field is strongly damped<sup>1</sup> [192]. As a consequence, this tells us that if we are interested in finding a simple, analytical solution to Eq. (6.1), only  $\theta = \angle(\vec{B}, \vec{k}) = 0$  and  $\theta = \pi/2$  are feasible choices because any other angle of incidence will likely imply a “bending” of the propagation direction of the photons, obstructing, e.g., an effective one-dimensional treatment of this problem. Among these two choices, it is then suggestive to specialize to the undamped mode, i.e.,  $\theta = 0$ , as in this situation the proper-time integral can be evaluated exactly whilst the full momentum dependence is retained.

It is precisely this alignment that will be studied in the following<sup>2</sup>.

As outlined in App. C, for  $\theta = 0$ , the magnetic field does not introduce any additional externally set direction as compared to the zero-field case and Eq. (6.1) simplifies considerably. Note that this constitutes a choice which is disfavored in polarization mea-

---

<sup>1</sup>This behavior is reminiscent of Alfvén modes, characterizing magnetohydrodynamic propagation modes in parallel to the magnetic field lines for “superstrong” magnetic fields. In a naive picture, photon propagation in strong magnetic fields is preferred along the external field direction, as the longitudinal momentum of the fermionic intermediate state remains unaffected by the magnetic field whilst the orthogonal modes can acquire an effective mass via the Landau level quantization of the charged intermediate states.

<sup>2</sup>Studies on the  $\theta \neq 0$  situation have also been performed in the perturbative small  $B$  situation [196].

measurements and standard LSW-type setups as it yields vanishing effects in this limit, cf. Sect. 2.2. For this alignment,  $\vec{k} \parallel \vec{B}$ , the polarization tensor can be written as

$$\Pi^{\mu\nu}(k|B) = P_{\perp}^{\mu\nu} \Pi_{\perp}(k|B) + g_{\perp}^{\mu\nu} \Pi_{\parallel}(k|B) . \quad (6.2)$$

As outlined in App. C, for  $\theta = \sphericalangle(\vec{B}, \vec{k}) = 0$ , the transversal projector  $P_{\text{T}}^{\mu\nu} = g^{\mu\nu} - \frac{k^{\mu}k^{\nu}}{k^2}$  can essentially be decomposed into propagation modes corresponding to orthogonal and “tilted” polarization modes:  $P_{\text{T}}^{\mu\nu} = g_{\perp}^{\mu\nu} + P_{\perp}^{\mu\nu}$ , where we have adapted the notation of [193]. To study the LSW scenario in full generality, all propagation modes,  $\perp$  and  $\parallel$ , have to be accounted for. However, it is found that the decomposition of the internal momentum integration of the polarization tensor can be performed in analogy to the zero-field situation only for the  $\perp$  mode, see below. Thus, for a primary case study, we specialize to the evaluation of this mode. Furthermore, we choose the angle of incidence for the photons to be orthogonal to the barrier such that the photons do not have a momentum component in parallel to the wall.

Dropping Lorentz indices, the equation of motion, Eq. (6.1) for the tilted propagation modes  $A_{\perp}^{\mu} = P_{\perp}^{\mu\nu} A_{\nu}$  reduces to

$$(k^2 + \Pi_{\perp}(k|B)) A_{\perp}(k) = 0 . \quad (6.3)$$

The direction of photon propagation is denoted as  $x$ -direction in the following. The light blocking barrier, cf. Fig. 6.1, breaks translational invariance<sup>3</sup> in  $x$ -direction in our setting. Here, the barrier is assumed to extend from  $x = 0$  to  $x = d$ , having an infinite extension along the  $(y, z)$ -plane. Introducing partial Fourier transforms of the photons and the polarization tensor,

$$A_{\perp}(x, \omega) = \int_{-\infty}^{\infty} \frac{dk_x}{2\pi} e^{ik_x x} A_{\perp}(k) , \quad (6.4)$$

$$\Pi_{\perp}(x - x', \omega|B) = \int_{-\infty}^{\infty} \frac{dk_x}{2\pi} e^{i(x-x')k_x} \Pi_{\perp}(k|B) , \quad (6.5)$$

the equations of motion become

$$(\omega^2 + \partial_x^2) A_{\perp}(x, \omega) = \underbrace{\int_{-\infty}^{\infty} dx' \Pi_{\perp}(x - x', \omega|B) A_{\perp}(x', \omega)}_{=: j_{\perp}(x, \omega|B)} , \quad (6.6)$$

---

<sup>3</sup>Note carefully in the derivation of Eq. (6.1), translational invariance was assumed for the fluctuations. Although translational invariance is broken for the photons by the insertion of the barrier, it is maintained for the loop as the wall remains unnoticed by the minicharged particles.

where we have defined the fluctuation induced current  $j_{\perp}$ . As in the setting proposed in [96], we choose reflecting<sup>4</sup> boundary conditions for the incident photons on the left hand side of the barrier (at  $x = 0$ ). However, the calculation could easily be generalized to other boundary conditions. Accordingly, the induced current within and beyond the barrier is given by

$$j_{\perp}(x > 0, \omega|B) = \int_{-\infty}^0 dx'' \Pi_{\perp}(x - x'', \omega|B) a(\omega) \sin(\omega x''), \quad (6.7)$$

with the amplitude  $a(\omega)$  of the incident photons.

Lastly, to obtain the photon-to-photon transition probability characterizing the tunneling process, the resultant induced outgoing wave on the right hand side of the barrier has to be determined. As we want to assure in the following that minicharged loops are closed again, i.e., to maximize the reconversion rate, we consider the outgoing photons asymptotically for detector positions far beyond the barrier at  $x \gg d$ , yielding

$$A_{\perp, \text{ind}}(x \gg d, \omega|B) = i \int_d^{\infty} dx' \frac{e^{i\omega(x-x')}}{2\omega} j_{\perp}(x', \omega|B), \quad (6.8)$$

where we have employed the free outgoing Green's function for the operator  $(\omega^2 + \partial_x^2)$  and restricted ourselves to the right-moving, i.e., transmitted components of the outgoing photon field.

Thus, combining Eq. (6.7) and Eq. (6.8), the photon transition amplitude for the  $\perp$  mode can finally be written as

$$P_{\perp, \gamma \rightarrow \gamma} = \lim_{x \rightarrow \infty} \left| \frac{A_{\perp, \text{ind}}(x, \omega)}{a(\omega)} \right|^2 = \frac{1}{4\omega^2} \left| \int_d^{\infty} dx' \int_{-\infty}^0 dx'' \Pi_{\perp}(x' - x'') \sin(\omega x'') e^{-i\omega x'} \right|^2, \quad (6.9)$$

where we have dropped the explicit reference to the magnetic field  $B$  in the arguments of the functions for reasons of clarity.

## 6.1.2 Polarization tensor in a magnetic field at zero incidence

### Photon polarization tensor in momentum space

The first step to take in order to determine the transition probability for LSW via virtual MCPs is to find an appropriate treatment of the polarization tensor. Its full analytical expression in the alignment  $\vec{B} \parallel \vec{k}$  for the  $\perp$  propagation mode is given by

$$\Pi_{\perp}(k) = \frac{k^2 \alpha \epsilon^2}{2\pi} \int_0^1 d\nu (1 - \nu^2) \left[ \ln \left( \frac{m^2}{2\epsilon \epsilon B} \right) - \Psi \left( \frac{\Phi_0}{2\epsilon \epsilon B} \right) - \frac{\epsilon \epsilon B}{\Phi_0} \right], \quad (6.10)$$

---

<sup>4</sup>This choice is in agreement with the use of a cavity on the front side of the wall.

cf. [193–195] as well as Eq. (C.18), where  $\Psi(\xi) = \frac{d}{d\xi} \ln \Gamma(\xi)$  denotes the Digamma function, and we have employed the following definition

$$\Phi_0 = m^2 + k^2 \frac{1 - \nu^2}{4} - i\eta. \quad (6.11)$$

For the sake of clarity, in this chapter  $m$  (rather than  $m_\epsilon$ ) gives the mass of the minicharged particles<sup>5</sup> of charge  $\epsilon e$ . In Eq. (6.11), we have also explicitly kept track of the  $-i\eta$  prescription of the fermion Green’s function implementing causality in the complex  $k^2$  plane.

Different representations of the Digamma function can be used to study the various physically relevant parameter regimes, cf. App. C. A perturbative small field expansion is most conveniently obtained from Eq. (6.10) using the asymptotic<sup>6</sup> series expansion of the Digamma function for large arguments from [198], see also Eq. (C.25). In consequence, Eq. (6.10) becomes

$$\Pi_{\perp}(k) = \frac{k^2 \alpha \epsilon^2}{2\pi} \int_0^1 d\nu (1 - \nu^2) \left[ \ln \left( \frac{m^2}{\Phi_0} \right) + \frac{1}{12} \left( \frac{2\epsilon e B}{\Phi_0} \right)^2 + \mathcal{O}(B^4) \right]. \quad (6.12)$$

The contributions linear in  $B$  cancel out, and the expansion in Eq. (6.12) is in even powers of the magnetic field, in full agreement with Furry’s theorem. On the other hand, the  $B$ -independent logarithmic term in Eq. (6.12) contains the zero-field result. Using integration by parts, it can be rewritten into the representation of the zero-field polarization tensor<sup>7</sup> as employed in [96],

$$\Pi(k)|_{B=0} = \frac{(k^2)^2 \alpha \epsilon^2}{4\pi} \int_0^1 d\nu \left( \frac{\nu^2}{3} - 1 \right) \frac{\nu^2}{\Phi_0}. \quad (6.13)$$

Most importantly, besides the perturbative small-field limit, an exact series representation of the Digamma function is available [177], cf. also Eq. (C.23). Based on this representation, Eq. (6.10) can be written as

$$\Pi_{\perp}(k) = \frac{k^2 \alpha \epsilon^2}{2\pi} \int_0^1 d\nu (1 - \nu^2) \left( \left[ \frac{\epsilon e B}{\Phi_0} + \gamma + \ln \left( \frac{m^2}{2\epsilon e B} \right) \right] - \sum_{n=1}^{\infty} \frac{\Phi_0}{n(\Phi_0 + 2\epsilon e B n)} \right). \quad (6.14)$$

Eqs. (6.12) and (6.14) serve as the starting point of our further calculations.

<sup>5</sup>In the subsequent considerations our focus is on minicharged spin-1/2 Dirac fermions. Remarks on the physics of bosonic spin-0 minicharged particles are essentially given in Sects. 6.1.4 and 6.2.3.

<sup>6</sup>The fact that an asymptotic series appears here does not come unexpectedly, cf., e.g., [197], but should advise us to carefully check on the range of validity of this series later on.

<sup>7</sup>Note that the zero-field limit is contained in both propagation modes:  $\perp$  as well as  $\parallel$ . For this reason, we drop the label “ $\perp$ ” here.

### Towards the polarization tensor in position space

In a next step, we aim at transforming the polarization tensor to position space through Eq. (6.5) as it enters the transition probability in this form, cf. Eq. (6.9). Studying the explicit structure of  $\Pi_{\perp}(k)$ , several observations simplify the further discussion. Firstly, the evaluation of Eq. (6.9) does not necessitate the Fourier transformation of all the terms present in Eqs. (6.12) and (6.14), respectively. As the transition amplitude involves further integrations over the spatial coordinates in the argument of  $\Pi_{\perp}(x - x', \omega)$ , it holds that  $x - x' > 0$  always. Thus, terms whose momentum dependence is given by an overall factor of  $k^2$  only, do not contribute since

$$\int_{-\infty}^{\infty} \frac{dk_x}{2\pi} e^{i(x-x')k_x} k^2 = -(\omega^2 + \partial_x^2) \int_{-\infty}^{\infty} \frac{dk_x}{2\pi} e^{i(x-x')k_x} = -(\omega^2 + \partial_x^2) \delta(x - x') \quad (6.15)$$

always vanishes for  $x - x' > 0$ . Therefore, we subsequently omit terms exhibiting this momentum dependence. Moreover, note that  $x - x' > 0$  also implies that, in performing the  $k_x$ -integration in Eq. (6.5), the integration contour has to be closed in the upper half-plane.

With these preparations, we now explicitly turn to the Fourier transformation of the polarization tensor in Eqs. (6.12) and (6.14). Notably, all residual terms to be considered in the Fourier transformation are of the general form

$$\begin{aligned} & \int_0^1 d\nu (1 - \nu^2) \int_{-\infty}^{\infty} \frac{dk_x}{2\pi} e^{i(x-x')k_x} \frac{P(k_x)}{(\Phi_0 + 2\epsilon\epsilon Bn)^l} \\ &= \int_0^1 d\nu \underbrace{\frac{4^l}{(1 - \nu^2)^{l-1}} \int_{-\infty}^{\infty} \frac{dk_x}{2\pi} \frac{e^{i(x-x')k_x} P(k_x)}{\left[ k_x^2 - \omega^2 + \frac{4m_n^2}{1-\nu^2} - i\eta \right]^l}}_{=:h(\nu)}, \end{aligned} \quad (6.16)$$

with  $n \in \mathbb{N}_0$  and  $l \in \mathbb{N}$ . For later reference, the integrand of the  $\nu$ -integral is labeled by  $h(\nu)$ , wherein any reference to further variables is omitted.  $P(k_x)$  denotes a polynomial in  $k_x$ , i.e., as obvious from Eqs. (6.12) and (6.14), either refers to  $P(k_x) = k^2$  or  $P(k_x) = k^2\Phi_0$ . Furthermore, we introduced the  $n$ -dependent “effective mass squared”

$$m_n^2 \equiv m^2 + 2\epsilon\epsilon Bn, \quad (6.17)$$

implying in particular  $m_0 \equiv m$ .

Our next task is to perform the  $k_x$ -integration in Eq. (6.16) explicitly. As Eq. (6.16) corresponds to the most basic building block constituting Eqs. (6.12) and (6.14), this allows us to discuss all the complications that arise in the evaluation of Eq. (6.5). The evaluation of the  $k_x$ -integral with the Residue theorem requires care, as the location of the poles in the complex  $k_x$ -plane depends on the further integration parameter  $\nu$ . For

given  $\omega > 2m_n$ , the quantity  $\omega^2 - \frac{4m_n^2}{1-\nu^2}$  exhibits a sign-change as a function of  $\nu$ . Defining

$$\lambda_n = \sqrt{1 - \frac{4m_n^2}{\omega^2(1-\nu^2)}}, \quad (6.18)$$

and

$$\kappa_n = \sqrt{\frac{4m_n^2}{\omega^2(1-\nu^2)} - 1}, \quad (6.19)$$

an analysis of the integrand in Eq. (6.16) shows that its poles in the complex  $k_x$ -plane are located at

$$\begin{aligned} k_x &= \pm\omega i\kappa_n \pm (1+i)\eta & \text{for } \omega^2 &\leq \frac{4m_n^2}{1-\nu^2}, \\ k_x &= \pm\omega\lambda_n \pm (1+i)\eta & \text{for } \omega^2 &\geq \frac{4m_n^2}{1-\nu^2}, \end{aligned} \quad (6.20)$$

suggesting an  $n$ -dependent decomposition of the  $\nu$ -integral of the following form:

$$\int_0^1 d\nu h(\nu) \rightarrow \int_0^{\Re\sqrt{1-\frac{4m_n^2}{\omega^2}}} d\lambda_n \left[ \frac{d\nu}{d\lambda_n} h(\nu) \right]_{\nu=\sqrt{1-\frac{4m_n^2}{\omega^2(1-\lambda_n^2)}}} + \int_{\Re\sqrt{\frac{4m_n^2}{\omega^2}-1}}^{\infty} d\kappa_n \left[ \frac{d\nu}{d\kappa_n} h(\nu) \right]_{\nu=\sqrt{1-\frac{4m_n^2}{\omega^2(1+\kappa_n^2)}}}. \quad (6.21)$$

In [96], a similar<sup>8</sup> decomposition is employed for  $n = 0$ . Subsequently, we stick to the above decomposition.

It is necessary to distinguish two cases: Whereas for  $\omega \leq 2m_n$  there is only the  $\kappa_n$ -integral, for  $\omega > 2m_n$  both the  $\kappa_n$ - and  $\lambda_n$ -integrals contribute. By virtue of the pole structure in the momentum-integration, cf. Eq. (6.20), the integrand of the  $\kappa_n$ -part is exponentially damped with increasing  $\kappa_n$ , and the  $\lambda_n$ -part is oscillating as a function of  $\lambda_n$ . Following the decomposition in Eq. (6.21), it is suggestive to label contributions due to  $\kappa_n$  by “ $\leq$ ”, and contributions due to  $\lambda_n$  by “ $>$ ”, see below. As after the substitution in Eq. (6.21)  $\kappa_n$  and  $\lambda_n$  are nothing but integration parameters, we subsequently omit the index  $n$  and simply use  $\kappa$  and  $\lambda$  instead. Moreover note, that whereas we omit any explicit reference to the  $i\eta$ -prescription in the remainder, one should always recall the implicit prescriptions  $\lambda \rightarrow \lambda + (1+i)\eta$  and  $i\kappa \rightarrow i\kappa + (1+i)\eta$ .

## The photon transition amplitude

The last open issue in determining the photon transition amplitude is the evaluation of the two position-space integrals in Eq. (6.9).

<sup>8</sup>A decomposition of this form for the  $\perp$  mode, cf. Eq. (C.18), is not as easily available due to the dissimilar dependence of the polarization tensor on  $\nu$ .



This can be achieved by noting that

$$\int_d^\infty dx' \int_{-\infty}^0 dx'' [i(x' - x'')]^l e^{i\omega(x' - x'')\lambda} \sin(\omega x'') e^{-i\omega x'} = \frac{ie^{-i\omega d}}{\omega^{2+l}} (\partial_\lambda)^l \left[ \frac{e^{i\omega d \lambda}}{(1 - \lambda)^2 (1 + \lambda)} \right], \quad (6.22)$$

where  $l \in \mathbb{N}_0$ , and a corresponding equation for  $\kappa$ , which can be obtained from Eq. (6.22) by substituting  $\lambda \rightarrow i\kappa$ . Next, we rewrite the photon transition probability in Eq. (6.9) as

$$P_{\perp, \gamma \rightarrow \gamma} = \frac{\alpha^2 \epsilon^4}{36\pi^2} |f_{\leq} + f_{>}|^2, \quad (6.23)$$

where we have introduced the dimensionless auxiliary functions  $f_{\leq}$  and  $f_{>}$  analogously to [96]. Due to the modulus in Eq. (6.23), we do not have to care for global phase factors in the definition of the auxiliary functions, and drop them in the following.

Before turning to the situation of a nonvanishing external magnetic field, let us state, as a reminder, the auxiliary functions in the zero-field limit. Starting with the zero-field polarization tensor of Eq. (6.13), one finds [96]:

$$f_{\leq}^{(\text{zero})} = \int_{\Re\sqrt{\frac{4m^2}{\omega^2}-1}}^\infty d\kappa \frac{e^{-\omega d \kappa}}{i + \kappa} \frac{\sqrt{1 + \kappa^2 - \frac{4m^2}{\omega^2}} \left(1 + \kappa^2 + \frac{2m^2}{\omega^2}\right)}{(1 + \kappa^2)^{3/2}}, \quad (6.24)$$

$$f_{>}^{(\text{zero})} = \int_0^{\Re\sqrt{1 - \frac{4m^2}{\omega^2}}} d\lambda \frac{e^{i\omega d \lambda}}{1 - \lambda} \frac{\sqrt{1 - \lambda^2 - \frac{4m^2}{\omega^2}} \left(1 - \lambda^2 + \frac{2m^2}{\omega^2}\right)}{(1 - \lambda^2)^{3/2}}. \quad (6.25)$$

Note, that our notation slightly differs from [96] as we would like to emphasize that the  $\kappa$ -integral also contributes when the condition  $\omega = 2m$  is fulfilled exactly. In addition, we have introduced an upper label for the auxiliary functions, allowing us to distinguish them in the various limiting cases discussed below. For later reference, let us also state the transition probability in the limit of vanishing external fields, which reads, cf. Eq. (6.23),

$$P_{\gamma \rightarrow \gamma}^{(\text{zero})} = \frac{\alpha^2 \epsilon^4}{36\pi^2} |f_{\leq}^{(\text{zero})} + f_{>}^{(\text{zero})}|^2. \quad (6.26)$$

Subsequently, we investigate the implications for the transition probability for  $B \neq 0$ .

### 6.1.3 Transition amplitude in regimes of different field strength

#### Transition amplitude for weak magnetic fields

It is instructive to determine the transition probability in the presence of a weak magnetic field first, which can be treated as a small, perturbative correction to the zero-field case.

Thus, we focus on the auxiliary functions derived from the polarization tensor in the limit of “weak magnetic fields”, see Eq. (6.12) and also Fig. 6.2. In this context, we already

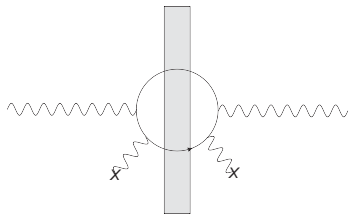


Figure 6.2: LSW scenario in the perturbative limit with two couplings to the external field. For parameters corresponding to a feasible experimental setup, the validity of the approximation ceases to hold far before the perturbative correction can sizably outmatch the corresponding zero-field process, cf. Sect. 6.2.1.

encounter some generic features of the auxiliary functions, facilitating the discussion of the fully nonperturbative result below. Following the steps outlined in Sect. 6.1.2, one arrives to order  $B^2$  at

$$f_{\leq}^{(\text{weak})} = \frac{2B^2\epsilon^2e^2}{\omega^4} \int_{\Re\sqrt{\frac{4m^2}{\omega^2}-1}}^{\infty} d\kappa e^{-\omega d\kappa} \frac{d\omega\kappa(i+\kappa) + i + 2\kappa}{\kappa^2(i+\kappa)^2\sqrt{1+\kappa^2}\sqrt{1+\kappa^2-\frac{4m^2}{\omega^2}}}. \quad (6.27)$$

The corresponding function  $f_{>}$  can be obtained from  $f_{\leq}$  by substituting  $\kappa \rightarrow -i\lambda$  and changing the integration boundaries accordingly (cf. Eq. (6.21)), yielding

$$f_{>}^{(\text{weak})} = \frac{2B^2\epsilon^2e^2}{\omega^4} \int_0^{\Re\sqrt{1-\frac{4m^2}{\omega^2}}} d\lambda e^{i\omega d\lambda} \frac{id\omega\lambda(1-\lambda) - 1 + 2\lambda}{\lambda^2(1-\lambda)^2\sqrt{1-\lambda^2}\sqrt{1-\lambda^2-\frac{4m^2}{\omega^2}}}. \quad (6.28)$$

This expansion in  $B^2$  can be generalized to arbitrary orders using the corresponding asymptotic expansion of the Digamma function [198], cf. Eq. (C.25). Notably, the analytical structure of Eqs. (6.27) and (6.28) incorporates various interesting differences with respect to the zero-field case.

Firstly, we focus on the special situation where  $\omega = 2m$  and only Eq. (6.27) contributes. Noteworthy, the  $\kappa$ -integration is found to diverge for all values of  $\omega = 2m$  and  $d$ . As there is no such divergence in the absence of external fields (cf. Eq. (6.24)), this divergence or “resonance phenomenon” can be considered as a genuine manifestation of the external magnetic field. Let us remark that this has already been discussed by previous authors, see, e.g., [199–202], in the context of quantum electrodynamics, but becomes particularly relevant for minicharged particles. This divergence signals a break down of unitarity in our calculation, as it would predict an arbitrarily large number of outgoing photons for any small number of incoming photons. This unitarity violation is a consequence of the idealized limit of a perfectly coherent infinite incoming wave train. A proper treatment of the resonances requires to take, e.g., the finite width of the laser into account. As this may indeed lead to a strong sensitivity to minicharged degrees of freedom, a careful analysis of these resonances seems to be worthwhile. Here, however, we continue to work in the perfectly coherent wave limit and ignore potential enhancements arising from such resonances.

Secondly, we point out some general features of Eqs. (6.27) and (6.28). Whereas the  $\kappa$ - and  $\lambda$ -integrations can easily be performed numerically for  $\omega < 2m$ , a direct numerical evaluation becomes tedious for  $\omega \geq 2m$ . In this case the integrand in Eq. (6.27) *seems* to diverge at the lower end and that in Eq. (6.28) at both the lower and the upper integration boundaries, respectively. However, recall the implicit  $i\eta$ -prescription from Sect. 6.1.2, ensuring that divergencies do not lie on the integration contours. It turns out that for  $\omega \neq 2m$ , i.e., apart from the true divergence at  $\omega = 2m$  just discussed, the encountered superficial divergencies can be circumnavigated using integration by parts:

By means of the following identity for  $\omega \neq 2m$ ,

$$\int d\kappa \frac{1}{\kappa^2 \sqrt{1 + \kappa^2 - \frac{4m^2}{\omega^2}}} = \frac{\sqrt{1 + \kappa^2 - \frac{4m^2}{\omega^2}}}{\left(\frac{4m^2}{\omega^2} - 1\right) \kappa} + C, \quad (6.29)$$

with integration constant  $C$ , Eq. (6.27) can be rewritten as

$$f_{<}^{(\text{weak})} = \frac{2B^2 \epsilon^2 e^2}{\omega^4 \left(1 - \frac{4m^2}{\omega^2}\right)} \int_{\Re \sqrt{\frac{4m^2}{\omega^2} - 1}}^{\infty} d\kappa \sqrt{1 + \kappa^2 - \frac{4m^2}{\omega^2}} \times \frac{[\omega d(2i - 3\kappa) - \omega^2 d^2(1 + \kappa^2)](i + \kappa) - 4\kappa + i}{(i + \kappa)^2(1 + \kappa^2)^{3/2}} e^{-\omega d \kappa}, \quad (6.30)$$

and a surface term. Note that the lower label in Eq. (6.30) now is “<” as the case  $\omega = 2m$  has been excluded explicitly. Above, the surface term of the integration by parts has been omitted as it vanishes identically for  $\omega < 2m$  and for  $\omega > 2m$  cancels with the corresponding surface term arising in the analogous integration by parts of Eq. (6.28), as can be easily verified by taking into account the explicit  $i\eta$ -prescription (cf. the discussion below Eq. (6.21)).

Correspondingly, employing Eq. (6.29) with  $\kappa \rightarrow -i\lambda$ , Eq. (6.28) becomes

$$f_{>}^{(\text{weak})} = \frac{2B^2 \epsilon^2 e^2}{\omega^4 \left(1 - \frac{4m^2}{\omega^2}\right)} \int_0^{\Re \sqrt{1 - \frac{4m^2}{\omega^2}}} d\lambda \sqrt{1 - \lambda^2 - \frac{4m^2}{\omega^2}} \times \frac{[\omega^2 d^2(1 - \lambda^2) - i\omega d(2 + 3\lambda)](1 - \lambda) - 4\lambda - 1}{(1 - \lambda)^2(1 - \lambda^2)^{3/2}} e^{i\omega d \lambda}, \quad (6.31)$$

where we have again omitted the surface term. As Eq. (6.31) only contributes for  $\omega > 2m$  and, as just discussed above, the surface term in this case cancels with the one arising in Eq. (6.30), the expressions in Eqs. (6.30) and (6.31) constitute the full result for  $\omega \neq 2m$ . These are divergence-free and thus perfectly suited for numerical evaluation.

Finally, we combine the zero-field contributions with the corrections due to a weak external magnetic field to obtain the photon transition probability for weak magnetic fields through Eq. (6.23).

The transition probability then reads

$$P_{\perp, \gamma \rightarrow \gamma}^{(\text{pert})} = \frac{\alpha^2 \epsilon^4}{36\pi^2} \left| f_{\leq}^{(\text{zero})} + f_{>}^{(\text{zero})} + f_{<}^{(\text{weak})} + f_{>}^{(\text{weak})} \right|^2. \quad (6.32)$$

Let us remark at this point, that so far we have not yet specified the dimensionless expansion parameter employed in the perturbative expansion explicitly, but rather focused on the structure of the arising contributions. The explicit form of the expansion parameter and therewith also the area of validity of the perturbative expansion is discussed in the context of the strong field limit below.

Lastly, it is instructive to note, that naive analytic asymptotics for the limit  $\omega \gg 2m$ , being the limiting case of greatest physical interest, cannot be provided by means of an expansion in the dimensionless parameter  $\frac{2m}{\omega} \ll 1$ . To see this, it is useful to rescale the variables in Eq. (6.31) as  $\lambda \rightarrow \tilde{\lambda} \sqrt{1 - \frac{4m^2}{\omega^2}}$  such that the upper integration boundary becomes 1 and the phase in the exponent becomes  $\omega d\tilde{\lambda} \sqrt{1 - \frac{4m^2}{\omega^2}}$ . A subsequent expansion in  $\frac{2m}{\omega}$  then inevitably results in an unphysical divergence at  $\tilde{\lambda} = 1$ .

Correspondingly, even for  $\omega \gg 2m$  we will stick to a full numerical evaluation of Eq. (6.32). Note that rescaling  $\lambda$  as described above is also useful for this numerical evaluation, which will be performed in Sect. 6.2.1. There, it will be particularly interesting to check if Eq. (6.32) can provide for improved experimental bounds in the limit of sole  $\perp$  mode propagation in the range of the validity of the approximation.

### Towards the photon transition amplitude in the limit of strong magnetic fields

Given the structure of the sum within Eq. (6.14), the strong-field limit is significantly more complicated to obtain. The structure of the  $B$  dependence of the final expression cannot be easily read off from Eq. (6.14), as it will be affected by the  $k_x$  integration.

Proceeding in the decomposition of the polarization tensor as outlined above, one obtains the auxiliary functions:

$$f_{\leq}^{(\text{full})} = \frac{12B\epsilon em^2}{\omega^4} \int_{\Re\sqrt{\frac{4m^2}{\omega^2}-1}}^{\infty} d\kappa \frac{e^{-\omega d\kappa}}{(1+\kappa^2)^{3/2} (i+\kappa) \sqrt{1+\kappa^2 - \frac{4m^2}{\omega^2}}} + \sum_{n=1}^{\infty} \frac{48B\epsilon em_n^2}{\omega^4} \int_{\Re\sqrt{\frac{4m_n^2}{\omega^2}-1}}^{\infty} d\kappa \frac{e^{-\omega d\kappa}}{(1+\kappa^2)^{3/2} (i+\kappa) \sqrt{1+\kappa^2 - \frac{4m_n^2}{\omega^2}}}, \quad (6.33)$$

as well as

$$\begin{aligned}
 f_{>}^{(\text{full})} = & \frac{12B\epsilon\epsilon m^2}{\omega^4} \int_0^{\Re\sqrt{1-\frac{4m^2}{\omega^2}}} d\lambda \frac{e^{i\omega d\lambda}}{(1-\lambda^2)^{3/2}(1-\lambda)\sqrt{1-\lambda^2-\frac{4m^2}{\omega^2}}} \\
 & + \sum_{n=1}^{\infty} \frac{48B\epsilon\epsilon m_n^2}{\omega^4} \int_0^{\Re\sqrt{1-\frac{4m_n^2}{\omega^2}}} d\lambda \frac{e^{i\omega d\lambda}}{(1-\lambda^2)^{3/2}(1-\lambda)\sqrt{1-\lambda^2-\frac{4m_n^2}{\omega^2}}} . \quad (6.34)
 \end{aligned}$$

Note that Eqs. (6.33) and (6.34) together with Eq. (6.23) constitute the full nonperturbative transition probability for arbitrary field strengths.

Obviously, the term in the first line of Eq. (6.33) and Eq. (6.34), respectively, and the terms in the second line are of exactly the same structure. They agree with each other besides  $m \leftrightarrow m_n$  and a relative factor of four. Note however that the term in the first line of Eq. (6.33) exhibits a divergence for  $\omega = 2m$ . Recall that for this choice a divergence has already been encountered in the weak field approximation above. Correspondingly, the terms in the second line of Eq. (6.33) give rise to divergencies for  $\omega = 2m_n$ . Note that these divergencies were already identified by previous authors on the level of the polarization tensor, e.g., [199–202].

In summary we find divergencies of the photon transition amplitude for all  $\omega = 2m_n$ ,  $n \in \mathbb{N}_0$ . Let us emphasize that these divergencies arise as a genuine feature of the full nonperturbative expression of the polarization tensor in a nonvanishing field, cf. Eq. (6.10). Intriguingly, the divergencies for  $n \in \mathbb{N}$  are outside the scope of the perturbative weak field expansion.

Also, as Eqs. (6.33) and (6.34) are the full nonperturbative expressions, it should in particular be possible to re-extract the zero-field result as a limiting case. In particular, the regularity of the zero-field contribution at  $\omega = 2m$  has to be regained. It turns out that the zero-field contribution is contained in the sum over infinitely many terms in the second lines of Eqs. (6.33) and (6.34) and can indeed be recovered. This is demonstrated later, in App. F, for clarity.

Note that an explicit evaluation of the full auxiliary functions for arbitrary field strengths does not seem feasible, due to the infinitely many terms with concurrent integrations to be considered in the sum. Thus we subsequently aim at the determination of the leading contribution in the presence of a strong magnetic field.

To this end, we proceed similar to the limit of weak magnetic fields and rewrite Eqs. (6.33) and (6.34) using integration by parts and employ Eq. (6.29) with the substitution  $m \rightarrow m_n$ . Accordingly, these integrations are now only possible for  $\omega \neq 2m_n$  for all  $n \in \mathbb{N}_0$ . As discussed previously, the resonances at  $\omega = 2m_n$  violate unitarity and cannot be drawn upon for physical predictions.

Eqs. (6.33) and (6.34) can be rewritten as

$$\begin{aligned}
 f_{<}^{(\text{full})} &= \frac{12B\epsilon em^2}{\omega^4(1 - \frac{4m^2}{\omega^2})} \int_{\Re\sqrt{\frac{4m^2}{\omega^2}-1}}^{\infty} d\kappa \frac{[2(1 - \kappa^2) - \omega d\kappa(1 + \kappa^2) + i\kappa] e^{-\omega d\kappa}}{(1 + \kappa^2)^{5/2} (i + \kappa)} \sqrt{1 + \kappa^2 - \frac{4m^2}{\omega^2}} \\
 &+ \sum_{n=1}^{\infty} \frac{48B\epsilon em_n^2}{\omega^4(1 - \frac{4m_n^2}{\omega^2})} \int_{\Re\sqrt{\frac{4m_n^2}{\omega^2}-1}}^{\infty} d\kappa \frac{[2(1 - \kappa^2) - \omega d\kappa(1 + \kappa^2) + i\kappa] e^{-\omega d\kappa}}{(1 + \kappa^2)^{5/2} (i + \kappa)} \sqrt{1 + \kappa^2 - \frac{4m_n^2}{\omega^2}} ,
 \end{aligned} \tag{6.35}$$

$$\begin{aligned}
 f_{>}^{(\text{full})} &= \frac{12B\epsilon em^2}{\omega^4(1 - \frac{4m^2}{\omega^2})} \int_0^{\Re\sqrt{1 - \frac{4m^2}{\omega^2}}} d\lambda \frac{[2(1 + \lambda^2) + i\omega d\lambda(1 - \lambda^2) + \lambda] e^{i\omega d\lambda}}{(1 - \lambda^2)^{5/2} (1 - \lambda)} \sqrt{1 - \lambda^2 - \frac{4m^2}{\omega^2}} \\
 &+ \sum_{n=1}^{\infty} \frac{48B\epsilon em_n^2}{\omega^4(1 - \frac{4m_n^2}{\omega^2})} \int_0^{\Re\sqrt{1 - \frac{4m_n^2}{\omega^2}}} d\lambda \frac{[2(1 + \lambda^2) + i\omega d\lambda(1 - \lambda^2) + \lambda] e^{i\omega d\lambda}}{(1 - \lambda^2)^{5/2} (1 - \lambda)} \sqrt{1 - \lambda^2 - \frac{4m_n^2}{\omega^2}} .
 \end{aligned} \tag{6.36}$$

In contrast to the integration by parts in the weak field case, here the respective surface terms in both the  $\kappa$ - and the  $\lambda$ -contributions vanish themselves. The change of the lower label from “ $\leq$ ” in Eq. (6.33) to “ $<$ ” in Eq. (6.35) now explicitly excludes  $\omega = 2m_n$  for all  $n \in \mathbb{N}_0$ .

In analogy to the zero-field limit, the contribution due to  $f_{>}$  vanishes identically for  $\omega < 2m$ . This immediately follows from the fact that  $m_n < m_{n+1}$ , cf. Eq. (6.17). Also, for  $\omega > 2m$ , the upper boundary of the  $\lambda$ -integral in the sum terms of Eq. (6.36) vanishes identically if  $n$  exceeds

$$n_{\max} = \left\lceil \frac{\omega^2 - 4m^2}{8\epsilon e B} \right\rceil, \tag{6.37}$$

where  $\lceil \dots \rceil$  denotes the smallest integer not less than the argument. Thus, for given experimental parameters  $\{\omega, B\}$  and minicharges  $\{\epsilon, m\}$ , the sum is always over a finite number of terms only.

In particular, if  $n_{\max} = 1$ , i.e.,  $\omega < 2m_1$ , the contribution in the second line of Eq. (6.36) completely vanishes. Let us have a closer look at this limiting case. For  $\frac{2\epsilon e B}{m^2} \ll 1$ , the inequality  $\omega < 2m_1$  reduces to  $\omega < 2m$ . In the opposite limit  $\frac{2\epsilon e B}{m^2} \gg 1$ , it amounts to  $\frac{8\epsilon e B}{\omega^2} > 1$ . Thus, for external magnetic fields fulfilling the condition  $\frac{8\epsilon e B}{\omega^2} > 1$ , Eq. (6.36) reduces to its first line.

### Extracting the strong field limit of the transition probability

Subsequently we argue that the sum in the second line of Eq. (6.36) can be considered as subleading and hence be neglected in a much larger regime. As  $m_n$ , and therewith in particular the integration boundaries in the terms of the sum, exhibit an explicit

dependence on the magnetic field strength  $B$ , disentangling the magnitude and importance of the various contributions in Eq. (6.36) is a nontrivial task. The representations of Eqs. (6.35) and (6.36) have the advantage that the integrands do not exhibit any poles within the range of integration, and the respective contributions are manifestly finite. In particular, whereas the integrand in Eq. (6.35) is always finite along the real  $\kappa$ -axis, the integrand in Eq. (6.36) diverges outside the integration interval at  $\lambda = 1$ .

Let us now turn to the situation where  $\omega \gg 2m$ , which from a phenomenological point of view, is the parameter regime of main interest for light MCPs. As the divergence at  $\lambda = 1$  then just lies outside the interval of integration, the main contribution to Eq. (6.36) should stem from the vicinity of the upper integration boundary. Moreover, Eq. (6.36) is expected to dominate the contribution of Eq. (6.35) due to two reasons. Firstly, the domain the parameter  $\kappa$  is integrated over is well separated from any potential divergencies of the integrand (located at  $\kappa = \pm i$ ), in contrast to the integration interval of  $\lambda$ . Secondly, the integrand in Eq. (6.35) is exponentially suppressed as a function of the parameter  $\omega d \kappa$ . In particular for case of  $\omega d > 1$  (which must be certainly obeyed in experiments), it receives its main contribution from a tiny interval just above the lower integration boundary. For the dominant contribution, we hence focus on Eq. (6.36).

For  $\omega \gg 2m$ , the sum in the second line of Eq. (6.36) in general contributes for  $n \leq n_{\max}$  (cf. above). The explicit reference to the real part in the upper integration boundary can be omitted for these  $n$ . Starting from  $\lambda = 0$ , the integrands in Eq. (6.36) rapidly increase with  $\lambda$ . In the vicinity of the upper limit, the factor  $\sqrt{1 - \lambda^2 - \frac{4m_n^2}{\omega^2}}$  guarantees that the integrand is bent back and vanishes exactly at the upper integration boundary. The peak is close to the upper limit and more pronounced for large  $\omega$ .

On the other hand, the main contribution to Eq. (6.36) is expected to be due to small  $n$ , fulfilling  $\omega \gg 2m_n$ , as for these terms the upper integration boundary of the  $\lambda$ -integral comes closest to the divergence at  $\lambda = 1$ . In order to estimate its magnitude we focus on the integrands in the vicinity of the divergence at  $\lambda = 1$ , as this regime is assumed to dictate the magnitude of the  $\lambda$ -integral in the respective terms in the sum. This suggests to approximate the common part of the integrands for  $\lambda$  near 1 as

$$\frac{[2(1 + \lambda^2) + i\omega d \lambda(1 - \lambda^2) + \lambda] e^{i\omega d \lambda}}{(1 - \lambda^2)^{5/2} (1 - \lambda)} = -\frac{5}{4\sqrt{2}} \frac{e^{i\omega d}}{(1 - \lambda)^{7/2}} + \mathcal{O}((1 - \lambda)^{-5/2}), \quad (6.38)$$

and the term discriminating the various terms in the sum as

$$\sqrt{1 - \lambda^2 - \frac{4m_n^2}{\omega^2}} \approx \sqrt{2} \left( \sqrt{1 - \frac{4m_n^2}{\omega^2}} - \lambda \right)^{1/2}. \quad (6.39)$$

This approximation retains the important feature that the integrand vanishes at the upper integration boundary, a behavior that would be spoiled by a naive series expansion

about  $\lambda = 1$ . Moreover, the so-approximated integrand can be integrated explicitly, and afterwards be expanded in terms of  $\frac{2m_n}{\omega} \ll 1$ . Combining Eqs. (6.38) and (6.39) we get to leading order in  $\frac{2m_n}{\omega} \ll 1$

$$-\frac{5}{4} \int_0^{\sqrt{1-\frac{4m_n^2}{\omega^2}}} d\lambda \frac{\left(\sqrt{1-\frac{4m_n^2}{\omega^2}} - \lambda\right)^{1/2} e^{i\omega d}}{(1-\lambda)^{7/2}} = -\frac{4}{3} \left(\frac{\omega^2}{4m_n^2}\right)^2 e^{i\omega d} + \mathcal{O}\left(\frac{\omega^2}{4m_n^2}\right). \quad (6.40)$$

If in addition  $\frac{2\epsilon\epsilon B}{m^2} \gg 1$ , the term in the first line of Eq. (6.36) is of order  $\sim \frac{2\epsilon\epsilon B m^2}{\omega^4} \frac{\omega^4}{m^4} = \frac{2\epsilon\epsilon B}{m^2} \gg 1$ , whereas the first terms in the sum in the second line are  $\sim \frac{2\epsilon\epsilon B m^2}{\omega^4} \frac{\omega^4}{4\epsilon^2 e^2 B^2 n^2} = \frac{m^2}{2\epsilon\epsilon B n^2} \ll 1$ , and therewith suppressed in particular for larger  $n$ : With increasing  $n$ , the individual terms become less important, as the upper integration boundary starts to deviate progressively from  $\lambda = 1$ .

Finally, the limit  $\omega \gtrsim 2m_n$  has to be discussed. Due to the factor  $(1 - \frac{4m_n^2}{\omega^2})$  in the denominator of the second line in Eq. (6.36), one might expect a significant contribution. However, expanding the integrand of the accompanying  $\lambda$ -integral around  $\lambda = 0$ , one finds

$$\int_0^{\sqrt{1-\frac{4m_n^2}{\omega^2}}} d\lambda \sqrt{1-\frac{4m_n^2}{\omega^2}} = 1 - \frac{4m_n^2}{\omega^2}, \quad (6.41)$$

giving rise to a contribution of order  $\sim \frac{\epsilon\epsilon B}{\omega^2}$ , which is substantially suppressed compared to the contribution of the term in the first line of Eq. (6.36). In summary, we have demonstrated that the first line of Eq. (6.36) constitutes the leading contribution in the limit  $\omega \gg 2m$ ,  $\frac{2\epsilon\epsilon B}{m^2} \gg 1$  and  $\omega d > 1$ .

Noteworthy, the very same discussion can also be applied to the auxiliary functions in the weak-field limit, cf. Eqs. (6.30) and (6.31). As the leading behavior of the integral in Eq. (6.31) coincides with that in Eq. (6.38) for  $m_n \rightarrow m$ , we can ultimately identify the expansion parameter in the weak field expansion. We find that such an expansion is trustworthy only in the regime where  $\frac{2\epsilon\epsilon B}{m^2} \ll 1$ .

As argued, the first line of Eq. (6.36) dominates the transition probability in the physically most relevant limit. In our numerical studies below, the other contributions such as the first line of Eq. (6.35) will nevertheless be included. The numerical results confirm our analytical line of argument. To summarize: In the limit of strong magnetic fields, the auxiliary functions  $f_{<}$  and  $f_{>}$  are well approximated by

$$f_{<}^{(\text{strong})} = \frac{12B\epsilon\epsilon m^2}{\omega^4 \left(1 - \frac{4m^2}{\omega^2}\right)} \int_{\Re\sqrt{\frac{4m^2}{\omega^2}-1}}^{\infty} d\kappa e^{-\omega d\kappa} \frac{2(1-\kappa^2) - \omega d\kappa(1+\kappa^2) + i\kappa}{(1+\kappa^2)^{5/2}(i+\kappa)} \sqrt{1+\kappa^2 - \frac{4m^2}{\omega^2}}, \quad (6.42)$$



and correspondingly

$$f_{>}^{(\text{strong})} = \frac{12B\epsilon em^2}{\omega^4 \left(1 - \frac{4m^2}{\omega^2}\right)} \int_0^{\Re\sqrt{1 - \frac{4m^2}{\omega^2}}} d\lambda e^{i\omega d\lambda} \frac{2(1 + \lambda^2) + i\omega d\lambda(1 - \lambda^2) + \lambda\sqrt{1 - \lambda^2 - \frac{4m^2}{\omega^2}}}{(1 - \lambda^2)^{5/2}(1 - \lambda)}. \quad (6.43)$$

The validity of this approximation is well confirmed by numerics in the experimentally relevant strong-field limit. Inserting the auxiliary functions Eqs. (6.42) and (6.43) into Eq. (6.23), we finally obtain the transition probability in the strong field limit, characterized by  $\frac{2\epsilon e B}{m^2} \gg 1$  and the additional constraints  $\omega \gg 2m$  and  $\omega d > 1$ ,

$$P_{\perp, \gamma \rightarrow \gamma}^{(\text{strong})} = \frac{\alpha^2 \epsilon^4}{36\pi^2} \left| f_{<}^{(\text{strong})} + f_{>}^{(\text{strong})} \right|^2. \quad (6.44)$$

Let us also remark at this point that the leading contribution to the photon transition amplitude is expected to depend on the thickness of the barrier  $d$  only via a phase factor  $e^{i\omega d}$ , as can be seen, for instance, in Eqs. (6.38-6.40). The transition probability, in which phase factors drop out, should show almost no  $d$  dependence in the strong field limit, as long as the Compton wavelength remains the dominant length scale.

In Sect. 6.2.1, we employ Eq. (6.44) in order to predict experimentally achievable MCP exclusion limits in an idealized limit of sole  $\perp$  mode propagation. There, we evaluate this strong field transition probability fully numerically. Nevertheless, it is useful to extract the asymptotic behavior of Eq. (6.44). As argued above, for  $\omega \gg 2m$ , Eq. (6.44) is very well approximated by  $f_{<}^{(\text{strong})}$  alone. Thus, employing the leading order estimate of Eq. (6.40) for the  $\lambda$  integral at  $n = 0$  in Eq. (6.43), one obtains as asymptotic behavior of the strong field transition probability for  $\omega \gg 2m$

$$P_{\perp, \gamma \rightarrow \gamma}^{(\text{strong})} \simeq \alpha^2 \frac{\epsilon^4}{36\pi^2} \left( B \frac{\epsilon e}{m^2} \right)^2. \quad (6.45)$$

Finally, to make contact with the intermediate transition regime  $\frac{2\epsilon e B}{m^2} \simeq 1$ , which is in principle contained in Eqs. (6.35) and (6.36) but, as discussed above, numerically hard to handle, it is useful to introduce an interpolating behavior for the transition amplitude by combining the zero-field and strong magnetic-field limits of the transition amplitude. Near  $\frac{2\epsilon e B}{m^2} \gtrsim 1$ , the terms neglected in Eqs. (6.42) and (6.43) become increasingly important and have to be accounted for. On the other hand, we will find in Sect. 6.2.1, that the zero-field contribution dominates the transition probability at  $\frac{2\epsilon e B}{m^2} \lesssim 1$ . Consequently, to link the approximations in the regimes  $\frac{2\epsilon e B}{m^2} \gg 1$  and  $\frac{2\epsilon e B}{m^2} \ll 1$  throughout the region where  $\frac{2\epsilon e B}{m^2} \simeq 1$ , we define

$$P_{\perp, \gamma \rightarrow \gamma}^{(\text{trans})} = \frac{\alpha^2 \epsilon^4}{36\pi^2} \left| f_{\leq}^{(\text{zero})} + f_{>}^{(\text{zero})} + f_{<}^{(\text{strong})} + f_{>}^{(\text{strong})} \right|^2. \quad (6.46)$$

### 6.1.4 Transition amplitude for scalar minicharged particles

It is worthwhile to study in brief the corresponding LSW scenario for scalar minicharged particles. As outlined in App. C, the analog of Eq. (6.10) for scalar minicharges reads

$$\Pi_{\perp}^{\text{sc}} = \frac{k^2 \alpha \epsilon^2}{4\pi} \int_0^1 d\nu \nu^2 \left[ \ln \left( \frac{2m^2}{\epsilon \epsilon B} \right) + \Psi \left( \frac{\Phi_0}{2\epsilon \epsilon B} \right) - 2\Psi \left( \frac{\Phi_0}{\epsilon \epsilon B} \right) \right], \quad (6.47)$$

cf. Eq. (C.22), where  $\Phi_0$  is defined as in Eq. (6.11). Following the same steps as employed in the derivation of Eqs. (6.33) and (6.34) in Sect. 6.1.3, we find the full auxiliary functions in the scalar case

$$f_{\leq}^{(\text{sc}, \text{full})} = \frac{3\epsilon \epsilon B}{\omega^2} \sum_{j=0}^{\infty} \int_{\Re \sqrt{\frac{4m_j^2}{\omega^2} - 1}}^{\infty} d\kappa \frac{e^{-\omega d \kappa}}{(1 + \kappa^2)^{3/2} (i + \kappa)} \sqrt{1 + \kappa^2 - \frac{4m_j^2}{\omega^2}}, \quad (6.48)$$

as well as

$$f_{>}^{(\text{sc}, \text{full})} = \frac{3\epsilon \epsilon B}{\omega^2} \sum_{j=0}^{\infty} \int_0^{\Re \sqrt{1 - \frac{4m_j^2}{\omega^2}}} d\lambda \frac{e^{i\omega d \lambda}}{(1 - \lambda^2)^{3/2} (1 - \lambda)} \sqrt{1 - \lambda^2 - \frac{4m_j^2}{\omega^2}}, \quad (6.49)$$

where we have defined  $m_j^2 = m^2 + \epsilon \epsilon B (2j + 1)$  and  $j \in \mathbb{N}_0$ . Building on the insights gained in the discussion of the fermionic minicharges, we can make a few interesting observations.

Firstly, as in Eq. (6.48), the factor  $\sqrt{1 - \lambda^2 - \frac{4m_j^2}{\omega^2}}$  appears immediately in the numerator as in the zero-field case, we do not encounter any resonances at  $\omega = 2m_j$  for scalar minicharged particles (cf. also [201]).

Secondly, for scalar minicharged particles it seems rather hard to extract a leading contribution to the photon transition amplitude in the strong field limit as defined and discussed in Sect. 6.1.3. In particular, there is no clear separation of scales analogous to the fermionic case, where  $m_0^2 \ll m_n^2$  for  $n \in \mathbb{N}$ . The physical reason for this feature will be elaborated on in more detail in Sect. 6.2.3.

### 6.1.5 Range of validity and general limitations

Lastly, we would like to comment shortly on the range of validity and limitations of our estimates for the photon transition probability for the  $\perp$  mode in the limit of very low minicharge masses. These considerations are intended to be on a more general level.

Given the simplifying assumption of a spatially infinitely extended, homogeneous magnetic field, let us first focus on the limitations arising from the fact that in an experiment the region penetrated by the magnetic field is finite. Realizing that the spatial extent of the virtual particle loop is characterized by the Compton-wavelength, i.e., the inverse mass  $m^{-1}$ , of the encircling virtual particles, a natural criterion on the validity of the

assumption of an infinitely extended field arises. Accordingly, as a rough estimate, the inverse masses of the probed minicharges should not exceed the diameter of the region penetrated by the magnetic field, cf. also Sect. 6.2.1. Note that this constitutes a *physical* IR-cutoff to the formally divergent transition amplitudes in the limit of small minicharge masses.

In addition, besides this essentially experimentally motivated constraint, recall that our calculation is based on the polarization tensor in an external magnetic field at one-loop level. Thus it certainly also has to be expected to become unreliable as soon as higher loop corrections can no longer be considered as negligible. However, as higher loop calculations go beyond the scope of this study, the subsequent considerations cannot go beyond the level of educated guesses. In Sect. 6.1.3, we showed that for very small minicharge masses  $\omega \gg 2m$  and in the strong-field limit the leading contribution to the transition amplitude is  $\sim \frac{2\epsilon\epsilon B}{m^2} \gg 1$ , where the linear scaling with the external field can be attributed to the minicharge loop alone.

At two loop level, no new charged loops modify the tunneling process - the one-loop diagram is rather corrected by an additional virtual photon line. Thus, we expect only two additional couplings to enter, such that the two-loop correction in the above limit can be estimated to be  $\sim \epsilon^2\alpha\frac{2\epsilon\epsilon B}{m^2}$ . However, as  $\epsilon \ll 1$  one would therefore not expect the two-loop correction to invalidate our results obtained at one-loop level. Only at three loop level, additional fermion loops have to be considered. Assuming that the scaling with the external field *factorizes* for the two loops, the leading term for the three loop correction would be  $\sim (\epsilon^2\alpha)^2(\frac{2\epsilon\epsilon B}{m^2})^2$  for small minicharged masses. In this case, the three loop correction would outmatch the one-loop contribution if  $\epsilon^4\alpha^2\frac{2\epsilon\epsilon B}{m^2} \gg 1$ . However, again since  $\epsilon \ll 1$ , this could happen only for very large magnetic field strengths, and will not interfere with the exclusion bounds for our setup, cf. Sect. 6.2.1.

In summary, the experimental limitations to establish homogeneous magnetic fields on the scale of large Compton wavelength  $\sim 1/m$  appear to induce the most relevant constraints in the IR. We stress however that the factorization assumption used above has to be checked by explicit higher-loop calculations.

Certainly, also this discussion of the IR behavior being based on a *perturbative* expansion in the number of dressed loops does not necessarily grasp all effects that could arise in a nonperturbative treatment of the effective action.

## 6.2 MCP discovery potential for the $\perp$ mode

In the following, we specify several details of an experimental setup inspired by current technological capabilities. We then derive exclusion bounds in an idealized limit for which all propagating photons are assumed to be coupled into the  $\perp$  mode in order to illustrate

the discovery potential of LSW via virtual minicharged particles. Let us emphasize that at this point we have not yet specified if and how the probe photons can be coupled entirely into the  $\perp$  mode in an experiment. In fact, this issue is debated in the literature, cf., e.g., [193, 194].

Of course, experimental insight on this matter is difficult to obtain, as the critical field strength of QED is not (yet) accessible in experiments. However, in order to investigate the possible existence of minicharged particles, it becomes important to raise this question again. In any case, analytical insights into the  $\perp$  polarization modes are not as straightforwardly available. In addition, the physical features that are prominent in the idealized limit of the sole  $\perp$  propagation mode most likely also persist in the calculation for the full transversal photon field which is given as a combination of the  $\perp$  and  $\parallel$  modes, see App. C. For this reason, we study the LSW discovery potential for the  $\perp$  mode in detail, and postpone a discussion of a feasible experimental setup which provides for a maximum coupling to the  $\perp$  mode to Sect. 6.3.

As already emphasized in the preface to this chapter, the LSW scenario via virtual minicharges, cf. Fig. 6.1, has the potential to provide *direct* limits on  $\epsilon$ . For this reason it will be instructive to compare the discovery potential of our setup to exclusion limits derived from PVLAS polarization measurements rather than existing LSW data. Although the former are less stringent in comparison to, e.g., ALPS LSW bounds, they do not rely on a hidden-photon intermediate state (cf. Fig. 2.5).

Firstly, one might think, that the smallest accessible minicharge mass scale is set by the scale of the employed vacuum beam tube diameter within the optical cavity. The latter is used to enlarge the light power in the WISP production region on the side of the incident photons. However, as the minicharges interact extremely weakly with the magnet material or all other parts of the setup, the diameter of the beam tube and other components are not relevant. Rather, the limiting length scale for the resolvable minicharge mass is determined by the extent of the homogeneous external magnetic field as well as the spatial separation between the photon source and the photon detector alone. More specifically, the spatial and temporal homogeneity of the magnetic field should be comparable to or larger than the Compton wavelength of the minicharged particle. If the probe laser and the photon detector can be placed at arbitrary distances to the wall, the extent of the magnetic field constitutes the limiting scale for the accessible minicharge masses. Thus, employing conventional dipole magnets as used in accelerators or even common nuclear magnetic resonance (NMR) machines, resolving minicharge masses of  $m_\epsilon \gtrsim 4 \times 10^{-7} \text{eV}$  which correspond to magnetic field radii of  $\sim 0.5 \text{m}$  seems feasible. In Figs. 6.3 and 6.4 we use a conservative value of  $B = 5 \text{T}$  for the estimate, which could be produced by a HERA dipole magnet as used in ALPS or even a today's NMR machine.

Secondly, we employ many state-of-the-art parameters as successfully installed at ALPS: The probe laser beam provides visible light at a wavelength of 532nm, i.e.,  $\omega = 2.33$  eV corresponding to a frequency doubled 1064nm standard light source. Note that for the purpose of detecting regenerated photons, the detector efficiency and particularly the detector noise play a crucial role. The best noise curves are usually obtained with detectors for visible light that have rather poor efficiency in the infrared. On the other hand, lasers at the infrared can reach higher intensities and thus constitute the better choice for the photon source.

Thirdly, we give an estimate for the thickness of the light-blocking barrier which was assumed to be perfectly reflecting in our theoretical considerations, cf. Sect. 6.1.1. For ALPS, the light blocking barrier is realized by a high-quality steel block with thickness  $d = 1.8\text{cm} \hat{=} 9.1 \times 10^4 \text{eV}^{-1}$  [203]: As for ALPS the barrier traversing particles are real, the thickness of the wall does not play a crucial role for the conversion probability in the limit of vanishing WISP-to-matter coupling.

By contrast, in our setup, the experiment exhibits an intrinsic sensitivity on the wall thickness: For minicharge masses corresponding to Compton wavelengths smaller than the wall thickness, the tunneling process is obstructed, whereas for greater Compton wavelengths, the process becomes *independent* of the thickness of the barrier. To demonstrate this we give exclusion limits for two different thicknesses of the wall corresponding to  $d = 1\text{mm} \hat{=} 5.1 \times 10^3 \text{eV}^{-1}$  and  $d = 1\mu\text{m} \hat{=} 5.1 \text{eV}^{-1}$ , where the former is a feasible and the latter an ambitious aim for a thin-layer optical coating of a thin substrate. However, as already noted below Eq. (6.44), exploring large Compton wavelengths, i.e., small minicharge masses is even possible with *thicker barriers*, as, e.g., used in the ALPS experiment. Technically, the numerical evaluation of the auxiliary function  $f_{>}$  becomes considerably more difficult for thicker barriers, see below. For this reason, we limit ourselves to the a numerical evaluation for the  $d$ -values stated above.

With all experimental parameters which enter the transition probabilities set, we proceed to the evaluation of the experimental observable in the proposed LSW scenario, which is the outgoing photon number behind the light-blocking barrier:

$$n_{\text{out}} = \mathcal{N} n_{\text{in}} P_{\perp, \gamma \rightarrow \gamma} . \quad (6.50)$$

As in all LSW scenarios, the lever arm for probing small minicharge couplings is the large number of incoming photons  $n_{\text{in}}$  on the right hand side of Eq. (6.50) vs. the – in principle – single photon detection possible with modern avalanche photodiodes. In addition, we introduce a variable  $\mathcal{N}$  which shall account for the option of installing a regeneration cavity on the right hand side of the wall, cf. [93]. Without a cavity one the regeneration side one has  $\mathcal{N} = 1$ .

As emphasized, it remains to be determined how many photons can be coupled into the  $\perp$  mode. Certainly, in an ideal situation, this would be possible for all incoming photons. However, as we have stated the explicit  $\epsilon$  dependence in the transition probabilities in the different limits, the corresponding exclusion plot could be easily rescaled if in fact fewer photons can be coupled into the  $\perp$  mode. Thus, with this limitation in mind, we assume as an incoming to outgoing photon ratio  $n_{\text{in}}/n_{\text{out}} = 10^{25}$  as realized for ALPS, which already accounts for additional parameters of the experimental realization such as the use of a front-side cavity, effective detector sensitivity and running time, cf. [77].

Lastly, let us comment on the numerical evaluation of Eq. (6.50). Herein the greatest challenge is the numerical evaluation of the auxiliary function  $f_{>}$  contributing to the transition probability  $P_{\perp, \gamma \rightarrow \gamma}$ . As seen in Sect. 6.1.2, the integrand of the  $\lambda$ -integral in  $f_{>}$  can generically have a highly oscillatory behavior (depending on the exact parameter set  $d, \omega, m$ ) in all limits (without or with external  $B$  field): Rescaling the integration variable as  $\lambda \rightarrow \tilde{\lambda} \sqrt{1 - \frac{4m^2}{\omega^2}}$ , it can be seen that the numerical evaluation becomes increasingly difficult at the upper integration boundary  $\tilde{\lambda} \lesssim 1$  for larger values of  $d\sqrt{\omega^2 - 4m^2}$ , constituting the oscillation's frequency. For thicker walls and masses obeying  $\omega \gg 2m$ , the frequency of oscillations is always very large and becomes only slightly smaller for larger minicharge masses  $\omega \gtrsim 2m$ . In addition, as the amplitude of the oscillation becomes also very large near  $\tilde{\lambda} \lesssim 1$ , cf. discussion below Eq. (6.36), one runs into difficulties in the numerical evaluation of the  $\tilde{\lambda}$ -integral especially at small  $m$ . To circumnavigate this problem, it is helpful to split the  $\tilde{\lambda}$ -integral at an appropriate cutoff value  $\tilde{\lambda}_c(d, \omega, m)$  which depends on the set of variables used and in addition also depends on the employed numerical integration routine. Substituting  $\tilde{\lambda} \rightarrow 1/R$  above the cutoff, one can then rewrite the integral as:  $\int_0^1 d\tilde{\lambda} = \int_0^{\tilde{\lambda}_c} d\tilde{\lambda} + \int_1^{1/\tilde{\lambda}_c} dR/R^2$ . In this manner, the numerical routine can treat the problematic region separately at slightly reduced oscillatory phase and amplitude.

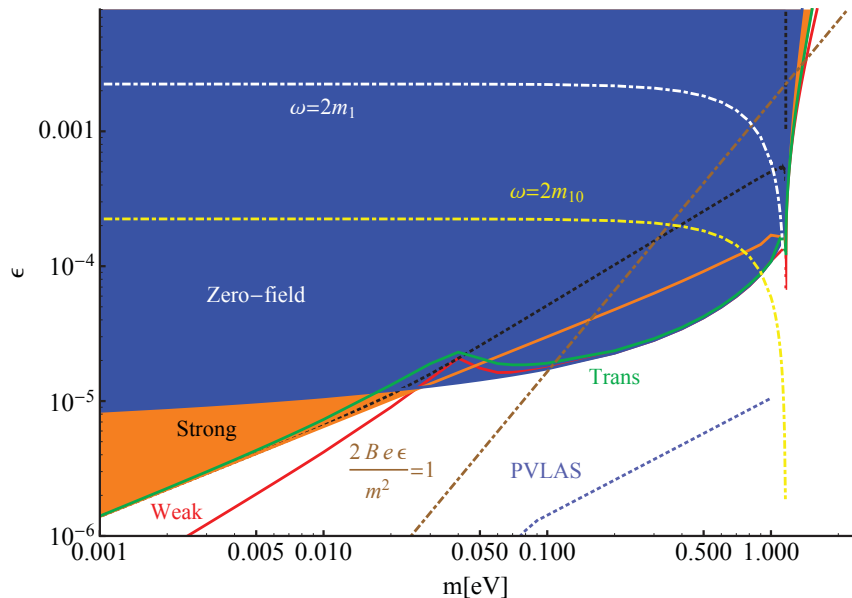
In contrast to the  $\lambda$ -contribution, the  $\kappa$ -integral is always decaying and never oscillatory, cf. Sect. 6.1.2. Nevertheless, for numerical evaluation, a similar rescaling procedure for  $\omega < 2m$  as  $\kappa \rightarrow \tilde{\kappa} \sqrt{\frac{4m^2}{\omega^2} - 1}$  such that the upper integration becomes 1 is consistent, cf. Eq. (6.30). For  $\omega > 2m$ , the numerical evaluation of the  $\kappa$ -integral is straightforward and requires no special attention.

### 6.2.1 Prospective exclusion bounds for minicharged fermions

With the above preparations, we are now in the position to determine an exclusion plot for minicharged fermions in the fractional-charge-mass plane. Employing the outgoing photon number, Eq. (6.50), together with the different transition probabilities derived in Sect. 6.1.3, we compute the prospective bounds for the experimental parameter set introduced above, dividing the exclusion plot into an upper right and a lower left half,

cf. Figs. 6.3 and 6.4, respectively. The two plots concentrate on the meV mass range (Fig. 6.3) and on a mass range including very small masses (Fig. 6.4) to highlight different physical features arising in the different limiting cases. The colored areas correspond to the parameter regimes that are accessible by the proposed experimental setup.

Figure 6.3:  $\perp$  mode exclusion bounds in the fractional charge-mass plane for “larger” minicharge masses. The blue area denotes the zero-field limit, whereas the red line corresponds to the perturbative  $\mathcal{O}(B^2)$ -approximation. The perturbative correction is only valid for  $\frac{2\epsilon\epsilon B}{m^2} \ll 1$  and hence holds only in the region to the far right of the brown dot-dashed line, depicting  $\frac{2\epsilon\epsilon B}{m^2} = 1$ . It clearly breaks



down long before it improves bounds from the zero-field limit. The orange area denotes the area that can be excluded in the strong magnetic field limit by virtue of Eq. (6.44) for a wall thickness of  $d = 1\text{mm}$ , whereas the black dotted line corresponds to a thickness of  $d = 1\mu\text{m}$  in the strong-field case. It is visible that the bounds become independent of the wall thickness below  $m \approx 5 \times 10^{-3}\text{eV}$ . The strong  $B$ -field approximation is valid for  $\frac{2\epsilon\epsilon B}{m^2} \gg 1$ , whereas the green line nicely interpolates between the strong and weak field limits at  $\frac{2\epsilon\epsilon B}{m^2} \simeq 1$ . Within the area excluded in the zero-field situation, we give the resonance condition  $\omega = 2m_n$  for  $n = 1$  and  $n = 10$  as a paradigm. In addition, in light blue, PVLAS limits are depicted, cf. also Fig. 6.4.

Fig. 6.3 displays the mass-coupling plane for “large” minicharge masses of  $m = 10^{-3}\text{eV}$  up to  $m = 2\text{eV}$ . Although this mass range is apparently irrelevant in terms of discovery potential for minicharged fermions as the colored regions are all already excluded by PVLAS [25] polarization data (cf. the dotted light blue line), we can nevertheless gain several interesting physical insights. Firstly, one can see that for masses greater than  $m \gtrsim 0.03\text{eV}$ , the best exclusion bounds are already obtained in a zero-field setting with  $d = 1\mu\text{m}$  (denoted by the blue shaded area) as described through Eq. (6.26). As already discussed in [96], going to the smallest considered masses of  $m = 4 \times 10^{-7}\text{eV}$  in this setup, the zero-field line decreases with a logarithmic dependence and finally reaches a fractional coupling of  $\epsilon \simeq 6 \times 10^{-6}$ , cf. also Fig. 6.4.

In red, we plot the discovery potential for  $\perp$  mode propagation in the limit of weak magnetic fields, cf. Eq. (6.32). As argued in Sect. 6.1.3, this perturbative correction is only valid as long as  $\frac{2ceB}{m^2} \ll 1$ . As we depict  $\frac{2ceB}{m^2} = 1$  as brown dot-dashed line in Fig. 6.3, the perturbative correction can be expected to be trustworthy only to the very right of this line and its limit of validity clearly is exceeded long before it can improve the zero-field bounds. Therefore, the perturbative result *cannot* account for a new physics discovery potential with the chosen set of parameters and it is found that the nonperturbative results will be crucial to the exploration of an hitherto untested minicharge parameter range.

A distinct feature discriminating the zero-field situation from the finite magnetic field case is certainly the resonance at  $\omega = 2m$ , corresponding to  $m = 1.165\text{eV}$  for our parameters, as visible in Fig. 6.3. This phenomenon certainly deserves further attention. However, for reasons of clarity we defer the discussion of this particular resonance and all the other resonances at  $\omega = 2m_n$  ( $n \in \mathbb{N}$ ), as encountered in Sect. 6.1.3 to Sect. 6.2.2.

As argued in Sect. 6.1.3, for  $\frac{2ceB}{m^2} \gg 1$ , i.e., to the very left of the brown dot-dashed line, we are in the range of validity of the strong  $B$ -field approximation cf. Eq. (6.44). The strong magnetic field limit is plotted for two thicknesses of the walls corresponding to the orange area with  $d = 1\mu\text{m}$  and the black dotted line corresponding to  $d = 1\text{mm}$ . As expected, for smaller minicharge masses, these lines fall on top of each other, as the wall thickness becomes insignificant for minicharges with smaller masses corresponding to larger Compton wavelengths, cf. also the discussion in Sect. 6.2.3 below. This behavior is found approximately below  $m \simeq 6 \times 10^{-3}\text{eV}$ . Note that this constitutes a nontrivial full numerical check of the auxiliary function's behavior which was also extracted analytically to leading order, below Eq. (6.44). Going to larger masses, the lines are found to separate, where, according to intuition, the thicker wall always results in worse exclusion bounds in comparison to the thinner wall. Also, for both lines, as already encountered in the weak magnetic field situation, a resonance at  $\omega = 2m$  is clearly visible, cf. also Sect. 6.2.2.

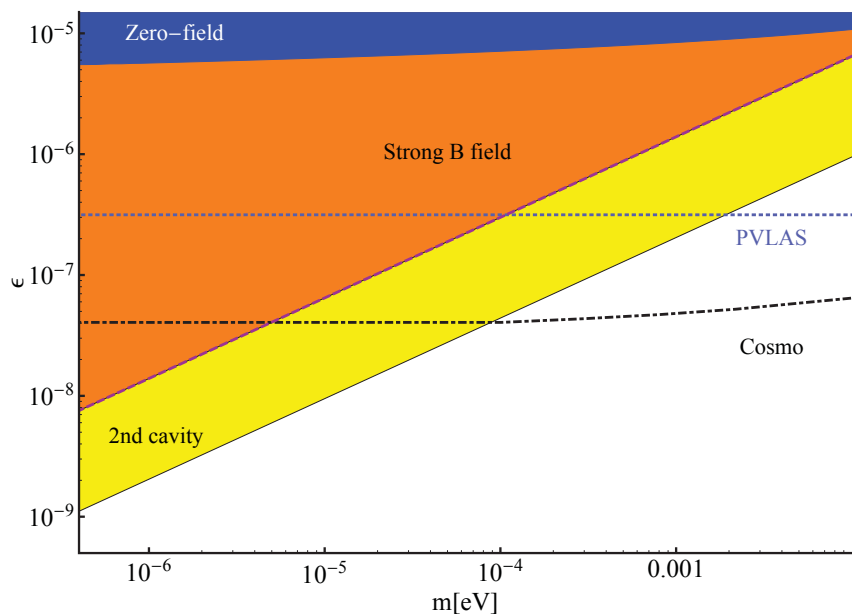
However, this resonance lies within a region where  $\frac{2ceB}{m^2} < 1$ , such that the strong field approximation cannot be expected to hold anymore. Rather, the weak field approximation should be trusted close to the resonance at  $\omega = 2m$ . Accordingly, the limit of strong magnetic fields is only valid for lower minicharge masses and will be discussed in Fig. 6.4 in more detail. Finally, before turning to small masses in Fig. 6.4, let us make contact with the region  $\frac{2ceB}{m^2} \simeq 1$  in Fig. 6.3, in which is a priori neither included in the strong nor in the weak field approximation. As a green line, we plot in Fig. 6.3 the transition behavior, where the strong field behavior is added to the zero-field contribution, cf. Eq. (6.46). As expected, for  $\frac{2ceB}{m^2} \ll 1$  the strong field contribution in the transition curve plays no role and the best limits are provided by the zero-field part alone, whereas for  $\frac{2ceB}{m^2} \gg 1$ , the strong-field contribution dominates the green transition curve. Near  $\frac{2ceB}{m^2} \simeq 1$ , i.e., near



the brown dot-dashed line, it can be seen that the green line nicely arranges the transition from the strong-field through the weak-field probabilities leading finally into the zero-field limit. However, again, as this region is safely excluded by PVLAS polarization data, we now abandon the discussion of Fig. 6.3 and turn to lower minicharge masses, where our setup could have the prospect of new physical discoveries.

In Fig. 6.4 we present exclusion bounds in the lower half of the fractional charge-mass plane ranging from minicharge masses of  $m = 4 \times 10^{-7} \text{eV}$  to  $m = 10^{-2} \text{eV}$ . The orange-colored area depicts the parameter space that could be excluded in the strong magnetic field limit by virtue of Eq. (6.44) for a wall thickness of  $d = 1 \mu\text{m}$ , cf. also Fig. 6.3, whereas the yellow area in addition assumes resonant regeneration with a second cavity installed behind the wall employing  $\mathcal{N} = 10^5$ . As in total the transition probability  $P_{\perp, \gamma \rightarrow \gamma}^{(strong)} \sim \epsilon^6$ , cf. Eq. (6.44) as well as Eq. (6.45), the use of a second cavity yields almost an order of magnitude better exclusion bounds. Note that in order to achieve the same effect by tuning the magnetic field strength alone, one would correspondingly need to enhance the magnetic field by a factor of  $\sqrt{10^5}$  as it enters effectively by its square. This would demand for magnetic fields of  $B \sim 1.5 \times 10^3 \text{T}$ , corresponding to field strengths that can only be obtained in highly focused lasers in a laboratory. However, there of course the extent of the field itself would be limited to a smaller region. Thus, a large effort on the optics side seems to outweigh by its benefits the employment of stronger magnetic fields due to the merely *linear*  $B$ -dependence of the amplitude.

Figure 6.4:  $\perp$  mode exclusion bounds in the fractional charge-mass plane for “small” minicharge masses. The blue area denotes the excluded region in the zero-field limit, whereas the orange-colored area depicts the parameter space that could be excluded in the strong magnetic field limit by virtue of Eq. (6.44), whereas the yellow area in addition assumes resonant regeneration with a second cavity behind the wall employing  $\mathcal{N} = 10^5$ .



The light-blue dotted line denotes limits [58] derived from PVLAS polarization measurements [25], whereas the lower dot-dashed line in black refers to the best model-independent cosmological bounds obtained from CMB data [104]. The pink dashed line gives the asymptotics according to Eq. (6.45).

To compare our strong-field results for the  $\perp$  mode with current experimental limits, we give, as upper dotted line in Fig. 6.4 the exclusion limits [58] provided by PVLAS polarization measurements [25], whereas the lower dot-dashed line labels the best model-independent cosmological bounds obtained from CMB data [104].

We find that in the limit of sole  $\perp$  mode propagation the LSW scenario via virtual minicharged fermionic particle-antiparticle states could improve PVLAS polarization data below  $m \lesssim 10^{-4}\text{eV}$  and even outmatch cosmological bounds derived from CMB data below  $m \lesssim 5 \times 10^{-6}\text{eV}$ . Employing a cavity on the regeneration side, these values can be improved to outmatch PVLAS bounds for  $m \lesssim 2 \times 10^{-3}\text{eV}$  and to outmatch cosmological bounds at  $m \lesssim 9 \times 10^{-5}\text{eV}$ , cf. the yellow-shaded area in Fig. 6.4.

### 6.2.2 Fermionic resonances in the nonperturbative result

Let us briefly discuss the resonances found in Sect. 6.1.3 and their potential impact on the exclusion plot in Sect. 6.2.1. This discussion represents a first glance at these resonances; a more comprehensive study including phenomenological predictions requires to go beyond our present formalism and has, for instance, to deal with wave packets of finite width. In addition, the discussion of the resonance structure has to be extended to include also the  $\perp$  propagation modes.

Let us first comment on the resonance at  $\omega = 2m$  as found both in the strong field limit and in the perturbative weak field expansion. This resonance, as prominently visible at  $m = 1.165\text{eV}$  in Fig. 6.3, is independent of other external parameters such as the magnetic field strength. However, one can see that even for small step sizes around the resonance (in the graph, we have chosen  $\Delta m = 10^{-3}\text{eV}$  as absolute step size close to the resonance, i.e. between 1.1eV and 2eV, and ten points per order of magnitude away from the resonance), the resonance is not particularly broad.

In addition to this overall resonance at  $\omega = 2m$ , which can be seen already in the contribution  $\sim B^2$  in the perturbative weak field approximation, one has a resonant structure at  $\omega = 2m_n$  for  $n \in \mathbb{N}$  in the *full nonperturbative* transition amplitude, being invisible in the perturbative result. In Fig. 6.3 these are shown exemplarily for  $n = 1$  and  $n = 10$  continuing to decrease at linear spacing with each successive higher order of magnitude in  $n$ . Apparently, for fixed  $B$  and  $\omega$ , the resonance condition  $\omega = 2m_n$  is, for a given  $n \in \mathbb{N}$ , always met by some set of parameters  $\{\epsilon, m\}$ , leading to an enhanced probability of light-shining-through-walls if a particle with the corresponding values of  $\{\epsilon, m\}$  exists. In case of a signal, it would be necessary to study the parameter dependence of the signal on  $\omega$  or  $B$ , in order to identify the  $n$  value corresponding to the order of the resonance in the  $\{\epsilon, m\}$  plane. Due to the structurally similar functional dependence of the contributions giving rise to resonances at higher  $n$  visible in Eqs. (6.35) and (6.36), the resonant structures at non-zero  $n$  are expected to be rather sharp, in analogy to the

resonance at  $\omega = 2m$ . A slight detuning, e.g., in  $B$  is expected to immediately “kick” the minicharges off the resonance. However, note that as in Eqs. (6.35) and (6.36) the dependence on  $\epsilon$  is also implicit in the integration boundary, a solid numerical study of this behavior is more involved.

As shown in Sect. 6.1.4 these resonances are absent for scalar minicharged particles, see also [201]. Thus, if the resonances can indeed be utilized in an experiment, they could serve to determine the spin and mass of the minicharged particles.

Let us emphasize again that the divergencies occurring in our transition probability related to the resonances signalize a break down of unitarity in our calculation. Being a consequence of the idealized limit of a perfectly coherent infinite incoming wave, a proper treatment of the resonances requires to account for the finite width of the laser and/or the spatio-temporal inhomogeneity of the magnetic field.

In summary, let us state, that the exclusion limits depicted for the large  $B$  (aside from the resonances) limit denote a primary estimate for the discovery potential of the experiment in the limit where photon propagation is entirely assigned to the  $\perp$  mode.

### 6.2.3 Physics of the low-mass enhancement phenomenon

As emphasized, a comprehensive study of this LSW scenario needs to carefully account for all photon propagation modes,  $\perp$  and  $\parallel$ . Nevertheless, it is worthwhile to already interpret the physics of the low-mass enhancement phenomenon present in the  $\perp$  mode as it seems capable of improving the most recent laboratory bounds in the lower mass range in such a pronounced way. Most obviously, PVLAS bounds as well as other bounds derived from LSW data *saturate* in the limit of small minicharge masses, i.e., the transition amplitude becomes  $m$ -independent in this limit, as predicted by the polarization tensor for propagation in *free* space, cf. [52, 58] as well as Eq. (2.20). In these calculations, following [54], the proper-time integration within the polarization tensor is performed in the limit  $\omega \sin \theta/m \gg 1$  and  $k^2 = 0$ , i.e., on the light cone.

By contrast, in the LSW scenario via virtual particles, translational invariance is explicitly broken at the level of the photon-to-photon transition amplitude, even in the formal limit of  $d \rightarrow 0$  by the specification of a boundary condition for the incident photons on the wall. As a result any approximation strategy that treats  $k^2$  as a *constant*, or particularly  $k^2 = 0$ , is rendered inapplicable, cf. Sect. 6.1.1. Note in addition, for  $\theta = 0$ , an expansion of the polarization tensor in terms of  $\omega \sin \theta/m \gg 1$  is of course inapplicable. Rather, our calculation relies on exact, nonperturbative results for the polarization tensor in the  $\vec{k} \parallel \vec{B}$  situation, as detailed in App. C. With respect to the exclusion bounds, we find that in our specific setting the asymptotic behavior for small minicharge masses differs drastically from the behavior observed at polarization measurements and the bounds derived from the scenario with hidden photons (cf. Fig. 2.5), underlying common LSW

experiments with minicharges. Our scenario for the  $\perp$  mode does not result in saturation, rather, towards smaller minicharge masses the transition amplitude grows  $\sim 1/m^2$  to leading order in the limit of small masses, cf. the discussion below Eq. (6.40) as well as Eq. (6.45). Effectively this amounts to a quartic gain in the transition probability as a function of the minicharges' Compton wavelength, i.e., the “loop size”. On the other hand, as demonstrated, the dependence of the transition probability on the explicit thickness of the wall becomes asymptotically negligible for smaller  $m$ : Recall that our calculation formally accounts for all the incident  $\perp$  probe photons to split into a virtual particle-antiparticle pair at any instance between the photon source and the light-blocking barrier, and conversely allows for a recombination of the virtual particle-antiparticle pair anywhere between the back side of the wall and the detector. As argued above, for a given minicharge mass, sizable contributions to the photon transition amplitude however only arise from an interval of extension of  $\mathcal{O}(m^{-1})$  around the wall. Thus, for tiny minicharge masses  $m^{-1} \gg d$  the region where recombination to photons is forbidden (i.e., within the barrier of width  $d$ ) is significantly outsized by an interval of  $\mathcal{O}(m^{-1})$  where it is possible, resulting in an only subleading  $d$ -dependence of the transition probability.

In particular, note that an analogous reasoning also opens up a more intuitive way to understand why for tiny minicharge masses the contributions to the photon transition amplitude due to non-zero  $n$  are essentially negligible in the strong field limit  $\frac{2ceB}{m^2} \gg 1$ . As pointed out in Sect. 6.1.3, besides an overall factor of four compared to the  $n = 0$  term, the structure of the terms in the sum in Eqs. (6.33) and (6.34) constituting the full transition amplitude is the same. They only differ by their  $n$ -dependent effective mass  $m_n$ . Assuming that the respective contributions can thus be associated with loop sizes of  $\mathcal{O}(m_n^{-1})$ , particularly for  $m_n \gg m$ , as true in the strong field limit, contributions from  $n \geq 1$  can be neglected confidently.

Whereas it is well known that the photon polarization tensor in an external magnetic field can be determined as a sum over infinitely many Landau levels cf., e.g., [200, 201], here we contrarily started with its full analytical expression in the limit of  $\sphericalangle(\vec{B}, \vec{k}) = 0$ , in the  $\perp$  mode derived in the proper-time representation, see App. C. Only after performing the steps outlined in Sect. 6.1.1, and by employing the exact series representation of the Digamma function, we finally recover the Landau-level structure on the level of the photon transition amplitude. The Landau-level picture also provides an understanding of the enhancement of the effect in the small-mass/strong-field limit as compared to the zero-field setting: In contrast to the zero-field setting, spatial momenta orthogonal to the field are quantized into Landau levels in the presence of a magnetic field. Effectively, this amounts to a dimensional reduction from  $3+1$  to  $1+1$  dimensions as the quantized levels can carry momenta only along the longitudinal and the time-like direction. In effect, the log-like increase of the transition probability is converted into a power-law behavior.

Remarkably, the interpretation of our results in terms of Landau levels allows us to motivate both the relative factor of  $1/4$  between the  $n = 0$  and  $n \geq 1$  contributions in Eqs. (6.33) and (6.34), as well as the differences in the results for fermionic and scalar minicharged particles: As the incident probe photons do not have a momentum component orthogonal to the magnetic field, it follows that the transversal momenta of the virtual particle-antiparticle state must add up to zero. In a magnetic field the orthogonal momentum component of charged particles is quantized. As the effective mass squared associated with a given Landau level is defined as the sum of the particles mass squared and its orthogonal momentum component squared, cf., e.g., Eq. (B.9), momentum conservation of the orthogonal components implies that

$$M_{j,\sigma}^2 = M_{j',\sigma'}^2, \quad (6.51)$$

where  $M_{j,\sigma}$  and  $M_{j',\sigma'}$  refer to the effective mass of the particle and its antiparticle in the  $j$ th and  $j'$ th Landau level ( $j, j' \in \mathbb{N}_0$ ), respectively.  $\sigma$  and  $\sigma'$  denote spin degrees of freedom of the particle and its antiparticle. The summation index  $n$  in Eqs. (6.33) and (6.34) has, however, still to be related to the index pair  $j, \sigma$ .

In particular, the effective mass  $m_n$  as introduced in Eq. (6.17), does not coincide with the single-particle mass  $M_{j,\sigma}$  arising in a diagonalization of the Dirac operator. From Eq. (B.9), setting the orthogonal momentum component to zero and with  $e \rightarrow \epsilon e$ , we find that the effective mass is rather given as

$$M_{j,\sigma}^2 = m^2 + \epsilon e B(2j + 1 + \sigma) \quad \text{with } j \in \mathbb{N}_0. \quad (6.52)$$

Here,  $\sigma$  refers to spin components of the minicharged particles, i.e.,  $\sigma = \pm 1$  for fermionic and  $\sigma = 0$  for scalar minicharged particles.

Whereas the lowest possible effective mass squared for fermionic minicharges is given by  $m^2$ , for scalar minicharged particles it is rather  $m_1^2 = m^2 + 2\epsilon e B$ . Moreover, it is now straightforward to show that for fermionic minicharged particles, there is only one possibility to fulfill Eq. (6.51) under the additional requirement  $M_{j,\sigma}^2 = m^2$ , namely  $j = j' = 0$  and  $\sigma = \sigma' = -1$ . On the contrary, for a given  $n \in \mathbb{N}$ , there are always four possibilities to fulfill Eq. (6.51) under the additional requirement  $M_{j,\sigma}^2 = m_n^2$  for fermionic particles,

1.  $j = j' = n$             whilst  $\sigma = \sigma' = -1$ ,
2.  $j = j' = n - 1$        whilst  $\sigma = \sigma' = +1$ ,
3.  $j = n, j' = n - 1$    whilst  $\sigma = -1$  and  $\sigma' = +1$ ,
4.  $j = n - 1, j' = n$    whilst  $\sigma = +1$  and  $\sigma' = -1$ .

This explains the relative factor of  $1/4$  between the terms with  $n = 0$  and  $n > 0$  in Eqs. (6.33) and (6.34). For scalar minicharged particles on the other hand, Eq. (6.51) immediately implies  $j = j'$ , and thus the same weight for all sum terms, as found in the explicit calculation for scalar minicharges, cf. Sect. 6.1.4. As the lowest effective mass for scalar minicharges is  $m_1$ , for scalar minicharged particles with tiny masses we thus do not expect to obtain exclusion bounds compatible with those obtained for fermionic minicharges, basically due to the fact that the lowest effective mass in the external magnetic field coincides with the free mass term  $m$ .

### 6.3 Advantages and perspectives of “virtual LSW”

In this chapter, we have investigated an LSW scenario based on the tunneling via virtual minicharged particles in a magnetic field. From a phenomenological perspective, we have quantified the discovery potential for the  $\perp$  propagation mode at zero incidence in a first case study and interpreted the physical mechanisms which underlie our findings. In order to tackle this LSW scenario analytically, it was essential to focus on photon propagation along the field lines, as only in this configuration, full photon momentum dependence of the polarization tensor can be maintained. In addition, as shown in previous studies of the polarization tensor for strong magnetic fields, only at zero incidence, photon propagation proceeds undamped in the strong field limit [192].

At this point, continuative studies into several directions are in order.

Firstly, as stressed before, for a comprehensive study of this LSW scenario, an inclusion of all the photon propagation modes which occur at zero incidence is necessary. In particular, it would be interesting to see to which extent the zeroth Landau level can contribute to the tunneling process in the  $\perp$  modes. Next, for zero incidence, it is unclear how many photons are coupled into the respective propagation modes in the crossover from a region without external magnetic field into the region permeated by the field, and vice versa. Thus, it is desirable to find a setup which assures a maximal coupling to the  $\perp$  mode. Presumably, this is most easily possible by replacing the optical photon cavity through a microwave cavity as studied, e.g., in [90]. This amounts to a few modifications in our calculations which can, however, be implemented straightforwardly. Staying within an optical setting, it is worthwhile to note that also Gaussian or Bessel beams can be expected to exhibit a coupling to the  $\perp$  mode.

As shown, the range of testable minicharge masses grows with larger spatial extent of the external magnetic field. It thus seems interesting to consider this tunneling phenomenon for the spatially most extended fields. For instance, one could think of probing for minicharges using the earth’s magnetic field alone. As this provides for field strengths of only  $B \sim 50\mu\text{T}$ , depending on the exact geographical location, the achievable bounds

immediately drop by a factor of  $\sim 10^5$  (compare to  $B = 5\text{T}$  used above), but profit from a spatial extent considerably larger than 1m and thus make very light MCPs possibly accessible. However, it has to be checked carefully, whether the approximation of homogeneous<sup>9</sup> fields is still justified in such cases.

In addition, our setting assumed an infinite distance between the photon source and detector. As a next step, the influence of finite intervals should thus be taken into account. In particular, it seems probable that oscillations of the transition probability as a function of this interval length might arise as in similar tree-level processes, cf., e.g., Eq. (2.27). In any case, our results should still hold if the spatial separation between the photon source and the detector is much larger than the extent of the magnetic field.

Also, the resonances occurring for the Dirac fermionic minicharges deserve further attention. If the associated transition probabilities are rendered finite for calculations with, e.g., finite wave packets, the resonances may allow to explore an even larger parameter space, in particular also for large minicharge masses. Lastly, diffractive effects for non-parallel propagation with respect to the magnetic field lines or multiphoton processes could also profit from the low mass enhancement mechanism.

It is certainly also worthwhile to think about phenomenology beyond this LSW scenario or a related setup employing microwave cavities. As argued, implications of the limit of magnetic (and also electric) fields beyond the critical field strength which are only of academic interest in QED, gain particular importance if the existence of minicharged particles is investigated. Specifically, if minicharged particles with  $\epsilon e B/m^2 \gg 1$  exist, they would strongly effect all directions of photon propagation in a magnetic field. Thus, it seems promising to think about exploiting this feature in diffractive measurements.

In summary, we think that the results presented in this chapter [204] can be the basis for further promising theoretical and experimental investigations on minicharged particles.

---

<sup>9</sup>It is interesting to note that in solenoids or the Helmholtz-coil configuration as, e.g., in studied in Chapt. 4, high, homogeneous field strengths are most easily obtained along the field lines, rendering these field sources also worthwhile to be considered further for this LSW scenario.

*“Was heißt und zu welchem Ende*

# Chapter 7

*studiert man eigentlich Physik?”*

sehr frei nach Friedrich Schiller

## Résumé and concluding remarks

In this thesis we have aimed at advancing two distinct classical probes of the vacuum of quantum electrodynamics from a perspective which focused on experimental applicability: geometry dependencies for Casimir-Polder phenomena as well as manifold optical probes of the vacuum structure. For the latter we have also explored and quantified their potential use in the search for particles beyond the standard model at low energy scales.

As most intuitively visible in the functional integral formulation of QFT, the vacuum state is determined by all possible field configurations of the quantum fields weighted by a complex phase factor which is their classical action functional. As outlined in chapter 2, by restricting these fluctuation modes through the insertion of boundaries or modifying them via their coupling to external fields, the vacuum can be understood and treated effectively as a medium. Testing the properties of this medium in experiments with concurrent theoretical predictions not only teaches us about the behavior of the underlying known field content of the vacuum, but also helps us to investigate the possible existence of as yet undiscovered particles. Remarkably, some major challenges of modern particle physics such as, e.g., the nature of dark matter can thereby be tackled in laboratory experiments.

To correctly describe the global behavior of the altered properties of the vacuum, correlations on all length scales need to be accounted for, as is a main finding of chapter 3. There, we studied quantum forces arising within the vacuum by the deformation of its fluctuation modes through a set of boundaries. In particular, starting with a case-study for scalar fields, we investigated a nontrivial Casimir-Polder setting that ruled out the possibility of a perturbative ordering of length scales. Devising a nonperturbative treatment for this configuration, we parameterized the deviation of the distance power-law behavior from the planar setting through an anomalous dimension. Among other results, we could show that a universality regime exists at larger distances in which the fluctuation modes average over the shape of the corrugation.

We then moved on to investigating the quantum vacuum by deforming its fluctuation modes by a second means, namely through the application of external electromagnetic



fields. In chapter 4, we suggested probing for quantum nonlinearities by combining the strong points of two modern experimental advances: gravitational-wave interferometers attain the capability of most sensitive interferometric measurements at frequency variations of several hundred Hertz. On the other hand, pulsed magnets from high-magnetic field laboratories can provide for the strongest macroscopic field strengths at just about this temporal variation. Thus, we showed that a combination of these two technologies would not only result in a promising tool for the detection of QED nonlinearities but also give unprecedented insights into the allowed parameter space for minicharged particles and axion-like particles.

In chapter 5, we pushed accessible laboratory field-strengths to their limits by modeling an all-laser based setup for the search for the QCD axion and axion-like particles. Utilizing the sensitivity of the probe beam to inhomogeneities of the external beam, we showed that the frequency shift of a probe beam constitutes a useful observable for axion-photon interactions. This effect, being reminiscent of sum- and difference-frequency generation within a medium with nonlinear optical properties, was shown to be attainable in a setup employing only one high-intensity laser. In essence, such a setup was argued to be well suited for searches for axion-like particles and the axion within the  $\mathcal{O}(\text{eV})$ -mass range. In that sense, the rapidly evolving field of high-intensity laser physics could contribute to complement established laboratory axion searches.

In chapter 6, we once more turned to investigating a favorable setup in the quest for minicharged particles. We considered a light-shining-through-walls scenario in a magnetic field which relied on the transition of a light-blocking barrier via virtual particle-antiparticle intermediate states that do not interact with the barrier. We relied on non-perturbative insights into the polarization tensor in an external magnetic field, which were shown to be essential to this study: The IR modes of the photon polarization tensor can lead to a characteristic low-mass enhancement in the transition probability, which favors the tunneling process via virtual particle intermediate states for small masses as compared to many established scenarios. However, we found that only in an external magnetic field of the size of the Compton wavelength of the minicharged particle, this enhancement can in principle be via a power-law dependence on the mass: In a first case study for the  $\perp$  propagation mode of the incoming probe photons, we outlined the details of a feasible experimental setup for this scenario based on established technology. We detailed on the physical mechanisms underlying the observed low-mass enhancement mechanism for fermions and proposed different scenarios which can lead to improved searches for minicharged particles based on our results.

On more general grounds, even as we in principle know well how to describe particle interactions through quantum field theory, a good understanding of many of their implications and the physical mechanisms underlying their most important features is still

lacking, particularly in the nonperturbative regime. Even in the theory that allows for among the most precise predictions and measurements, namely quantum electrodynamics, a qualitative and quantitative understanding of many aspects of phenomena such as Casimir forces and nonlinear light propagation still demands for continued theoretical and experimental effort.

On the other hand, we also have good reason to believe that our picture of particle interactions – the standard model – cannot be the final status of our understanding of particles physics (even when gravity is left aside). From a modern point of view, the standard model is presumably only an effective description accounting for the effective degrees of freedom in a finite range of scales.

For example, enduring questions – which also relate to the topics of this thesis – concern the nature of dark matter, the strong CP problem or the predicted existence of additional “hidden” particles that often come along with proposals for UV completions of the standard model (such as string theories). In a time where modern colliders reach the TeV scale, it seems likely that some insights on the answer to these questions can be obtained in the next decades. On the other hand, colliders are often not the best means to search for hints of new physics if it emerges as weakly interacting particles at lower energy scales such as, e.g., the axion.

Therefore, it seems to be the best way to gain comprehensive insights into physics beyond the standard model by a combined effort of high-energy collider experiments, astrophysical observations and low-energy (optical) probing since they are in several aspects complementary. Of these options, an attractive feature characterizing optical searches seems to be that they often require comparatively little technical and personnel effort.

For this reason, it would be our sincere wish to see some of our theoretical investigations being tested in an experiment.

# Bibliography

- [1] L. H. Ryder, “Quantum Field Theory,” Cambridge, Uk: Univ. Pr. (1985) 443p.
- [2] M. E. Peskin and D. V. Schroeder, “An Introduction to quantum field theory,” Reading, USA: Addison-Wesley (1995) 842 p.
- [3] S. Weinberg, “The Quantum Theory of Fields. Vol. 1: Foundations,” Cambridge, UK: Univ. Pr. (1995) 609 p.
- [4] S. Weinberg, “The Quantum Theory of Fields. Vol. 2: Modern applications,” Cambridge, UK: Univ. Pr. (1996) 489 p.
- [5] P. W. Milonni, “The Quantum vacuum: An Introduction to quantum electrodynamics,” Boston, USA: Academic (1994) 522 p.
- [6] W. Greiner and J. Reinhardt, “Quantum electrodynamics,” Berlin, Germany: Springer (1992) 308 p.
- [7] R. L. Jaffe, “The Casimir effect and the quantum vacuum,” *Phys. Rev. D* **72**, 021301 (2005) [arXiv:hep-th/0503158].
- [8] H.B.G. Casimir, “On The Attraction Between Two Perfectly Conducting Plates,” *Kon. Ned. Akad. Wetensch. Proc.* **51**, 793 (1948).
- [9] H.B.G. Casimir and D. Polder, “The Influence of Retardation on the London-van der Waals Forces,” *Phys. Rev.* **73**, 360 (1948).
- [10] H. Gies, “Introduction to the functional RG and applications to gauge theories,” arXiv:hep-ph/0611146.
- [11] C. S. Fischer, “Infrared properties of QCD from Dyson-Schwinger equations,” *J. Phys. G* **32** (2006) R253 [arXiv:hep-ph/0605173].
- [12] W. Heisenberg and H. Euler, “Folgerungen aus der Diracschen Theorie des Positrons,” *Zeitschr. Phys.* **98** 714 (1936).  
An English translation of the original publication is available on the arXiv: “Consequences Of Dirac’s Theory Of Positrons,” [arXiv:physics/0605038]
- [13] V. Weisskopf, “Über die Elektrodynamik des Vakuums auf Grund der Quantentheorie des Elektrons,” *Kong. Dans. Vid. Selsk. Math-fys. Medd.* **XIV**, 166 (1936).  
English translation in “Early Quantum Electrodynamics: A Source Book,” A. I. Miller, Cambridge, Uk: Univ. Pr. (1994) 265 p.  
and also at  
<http://users.physik.fu-berlin.de/~kleinert/kleinert/?p=histpapers>

- [14] J. S. Schwinger, "On gauge invariance and vacuum polarization," *Phys. Rev.* **82**, 664 (1951).
- [15] G. V. Dunne, "Heisenberg-Euler effective Lagrangians: Basics and extensions," In \*Shifman, M. (ed.) et al.: From fields to strings, vol. 1\* 445-522. [hep-th/0406216].
- [16] T. Erber, "Velocity of Light in a Magnetic Field," *Nature* **190**, 25 (1961).
- [17] R. Baier and P. Breitenlohner, "Photon propagation in external fields," *Act. Phys. Austriaca* **25**, 212 (1967).
- [18] R. Baier and P. Breitenlohner, "The vacuum refraction index in the presence of external fields," *Nuov. Cim. B* **47** 117 (1967).
- [19] S. L. Adler, "Photon splitting and photon dispersion in a strong magnetic field," *Annals Phys.* **67**, 599 (1971).
- [20] L. F. Urrutia, "Vacuum Polarization in Parallel Homogeneous Electric and Magnetic Fields," *Phys. Rev.* **D17**, 1977 (1978).
- [21] E. Brezin and C. Itzykson, "Polarization phenomena in vacuum nonlinear electrodynamics," *Phys. Rev.* **D3**, 618-621 (1971).
- [22] W. Dittrich and H. Gies, "Vacuum birefringence in strong magnetic fields," arXiv:hep-ph/9806417.
- [23] L. Lilje, E. Kako, D. Kostin, A. Matheisen, W. D. Moeller, D. Proch, D. Reschke, K. Saito *et al.*, "Achievement of 35-MV/m in the superconducting nine cell cavities for TESLA," *Nucl. Instrum. Meth.* **A524**, 1-12 (2004). [physics/0401141].
- [24] E. Zavattini *et al.*, "Experimental observation of optical rotation generated in vacuum by a magnetic field," *Phys. Rev. Lett.* **96** (2006) 110406. [hep-ex/0507107].
- [25] E. Zavattini *et al.*, "New PVLAS results and limits on magnetically induced optical rotation and ellipticity in vacuum," *Phys. Rev. D* **77**, 032006 (2008) [arXiv:0706.3419 [hep-ex]].
- [26] M. Bregant *et al.* [PVLAS Collaboration], "Limits on Low Energy Photon-Photon Scattering from an Experiment on Magnetic Vacuum Birefringence," *Phys. Rev. D* **78**, 032006 (2008) [arXiv:0805.3036 [hep-ex]].
- [27] S. J. Chen, H. H. Mei and W. T. Ni, "Q & A experiment to search for vacuum dichroism, pseudoscalar-photon interaction and millicharged fermions," *Mod. Phys. Lett. A* **22**, 2815 (2007).
- [28] R. Battesti *et al.*, "The BMV experiment: a novel apparatus to study the propagation of light in a transverse magnetic field," *Eur. Phys. J. D* **46**, 323 (2008).
- [29] B. Marx *et al.*, "Determination of high-purity polarization state of X-rays," *Opt. Comm.* **284**, 915 (2011).
- [30] T. Heinzl, B. Liesfeld, K. U. Amthor, H. Schworer, R. Sauerbrey and A. Wipf, "On the observation of vacuum birefringence," *Opt. Commun.* **267**, 318 (2006).

- [31] T. Heinzl, D. Seipt, B. Kampfer, “Beam-Shape Effects in Nonlinear Compton and Thomson Scattering,” *Phys. Rev.* **A81**, 022125 (2010). [arXiv:0911.1622 [hep-ph]].
- [32] H. Schworer, B. Liesfeld, H.-P. Schlenvoigt, K.-U. Amthor, R. Sauerbrey, “Thomson-Backscattered X Rays From Laser-Accelerated Electrons,” *Phys. Rev. Lett.* **96**, 014802 (2006).
- [33] A. Ringwald, “Fundamental physics at an x-ray free electron laser,” [hep-ph/0112254].
- [34] H. Gies, “Strong laser fields as a probe for fundamental physics,” *Eur. Phys. J. D* **55**, 311 (2009) [arXiv:0812.0668 [hep-ph]].
- [35] M. Marklund and J. Lundin, “Quantum Vacuum Experiments Using High Intensity Lasers,” *Eur. Phys. J. D* **55**, 319 (2009) [arXiv:0812.3087 [hep-th]].
- [36] T. Heinzl and A. Ilderton, “Exploring high-intensity QED at ELI,” *Eur. Phys. J. D* **55**, 359 (2009) [arXiv:0811.1960 [hep-ph]].
- [37] T. Heinzl and A. Ilderton, “Extreme field physics and QED,” arXiv:0809.3348 [hep-ph].
- [38] B. King, A. Di Piazza, Ch. Keitel, “A matterless double slit,” *Nature Photonics* **4**, 92 (2010).
- [39] G. V. Dunne, “New Strong-Field QED Effects at ELI: Nonperturbative Vacuum Pair Production,” *Eur. Phys. J. D* **55**, 327 (2009) [arXiv:0812.3163 [hep-th]].
- [40] H. Gies, “External Fields as a Probe for Fundamental Physics,” *J. Phys. A* **41**, 164039 (2008). [arXiv:0711.1337 [hep-ph]].
- [41] J. Jaeckel and A. Ringwald, “The Low-Energy Frontier of Particle Physics,” *Ann. Rev. Nucl. Part. Sci.* **60**, 405-437 (2010). [arXiv:1002.0329 [hep-ph]].
- [42] J. Redondo and A. Ringwald, “Light shining through walls,” *Contemporary Physics*, **52**, 3 (2011) [arXiv:1011.3741 [hep-ph]].
- [43] S. G. Karshenboim, “Precision physics of simple atoms: QED tests, nuclear structure and fundamental constants,” *Phys. Rept.* **422**, 1 (2005) [arXiv:hep-ph/0509010].
- [44] B. Holdom, “Two U(1)’s And Epsilon Charge Shifts,” *Phys. Lett. B* **166**, 196 (1986).
- [45] L. B. Okun, “Limits of Electrodynamics: Paraphotons?,” *Sov. Phys. JETP* **56**, 502 (1982) [*Zh. Eksp. Teor. Fiz.* **83**, 892 (1982)].
- [46] S. Abel, J. Santiago, “Constraining the string scale: From Planck to weak and back again,” *J. Phys. G* **G30**, R83-R111 (2004). [hep-ph/0404237].
- [47] S. A. Abel, M. D. Goodsell, J. Jaeckel, V. V. Khoze, A. Ringwald, “Kinetic Mixing of the Photon with Hidden U(1)s in String Phenomenology,” *JHEP* **0807**, 124 (2008). [arXiv:0803.1449 [hep-ph]].
- [48] F. Brümmer, J. Jaeckel, “Minicharges and Magnetic Monopoles,” *Phys. Lett.* **B675**, 360-364 (2009). [arXiv:0902.3615 [hep-ph]].

- [49] F. Brümmer, J. Jaeckel, V. V. Khoze, “Magnetic Mixing: Electric Minicharges from Magnetic Monopoles,” *JHEP* **0906**, 037 (2009). [arXiv:0905.0633 [hep-ph]].
- [50] M. Ahlers, H. Gies, J. Jaeckel and A. Ringwald, “On the particle interpretation of the PVLAS data: Neutral versus charged particles,” *Phys. Rev. D* **75**, 035011 (2007). [arXiv:hep-ph/0612098].
- [51] S. Davidson, S. Hannestad and G. Raffelt, “Updated bounds on milli-charged particles,” *JHEP* **0005**, 003 (2000). [arXiv:hep-ph/0001179].
- [52] W. Dittrich and H. Gies, “Probing the quantum vacuum. Perturbative effective action approach in quantum electrodynamics and its application,” *Springer Tracts Mod. Phys.* **166**, 1 (2000).
- [53] A. Di Piazza, K. Z. Hatsagortsyan and C. H. Keitel, “Light diffraction by a strong standing electromagnetic wave,” *Phys. Rev. Lett.* **97**, 083603 (2006) [arXiv:hep-ph/0602039].
- [54] W. y. Tsai and T. Erber, “The Propagation Of Photons In Homogeneous Magnetic Fields: Index Of Refraction,” *Phys. Rev. D* **12**, 1132, (1975).
- [55] H. Gies, J. Jaeckel and A. Ringwald, “Polarized light propagating in a magnetic field as a probe of millicharged fermions,” *Phys. Rev. Lett.* **97**, 140402 (2006). [arXiv:hep-ph/0607118].
- [56] F. Della Valle, G. Di Domenico, U. Gastaldi, E. Milotti, R. Pengo, G. Ruoso and G. Zavattini, “Towards a direct measurement of vacuum magnetic birefringence: PVLAS achievements,” *Opt. Comm.* , **283**, 21 (2010).
- [57] B. Döbrich and F. Karbstein, in preparation (2011).
- [58] M. Ahlers, H. Gies, J. Jaeckel, J. Redondo and A. Ringwald, “Laser experiments explore the hidden sector,” *Phys. Rev. D* **77**, 095001 (2008) [arXiv:0711.4991 [hep-ph]].
- [59] S. Weinberg, “A New Light Boson?,” *Phys. Rev. Lett.* **40**, 223 (1978).
- [60] F. Wilczek, “Problem Of Strong P And T Invariance In The Presence Of Instantons,” *Phys. Rev. Lett.* **40**, 279 (1978).
- [61] R. D. Peccei and H. R. Quinn, “Constraints Imposed By CP Conservation In The Presence Of Instantons,” *Phys. Rev. D* **16**, 1791 (1977).
- [62] R. D. Peccei and H. R. Quinn, “CP Conservation In The Presence Of Instantons,” *Phys. Rev. Lett.* **38**, 1440 (1977).
- [63] G. Gabadadze and M. Shifman, “QCD vacuum and axions: What’s happening?,” *Int. J. Mod. Phys. A* **17**, 3689 (2002) [arXiv:hep-ph/0206123].
- [64] J. Jaeckel, “Axions, their relatives and prospects for the future,” *J. Phys. Conf. Ser.* **65**, 012008 (2007). [hep-ph/0702060 [HEP-PH]].

- [65] C. A. Baker, D. D. Doyle, P. Geltenbort, K. Green, M. G. D. van der Grinten, P. G. Harris, P. Iaydjiev, S. N. Ivanov *et al.*, “An Improved experimental limit on the electric dipole moment of the neutron,” *Phys. Rev. Lett.* **97**, 131801 (2006). [hep-ex/0602020].
- [66] J. E. Kim, “Light Pseudoscalars, Particle Physics and Cosmology,” *Phys. Rept.* **150**, 1-177 (1987).
- [67] E. Masso and R. Toldra, “On a Light Spinless Particle Coupled to Photons,” *Phys. Rev. D* **52**, 1755 (1995) [arXiv:hep-ph/9503293].
- [68] L. Maiani, R. Petronzio and E. Zavattini, “Effects of nearly massless, spin zero particles on light propagation in a magnetic field,” *Phys. Lett. B* **175**, 359 (1986).
- [69] G. Raffelt and L. Stodolsky, “Mixing of the photon with low mass particles,” *Phys. Rev. D* **37**, 1237 (1988).
- [70] H. Primakoff, “Photo-Production of Neutral Mesons in Nuclear Electric Fields and the Mean Life of the Neutral Meson,” *Phys. Rev.* **81**, 899 (1951).
- [71] R. Cameron *et al.*, “Search for nearly massless, weakly coupled particles by optical techniques,” *Phys. Rev. D* **47** (1993) 3707.
- [72] P. Sikivie, “Experimental tests of the invisible axion,” *Phys. Rev. Lett.* **51** (1983) 1415 [Erratum-ibid. **52** (1984) 695].
- [73] A. A. Anselm, “Arion  $\leftrightarrow$  photon oscillations in a steady magnetic field. (in russian),” *Yad. Fiz.* **42** (1985) 1480.
- [74] M. Gasperini, “Axion Production by Electromagnetic Fields,” *Phys. Rev. Lett.* **59** (1987) 396.
- [75] K. Van Bibber, N. R. Dagdeviren, S. E. Koonin, A. Kerman, H. N. Nelson, “Proposed experiment to produce and detect light pseudoscalars,” *Phys. Rev. Lett.* **59**, 759-762 (1987).
- [76] M. Ahlers, J. Jaeckel, A. Ringwald, “The Discovery Potential of Laser Polarization Experiments,” *Phys. Rev.* **D79**, 075017 (2009). [arXiv:0812.3150 [hep-ph]].
- [77] K. Ehret *et al.*, “New ALPS Results on Hidden-Sector Lightweights,” *Phys. Lett. B* **689**, 149 (2010) [arXiv:1004.1313 [hep-ex]].
- [78] P. Arias, J. Jaeckel, J. Redondo and A. Ringwald, “Optimizing Light-Shining-through-a-Wall Experiments for Axion and other WISP Searches,” *Phys. Rev.* **D82**, 115018 (2010). [arXiv:1009.4875 [hep-ph]].
- [79] K. Ehret *et al.* [ALPS collaboration], “Resonant laser power build-up in ALPS - a ‘light-shining-through-walls’ experiment -,” *Nucl. Instrum. Meth. A* **612**, 83 (2009) [arXiv:0905.4159 [physics.ins-det]].
- [80] A. V. Afanasev, O. K. Baker and K. W. McFarlane, “Production and detection of very light spin-zero bosons at optical frequencies,” arXiv:hep-ph/0605250;

- [81] A. Afanasev *et al.*, “New Experimental limit on Optical Photon Coupling to Neutral, Scalar Bosons,” *Phys. Rev. Lett.* **101**, 120401 (2008) [arXiv:0806.2631 [hep-ex]].
- [82] A. S. Chou *et al.*, “Search for axion-like particles using a variable baseline photon regeneration technique,” *Phys. Rev. Lett.* **100**, 080402 (2008). [arXiv:0710.3783 [hep-ex]].
- [83] J. H. Steffen and A. Upadhye, “The GammeV suite of experimental searches for axion-like particles,” *Mod. Phys. Lett. A* **24**, 2053 (2009) [arXiv:0908.1529 [hep-ex]].
- [84] P. Pagnat *et al.* [OSQAR Collaboration], “First results from the OSQAR photon regeneration experiment: No light shining through a wall,” *Phys. Rev.* **D78**, 092003 (2008). [arXiv:0712.3362 [hep-ex]].
- [85] C. Robilliard *et al.*, “No light shining through a wall,” *Phys. Rev. Lett.* **99**, 190403 (2007). [arXiv:0707.1296 [hep-ex]].
- [86] U. Kotz, A. Ringwald, T. Tschentscher, “Production and Detection of Axion-Like Particles at the VUV-FEL: Letter of Intent,” [hep-ex/0606058].
- [87] R. Rabadan, A. Ringwald, K. Sigurdson, “Photon regeneration from pseudoscalars at X-ray laser facilities,” *Phys. Rev. Lett.* **96**, 110407 (2006). [hep-ph/0511103].
- [88] R. Battesti, M. Fouche, C. Detlefs, T. Roth, P. Berceau, F. Duc, P. Frings, G. L. J. A. Rikken and C. Rizzo “A Photon Regeneration Experiment for Axionlike Particle Search using X-rays,” *Phys. Rev. Lett.* **105**, 250405 (2010). [arXiv:1008.2672 [hep-ex]].
- [89] F. Hoogeveen, “Terrestrial axion production and detection using RF cavities,” *Phys. Lett.* **B288**, 195-200 (1992).
- [90] J. Jaeckel and A. Ringwald, “A Cavity Experiment to Search for Hidden Sector Photons,” *Phys. Lett. B* **659**, 509 (2008) [arXiv:0707.2063 [hep-ph]].
- [91] F. Hoogeveen, T. Ziegenhagen, “Production and detection of light bosons using optical resonators,” *Nucl. Phys.* **B358**, 3-26 (1991).
- [92] P. Sikivie, D. B. Tanner and K. van Bibber, “Resonantly enhanced axion - photon regeneration,” *Phys. Rev. Lett.* **98**, 172002 (2007) [arXiv:hep-ph/0701198].
- [93] J. G. Hartnett, J. Jaeckel, R. G. Povey, M. E. Tobar, “Resonant Regeneration in the Sub-Quantum Regime: A Demonstration of fractional quantum interference,” *Phys. Lett.* **B698**, 346-352 (2011). [arXiv:1101.4089 [quant-ph]].
- [94] S. L. Adler, J. Gamboa, F. Mendez and J. Lopez-Sarrion, “Axions and ‘Light Shining Through a Wall’: A Detailed Theoretical Analysis,” *Annals Phys.* **323**, 2851 (2008) [arXiv:0801.4739 [hep-ph]].
- [95] M. Ahlers, H. Gies, J. Jaeckel, J. Redondo and A. Ringwald, “Light from the Hidden Sector,” *Phys. Rev. D* **76**, 115005 (2007) [arXiv:0706.2836 [hep-ph]].
- [96] H. Gies and J. Jaeckel, “Tunneling of the 3rd kind,” *JHEP* **0908**, 063 (2009). [arXiv:0904.0609 [hep-ph]].



- [97] S. Moriyama, M. Minowa, T. Namba *et al.*, “Direct search for solar axions by using strong magnetic field and x-ray detectors,” *Phys. Lett.* **B434**, 147 (1998). [hep-ex/9805026].
- [98] D. M. Lazarus, G. C. Smith, R. Cameron *et al.*, “A Search for solar axions,” *Phys. Rev. Lett.* **69**, 2333-2336 (1992).
- [99] Y. Inoue, Y. Akimoto, R. Ohta *et al.*, “Search for solar axions with mass around 1 eV using coherent conversion of axions into photons,” *Phys. Lett.* **B668**, 93-97 (2008). [arXiv:0806.2230 [astro-ph]].
- [100] K. Zioutas *et al.* [ CAST Collaboration ], “First results from the CERN Axion Solar Telescope (CAST),” *Phys. Rev. Lett.* **94**, 121301 (2005). [hep-ex/0411033].
- [101] S. Andriamonje *et al.* [ CAST Collaboration ], “An Improved limit on the axion-photon coupling from the CAST experiment,” *JCAP* **0704**, 010 (2007). [hep-ex/0702006 [HEP-EX]].
- [102] E. Arik *et al.* [CAST Collaboration], “Probing eV-scale axions with CAST,” *JCAP* **0902**, 008 (2009) [arXiv:0810.4482 [hep-ex]].
- [103] G. G. Raffelt, “Stars as laboratories for fundamental physics: The astrophysics of neutrinos, axions, and other weakly interacting particles,” Chicago, USA: Univ. Pr. (1996) 664 p.
- [104] A. Melchiorri, A. Polosa and A. Strumia, “New bounds on millicharged particles from cosmology,” *Phys. Lett. B* **650**, 416 (2007). [arXiv:hep-ph/0703144].
- [105] M. Ahlers, L. A. Anchordoqui, M. C. Gonzalez-Garcia, “Quantum Decoherence of Photons in the Presence of Hidden U(1)s,” *Phys. Rev.* **D81**, 085025 (2010). [arXiv:0910.5483 [hep-ph]].
- [106] C. Burrage, J. Jaeckel, J. Redondo, A. Ringwald, “Late time CMB anisotropies constrain mini-charged particles,” *JCAP* **0911**, 002 (2009). [arXiv:0909.0649 [astro-ph.CO]].
- [107] J. Jaeckel, E. Masso, J. Redondo, A. Ringwald and F. Takahashi, “The Need for Purely Laboratory-Based Axion-Like Particle Searches,” *Phys. Rev. D* **75**, 013004 (2007) [arXiv:hep-ph/0610203].
- [108] E. Masso, J. Redondo, “Compatibility of CAST search with axion-like interpretation of PVLAS results,” *Phys. Rev. Lett.* **97**, 151802 (2006). [hep-ph/0606163].
- [109] J. Redondo, “Can the PVLAS particle be compatible with the astrophysical bounds?,” PhD thesis, University of Barcelona (2007) [arXiv:0807.4329 [hep-ph]].
- [110] A. Lindner, (ed.), J. Redondo, (ed.), A. Ringwald, (ed.), “Axions, WIMPs and WISPs. Proceedings, 4th Patras Workshop, PATRAS08, Hamburg, Germany, June 18-21, 2008,”
- [111] J. Jackel, (ed.), A. Lindner, (ed.), J. Redondo, (ed.), “Axions, WIMPs and WISPs. Proceedings, 5th Patras Workshop, PATRAS 2009, Durham, UK, July 13-17, 2009,”

- [112] L. Baudis, M. Schumann “Axions, WIMPs and WISPs. Proceedings, 6th Patras Workshop, PATRAS 2009, Zurich, Switzerland, July 5-9, 2010,”
- [113] L. D. Duffy, P. Sikivie, D. B. Tanner *et al.*, “A high resolution search for dark-matter axions,” *Phys. Rev.* **D74**, 012006 (2006). [astro-ph/0603108].
- [114] J. D. Bekenstein, “The Modified Newtonian Dynamics: MOND and its implications for new physics,” [astro-ph/0701848 [ASTRO-PH]].
- [115] D. Clowe, M. Bradac, A. H. Gonzalez, M. Markevitch, S. W. Randall, C. Jones, D. Zaritsky, “A direct empirical proof of the existence of dark matter,” *Astrophys. J.* **648**, L109-L113 (2006). [astro-ph/0608407].
- [116] J. E. Moody and F. Wilczek, “New Macroscopic Forces?,” *Phys. Rev.* **D30**, 130 (1984).
- [117] S. A. Hoedl, F. Fleischer, E. G. Adelberger, B. R. Heckel, “Improved Constraints on an Axion-Mediated Force,” *Phys. Rev. Lett.* **106**, 041801 (2011).
- [118] J. Jaeckel and S. Roy, “Spectroscopy as a test of Coulomb’s law: A Probe of the hidden sector,” *Phys. Rev.* **D82**, 125020 (2010). [arXiv:1008.3536 [hep-ph]].
- [119] J. Jaeckel, “Probing Minicharged Particles with Tests of Coulomb’s Law,” *Phys. Rev. Lett.* **103**, 080402 (2009) [arXiv:0904.1547 [hep-ph]].
- [120] H. Gies, J. Jaeckel and A. Ringwald, “Accelerator Cavities as a Probe of Millicharged Particles,” *Europhys. Lett.* **76**, 794 (2006) [arXiv:hep-ph/0608238].
- [121] R. G. Povey, J. G. Hartnett, M. E. Tobar, “Microwave cavity hidden sector photon threshold crossing,” [arXiv:1105.6169 [physics.ins-det]].
- [122] R. S. Decca, D. Lopez, E. Fischbach, G. L. Klimchitskaya, D. E. Krause and V. M. Mostepanenko, “Tests of new physics from precise measurements of the Casimir pressure between two gold-coated plates,” *Phys. Rev. D* **75**, 077101 (2007) [arXiv:hep-ph/0703290].
- [123] M. Bordag, U. Mohideen and V. M. Mostepanenko, “New developments in the Casimir effect,” *Phys. Rept.* **353**, 1 (2001) [arXiv:quant-ph/0106045].
- [124] H. B. Chan, Y. Bao, J. Zou, R. A. Cirelli, F. Klemens, W. M. Mansfield, C. S. Pai, “Demonstrating the strong geometry dependence of the Casimir force on a surface with deep, nanoscale corrugations,” *Int. J. Mod. Phys.* **A25**, 2212-2222 (2010).
- [125] J. Blocki, J. Randrup, W. J. Swiatecki, C. F. Tsang, “Proximity forces,” *Annals Phys.* **105**, 427-462 (1977).
- [126] K. A. Milton, “Resource Letter VWCPF-1: Van der Waals and Casimir-Polder forces,” [arXiv:1101.2238 [cond-mat.other]].
- [127] M. DeKieviet, D. Dubbers, C. Schmidt, D. Scholz and U. Spinola, “<sup>3</sup>He Spin Echo: New Atomic Beam Technique for Probing phenomena in the neV Range,” *Phys. Rev. Lett.* **75**, 1919 (1995).

- [128] V. Druzhina and M. DeKieviet, “Experimental Observation of Quantum Reflection far from Threshold,” *Phys. Rev. Lett.* **91**, 193202 (2003).
- [129] M. Bordag, D. Robaschik and E. Wieczorek, “Quantum Field Theoretic Treatment Of The Casimir Effect. Quantization Procedure And Perturbation Theory In Covariant Gauge,” *Annals Phys.* **165**, 192 (1985).
- [130] T. Emig, A. Hanke and M. Kardar, “Probing the Strong Boundary Shape Dependence of the Casimir Force,” *Phys. Rev. Lett.* **87**, 260402 (2001). [arXiv:cond-mat/0106028].
- [131] F. Glowna, Diploma thesis, Friedrich-Schiller University Jena (2010).
- [132] B. Döbrich, Diploma thesis, Ruprecht-Karls University Heidelberg (2008).
- [133] T. Emig, N. Graham, R. L. Jaffe, M. Kardar, “Casimir forces between arbitrary compact objects,” *Phys. Rev. Lett.* **99**, 170403 (2007). [arXiv:0707.1862 [cond-mat.stat-mech]].
- [134] A. Bulgac, P. Magierski and A. Wirzba, “Scalar Casimir effect between Dirichlet spheres or a plate and a sphere,” *Phys. Rev. D* **73**, 025007 (2006) [arXiv:hep-th/0511056].
- [135] H. Gies and K. Klingmüller, “Casimir effect for curved geometries: PFA validity limits,” *Phys. Rev. Lett.* **96**, 220401 (2006) [arXiv:quant-ph/0601094].
- [136] T. Emig, “Fluctuation-induced quantum interactions between compact objects and a plane mirror,” *J. Stat. Mech.* **0804**, P04007 (2008).
- [137] P. A. Maia Neto, A. Lambrecht, and S. Reynaud, “Casimir energy between a plane and a sphere in electromagnetic vacuum,” *Phys. Rev. A* **78**, 012115 (2008).
- [138] B. Döbrich, M. DeKieviet and H. Gies, “Scalar Casimir-Polder Forces For Uniaxial Corrugations,” *Phys. Rev. D* **78**, 125022 (2008).
- [139] B. Döbrich, H. Gies and M. DeKieviet, “Nonperturbative access to Casimir-Polder forces,” arXiv:0910.5889 [quant-ph].
- [140] A. M. Contreras-Reyes, R. Guerout, P. A. M. Neto, D. A. R. Dalvit, A. Lambrecht, S. Reynaud, “Casimir-Polder interaction between an atom and a dielectric grating,” *Phys. Rev.* **A82**, 052517 (2010). [arXiv:1010.0170 [quant-ph]].
- [141] S. Reynaud, A. Canaguier-Durand, R. Messina, A. Lambrecht, P. A. M. Neto, “The Scattering Approach to the Casimir Force,” *Int. J. Mod. Phys.* **A25**, 2201-2211 (2010). [arXiv:1001.3375 [quant-ph]].
- [142] S. J. Rahi, T. Emig and R. L. Jaffe, “Geometry and material effects in Casimir physics: Scattering theory,” arXiv:1007.4355 [quant-ph].
- [143] H. Gies, K. Langfeld and L. Moyaerts, “Casimir effect on the worldline,” *JHEP* **0306**, 018 (2003). [arXiv:hep-th/0303264].

- [144] U. Warring, V. Druzhinina, L. Arntzen, T. Stöferle and M. DeKieviet, in preparation.
- [145] B.S. Zhao, H.C. Schewe, G. Meijer and W. Schöllkopf, “Coherent Reflection of He Atom Beams from Rough Surfaces at Grazing Incidence,” *Phys. Rev. Lett.* **105**, 133203 (2010).
- [146] D. Boer and J. W. Van Holten, “Exploring the QED vacuum with laser interferometers,” arXiv:hep-ph/0204207.
- [147] V. I. Denisov, I. V. Krivchenkov and N. V. Kravtsov, “Experiment for measuring the post Maxwellian parameters of nonlinear electrodynamics of vacuum with laser interferometer techniques,” *Phys. Rev. D* **69**, 066008 (2004).
- [148] G. Zavattini and E. Calloni, “Probing For New Physics and Detecting non linear vacuum QED effects using gravitational wave interferometer antennas,” *Eur. Phys. J. C* **62**, 459 (2009) [arXiv:0812.0345 [physics.ins-det]].
- [149] P. R. Saulson, “Fundamentals of interferometric gravitational wave detectors,” Singapore, Singapore: World Scientific (1994) 299 p.
- [150] K. S. Thorne, “Gravitational waves,” arXiv:gr-qc/9506086.
- [151] D. G. Blair, (ed.), “The Detection of gravitational waves,” Cambridge, UK: Univ. Pr. (1991) 481 p.
- [152] <https://www.advancedligo.mit.edu>
- [153] <http://www.geo600.uni-hannover.de>
- [154] D. Shoemaker, private communication.
- [155] J. R. Smith [ LIGO Scientific Collaboration ], “The Path to the enhanced and advanced LIGO gravitational-wave detectors,” *Class. Quant. Grav.* **26**, 114013 (2009). [arXiv:0902.0381 [gr-qc]].
- [156] B. F. Schutz, “The Detection Of Gravitational Waves,” in *Proc. Les Houches School on Astrophysical Sources of Gravitational Radiation*, Cambridge UP (1995).
- [157] K. S. Thorne, “Gravitational Radiation,” In \*Hawking, S.W. (ed.), Israel, W. (ed.): Three hundred years of gravitation\*, 330-458. (see Book Index).
- [158] J. Wosnitza, *et al.*, “Recent Developments at the Dresden High Magnetic Field Laboratory,” in 2006 IEEE International Conference on Megagauss Magnetic Field Generation and Related Topics, G.F. Kiuttu, *et al.* (ed.) 197 (2008).
- [159] J. Wosnitza, *et al.* “Science at the Dresden High Magnetic Field Laboratory,” Volume 1003, pp. 311-315 AIP Conference Proceedings (2008).
- [160] J. Wosnitza, *et al.*, “Dresden Pulsed Magnetic Field Facility,” *J. Magn. Magn. Mat.* **310**, 2728 (2007).
- [161] T. Hermannsdörfer, private communication.

- [162] B. Döbrich and H. Gies, “Interferometry of light propagation in pulsed fields,” *Europhys. Lett.* **87**, 21002 (2009) [arXiv:0904.0216 [hep-ph]].
- [163] B. Döbrich and H. Gies, “Interferometry in pulsed fields,” arXiv:0910.5692 [hep-ph].
- [164] <http://www.hzdr.de>
- [165] D. Strickland and G. Mourou, “Compression of amplified chirped optical pulses,” *Opt. Commun.* **56**, 219 (1985).
- [166] <http://www.extreme-light-infrastructure.eu>
- [167] M. C. Huang, P. Sikivie, “The Structure Of Axionic Domain Walls,” *Phys. Rev.* **D32**, 1560 (1985).
- [168] F. Wilczek, “Two Applications Of Axion Electrodynamics,” *Phys. Rev. Lett.* **58**, 1799 (1987).
- [169] K. -M. Lee, “Topological Mass Terms on Axion Domain Walls,” *Phys. Rev.* **D35**, 3286 (1987).
- [170] X. -L. Qi, T. Hughes, S. -C. Zhang, “Topological Field Theory of Time-Reversal Invariant Insulators,” *Phys. Rev. B* **78**, 195424 (2008) [arXiv:0802.3537 [cond-mat.mes-hall]].
- [171] A. M. Essin, J. E. Moore, D. Vanderbilt, “Magnetoelectric polarizability and axion electrodynamics in crystalline insulators,” *Phys. Rev. Lett.* **102**, 146805 (2009) [arXiv:0810.2998 [cond-mat.mes-hall]].
- [172] L.W. Davis, “Theory of electromagnetic beams,” *Phys. Rev. A* **19**, 1177-1179 (1979).
- [173] J. P. Barton and D. R. Alexander, “Fifth-order corrected electromagnetic field components for a fundamental Gaussian beam,” *J. Appl. Phys.* **66**, 2800 (1989).
- [174] K. T. McDonald, “Gaussian Laser Beams and Particle Acceleration,” <http://physics.princeton.edu/~mcdonald/accel/gaussian.pdf>
- [175] L. G. Gouy, “Sur une propriete nouvelle des ondes lumineuses,” *C.R. Acad. Sci. Paris* **110**, 1251 (1890).
- [176] S. Feng and H. Winful, “Physical origin of the Gouy phase shift,” *Opt. Lett.* **26**, 485-487 (2001).
- [177] I. S. Gradshteyn and I. M. Ryzhik, “Table of Integrals, Series, and Products,” Fifth Edition, Academic Press, UK (1994).
- [178] R. W. Boyd, “Nonlinear Optics,” Third Edition, Academic Press, (2008).
- [179] P. A. Franken, A. E. Hill, C. W. Peters and G. Weinreich “Generation of optical harmonics,” *Phys. Rev. Lett.* **7**, 118-119 (1961).  
(It is amusing to note that the “proof” for the second harmonic has been removed by the copy editor.)

- [180] M. Hornung, R. Bödefeld, M. Siebold, A. Kessler, M. Schnepf, R. Wachs, A. Sävert, S. Podleska, S. Keppler, J. Hein and M.C. Kaluza, “Temporal pulse control of a multi-10 TW diode-pumped Yb:Glass laser” *Appl. Phys. B* **101**, 93-102 (2010).
- [181] A.E. Siegman, “Lasers,” University Science books, Mill Valey U.S.A. (1986).
- [182] <http://www.lightcon.com/index.php?topas-products>
- [183] B. Döbrich and H. Gies, “Axion-like-particle search with high-intensity lasers,” *JHEP* **1010**, 022 (2010) [arXiv:1006.5579 [hep-ph]].
- [184] B. Döbrich and H. Gies, “High-Intensity Probes of Axion-Like Particles,” arXiv:1010.6161 [hep-ph].
- [185] K. Homma, D. Habs, T. Tajima, “Probing the semi-macroscopic vacuum by higher-harmonic generation under focused intense laser fields,” [arXiv:1103.1748 [physics.optics]].
- [186] K. Homma, D. Habs and T. Tajima, “Probing semi-macroscopic vacua by high fields of lasers,” arXiv:1006.4533 [quant-ph].
- [187] D. Tommasini, A. Ferrando, H. Michinel and M. Seco, “Precision tests of QED and non-standard models by searching photon-photon scattering in vacuum with high power lasers,” *JHEP* **0911**, 043 (2009) [arXiv:0909.4663 [hep-ph]].
- [188] M. Kaluza, private communication.
- [189] D. Tommasini, H. Michinel, “Light by light diffraction in vacuum,” *Phys. Rev.* **A82**, 011803 (2010). [arXiv:1003.5932 [hep-ph]].
- [190] E. I. Guendelman, I. Shilon, G. Cantatore and K. Zioutas, “Photon Production From The Scattering of Axions Out of a Solenoidal Magnetic Field,” [arXiv:0906.2537 [hep-ph]].
- [191] D. B. Melrose, R. J. Stoneham, “Vacuum Polarization and Photon Propagation in a Magnetic Field,” *Nuovo Cim.* **A32**, 435-447 (1976).
- [192] A. E. Shabad, “Photon propagation in supercritical magnetic field,” arXiv:hep-th/0307214.
- [193] W. -Y. Tsai, T. Erber, “The Propagation of Photons in Homogeneous Magnetic Fields. 2. Dispersion Relations and Propagation Modes,” *Acta Phys. Austriaca* **45**, 245-254 (1976).
- [194] R. A. Cover, G. Kalman, “Longitudinal, massive photon in an external magnetic field,” *Phys. Rev. Lett.* **33**, 1113-1116 (1974).
- [195] P. Bakshi, G. Kalman, R. A. Cover, “Electromagnetic Response in Strong Magnetic Fields. General Formalism and Vacuum Polarization for Parallel Propagation,” *Phys. Rev.* **D14**, 2532-2542 (1976).
- [196] N. Neitz, Diploma thesis, Friedrich-Schiller University Jena (2010).

- [197] G. V. Dunne, “Perturbative - nonperturbative connection in quantum mechanics and field theory,” [hep-th/0207046].
- [198] G. V. Dunne and C. Schubert, “Bernoulli number identities from quantum field theory,” [math/0406610 [math-nt]].
- [199] A. E. Shabad, “Cyclotronic resonance in the vacuum polarization,” *Lett. Nuovo Cim.* **3S2**, 457 (1972).
- [200] A. E. Shabad, “Photon Dispersion in a Strong Magnetic Field,” *Annals Phys.* **90**, 166 (1975).
- [201] N. S. Witte, “Polarization of the magnetized and spinor vacua,” *J. Phys.A:Math.Gen.* **23**, 5257 (1990).
- [202] A. E. Shabad and V. V. Usov, “Propagation of  $\gamma$ -Radiation in Strong Magnetic Fields of Pulsars,” *Astrophysics and Space Science* **102**, 2 (1984).
- [203] Ernst-Axel Knabbe, private communication.
- [204] B. Döbrich, H. Gies, N. Neitz and F. Karbstein, in preparation (2011).
- [205] Lecture on Functional Determinants in Quantum Field Theory given by Gerald Dunne at the 14th WE Heraeus Saalburg summer school in Wolfersdorf (2008).  
Lecture notes taken by Babette Döbrich and exercises with solutions by Oliver Schlotterer (2009). Available at  
<http://www.itp.uni-hannover.de/~lechtenf/Events/Lectures/dunne.pdf>
- [206] C. Itzykson and J.-B. Zuber, “Quantum field theory,” McGraw-Hill, New York, 1980.
- [207] U. D. Jentschura, H. Gies, S. R. Valluri, D. R. Lamm and E. J. Weniger, “QED effective action revisited,” *Can. J. Phys.* **80** (2002) 267 [arXiv:hep-th/0107135].
- [208] F. Sauter, “Über das Verhalten eines Elektrons im homogenen elektrischen Feld nach der relativistischen Theorie Diracs,” *Z. phys.* **69**, 742 (1931).  
English translation, e.g., at  
<http://users.physik.fu-berlin.de/~kleinert/kleinert/?p=histpapers>
- [209] E. Brezin, C. Itzykson, “Pair production in vacuum by an alternating field,” *Phys. Rev.* **D2**, 1191-1199 (1970).
- [210] D. L. Burke, R. C. Field, G. Horton-Smith, T. Kotseroglou, J. E. Spencer, D. Walz, S. C. Berridge, W. M. Bugg *et al.*, “Positron production in multi - photon light by light scattering,” *Phys. Rev. Lett.* **79**, 1626-1629 (1997).
- [211] H. Hu, C. Müller, C. H. Keitel, “Complete QED theory of multiphoton trident pair production in strong laser fields,” *Phys. Rev. Lett.* **105**, 080401 (2010). [arXiv:1002.2596 [physics.atom-ph]].
- [212] G. V. Dunne, “The search for the Schwinger effect: Nonperturbative vacuum pair production,” *Int. J. Mod. Phys.* **A25**, 2373-2381 (2010).

- [213] W. Dittrich, M. Reuter, “Effective Lagrangians In Quantum Electrodynamics,” Lect. Notes Phys. **220**, 1-244 (1985).
- [214] H. Euler, B. Kockel, “Über die Streuung von Licht an Licht nach der Diracschen Theorie,” Naturwiss. **23**, 246 (1935).
- [215] R. Karplus and M. Neuman, “The scattering of light by light,” Phys. Rev. **83**, 776-784 (1951).
- [216] Z. Bialynicka-Birula, I. Bialynicki-Birula, “Nonlinear effects in Quantum Electrodynamics. Photon propagation and photon splitting in an external field,” Phys. Rev. **D2**, 2341-2345 (1970).
- [217] S. L. Adler and C. Schubert, “Photon splitting in a strong magnetic field: Recalculation and comparison with previous calculations,” Phys. Rev. Lett. **77**, 1695 (1996) [arXiv:hep-th/9605035].
- [218] L. Meitner and H. Kösters “Über die Streuung kurzweilliger  $\gamma$ -Strahlen,” Z. Phys. **84**, 137 (1933).
- [219] R. R. Wilson, “Scattering of 1.33 Mev Gamma-Rays by an Electric Field,” Phys. Rev. **90**, 720-721 (1953).
- [220] S. Z. Akhmadaliev *et al.*, “Delbruck scattering at energies of 140-450 MeV,” Phys. Rev. C **58**, 2844 (1998).
- [221] S. Z. Akhmadaliev, G. Y. Kezerashvili, S. G. Klimenko, R. N. Lee, V. M. Malyshev, A. L. Maslennikov, A. M. Milov, A. I. Milstein *et al.*, “Experimental investigation of high-energy photon splitting in atomic fields,” Phys. Rev. Lett. **89**, 061802 (2002). [hep-ex/0111084].
- [222] C. Schubert, “Vacuum polarization tensors in constant electromagnetic fields. Part 1,” Nucl. Phys. B **585**, 407 (2000) [arXiv:hep-ph/0001288].
- [223] F. J. Dyson, “Divergence of perturbation theory in quantum electrodynamics,” Phys. Rev. **85**, 631-632 (1952).
- [224] H. J. Silverstone “High-order perturbation theory and its application to atoms in strong fields,” in Atoms in Strong Fields, edited by C. A. Nicolaides, C. W. Clark, and M. H. Nayfeh, (Plenum, New York, 1990), pp. 295-307.



# Appendix A

## Units, conventions and some useful numbers

As it is common, we have set  $\hbar = c = 1$  throughout the thesis. In addition, we employ Heaviside-Lorentz units, avoiding the roaming of factors  $1/4\pi$  in Maxwell's equations. The fine-structure constant is given as  $\alpha = e^2/4\pi$ . Although these choices simplify calculations, we must retranslate our results to the system of SI-units to give meaningful phenomenological estimates.

To make this connection, the following conversion table of selected measures is helpful:

length	1 m	$5.07 \times 10^6 \text{ eV}^{-1}$
time	1 s	$1.52 \times 10^{15} \text{ eV}^{-1}$
magnetic field strength	1 T	195.5 $\text{eV}^2$
energy	1 J	$6.24 \times 10^{18} \text{ eV}$
intensity	1 $\text{W}/\text{cm}^2$	$1.59 \times 10^{-6} \text{ eV}^4$
power	1 W	$4.11 \times 10^3 \text{ eV}^2$
mass	1 kg	$5.61 \times 10^{35} \text{ eV}$

As follows, the critical strengths of magnetic fields  $B_{\text{crit}} \simeq 4 \times 10^9 \text{T}$  and electric fields  $E_{\text{crit}} = 1 \times 10^{18} \text{V}/\text{m}$  in quantum electrodynamics unite at a value of  $m^2/e \simeq 9 \times 10^{11} \text{eV}^2$  in natural units. Accordingly, the critical intensity to be attained lies at  $I_{\text{crit}} \simeq 5 \times 10^{29} \text{W}/\text{cm}^2$ , which yet constitutes a very ambitious aim in the face of current technology, see, e.g., Chapt. 5.

To each particle or particle loop it is often useful to assign a length scale corresponding to its Compton wavelength. For electrons and positrons, as  $m \simeq 511 \text{keV}$ , this extent is  $\simeq 2 \times 10^{-6} \text{eV}^{-1} \hat{=} 4 \times 10^{-13} \text{m}$ . In addition, we associate a temporal extent of  $\simeq 1 \times 10^{-21} \text{s}$  with quantum fluctuations of these particles.

Except for Chapt. 6 and the associated App. C, where we have employed  $g = \text{diag}(-1, +1, +1, +1)$  as a metric in order to preserve easy comparability to established

literature, we have  $g = \text{diag}(+1, -1, -1, -1)$  as metric of our choice. The gamma-matrices obey the anti-commutation relation  $\{\gamma^\mu, \gamma^\nu\} = 2g^{\mu\nu}$  and the field strength tensor  $F^{\mu\nu}$  reads

$$F^{\mu\nu} = \begin{pmatrix} 0 & -E_x & -E_y & -E_z \\ E_x & 0 & -B_z & B_y \\ E_y & B_z & 0 & -B_x \\ E_z & -B_y & B_x & 0 \end{pmatrix}, \quad (\text{A.1})$$

while its dual is defined as

$$\tilde{F}^{\mu\nu} = \frac{1}{2} \epsilon^{\mu\nu\alpha\beta} F_{\alpha\beta}, \quad (\text{A.2})$$

where  $\epsilon^{\mu\nu\alpha\beta}$  is totally antisymmetric and we choose  $\epsilon^{0123} = 1$ .

A common choice of scalar and pseudoscalar Lorentz-invariants reads<sup>1</sup>

$$F_{\mu\nu} F^{\mu\nu} = -2(\vec{E}^2 - \vec{B}^2) = -2(a^2 - b^2) = 4\mathcal{F}, \quad (\text{A.3})$$

$$F_{\mu\nu} \tilde{F}^{\mu\nu} = -4\vec{E} \cdot \vec{B} = -4a \cdot b = 4\mathcal{G}, \quad (\text{A.4})$$

such that the so-called secular invariants read

$$a = \sqrt{\sqrt{\mathcal{F}^2 + \mathcal{G}^2} - \mathcal{F}}, \quad (\text{A.5})$$

$$b = \sqrt{\sqrt{\mathcal{F}^2 + \mathcal{G}^2} + \mathcal{F}}. \quad (\text{A.6})$$

The term ‘secular invariant’ comes about as  $\pm b$  and  $\pm ia$  are eigenvalues of the constant ‘matrix’  $F_{\mu\nu}$ . If  $\mathcal{G} \neq 0$ , it is possible to boost the system into a Lorentz frame in which the electric and magnetic fields are (anti-)parallel, depending on the sign of  $\mathcal{G}$ . Conveniently, in the frame where  $\vec{E} \parallel \vec{B}$ , one can then associate  $a \leftrightarrow E$  and  $b \leftrightarrow B$ .

---

<sup>1</sup>Note carefully that the convention for the invariants  $a$  and  $b$  is by far not uniform in the literature. Our choice agrees with, e.g., [12, 15], but not with [52].

# Appendix B

## The Heisenberg-Euler Lagrangian in constant external fields

In this appendix, we give an evaluation<sup>1</sup> of functional determinant leading to the Heisenberg-Euler effective action. For simplicity, we restrict ourselves to a constant external magnetic field. As we take the electromagnetic field to be external, we are working, by definition, on the level of the one-loop approximation as radiative corrections to the loop are not accounted for.

For convenience, we give again the one-loop effective action of Eq. (2.10):

$$\Gamma^{(1)}[A] = -i \ln \det (-i\not{D} + m) , \quad (\text{B.1})$$

with  $\not{D} = \gamma_\mu(\partial^\mu - ieA^\mu)$ . In order to evaluate the spectrum of this operator, we first rewrite the argument of the determinant into a more useful representation<sup>2</sup>

$$\begin{aligned} \ln \det (-i\not{D} + m) &= \frac{1}{2} \left[ \ln \det (-i\not{D} + m) + \ln \det (-i\not{D} + m) \right] \\ &= \frac{1}{2} \ln \det (\not{D}^2 + m^2) \\ &= \frac{1}{2} \text{Tr} \left[ \ln (\not{D}^2 + m^2) \right] , \end{aligned} \quad (\text{B.2})$$

where a zero-field subtraction remains to be included, see below.

The evaluation of Eq. (B.2) for constant magnetic fields is considerably facilitated by the fact that the Landau levels appear as part of the spectrum. Nevertheless, even for known eigenvalues, the logarithm has to be cleverly dealt with. One adequate technique

---

<sup>1</sup>Here, we follow in parts the steps outlined in a lecture given by G. Dunne. The corresponding lecture notes have been made available with participation of the author, cf. [205].

<sup>2</sup>To check these identities, rewrite the “ $\ln \det$ ” into a “ $\text{Tr} \ln$ ”, insert  $\gamma_5 \gamma_5 = 1$  and make use of the cyclicity of the trace.

would be to employ a proper-time representation [14]. Here we follow a different approach, in which zeta function regularization is employed.

For this purpose, let us first introduce the Hurwitz zeta function, defined by

$$\zeta_{\text{H}}(s; z) := \sum_{n=0}^{\infty} \frac{1}{(n+z)^s}, \quad \text{if } \Re(s) > 1. \quad (\text{B.3})$$

Conveniently, using the integral representation of the gamma function, the zeta function can be analytically continued also to negative values of  $s$ . For the computation of the Heisenberg-Euler Lagrangian, we need to employ the relations

$$\zeta_{\text{H}}(-1; z) = \frac{z}{2} - \frac{z^2}{2} - \frac{1}{12} \quad (\text{B.4})$$

$$\zeta'_{\text{H}}(-1; z) = \frac{1}{12} - \frac{z^2}{4} - \zeta_{\text{H}}(-1, z) \ln z - \frac{1}{4} \int_0^{\infty} \frac{dt}{t^2} e^{-2zt} \left( \coth t - \frac{1}{t} - \frac{t}{3} \right), \quad (\text{B.5})$$

cf., e.g., [205].

Formally, one can relate the spectrum of an operator  $\mathcal{M}_{\lambda}$  with eigenvalues  $\lambda_n$  to a zeta function by defining

$$\zeta(s) := \text{Tr} \left( \frac{1}{\mathcal{M}_{\lambda}^s} \right) = \sum_{n=0}^{\infty} \frac{1}{\lambda_n^s} \quad (\text{B.6})$$

such that by taking the derivative of the zeta function with respect to  $s$  one finds

$$\zeta'(s) = - \sum_{n=0}^{\infty} \frac{\ln(\lambda_n)}{\lambda_n^s} \quad (\text{B.7})$$

$$\zeta'(0) = - \ln \left( \prod_{n=0}^{\infty} \lambda_n \right) = - \text{Tr} \ln (\mathcal{M}_{\lambda}) . \quad (\text{B.8})$$

The superiority of Eq. (B.8) is hidden in the fact that for the continuous eigenvalues (momenta) of an operator as in Eq. (B.2), we would find a divergent contribution when performing the trace-integral, demanding for regularization (and subsequent renormalization). Instead, in Eq. (B.8), once an analytic continuation of the zeta function to the required  $s$ -values is performed, a rather naive use of this identity will render a finite result.

In our context, the eigenvalues of the operator  $(\not{D}^2 + m^2)$  from Eq. (B.2) factorize into contributions that are continuous if parallel and discrete if orthogonal to the direction of the external magnetic field lines. The latter correspond to the relativistic generalization of the Landau levels, given by

$$\lambda_n = m^2 + \vec{k}_{\perp}^2 + eB(2n + 1 + \sigma), \quad (\text{B.9})$$

where  $\sigma = \pm 1$  encodes the spin components of the fermions, see, e.g., [206]. Thus, according to Eq. (B.8), we can translate the task of summing the logarithms of these eigenvalues into the evaluation of a Hurwitz zeta function as introduced in Eq. (B.3).

The relevant zeta function then reads

$$\zeta(s) = \frac{eB}{2\pi} \int \frac{d^2 k_\perp}{(2\pi)^2} \sum_{n=0}^{\infty} \sum_{\pm} \frac{\mu^{2s}}{(\vec{k}_\perp^2 + m^2 + eB(2n + 1 \pm 1))^s}. \quad (\text{B.10})$$

In the above equation, we have inserted the degeneracy factor for the Landau levels  $eBV_\perp/2\pi$ , and subsequently omitted the volume factor  $V_\perp$ , as well as the volumes of the integration over the parallel and time-like components  $V_\parallel V_t$ , as our final result (Eq. (B.17)) will be given in terms of a Lagrangian rather than an action. In addition, Eq. (B.10) carries a normalization constant  $\mu^2$  which will in the end be set equal to the rest energy of the electron  $m^2$ . Its purpose is to ensure that the one-loop correction vanishes in the limit  $B \rightarrow 0$ .

One can deal with Eq. (B.10) by performing the integration over the momenta first and subsequently evaluating<sup>3</sup> the spin and Landau level sums.

For the momentum integral we switch to polar coordinates and reverse differentiate giving

$$\int_{-\infty}^{\infty} d^2 k_\perp \frac{1}{(\vec{k}_\perp^2 + c)^s} = \pi \int_0^{\infty} dk \frac{d}{dk} \left( \frac{(k^2 + c)^{-s+1}}{-s+1} \right) = \frac{\pi}{(s-1) c^{s-1}}, \quad (\text{B.11})$$

such that Eq. (B.10) becomes

$$\zeta(s) = \frac{eB \mu^{2s}}{(2\pi)^3} \frac{\pi}{(s-1)} \sum_{n=0}^{\infty} \sum_{\pm} \frac{1}{(m^2 + eB(2n + 1 \pm 1))^{s-1}}. \quad (\text{B.12})$$

We then write out the spin sum explicitly and combine the terms as

$$\sum_{n=0}^{\infty} \left[ \frac{1}{(n + \frac{m^2}{2eB} + 1)^{s-1}} + \frac{1}{(n + \frac{m^2}{2eB})^{s-1}} \right] = 2 \zeta_H(s-1; \frac{m^2}{2eB}) - \left( \frac{m^2}{2eB} \right)^{1-s}, \quad (\text{B.13})$$

such that we can finally write the zeta function in a compact form

$$\zeta(s) = \frac{e^2 B^2}{2\pi^2} \left( \frac{\mu^2}{2eB} \right)^s \frac{1}{(s-1)} \left( \zeta_H \left( s-1; \frac{m^2}{2eB} \right) - \frac{1}{2} \left( \frac{m^2}{2eB} \right)^{1-s} \right). \quad (\text{B.14})$$

Following Eqs. (B.7) and (B.8), we now take the derivative of the zeta function and set  $s$  equal to zero. To bring the right hand sides of these equations into final form, we employ

---

<sup>3</sup>Note that in Chapt. 6 as well as App. C, we proceed in just the opposite way and regain a Landau-level type structure from an integral representation in which the level contributions are “hidden” at first.

the analytic continuations of the Hurwitz zeta function given in Eqs. (B.4) and (B.5) and normalize to  $\mu^2 = m^2$  in the end.

$$\begin{aligned} \zeta'(s) &= \frac{e^2 B^2}{2\pi^2} \left\{ \ln \left( \frac{\mu^2}{2eB} \right) \left( \frac{\mu^2}{2eB} \right)^s \frac{1}{(s-1)} \left[ \zeta_H \left( s-1; \frac{m^2}{2eB} \right) - \frac{1}{2} \left( \frac{m^2}{2eB} \right)^{1-s} \right] \right. \\ &\quad - \left( \frac{\mu^2}{2eB} \right)^s \frac{1}{(s-1)^2} \left[ \zeta_H \left( s-1; \frac{m^2}{2eB} \right) - \frac{1}{2} \left( \frac{m^2}{2eB} \right)^{1-s} \right] \\ &\quad \left. + \left( \frac{\mu^2}{2eB} \right)^s \frac{1}{(s-1)} \left[ \zeta_H \left( s-1; \frac{m^2}{2eB} \right) - \frac{1}{2} \left( \frac{m^2}{2eB} \right)^{1-s} \right] \right\} \quad (\text{B.15}) \end{aligned}$$

$$\zeta'(0) = \frac{e^2 B^2}{2\pi^2} \left\{ \frac{3}{4} \frac{m^2}{2eB^2} + \frac{1}{4} \int_0^\infty \frac{dt}{t^2} e^{-\frac{m^2 t}{eB}} \left[ \coth t - \frac{1}{t} - \frac{t}{3} \right] \right\}. \quad (\text{B.16})$$

The first term in Eq. (B.16) is independent of  $B$  and thus does not contribute on the level of the dynamics. Before we state the final result for the Heisenberg-Euler Lagrangian, we pull out a factor of  $1/t$  of the square bracket and substitute  $T = t/eB$

$$\mathcal{L}^{(1)} = -\frac{1}{8\pi^2} \int_0^\infty \frac{dT}{T^3} e^{-m^2 T} \left[ \frac{eBT}{\tanh(eBT)} - 1 - \frac{1}{3}(eBT)^2 \right]. \quad (\text{B.17})$$

Lastly, by realizing that  $x/\tanh(x) = 1 + x^2/3 + \mathcal{O}(x^4)$ , we see that the integral is safe at the lower  $T$  integration boundary for  $B \neq 0$  and vanishing in the limit  $B \rightarrow 0$ , as intended.

The above result also allows introduce the Heisenberg-Euler Lagrangian for nonvanishing electric fields which is closely associated with absorptive properties of the vacuum, see below. By Lorentz invariance, we know that the effective Lagrangian can only depend<sup>4</sup> on  $\mathcal{F}$  and  $\mathcal{G}^2$ , as defined in Eqs. (A.3) and (A.4).

Thus, by observing that in a parallel field configuration (cf. also the remark below Eq. (A.6))

$$\mathcal{L}(\mathcal{F}, \mathcal{G})|_{E \neq 0, B=0} = \mathcal{L}(-E^2/2, 0) = \mathcal{L}((-iE)^2/2, 0) = \mathcal{L}(\mathcal{F}, \mathcal{G})|_{E=0, B=-iE}, \quad (\text{B.18})$$

we see that we can obtain the Heisenberg-Euler Lagrangian for constant electric fields by substituting<sup>5</sup>  $B \rightarrow -iE$  in Eq. (B.17). Note that through this substitution, as the first term in the square brackets is transformed into  $eET/\tan(eET)$ , the Lagrangian picks up an imaginary part by virtue of the poles at  $T = n\pi/eE$ , where  $n = 1, 2, \dots$ . The physical meaning of this finding can be understood by recalling the relation between the energy functional and the vacuum persistence amplitude as stated in Eq. (2.1). As the energy functional  $W$  and the effective action  $\Gamma$  encode the same physical information, one has in Minkowski space the relation  $\exp(i\Gamma[E]) = \langle 0|0 \rangle_E$ . On the other hand, the probability for vacuum decay in the presence of an external electric field is  $P = 1 - |\langle 0|0 \rangle_E|^2 =$

<sup>4</sup>Note that the dependence on  $\mathcal{G}$  needs to be in even powers as this invariant is CP violating.

<sup>5</sup>Of course, this substitution disguises the fact that there is an ambiguity in the choice of sign  $B \rightarrow \pm iE$  depending relative direction of the electric and magnetic field vectors, cf., e.g., [207]. However, as this is not crucial to the present discussion, we disregard this issue in the following.

$1 - \exp(-2\Im\Gamma)$ . Thus, one finds that the imaginary part of the effective action can be associated with the number of produced electron-positron pairs in the external electric field. Likewise, the imaginary part of the Heisenberg-Euler Lagrangian can be associated with a pair production rate. This phenomenon is commonly referred to as Schwinger pair production honoring [14], however cf. also earlier work [12, 208]. Schwinger pair production constitutes – in theory as well as in experiment – a major research field<sup>6</sup> on its own.

Finally, we want to state the result for the full Heisenberg-Euler Lagrangian [12–14], i.e., for nonvanishing electric and magnetic fields. Employing the secular invariants  $a$  and  $b$ , cf. Eqs. (A.5) and (A.6), it can be written in a form that exhibits a close structural similarity to the result for purely magnetic or electric fields. One finds

$$\mathcal{L}_{\text{eff}} = \frac{1}{2} (a^2 - b^2) - \frac{1}{8\pi^2} \int_0^\infty \frac{dT}{T^3} e^{-m^2 T} \left( \frac{e^2 ab T^2}{\tanh(ebT) \tan(eaT)} - \frac{(b^2 - a^2) e^2 T^2}{3} - 1 \right), \quad (\text{B.19})$$

where we have reinstated the tree-level contribution  $\mathcal{L}^{(0)}$ , such that above  $\mathcal{L}_{\text{eff}} = \mathcal{L}^{(0)} + \mathcal{L}^{(1)}$ .

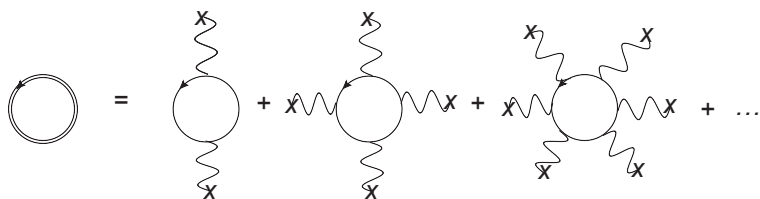


Figure B.1: Diagrammatic depiction of the Heisenberg-Euler Lagrangian of Eq. (B.19). The dressed loop (double line) depicts arbitrarily many insertions of the external field.

In Fig. B.1 we give a diagrammatic depiction of the Heisenberg-Euler Lagrangian. For completeness let us point to some of its most important phenomenological implications. By Furry’s theorem, only an even number of combined photon and external field insertions is admissible. Generating photon legs by functional differentiation of the one-loop effective action, see, e.g., [213], one obtains “photon-photon scattering” [214, 215] at four photon legs, “photon splitting” at three photon legs [216, 217], and “Delbrück scattering” at two photon legs [218, 219]. Note that by scattering photons off the electromagnetic fields in atoms<sup>7</sup>, Delbrück scattering [220] as well as photon splitting have been observed experimentally [221].

<sup>6</sup>For example, although dynamical pair production [209] in the perturbative, multiphoton regime has been observed at SLAC in the experiment 144 [210] (with first nonperturbative signatures, cf. [211]), pair production in the fully nonperturbative “tunneling-regime” still awaits experimental verification, see, e.g., the discussion in [212].

<sup>7</sup>Note that the vertex coupling is enhanced by virtue of the charge of the nucleus in this situation. Furthermore, for constant external fields, the lowest order contribution to “photon splitting” vanishes, cf. [19], rendering a rotation phenomenon in dipole magnets, cf. Fig. 2.3, due to this process negligible.

Lastly, we give the weak field limit of the Heisenberg-Euler Lagrangian, which will be relevant to our analyses in Chapt. 4. For today's experimentally available electromagnetic fields it is safe to approximate  $Ee \ll m^2$  and  $Be \ll m^2$ , and we can perturbatively expand the Lagrangian in the number of field insertions, cf. Fig. B.1. Thus, one finds up to quadratic order in the field strength:

$$\mathcal{L}_{\text{eff}} = \frac{1}{2} (\vec{E}^2 - \vec{B}^2) + \frac{2\alpha^2}{45m^4} (\vec{E}^2 - \vec{B}^2)^2 + 7\frac{2\alpha^2}{45m^4} (\vec{E}\vec{B})^2 . \quad (\text{B.20})$$

Let us remark, that although the above effective Lagrangian was worked out in the approximation of a constant external magnetic field, it can still be expected to hold if inhomogeneities of the field do not occur on a length or time scale on the order of the Compton wavelength of the electron, justifying its use in Chapt. 4.



# Appendix C

## On vacuum polarization in constant external magnetic fields

In the following, we give a very brief survey of the polarization tensor in external, purely magnetic fields. The presentation is intended such that it gathers all the necessary<sup>1</sup> facts that constitute the basis of our investigations of the light-shining-through-walls scenario in Chapt. 6. In particular, we focus on the situation in which the direction of the external magnetic field and the propagation direction of the photons coincide. Note that, as Chapt. 6 rederives and extends results of [96], we employ the corresponding metric conventions  $g = (-, +, +, +)$  such that  $k^2 = \vec{k}^2 - \omega^2$  in the following for easy comparability. On the other hand, the general literature on the polarization tensor particularly for arbitrary field configurations has become rather broad over the course of the years and we limit ourselves by referencing [52, 213] containing pedagogical résumés of the most important results.

### Vacuum polarization with charged Dirac spin-1/2 fermions

If, without restriction of generality,  $\vec{B}$  is chosen to point along the 1-direction, the 4-momentum of the photon and the metric can be decomposed into parallel and orthogonal components with respect to the 1-direction as

$$k^\mu = k_\parallel^\mu + k_\perp^\mu, \quad k_\parallel^\mu = (\omega, k^1, 0, 0), \quad k_\perp^\mu = (0, 0, k^2, k^3), \quad g^{\mu\nu} = g_\parallel^{\mu\nu} + g_\perp^{\mu\nu}. \quad (\text{C.1})$$

---

<sup>1</sup>A more elaborate discussion is under way [57].

According to this decomposition, the polarization tensor for spin-1/2 Dirac fermions in its proper-time representation can be written as [52]

$$\begin{aligned} \Pi^{\mu\nu}(k) = \frac{\alpha}{2\pi} \int_0^\infty \frac{ds}{s} \int_{-1}^{+1} \frac{d\nu}{2} \left\{ e^{-i\Phi_0 s} \frac{z}{\sin(z)} \left[ N_0 (g^{\mu\nu} k^2 - k^\mu k^\nu) \right. \right. \\ \left. \left. + (\tilde{N}_1 - N_0) (g_{\parallel}^{\mu\nu} k_{\parallel}^2 - k_{\parallel}^\mu k_{\parallel}^\nu) + (\tilde{N}_2 - N_0) (g_{\perp}^{\mu\nu} k_{\perp}^2 - k_{\perp}^\mu k_{\perp}^\nu) \right] + \text{c.t.} \right\}, \quad (\text{C.2}) \end{aligned}$$

where  $z = eBs$ ,  $B = |\vec{B}|$  and the so-called ‘‘contact-term’’ assures that the polarization tensor vanishes for vanishing fields

$$\text{c.t.} = -(1 - \nu^2) e^{-im^2 s} (g^{\mu\nu} k^2 - k^\mu k^\nu). \quad (\text{C.3})$$

Moreover, defining  $\theta = \sphericalangle(\vec{B}, \vec{k})$ , the short-hand

$$\Phi_0 = m^2 - \frac{1 - \nu^2}{4} \omega^2 + \left[ \frac{1 - \nu^2}{4} \cos^2 \theta + \frac{\cos \nu z - \cos z}{2z \sin z} \sin^2 \theta \right] \vec{k}^2 \quad (\text{C.4})$$

as well as the auxiliary functions

$$N_0 = \cos \nu z - \nu \sin \nu z \cot z, \quad \tilde{N}_1 = (1 - \nu^2) \cos z, \quad \tilde{N}_2 = 2 \frac{\cos \nu z - \cos z}{\sin^2 z}, \quad (\text{C.5})$$

are introduced. Note that in Eq. (C.2) as well as all subsequent representations of the polarization tensor, a prescription  $m^2 \rightarrow m^2 - i\eta$ , with an infinitesimal parameter  $\eta > 0$ , is implicitly understood to ensure convergence of the integral in the proper time representation. Physically, the integration over  $\nu$  governs the distribution of the momenta within the particle-antiparticle loop, cf., e.g., [20], whereas the proper-time integral comes about as part of a convenient representation of the inverse Dirac operator, cf. [14]. For polarimetry it is instructive to decompose the polarization tensor in Eq. (C.2) with respect to the different polarization modes. Such a decomposition is most intuitive if  $\theta = \sphericalangle(\vec{B}, \vec{k}) \neq 0$ . In this situation it is convenient to write

$$\begin{aligned} \Pi^{\mu\nu}(k) = \Pi_0(k) \underbrace{P_0^{\mu\nu}} + \Pi_{\parallel}(k) \underbrace{P_{\parallel}^{\mu\nu}} + \Pi_{\perp}(k) \underbrace{P_{\perp}^{\mu\nu}}, \\ := \left( g^{\mu\nu} - \frac{k^\mu k^\nu}{k^2} - P_{\parallel}^{\mu\nu} - P_{\perp}^{\mu\nu} \right) \quad := \left( g^{\mu\nu} - \frac{k_{\parallel}^\mu k_{\parallel}^\nu}{k_{\parallel}^2} \right) \quad := \left( g_{\perp}^{\mu\nu} - \frac{k_{\perp}^\mu k_{\perp}^\nu}{k_{\perp}^2} \right), \end{aligned} \quad (\text{C.6})$$

such that the sum of the projectors in Eq. (C.6) spans the transversal subspace:  $P_0^{\mu\nu} + P_{\parallel}^{\mu\nu} + P_{\perp}^{\mu\nu} = g^{\mu\nu} - \frac{k^\mu k^\nu}{k^2} \equiv P_{\text{T}}^{\mu\nu}$ . Here we speak of the transversal subspace as longitudinal photons, which are singled out by the projector  $P_{\text{L}}^{\mu\nu} = \frac{k^\mu k^\nu}{k^2}$ , would have their wave vector parallel to their amplitude  $\vec{k} \parallel \vec{E} \parallel \vec{A}$  in vacuum.

By the same reasoning,  $P_0^{\mu\nu}$  can be understood as projecting onto quasi-longitudinal or “tilted” polarization modes. The scalar functions  $\Pi_{\parallel}$ ,  $\Pi_{\perp}$  and  $\Pi_0$  belonging to Eq. (C.6) read [52]

$$\left\{ \begin{array}{c} \Pi_0 \\ \Pi_{\parallel} \\ \Pi_{\perp} \end{array} \right\} = \frac{\alpha}{2\pi} \int_0^{\infty} \frac{ds}{s} \int_{-1}^{+1} \frac{d\nu}{2} \times \left[ e^{-i\Phi_0 s} \frac{eBs}{\sin(eBs)} \left( \left\{ \begin{array}{c} 0 \\ N_0 - \tilde{N}_1 \\ \tilde{N}_2 - N_0 \end{array} \right\} \vec{k}^2 \sin^2 \theta + \left\{ \begin{array}{c} N_0 \\ \tilde{N}_1 \\ N_0 \end{array} \right\} k^2 \right) + \text{c.t.} \right], \quad (\text{C.7})$$

where the contact term now is

$$\text{c.t.} = -e^{-im^2 s} k^2 (1 - \nu^2). \quad (\text{C.8})$$

For  $\theta \neq 0$ , a further evaluation of Eq. (C.7) is possible through well-established approximation techniques, see, e.g., [54]. However, such techniques can mostly not be expected to be applicable for arbitrary photon momenta  $\vec{k}$ .

On the other hand, if  $\theta = 0$ , the polarization tensor simplifies considerably as no additional direction is singled out by the magnetic field as compared to the zero-field situation: Only separate contributions  $\sim \tilde{N}_1$  and  $\sim N_0$  remain along two different projector components. Note carefully that in *this* alignment,  $P_{\perp}^{\mu\nu} + P_0^{\mu\nu} = g_{\perp}^{\mu\nu}$  singles out the orthogonal polarization state  $\perp$ , whereas  $P_{\parallel}^{\mu\nu}$  now projects on the tilted modes. In order to avoid confusion, we adapt the notation  $P_{\parallel}^{\mu\nu} \equiv P_{\perp}^{\mu\nu}$  as introduced in [193] in order to highlight that  $\parallel$  does not refer to a state of polarization in this alignment. The polarization tensor then reads

$$\begin{aligned} \Pi^{\mu\nu}(k) &= P_{\perp}^{\mu\nu} k_{\parallel}^2 \frac{\alpha}{2\pi} \int_0^{\infty} \frac{ds}{s} \int_{-1}^{+1} \frac{d\nu}{2} \left[ \frac{z}{\sin(z)} \tilde{N}_1 e^{-i\Phi_0 s} - (1 - \nu^2) e^{-im^2 s} \right] \\ &+ g_{\perp}^{\mu\nu} k_{\parallel}^2 \frac{\alpha}{2\pi} \int_0^{\infty} \frac{ds}{s} \int_{-1}^{+1} \frac{d\nu}{2} \left[ \frac{z}{\sin(z)} N_0 e^{-i\Phi_0 s} - (1 - \nu^2) e^{-im^2 s} \right]. \quad (\text{C.9}) \end{aligned}$$

Notably, the proper-time integrals in Eq. (C.9) can be evaluated explicitly. To show this, employing  $s = \frac{z}{eB}$ , as well as  $\tilde{N}_1$  and  $N_0$  from Eq. (C.5), we rewrite the polarization tensor as

$$\begin{aligned} \Pi^{\mu\nu}(k) &= P_{\perp}^{\mu\nu} k_{\parallel}^2 \frac{\alpha}{2\pi} \int_{-1}^{+1} \frac{d\nu}{2} (1 - \nu^2) \int_0^{\infty} dz \left[ \cot(z) e^{-i\frac{\Phi_0}{eB} z} - \frac{e^{-i\frac{m^2}{eB} z}}{z} \right] \\ &+ g_{\perp}^{\mu\nu} k_{\parallel}^2 \frac{\alpha}{2\pi} \int_{-1}^{+1} \frac{d\nu}{2} \int_0^{\infty} dz \left[ \left( \frac{\cos(\nu z)}{\sin(z)} - \frac{\nu \sin(\nu z) \cot(z)}{\sin(z)} \right) e^{-i\frac{\Phi_0}{eB} z} - (1 - \nu^2) \frac{e^{-i\frac{m^2}{eB} z}}{z} \right]. \quad (\text{C.10}) \end{aligned}$$

To perform the integration over  $z$ , it is suggestive to dispose of the oscillatory behavior of the integrand by rotating the  $z$ -contour in the complex plane. However, this is not entirely straightforward: Keeping  $m$  and  $\omega$  fixed, the phase  $\Phi_0$  defined in Eq. (C.4), which at  $\theta = 0$  simplifies to

$$\Phi_0 = m^2 + (\vec{k}^2 - \omega^2) \frac{1 - \nu^2}{4} = \frac{1 - \nu^2}{4} \left( \vec{k}^2 - \omega^2 + \frac{4m^2}{1 - \nu^2} \right), \quad (\text{C.11})$$

is always positive if  $\omega < 2m$ , but exhibits a sign-change away from the light cone. To be specific, for  $k^2 \neq 0$ , Eq. (C.11) changes sign as function of  $|\vec{k}|$  for  $-1 \lesssim \nu \lesssim 1$  if  $\omega > 2m$ . Thus, a rotation of the  $z$ -contour is well-defined for  $\omega < 2m$  but not easily implemented for  $\omega > 2m$ . (Note that for  $\nu = \pm 1$ ,  $\Phi_0 = m^2$  and the contour rotation can be easily performed. In the following discussion, a restriction to  $-1 \lesssim \nu \lesssim 1$  should thus be understood in the  $\nu$  integral.)

In order to evaluate the proper-time integral for arbitrary relative magnitudes of  $\omega$  and  $m$ , we resort to a “trick” which was already employed in App. B, below Eq. (B.18). Realizing that the polarization tensor can depend on the external field only via Lorentz invariants [52], we can once again employ a “rotation”  $B \rightarrow -iE$ , such that the electric analog of Eq. (C.10) reads

$$\begin{aligned} \Pi^{\mu\nu}(k) = & P_{\perp}^{\mu\nu} k_{\parallel}^2 \frac{\alpha}{2\pi} \int_{-1}^{+1} \frac{d\nu}{2} (1 - \nu^2) \int_0^{\infty} dz \left[ \coth(z) e^{-i\frac{\Phi_0}{eE}z} - \frac{e^{-i\frac{m^2}{eE}z}}{z} \right] \\ & + g_{\perp}^{\mu\nu} k_{\parallel}^2 \frac{\alpha}{2\pi} \int_{-1}^{+1} \frac{d\nu}{2} \int_0^{\infty} dz \left[ \left( \frac{\cosh(\nu z)}{\sinh(z)} - \frac{\nu \sinh(\nu z) \coth(z)}{\sinh(z)} \right) e^{-i\frac{\Phi_0}{eE}z} - (1 - \nu^2) \frac{e^{-i\frac{m^2}{eE}z}}{z} \right]. \end{aligned} \quad (\text{C.12})$$

Here we have already rearranged the terms such that it is visible that the rotation effectively amounts to a conversion of the trigonometric functions into their hyperbolic analogs for convenience. Now, recalling the  $i\eta$  prescription for the mass terms in the exponents, the evaluation of the proper-time integration in Eq. (C.12) does in fact not necessitate a contour rotation. First, it is instructive to note that the expression in the second line of Eq. (C.12) can be rewritten using<sup>2</sup> integration by parts

$$-\int_0^{\infty} dz \frac{\nu \sinh(\nu z) \coth(z)}{\sinh(z)} e^{-\beta z} = -\nu^2 + \int_0^{\infty} dz \frac{-\nu^2 \cosh(\nu z) + \beta \nu \sinh(\nu z)}{\sinh(z)} e^{-\beta z}. \quad (\text{C.13})$$

---

<sup>2</sup>See also (D.25) in [52].

Next, employing Eqs. (3.551.2) (for the contact term) as well as (3.551.3) and (3.552.1) of [177], which can be written as

$$\int_0^\infty dz z^{\delta-1} e^{-\beta z} = \Gamma(\delta) \beta^{-\delta} = \delta^{-1} - \ln(\beta) - \gamma_E + \mathcal{O}(\delta), \quad \text{if } \Re(\beta) > 0 \ \& \ \Re(\delta) > 0, \quad (\text{C.14})$$

$$\begin{aligned} \int_0^\infty dz z^\delta e^{-\beta z} \coth(z) &= \Gamma(\delta + 1) [2^{-\delta} \zeta(\delta + 1, \beta/2) - \beta^{-\delta-1}] \\ &= \delta^{-1} - \Psi(\beta/2) - \gamma_E - \ln(2) - \beta^{-1} + \mathcal{O}(\delta), \quad \text{if } \Re(\beta) > 0 \ \& \ \Re(\delta) > 0, \end{aligned} \quad (\text{C.15})$$

$$\begin{aligned} \int_0^\infty dz z^\delta \frac{e^{-\beta z}}{\sinh(z)} &= \Gamma(\delta + 1) 2^{-\delta} \zeta\left(\delta + 1, \frac{\beta+1}{2}\right) \\ &= \delta^{-1} - \Psi\left(\frac{\beta+1}{2}\right) - \gamma_E - \ln(2) + \mathcal{O}(\delta), \quad \text{if } \Re(\beta) > -1 \ \& \ \Re(\delta) > 0, \end{aligned} \quad (\text{C.16})$$

respectively. Here,  $\gamma_E$  is the Euler-Mascheroni constant and  $\Psi(x) = \frac{d}{dx} \ln \Gamma(x)$  denotes the Digamma function which is discussed in detail below. The polarization tensor for the electric field, Eq. (C.12), becomes

$$\begin{aligned} \Pi^{\mu\nu}(k) &= P_\perp^{\mu\nu} k_\parallel^2 \frac{\alpha}{2\pi} \int_0^1 d\nu (1 - \nu^2) \left[ \ln\left(\frac{m^2}{2e(-iE)}\right) - \Psi\left(\frac{\Phi_0}{2e(-iE)}\right) - \frac{e(-iE)}{\Phi_0} \right] \\ &+ g_\perp^{\mu\nu} \left[ \frac{\alpha}{3\pi} k_\parallel^2 \left( \ln\left(\frac{m^2}{2e(-iE)}\right) - \frac{1}{2} \right) - \frac{\alpha}{2\pi} k_\parallel^2 \int_{-1}^1 \frac{d\nu}{2} \left( 1 - \nu^2 - \frac{\Phi_0}{e(-iE)} \nu \right) \Psi\left(\frac{1}{2} + \frac{\Phi_0}{2e(-iE)} + \frac{\nu}{2}\right) \right]. \end{aligned} \quad (\text{C.17})$$

Employing the reverse substitution  $E \rightarrow +iB$ , Eq. (C.10) can be finally written as

$$\begin{aligned} \Pi^{\mu\nu}(k) &\equiv P_\perp^{\mu\nu} \Pi_\perp(k|B) + g_\perp^{\mu\nu} \Pi_\perp(k|B) = \\ &P_\perp^{\mu\nu} k_\parallel^2 \frac{\alpha}{2\pi} \int_0^1 d\nu (1 - \nu^2) \left[ \ln\left(\frac{m^2}{2eB}\right) - \Psi\left(\frac{\Phi_0}{2eB}\right) - \frac{eB}{\Phi_0} \right] \\ &+ g_\perp^{\mu\nu} \left[ \frac{\alpha}{3\pi} k_\parallel^2 \left( \ln\left(\frac{m^2}{2eB}\right) - \frac{1}{2} \right) - \frac{\alpha}{2\pi} k_\parallel^2 \int_{-1}^1 \frac{d\nu}{2} \left( 1 - \nu^2 - \frac{\Phi_0}{eB} \nu \right) \Psi\left(\frac{1}{2} + \frac{\Phi_0}{2eB} + \frac{\nu}{2}\right) \right]. \end{aligned} \quad (\text{C.18})$$

Let us emphasize that the result of Eq. (C.18) has been obtained previously by different authors in equivalent forms, cf. [193–195].

### Vacuum polarization with charged spin-0 bosons

An analogous result for the polarization tensor with scalar fluctuations at  $\theta = \sphericalangle(\vec{B}, \vec{k}) = 0$  can be derived in the manner outlined above. Starting from the polarization tensor of

scalar QED, see, e.g., [222], one has as relevant auxiliary functions  $\tilde{N}_1^s = \nu^2$  as well as  $N_0^s = \frac{\nu \sin(\nu z)}{\sin(z)}$ . Thus, for purely magnetic fields at  $\vec{B} \parallel \vec{k}$  one finds

$$\begin{aligned} \Pi_s^{\mu\nu}(k) = & P_{\perp}^{\mu\nu} k_{\parallel}^2 \frac{\alpha}{4\pi} \int_{-1}^{+1} \frac{d\nu}{2} \nu^2 \int_0^{\infty} dz \left[ \frac{e^{-i\frac{\Phi_0}{eB}z}}{\sin(z)} - \frac{e^{-i\frac{m^2}{eB}z}}{z} \right] \\ & + g_{\perp}^{\mu\nu} k_{\parallel}^2 \frac{\alpha}{4\pi} \int_{-1}^{+1} \frac{d\nu}{2} \int_0^{\infty} dz \left[ \frac{\nu \sin(\nu z)}{\sin^2(z)} e^{-i\frac{\Phi_0}{eB}z} - \nu^2 \frac{e^{-i\frac{m^2}{eB}z}}{z} \right]. \end{aligned} \quad (\text{C.19})$$

Employing a rotation  $B \rightarrow -iE$  and by means of integration by parts:

$$\int_0^{\infty} dz \frac{\nu \sinh(\nu z)}{\sinh^2(z)} e^{-\beta z} = \nu^2 + \int_0^{\infty} dz \coth(z) (\nu^2 \cosh(\nu z) - \nu \beta \sinh(\nu z)) e^{-\beta z}, \quad (\text{C.20})$$

Eqs. (C.14-C.16) can be used to perform the integrals over  $z$  in Eq. (C.19) as outlined above. Employing the identity (which results by combining Eqs. (8.365.2) and (8.377) of [177])

$$\Psi\left(x + \frac{1}{2}\right) = 2\Psi(2x) - \Psi(x) - 2\ln(2), \quad (\text{C.21})$$

the scalar polarization tensor at zero incidence, Eq. (C.19), can be finally written as

$$\begin{aligned} \Pi_s^{\mu\nu}(k) \equiv & P_{\perp}^{\mu\nu} \Pi_{s,\perp}(k|B) + g_{\perp}^{\mu\nu} \Pi_{s,\perp}(k|B) = \\ & P_{\perp}^{\mu\nu} k_{\parallel}^2 \frac{\alpha}{4\pi} \int_0^1 d\nu \nu^2 \left[ \ln\left(\frac{2m^2}{eB}\right) + \Psi\left(\frac{\Phi_0}{2eB}\right) - 2\Psi\left(\frac{\Phi_0}{eB}\right) \right] \\ & + g_{\perp}^{\mu\nu} k_{\parallel}^2 \frac{\alpha}{4\pi} \left[ \frac{1}{3} \left( 1 + \ln\left(\frac{m^2}{2eB}\right) \right) - \int_{-1}^1 \frac{d\nu}{2} \left( \nu \frac{\Phi_0}{eB} + \nu^2 \right) \Psi\left(\frac{\frac{\Phi_0}{eB} + \nu}{2}\right) \right]. \end{aligned} \quad (\text{C.22})$$

In summary, Eqs. (C.18) and (C.22) constitute the vantage point of Chapt. 6 which discusses an LSW scenario via virtual minicharged Dirac fermions and scalar particles, respectively. These carry a fractional charge  $\epsilon e$ , cf. Sect. 2.2.1, such that in the context of minicharged particles all expressions stated above can be adapted after a substitution  $e \rightarrow \epsilon e$ .

### Representations and approximations of the Digamma function

For further evaluations of Eqs. (C.18) and (C.22) in an applied context, it is useful to note that the Digamma function has an exact series representation [177] reading

$$\Psi(x) = -\gamma_E - \frac{1}{x} + \sum_{n=1}^{\infty} \frac{x}{n(x+n)}. \quad (\text{C.23})$$

In addition, one has expansions for small and large [198] arguments, respectively,

$$\Psi(x) = -\gamma_E - \frac{1}{x} + \frac{\pi^2 x}{6} + \frac{\pi^4 x^3}{90} + \frac{1}{2} x^2 \Psi^{(2)}(1) + \frac{1}{24} x^4 \Psi^{(4)}(1) + \mathcal{O}(x^5) \quad (\text{C.24})$$

$$\Psi(x) = \ln(x) - \frac{1}{2x} - \frac{1}{12x^2} + \mathcal{O}\left(\frac{B_{2l}}{2l} \frac{1}{x^{2l}}\right), \quad (\text{C.25})$$

where  $l = 2, 3, 4, \dots$  and  $B_l$  denote Bernoulli numbers and  $\Psi^{(i)}$  is the  $i$ th derivative of the Digamma function. As a paradigm, we plot the exact Digamma function (blue dashed line) together with the series expansion for small arguments, cf. Eq. (C.24) in Fig. C.1 for a different number expansion terms  $\mathcal{O}(x^i)$ , with  $i = 1, 2, 3, 10, 45, 50$  which are shown in red, green, yellow, magenta, blue and brown, respectively. Note that the Digamma function diverges for  $x = 0$ . Nevertheless, one sees that the series expansion for small  $x$  describes it qualitatively well to all orders in the regime  $0 < x < 1$  within the shown plot range.

On the other hand, the series expansion for large arguments, Eq. (C.25), is given in Fig. C.2. We plot the exact Digamma function (blue dashed line) together with the series expansion for large arguments for  $\mathcal{O}(x^{-j})$ , with  $j = 1, 2, 4, 10, 20, 50$  shown in red, green, yellow, magenta, blue and brown, respectively. As visible, the convergence of this series expansion does not improve at large  $x$  with growing order as the sum over the terms involving Bernoulli numbers constitutes an asymptotic series<sup>3</sup>.

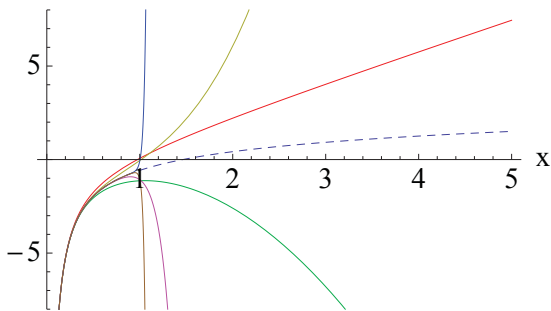


Figure C.1: Asymptotics of a series expansion of  $\Psi(x)$  for  $x \rightarrow 0$  cf. Eq. (C.24). The dashed blue line gives the exact Digamma function whereas the diversified colored lines denote selected expansion orders (see text) up to order  $\mathcal{O}(x^{50})$ . It can be seen that independent of the increase in the number of terms, the qualitative convergence of the perturbative series is satisfactory for  $x \ll 1$ .

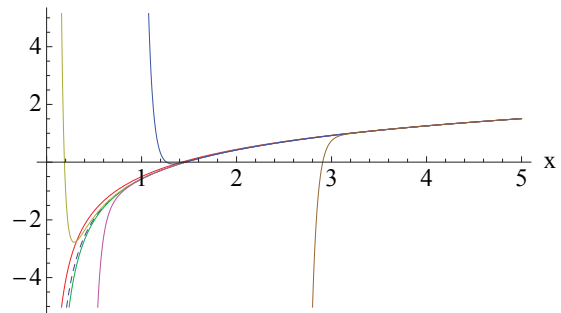


Figure C.2: Asymptotics of a series expansion of  $\Psi(x)$  for  $x \rightarrow \infty$ . The dashed blue line gives the exact Digamma function whereas the diversified colored lines denote selected expansion orders (see text) up to order  $\mathcal{O}(x^{-50})$ . It can be seen that with increasing the number of terms (from left to right), the convergence of the perturbative series worsens with increasing orders in the series, cf. Eq. (C.25).

<sup>3</sup>Note that this behavior is generic in perturbative QED, see, e.g., [15, 197, 223] and also perturbative quantum mechanics, see, e.g., [224].

# Appendix D

## Numerical supplement for the geometric vacuum probe

In the following, we detail on our implementation for the numerical evaluation of the Casimir-Polder potential for arbitrary uniaxial corrugations, cf. Chapt. 3. We proceed as follows: First, we solve the Green's function equation for the associated propagator  $\Delta\mathcal{M}_{12}$ , cf. Eq. (3.10), by discretizing the equation with respect to the spatially lateral coordinate  $x$ . The result is then plugged into Eq. (3.5), yielding the Casimir-Polder energy upon integration of  $\tilde{x}$  and  $\tilde{q}$ .

For the first step, we introduce two parameters:  $\pm L_x$  which labels the left and right cutoff of the spatial integration, and  $N_x$  denoting the number of spatial discretization sites, respectively. In the end, we remove the discretization by a continuum extrapolation  $N_x \rightarrow \infty$ .

In principle,  $L_x$  is a physical parameter encoding the physical size of the surface. Here, we will not make use of this option of studying finite-size effects, but compute the Casimir-Polder potential in the ideal infinite surface limit by extrapolating to  $L_x \rightarrow \infty$ . For this, we fix the position of the sphere above the plate at  $x = 0$  and choose a symmetric cutoff for  $x \in [-L_x, L_x]$ . The two limits, continuum ( $N_x \rightarrow \infty$ ) and infinite-length ( $L_x \rightarrow \infty$ ) limit, have to be taken such that the lattice spacing  $a_x = 2L_x/N_x$  also goes to zero,  $a_x \rightarrow 0$ . This can be ensured by choosing a suitable function  $L_x = L_x(N_x)$ , satisfying  $L_x(N_x \rightarrow \infty) \rightarrow \infty$  and  $L_x(N_x)/N_x \rightarrow 0$  as  $N_x \rightarrow \infty$ . In practice, we use

$$L_x(N_x) = \frac{a_{0x}}{2} \sqrt{N_x N_{0x}}, \quad (\text{D.1})$$

where  $a_{0x}$  defines a reference lattice spacing at a reference site number  $N_x = N_{0x}$ . Note that the lattice spacing  $a_x \equiv a_x(N_x) = 2L_x(N_x)/N_x = a_{0x} \sqrt{N_{0x}/N_x}$  goes to zero in the continuum limit  $N_x \rightarrow \infty$ , while  $L_x \rightarrow \infty$  approaches the infinite length limit. Therefore all these idealized limits are controlled by one parameter:  $N_x$ . In practice, the finite-



length corrections have always been found to be small compared to discretization effects. In general, it suffices to choose the reference lattice spacing such that typically  $L_x(N_{0x}) = 2H$ , where  $N_{0x}$  specifies the coarsest lattice in the calculation.

One serious complication arises when discretizing Eq.(3.10): due to the pole of the zeroth Bessel function  $K_0$  at its origin, the matrix  $\mathcal{M}_{11}^{ij}$  that emerges upon the discretization of the spatial arguments diverges in its diagonal entries, i.e., for the case when the spatial discretization sites lie on top of each other. Whereas these divergencies are integrable when solving the problem in the continuum, the discretized matrix becomes singular. Therefore, a regularization procedure is required that facilitates to first take the continuum limit before the regulator can safely be removed. Here, we use a UV regularization for the propagator in Eq. (3.7) for small arguments  $z$  controlled by a small parameter  $\epsilon$ :

$$\mathcal{M}_{11}(z) = \begin{cases} \frac{1}{2\pi}K_0(z) & , z \leq \epsilon \\ -\frac{1}{2\pi}(\ln(z + \epsilon) - K_0(\epsilon) - \ln(2\epsilon)) & , z > \epsilon \end{cases}, \quad (\text{D.2})$$

where  $z$  summarizes all arguments of the propagator including both spatial and momentum contributions, entering the Bessel function as a single argument, cf. Eq. (3.7). The physical result is expected to arise in the limits  $N_x \rightarrow \infty$  and  $\epsilon \rightarrow 0$  with the continuum limit to be taken first before the regulator is removed.

In a numerical calculation where  $N_x$  and  $\epsilon$  are always finite, the order of limits done by extrapolation requires a careful choice of  $N_x$  and  $\epsilon$ . It is already intuitively clear that smaller values of  $\epsilon$  require larger values of  $N_x$ , since the proper resolution of a more pronounced singularity for smaller  $\epsilon$  needs a finer lattice. As the pole in the inverse propagator on the corrugated surface  $S_1$  persists irrespectively of the corrugation, the numerical discretization and regularization errors can be tested in the planar situation where the analytical result is known (cf. remark below Eq. (3.9)): there, the dimensionless factor  $\alpha$  amounts to  $\frac{1}{4\pi}$ .

In Fig. D.1, we plot  $\alpha$  as a function of the inverse number of discretization sites  $1/N_x$  for different values of the cutoff  $\epsilon$  in the planar case. The values for  $\alpha$  depend linearly on  $1/N_x$  to a good approximation and appear to converge for different cutoffs  $\epsilon$  as  $1/N_x \rightarrow 0$ .

Next, we extrapolate the values for  $\alpha$  linearly to  $1/N_x = 0$ ; as the linearity persists to a good approximation for all values of  $N_x$  in Fig. D.1, it suffices to use only two data points for the extrapolation. We give two separate extrapolations for  $N_x = 80$ ,  $N_x = 100$  and  $N_x = 180$ ,  $N_x = 200$ , respectively. The result is plotted as a function of  $\epsilon$  in Fig. D.2. Recall that the analytical value for  $\alpha$  yields  $1/(4\pi) \approx 0.07958$  for the flat plate, which is chosen to be exactly the origin of the coordinate system in Fig. D.2.

The graphs in Fig. D.2 can in fact be divided into several regions. Consider, e.g., the lower curve: For values of  $\epsilon \lesssim 0.0045$ , the extrapolation  $1/N_x \rightarrow 0$  underestimates  $\alpha$  and even appears to diverge as  $\epsilon \rightarrow 0$ . This agrees with our expectation that the integrable

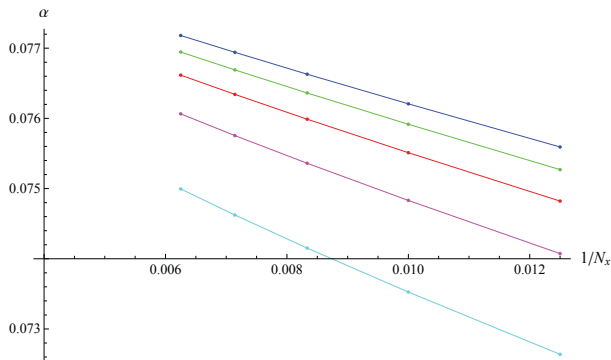


Figure D.1: Numerical values for the dimensionless contribution of the lowest-order trace term  $\alpha$  (3.5) in the plane-sphere configuration as a function of the inverse number of discretization sites  $N_x$  for five values of the cutoff parameter  $\epsilon$ ,  $\epsilon = 5 \times 10^{-5}, 2 \times 10^{-4}, 4 \times 10^{-4}, 6 \times 10^{-4}, 8 \times 10^{-4}$  from bottom to top. For fixed  $\epsilon$ , the result scales linearly with the discretization  $1/N_x$  to a good approximation and appears to converge with  $1/N_x \rightarrow 0$ , but it is also visible that the gradients of the curves grow as  $\epsilon \rightarrow 0$ .

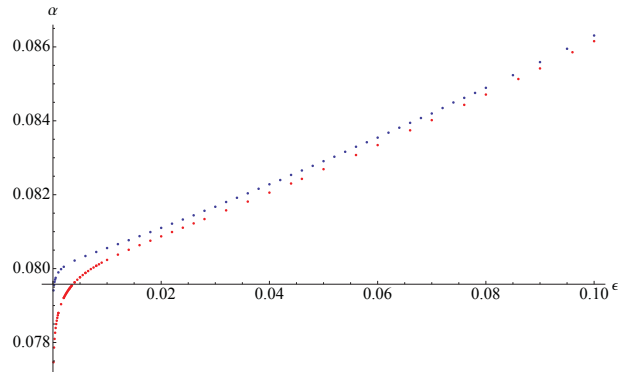


Figure D.2: Continuum limit for  $\alpha$  as defined in Eq. (3.5) after linear extrapolation to  $1/N_x \rightarrow 0$  (using  $1/N_x = 80$  and  $1/N_x = 100$  in the lower (red) and  $1/N_x = 180$  and  $1/N_x = 200$  data in the upper (blue) curve) as a function of the cutoff parameter  $\epsilon$  for values of  $10^{-4} < \epsilon < 0.1$ . The intersection between the two plot axes is chosen at  $\alpha = \frac{1}{4\pi}$ , which is the exact value for  $\alpha$  in the planar case.

singularity in the Green's function equation has not been properly resolved with the underlying discretization; higher values of  $N_x$  would be required for a more reliable estimate. This small- $\epsilon$  branch therefore corresponds to a region in parameter space where the result arising from the correct order of limits (first  $N_x \rightarrow \infty$ , then  $\epsilon \rightarrow 0$ ) is not yet visible.

At about  $\epsilon \gtrsim 0.01$ ,  $\alpha$  exhibits a clear linear growth with  $\epsilon$ . For  $\epsilon \gtrsim 0.04$ , higher power corrections become visible. We conclude that the cutoff-dependent factor  $\alpha(\epsilon)$  can well be approximated by a power series above the value of  $\epsilon \gtrsim 0.01$ ,

$$\alpha(\epsilon) = \alpha_0 + \alpha_1\epsilon + \alpha_2\epsilon^2 + \dots \quad (\text{D.3})$$

Thus, by extrapolating the values for  $\alpha$  to  $\epsilon = 0$  in the region where  $\alpha$  grows linearly with  $\epsilon$ , we obtain a cutoff-independent result  $\alpha_0$ . As for the extrapolation  $1/N_x \rightarrow 0$ , it suffices to use only two sites in  $\epsilon$  in the linear regime to extract  $\alpha_0$ ; of course, also more data points for a higher polynomial fit could easily be employed at the expense of computing time.

From Fig. D.2, we identify for the  $1/N_x = 80$  and  $1/N_x = 100$  data  $0.01 \lesssim \epsilon \lesssim 0.04$  as the region where  $\alpha(\epsilon)$  grows linearly with  $\epsilon$  with only very small higher-power corrections. Choosing the data points at  $\epsilon = 0.02$  and  $\epsilon = 0.025$  for a linear extrapolation, we obtain

$\alpha_0 = 0.07970$  which nicely matches the analytical value, the error being below 1%.<sup>1</sup> As a check of the continuum limit, an extrapolation using  $N_x = 180$  and  $N_x = 200$  sites (upper curve in Fig. D.2, again at  $\epsilon = 0.02$  and  $\epsilon = 0.025$ ) yields  $\alpha_0 = 0.0799554$ , which is also within 1% of the analytical value. The small deviations between these two results can be taken as a measure for the overall numerical uncertainty. One can see, that choosing larger values of  $N_x$  for the continuum extrapolation also results in an extension of the linear  $\epsilon$  regime to smaller  $\epsilon$  values.

It should be mentioned that the choice of required  $N_x$  values also depends on the corrugation parameters. For instance, for high values of the corrugation frequency, a better resolution is needed; as a rule of thumb, the lattice spacing  $a_x$  should always be smaller than the smallest dominant wave length of the corrugation. All numerical calculations for this work have been performed on a standard desktop computer with standard linear algebra packages. Depending on the discretization, the calculation of a typical data point including continuum limit and regulator removal takes on the order of seconds to several minutes. Since the linear-algebra routines scale with  $\sim N_x^3$ , the computational cost for very fine discretizations can rapidly increase.

---

<sup>1</sup>For the study of corrugated surfaces, we have carefully studied whether the interval linear in  $\epsilon$  is shifted and the extrapolation has to be adjusted accordingly. It turns out that the endpoints of the linear region are indeed slightly shifted for structured surfaces, but the sampling points  $\epsilon = 0.02$  and  $\epsilon = 0.025$  have always been in the linear region for all examples.

# Appendix E

## ALPs in high-intensity lasers at reversed interaction order

In this appendix we hand in the promised calculation for the conversion process at reversed interaction order. In the previous calculation, we have considered the interaction of two external lasers with frequencies  $\omega_{\perp}$  and  $\omega_{\parallel}$  with a probe beam  $\omega_{\text{in}}$ , in which the first, orthogonally propagating beam mediates the photon-axion conversion and the second, counter-propagating beam mediates the back-conversion from axions into photons.

However, if all beams are focused simultaneously onto the same spot as assumed in the setup, it is experimentally hardly distinguishable, which of the beams causes the conversion and back-conversion process, respectively. For this reason, we want to consider the process at interchanged interaction order  $\perp \leftrightarrow \parallel$ .

To this end, we employ the beam parameterization of the counter-propagating external beam, cf. Eqs. (5.24) and (5.25) for the photon-ALP-conversion process. Now, the electric as well as the magnetic component of the external field can interact which yields an extra factor of 2. Then, the ALP amplitude of Eq. (5.11) reads

$$\begin{aligned} \phi(z', t') = & g E_{\text{in}} E_{\parallel} \int_{-\infty}^{\infty} dz'' \frac{1}{\sqrt{1 + (z''/z_r^{\text{in}})^2}} \frac{1}{\sqrt{1 + (z''/z_r^{\parallel})^2}} \\ & \times \int_{-\infty}^{\infty} dt'' J_0 \left( m \sqrt{(t' - t'')^2 - |z' - z''|^2} \right) \theta \left( (t' - t'') - |z' - z''| \right) \\ & \times \sin \left( \omega_{\text{in}} t'' - k_{\text{in}} z'' + \arctan \left( \frac{z''}{z_r^{\text{in}}} \right) \right) \sin \left( \omega_{\parallel} t'' + k_{\parallel} z'' - \arctan \left( \frac{z''}{z_r^{\parallel}} \right) + \psi_{\parallel} \right) . \quad (\text{E.1}) \end{aligned}$$

We proceed analogously to the calculation in Chapt. 5 and perform the temporal integration after a substitution  $t'' \rightarrow t' - T$  and by virtue of of Eq. (5.13). Specializing

to  $|\omega_{\text{in}} \pm \omega_{\parallel}| > m$  and using the identity in Eq. (5.15) one finds that the equivalent to Eq. (5.14) reads

$$\begin{aligned} \phi(z', t') = & \frac{1}{4} g E_{\text{in}} E_{\parallel} \left[ \frac{i}{k_{\text{ax}}^+} e^{i(\omega_{\text{in}} + \omega_{\parallel})t'} e^{-i \text{sgn}(z' - z'') k_{\text{ax}}^+ z'} e^{i\psi_{\parallel}} \right. \\ & \times \int_{-\infty}^{\infty} dz'' \frac{1}{1 - i(z''/z_r^{\text{in}})} \frac{1}{1 + i(z''/z_r^{\parallel})} e^{i(-k_{\text{in}} + k_{\parallel} + \text{sgn}(z' - z'') k_{\text{ax}}^+) z''} \\ & - \frac{i \text{sgn}(\omega_{\text{in}} - \omega_{\parallel})}{k_{\text{ax}}^-} e^{i(\omega_{\text{in}} - \omega_{\parallel})t'} e^{-i \text{sgn}(z' - z'') \text{sgn}(\omega_{\text{in}} - \omega_{\parallel}) k_{\text{ax}}^- z'} e^{-i\psi_{\parallel}} \\ & \left. \times \int_{-\infty}^{\infty} dz'' \frac{1}{1 - i(z''/z_r^{\text{in}})} \frac{1}{1 - i(z''/z_r^{\parallel})} e^{i(-k_{\text{in}} - k_{\parallel} + \text{sgn}(z' - z'') \text{sgn}(\omega_{\text{in}} - \omega_{\parallel}) k_{\text{ax}}^-) z''} + \text{c.c.} \right], \quad (\text{E.2}) \end{aligned}$$

where here, according to the substitution  $\perp \leftrightarrow \parallel$ , the axion wave vector becomes a function of the frequency of the counter-propagating external field:  $k_{\text{ax}}^{\pm} = \sqrt{(\omega_{\text{in}} \pm \omega_{\parallel})^2 - m^2}$ .

Again, we find the characteristic structure of the ALP partial waves with frequencies  $\omega_{\text{ax}} = \omega_{\text{in}} \pm \omega_{\parallel}$ , which have transmitted ( $\text{sgn}(z' - z'') = +1$ ) and reflected ( $\text{sgn}(z' - z'') = -1$ ) contributions. The two remaining integrations over  $z''$  can be performed in the complex  $z''$ -plane. The respective integrals read

$$\begin{aligned} \int_{-\infty}^{\infty} dz \frac{\exp(i\delta k_{\parallel}^+ z)}{\left(1 - i\frac{z}{z_r^{\text{in}}}\right) \left(1 + i\frac{z}{z_r^{\parallel}}\right)} &= \frac{\pi z_r^{\text{in}} z_r^{\parallel}}{z_r^{\text{in}} + z_r^{\parallel}} \quad (\text{E.3}) \\ &\times \left[ (1 - \text{sgn}(\delta k_{\parallel}^+)) e^{\delta k_{\parallel}^+ z_r^{\text{in}}} + (1 + \text{sgn}(\delta k_{\parallel}^+)) e^{-\delta k_{\parallel}^+ z_r^{\parallel}} \right], \end{aligned}$$

$$\int_{-\infty}^{\infty} dz \frac{\exp(i\delta k_{\parallel}^- z)}{\left(1 - i\frac{z}{z_r^{\text{in}}}\right) \left(1 - i\frac{z}{z_r^{\parallel}}\right)} = -\frac{\pi z_r^{\text{in}} z_r^{\parallel}}{z_r^{\text{in}} - z_r^{\parallel}} \left[ (1 - \text{sgn}(\delta k_{\parallel}^-)) \left( e^{\delta k_{\parallel}^- z_r^{\text{in}}} - e^{\delta k_{\parallel}^- z_r^{\parallel}} \right) \right], \quad (\text{E.4})$$

where we have defined

$$\delta k_{\parallel}^+ = -k_{\text{in}} + k_{\parallel} + \text{sgn}(z' - z'') k_{\text{ax}}^+, \quad (\text{E.5})$$

$$\delta k_{\parallel}^- = -k_{\text{in}} - k_{\parallel} + \text{sgn}(z' - z'') \text{sgn}(\omega_{\text{in}} - \omega_{\parallel}) k_{\text{ax}}^-. \quad (\text{E.6})$$

In Eqs. (E.3) and (E.4), we encounter again the resonant structure of the conversion amplitude which can be attributed to the requirement of momentum conservation. As before, the sharp momentum cutoffs as induced by the signum functions are in fact relaxed by an integration over a finite interaction region. In analogy to the previous considerations, we determine the resonant mass  $m$ .

In vacuum, i.e.,  $\omega = k$  for fixed laser beam directions, Eqs. (E.5) and (E.6) become

$$\delta k_{\parallel}^{+} = -\omega_{\text{in}} + \omega_{\parallel} + \text{sgn}(z' - z'') \sqrt{(\omega_{\text{in}} + \omega_{\parallel})^2 - m^2} \stackrel{!}{\simeq} 0, \quad (\text{E.7})$$

$$\delta k_{\parallel}^{-} = -\omega_{\text{in}} - \omega_{\parallel} + \text{sgn}(z' - z'') \text{sgn}(\omega_{\text{in}} - \omega_{\parallel}) \sqrt{(\omega_{\text{in}} - \omega_{\parallel})^2 - m^2} \stackrel{!}{\simeq} 0. \quad (\text{E.8})$$

The condition in Eq. (E.7) is solved by setting

$$m \equiv m_{\parallel} = 2\sqrt{\omega_{\text{in}}\omega_{\parallel}} \quad (\text{E.9})$$

in the case of transmission for  $\omega_{\text{in}} > \omega_{\parallel}$  and reflection for  $\omega_{\text{in}} < \omega_{\parallel}$ . This can be understood intuitively: For momenta of the probe beam which are larger than the momenta of the counter-propagating beam, we find transmission, otherwise reflection of the ALP beam.

As in the previously considered setup, for  $\delta k_{\parallel}^{-}$  there exists no resonant mass. In the following, we thus again only keep the transmitted part of the sum-frequency solution  $\omega_{\text{ax}}^{+}$ . A justification for omitting the reflected part will be given below Eq. (E.15).

We have as a pendant to Eq. (5.22):

$$\begin{aligned} \phi^{(\text{T})}(z', t') \approx & -\frac{1}{2} \frac{\pi z_r^{\text{in}} z_r^{\parallel}}{z_r^{\text{in}} + z_r^{\parallel}} g E_{\text{in}} E_{\parallel} \frac{1}{k_{\text{ax}}^{+}} \sin((\omega_{\text{in}} + \omega_{\parallel})t' - k_{\text{ax}}^{+}z' + \psi_{\parallel}) \\ & \left[ (1 - \text{sgn}(\delta k_{\parallel}^{+})) e^{\delta k_{\parallel}^{+} z_r^{\text{in}}} + (1 + \text{sgn}(\delta k_{\parallel}^{+})) e^{-\delta k_{\parallel}^{+} z_r^{\parallel}} \right]. \quad (\text{E.10}) \end{aligned}$$

We now turn to the back-conversion of the ALPs into photons. However, as the external beam for the back-conversion propagates orthogonally to the  $z$ -axis, only the magnetic or electric field component can couple, cf. Eq. (5.23). However, due to the asymmetric coupling structure,  $e_{\text{out}}$  is not invariant under this choice, as discussed in Sec. 5.1.1.

As the ALP is massive, the contribution from the magnetic field component of the external beam will be larger, since it couples to the temporal derivative of  $\phi$ . We thus choose  $E_k^x = 0$  in the following.

Following the steps below Eq. (5.23), where  $B_k^y$  is now given through Eq. (5.9), we find that after the integrations over  $t'$  and  $z'$  for the back-conversion, we end up with

$$\begin{aligned} e_{\text{out}}(z, t) = & -\frac{1}{16} g^2 \pi^{3/2} \frac{z_r^{\text{in}} z_r^{\parallel}}{z_r^{\text{in}} + z_r^{\parallel}} w_0^{\perp} E_{\text{in}} E_{\parallel} E_{\perp} \frac{\omega_{\text{in}} + \omega_{\parallel}}{k_{\text{ax}}^{+}} \\ & \times \left[ (1 - \text{sgn}(\delta k_{\parallel}^{+})) e^{\delta k_{\parallel}^{+} z_r^{\text{in}}} + (1 + \text{sgn}(\delta k_{\parallel}^{+})) e^{-\delta k_{\parallel}^{+} z_r^{\parallel}} \right] \\ & \times \left[ \frac{1}{i} e^{i(\omega_{\text{in}} + \omega_{\parallel} + \omega_{\perp})(t - \text{sgn}(z - z')z)} e^{i(\psi_{\parallel} + \psi_{\perp})} e^{-\frac{1}{4}(w_0^{\perp} \delta k_{\perp}^{+})^2} \right. \\ & \left. - \frac{1}{i} e^{i(\omega_{\text{in}} + \omega_{\parallel} - \omega_{\perp})(t - \text{sgn}(z - z')z)} e^{i(\psi_{\parallel} - \psi_{\perp})} e^{-\frac{1}{4}(w_0^{\perp} \delta k_{\perp}^{-})^2} + \text{c.c.} \right], \quad (\text{E.11}) \end{aligned}$$

with the abbreviations

$$\delta k_{\perp}^{+} = -k_{\text{ax}}^{+} + \text{sgn}(z - z'')(\omega_{\text{in}} + \omega_{\parallel} + \omega_{\perp}) , \quad (\text{E.12})$$

$$\delta k_{\perp}^{-} = -k_{\text{ax}}^{+} + \text{sgn}(z - z'')(\omega_{\text{in}} + \omega_{\parallel} - \omega_{\perp}) . \quad (\text{E.13})$$

In Eq. (E.11), we encounter the familiar behavior of the reconverted photons. The outgoing electromagnetic wave is composed of two partial waves whose amplitude is tied to the vanishing of the sum of the momenta in the process:  $\delta k_{\perp}^{\pm}$ . As before, we are interested in the situation of concurrent momentum conservation in both conversion processes, under the constraint  $\omega_{\text{out}} \neq \omega_{\text{in}}$ . Thus, we rewrite Eqs. (E.12) and (E.13) as

$$-\delta k_{\perp}^{+} = \sqrt{(\omega_{\text{in}} + \omega_{\parallel})^2 - m^2} - \text{sgn}(z - z')(\omega_{\text{in}} + \omega_{\parallel} + \omega_{\perp}) \stackrel{!}{\simeq} 0 , \quad (\text{E.14})$$

$$-\delta k_{\perp}^{-} = \sqrt{(\omega_{\text{in}} + \omega_{\parallel})^2 - m^2} - \text{sgn}(z - z')(\omega_{\text{in}} + \omega_{\parallel} - \omega_{\perp}) \stackrel{!}{\simeq} 0 , \quad (\text{E.15})$$

where we have multiplied the equations by  $-1$ , which is justified since  $\delta k_{\perp}^{\pm}$  appears as a square in Eq. (E.11).

By comparing the above conditions for momentum conservation in the back-conversion process to the condition for the photon-ALP conversion in Eq. (E.7), we again find, that for positive frequencies only  $\delta k_{\perp}^{-}$  can be “matched” to the vanishing of  $\delta k_{\parallel}^{+}$  for transmission and the relation  $\omega_{\perp} = 2\omega_{\parallel}$ . As the frequency of the outgoing beam evaluates to  $\omega_{\text{out}} = \omega_{\text{in}} - \omega_{\parallel}$  in this situation, we again find that only the transmitted parts of both waves can propagate undamped, since the solution requires  $\omega_{\text{in}} > \omega_{\parallel}$  (cf. discussion below Eq. (E.8)).

In summary, we find for the outgoing electromagnetic wave at  $\omega_{\perp} = 2\omega_{\parallel}$  the transmitted part

$$e_{\text{out}}^{(\text{T})}(z, t) \approx \frac{1}{8} g^2 \pi^{3/2} \frac{z_r^{\text{in}} z_r^{\parallel}}{z_r^{\text{in}} + z_r^{\parallel}} w_0^{\perp} E_{\text{in}} E_{\parallel} E_{\perp} \frac{\omega_{\text{in}} + \omega_{\parallel}}{k_{\text{ax}}^{+}} e^{-\frac{1}{4}(w_0^{\perp} \delta k)^2} \\ \times \left[ (1 - \text{sgn}(\delta k)) e^{\delta k z_r^{\text{in}}} + (1 + \text{sgn}(\delta k)) e^{-\delta k z_r^{\parallel}} \right] \sin((\omega_{\text{in}} - \omega_{\parallel})(t - z) + \psi_{\parallel} - \psi_{\perp}) , \quad (\text{E.16})$$

where we have set  $\delta k_{\parallel}^{+} = \delta k_{\perp}^{-} = \delta k$ .

# Appendix F

## LSW via virtual MCPs: Re-extracting the zero-field limit

In this appendix we study how the zero-field auxiliary functions for “tunneling of the 3rd kind”, cf. Chapt. 6, can be regained from the full auxiliary functions for nonvanishing magnetic fields.

Whereas in the main text, cf. Sect. 6.1.2, the zero-field limit was extracted from a perturbative expansion of the polarization tensor, cf. Eq. (6.12), in this appendix we demonstrate that the zero-field limit can also be obtained from the full auxiliary functions valid for arbitrary field strengths, cf. Eqs. (6.33) and (6.34). This both serves as a consistency check for the full auxiliary functions and illustrates how the zero-field limit is contained in the nonperturbative result without the need to resort to a perturbative expansion.

However, the  $n$ -dependent decomposition of the  $\nu$ -integral as implemented in Eqs. (6.33) and (6.34) is of no avail for this purpose. Rather, it is more useful to apply the decomposition in Eq. (6.21) with  $n = 0$  to all terms in Eq. (6.14) as this then already coincides with the natural  $\kappa$ - and  $\lambda$ -decomposition in the zero-field limit (cf. Eqs. (6.24) and (6.25)). Apart from that, the calculation proceeds analogously, and Eq. (6.33) can be rewritten as

$$f_{\leq}^{(\text{full})} = \frac{12B\epsilon em^2}{\omega^4} \int_{\Re\sqrt{\frac{4m^2}{\omega^2}-1}}^{\infty} d\kappa \frac{1}{(1+\kappa^2)^{3/2} \sqrt{1+\kappa^2 - \frac{4m^2}{\omega^2}}} \times \left( \frac{e^{-\omega d \kappa}}{i + \kappa} + \sum_{n=1}^{\infty} \frac{2\kappa e^{-\omega d \sqrt{\kappa^2 + \frac{2\epsilon\epsilon B n}{m^2}(1+\kappa^2)}}}{\kappa^2 + \frac{2\epsilon\epsilon B n}{m^2}(1+\kappa^2) + i\sqrt{\kappa^2 + \frac{2\epsilon\epsilon B n}{m^2}(1+\kappa^2)}} \right). \quad (\text{F.1})$$

Whereas the  $n$ -independent term in Eq. (F.1) of course is not altered compared to Eq. (6.33), the contribution of the sum over  $n$  itself looks completely different. As before, the corresponding expression for  $f_{>}^{(\text{full})}$  immediately follows by setting  $\kappa \rightarrow -i\lambda$  and ad-



justing the integration boundaries accordingly. It thus is sufficient to limit the following discussion to  $f_{\leq}^{(\text{full})}$ .

Noting that the summation index  $n$  in Eq. (F.1) always appears in combination with a dimensionless factor of  $\frac{2\epsilon e B}{m^2}$ , we define  $\Delta l \equiv \frac{2\epsilon e B}{m^2}$  and rewrite Eq. (F.1) in the following form

$$f_{\leq}^{(\text{full})} = \frac{6m^4}{\omega^4} \int_{\Re\sqrt{\frac{4m^2}{\omega^2}-1}}^{\infty} d\kappa \frac{1}{(1+\kappa^2)^{3/2} \sqrt{1+\kappa^2 - \frac{4m^2}{\omega^2}}} \times \left( \Delta l \frac{e^{-\omega d \kappa}}{i+\kappa} + \sum_{n=1}^{\infty} \Delta l \frac{2\kappa e^{-\omega d \sqrt{\kappa^2+n\Delta l(1+\kappa^2)}}}{\kappa^2+n\Delta l(1+\kappa^2) + i\sqrt{\kappa^2+n\Delta l(1+\kappa^2)}} \right). \quad (\text{F.2})$$

In the limit  $B \rightarrow 0$  the first term vanishes, and the sum can be converted into an integral, setting  $n\Delta l \rightarrow l$  and  $\Delta l \rightarrow dl$ . This results in

$$f_{\leq}^{(\text{full})} \Big|_{B=0} = \int_{\Re\sqrt{\frac{4m^2}{\omega^2}-1}}^{\infty} d\kappa \frac{\frac{12m^4}{\omega^4} \kappa}{(1+\kappa^2)^{3/2} \sqrt{1+\kappa^2 - \frac{4m^2}{\omega^2}}} \times \int_0^{\infty} dl \frac{e^{-\omega d \sqrt{\kappa^2+l(1+\kappa^2)}}}{\kappa^2+l(1+\kappa^2) + i\sqrt{\kappa^2+l(1+\kappa^2)}}. \quad (\text{F.3})$$

Notably, the  $l$ -integral can be performed explicitly, yielding

$$f_{\leq}^{(\text{full})} \Big|_{B=0} = \frac{24m^4}{\omega^4} \int_{\Re\sqrt{\frac{4m^2}{\omega^2}-1}}^{\infty} d\kappa \frac{\kappa}{(1+\kappa^2)^{5/2}} \frac{1}{\sqrt{1+\kappa^2 - \frac{4m^2}{\omega^2}}} \text{E}_1 [i\omega d(1-i\kappa)], \quad (\text{F.4})$$

where  $\text{E}_1(x)$  denotes the exponential integral, defined as [177]

$$\text{E}_1(x) = \int_1^{\infty} dt e^{-xt} t^{-1} \quad \text{for } \Re(x) > 0. \quad (\text{F.5})$$

Using integration by parts

$$\frac{24m^4}{\omega^4} \int d\kappa \frac{\kappa}{(1+\kappa^2)^{5/2} \sqrt{1+\kappa^2 - \frac{4m^2}{\omega^2}}} = \frac{\sqrt{1+\kappa^2 - \frac{4m^2}{\omega^2}} \left(1+\kappa^2 + \frac{2m^2}{\omega^2}\right)}{(1+\kappa^2)^{3/2}} + C, \quad (\text{F.6})$$

with an integration constant  $C$ , Eq. (F.4) becomes

$$f_{\leq}^{(\text{full})} \Big|_{B=0} = \int_{\Re\sqrt{\frac{4m^2}{\omega^2}-1}}^{\infty} d\kappa e^{-\omega d \kappa} \frac{\sqrt{1+\kappa^2 - \frac{4m^2}{\omega^2}} \left(1+\kappa^2 + \frac{2m^2}{\omega^2}\right)}{(1+\kappa^2)^{3/2} (i+\kappa)}, \quad (\text{F.7})$$

and a surface term which vanishes for  $\omega \leq 2m$ , but not for  $\omega > 2m$  (note that a similar situation was encountered in Sect. 6.1.3 for the contribution  $\sim B^2$ ). Proceeding analogously with the  $\lambda$ -contribution, a corresponding expression for  $f_{>}^{(\text{full})}$  is obtained. The emerging surface term cancels with that in Eq. (F.7) for  $\omega > 2m$ , such that the surface terms can be omitted safely in both regimes,  $\omega \leq 2m$  and  $\omega > 2m$ , and the zero-field result can be written in the form of Eqs. (6.24) and (6.25).

# Danksagung (Acknowledgements)

An erster Stelle danke ich Holger Gies für sein fortgesetztes und beständiges Vertrauen in meine Arbeit. Neben seiner breiten physikalischen Expertise war seine durchwegs positive und ermutigende Sichtweise für mich eine unersetzliche Hilfe in den verschiedenen Projekten dieser Arbeit.

Für die Bereitschaft zur Übernahme des Zweitgutachtens und der damit einhergehenden Verpflichtungen, sowie für einige gute Diskussionen zu vielen Themen dieser Arbeit bedanke ich mich herzlich bei Jörg Jäckel.

Ein großer Dank gebührt der Deutschen Forschungsgemeinschaft für die Finanzierung der Arbeit innerhalb des Transregio 18 und die Unterstützung zur Teilnahme an zahlreichen Fachkonferenzen auch an fernen Orten durch den TR18 und das Graduiertenkolleg 1523. Der fachliche Austausch innerhalb des Transregio mit vielen Kollegen, insbesondere auch aus der Experimentalphysik war durchwegs lehrreich. Zudem hat die Möglichkeit, unbürokratisch exzellente Sprecher in das Seminar des Graduiertenkollegs einzuladen, diese Arbeit sehr befördert. Dafür sei auch dem Sprecher des Kollegs, Andreas Wipf, herzlich gedankt.

In Sachen Casimir unterstützte mich nach Kräften immer insbesondere Maarten DeKieviet. Desweiteren danke ich Thorsten Emig und Serge Reynaud für einige konstruktive Gespräche in diesem Zusammenhang. Nicht unerwähnt lassen möchte ich die Kollaboration mit Frank Glowna, der das Projekt in seiner Diplomarbeit erfolgreich weitergeführt hat.

Kompetente Ansprechpartner zu experimentellen Möglichkeiten gepulster Magnete und von Gravitationswelleninterferometern, waren insbesondere Achamveedu Gopakumar, Thomas Herrmannsdörfer, sowie Gerhard Schäfer.

Für einige Momente der Erleuchtung in meinem Verständnis der Laserphysik danke ich den Experimentalisten vom Institut für Quantenoptik und den Kollegen des Transregio 18, darunter insbesondere Maria Nicolai, sowie Malte Kaluza und Gerhard Paulus.

Die Überwindung scheinbar undurchscheinbarer Barrieren wurde ermöglicht durch die sehr gute Zusammenarbeit mit Felix Karbstein und manches Gespräch mit Norman Neitz. Für gewinnbringende Diskussionen über verschiedene Teilaspekte dieser Arbeit sei insbesondere Gerald Dunne, Tom Heinzl, Ben King, Antonino Di Piazza, Andreas Ringwald, Javier Redondo, sowie Giuseppe Ruoso gedankt. Zudem freue ich mich sehr über Gerald Dunes und Tom Heinzls Bereitschaft zur Erstellung von Gutachten zu dieser Arbeit.

Für weiterführende Diskussionsfreude im Büro bedanke ich mich bei Astrid Eichhorn und Daniel Scherer, sowie den weiteren Mitgliedern des Heidelberger Journal-Club Imports. Besten Dank auch für Korrekturvorschläge zur Arbeit v.a. an Astrid, Javier und Felix.

Nicht für fachliche, obschon sicher nicht weniger wichtige Unterstützung danke ich meiner Familie, der engsten Verwandtschaft und zahlreichen guten Freunden. Ihr Rückhalt gerade in Zeiten, in denen ein einzelner Mensch schwerlich auf sich alleine gestellt funktionieren kann, hat mich durch ebenjene getragen.

Diese Arbeit sei dem Andenken an meinen Vater gewidmet.

# Ehrenwörtliche Erklärung

Ich erkläre hiermit ehrenwörtlich, daß ich die vorliegende Arbeit selbständig, ohne unzulässige Hilfe Dritter und ohne Benutzung anderer als der angegebenen Hilfsmittel und Literatur angefertigt habe. Die aus anderen Quellen direkt oder indirekt übernommenen Daten und Konzepte sind unter Angabe der Quelle gekennzeichnet. Auch die Ergebnisse, die in Zusammenarbeit mit den Mitgliedern des Lehrstuhles für Quantenfeldtheorie in Jena und anderen Kooperationen entstanden sind, sind in der Arbeit entsprechend benannt.

Weitere Personen waren an der inhaltlich-materiellen Erstellung der vorliegenden Arbeit nicht beteiligt. Insbesondere habe ich hierfür nicht die entgeltliche Hilfe von Vermittlungs- bzw. Beratungsdiensten (Promotionsberater oder andere Personen) in Anspruch genommen. Niemand hat von mir unmittelbar oder mittelbar geldwerte Leistungen für Arbeiten erhalten, die im Zusammenhang mit dem Inhalt der vorgelegten Dissertation stehen. Die Arbeit wurde bisher weder im In- noch im Ausland in gleicher oder ähnlicher Form einer anderen Prüfungsbehörde vorgelegt.

Die geltende Promotionsordnung der Physikalisch-Astronomischen Fakultät ist mir bekannt.

Ich versichere ehrenwörtlich, dass ich nach bestem Wissen die reine Wahrheit gesagt und nichts verschwiegen habe.

Jena, den 20.10.2011

Babette Döbrich